University of Alberta

Application of femtosecond laser pulses to cells, tissues and embryos

by

Vikram Kohli

©

A thesis submitted to the Faculty of Graduate Studies and Research
in partial fulfillment of the requirements for the degree of

Doctor of Philosophy

Department of Electrical and Computer Engineering

Edmonton, Alberta
Fall 2008

Library and
Archives Canada

Published Heritage
Branch

395 Wellington Street
Ottawa ON K1A 0N4
Canada

Bibliothèque et
Archives Canada

Direction du
Patrimoine de l'édition

395, rue Wellington
Ottawa ON K1A 0N4
Canada

Your file Votre référence
ISBN: 978-0-494-46349-9
Our file Notre référence
ISBN: 978-0-494-46349-9

NOTICE:
The author has granted a non-exclusive license allowing Library and Archives Canada to reproduce, publish, archive, preserve, conserve, communicate to the public by telecommunication or on the Internet, loan, distribute and sell theses worldwide, for commercial or non-commercial purposes, in microform, paper, electronic and/or any other formats.

The author retains copyright ownership and moral rights in this thesis. Neither the thesis nor substantial extracts from it may be printed or otherwise reproduced without the author's permission.

AVIS:
L'auteur a accordé une licence non exclusive permettant à la Bibliothèque et Archives Canada de reproduire, publier, archiver, sauvegarder, conserver, transmettre au public par télécommunication ou par l'Internet, prêter, distribuer et vendre des thèses partout dans le monde, à des fins commerciales ou autres, sur support microforme, papier, électronique et/ou autres formats.

L'auteur conserve la propriété du droit d'auteur et des droits moraux qui protège cette thèse. Ni la thèse ni des extraits substantiels de celle-ci ne doivent être imprimés ou autrement reproduits sans son autorisation.

In compliance with the Canadian Privacy Act some supporting forms may have been removed from this thesis.

While these forms may be included in the document page count, their removal does not represent any loss of content from the thesis.

Conformément à la loi canadienne sur la protection de la vie privée, quelques formulaires secondaires ont été enlevés de cette thèse.

Bien que ces formulaires aient inclus dans la pagination, il n'y aura aucun contenu manquant.

Canada

Any fool can make things bigger, more complex, and more violent. It takes a touch of genius-and a lot of courage-to move in the opposite direction

A. Einstein

I am convinced all of humanity is born with more gifts than we know. Most are born geniuses and just get de-geniused rapidly.

Richard Buckminster Fuller

In loving memory of Dr. Joe Anderson & Sam Alexander:
A friend, a father and a mentor

Abstract

This thesis explores the novel applications of femtosecond laser pulses as a tool for manipulating complex biological systems. Chapter 1 begins with a brief introduction on our current understanding of femtosecond laser pulse interactions with biological material. Much of what we know about the interaction process is based on theoretical simulations and assumptions, but this nevertheless provides an important framework for understanding why femtosecond lasers have received widespread attention. In this chapter, the non-linear multiphoton absorption and cascade ionization processes are discussed, along with ionized electron densities, shockwave and cavitation bubble formation.

With an understanding of the laser-tissue interaction process, Chapter 2 presents results on cell isolation and membrane surgery of living mammalian cells. Using focused femtosecond laser pulses, focal adhesions joining fibroblast cells were successfully removed, providing a novel method for cell isolation. Fibroblast isolation was shown to occur without inducing morphological damage to the cells. Membrane surgery was also performed on living cells. Dissection cuts were made along both the short and long axes of the cell. After membrane dissection, the cell maintained its morphology without evidence of cell collapse or disassociation.

Chapter 3 discusses the use of femtosecond laser pulses to transiently permeabilize living mammalian cells for the introduction of exogenous foreign material. Individual cells were laser pulse permeabilized in the presence of a hyperosmotic carbohydrate solution. Material delivery was confirmed by measuring the volumetric response of cells permeabilized in varying osmolarities of sugar. The survival of

permeabilized cells in increasing hyperosmotic solutions was assessed using a membrane integrity assay. The intracellular accumulation of the sugar was theoretically determined using diffusion analysis.

Further demonstrating the novelty of the femtosecond laser, laser pulse surgery of an aquatic embryo, the zebrafish (*Danio rerio*), was also performed, Chapter 4. Utilizing transient pores that were formed in the embryonic cells of the zebrafish, an exogenous fluorescent probe, FITC, Streptavidin-conjugated quantum dots or plasmid DNA encoding EGFP (sCMV-EGFP) was introduced into the developing embryonic cells. Both FITC and the conjugated quantum dots were found to disperse throughout the cells as cleavage divisions of the blastomeres occurred. Gene expression of the plasmid DNA was seen in embryos reared to 24 hrs in various cells of the zebrafish body.

To determine if the laser pulse induced any short- or long-term effects on development, laser pulse manipulated embryos were reared to 2 and 7 days post-fertilization and compared to control embryos at the same developmental stages, Chapter 5. Light microscopy and scanning electron microscopy were used to compare whole body mosaics of the developed larvae. Key developmental morphological structures that were examined included the zebrafish fins, the ear, the olfactory pit and the neuromast patterning.

Chapter 6 concludes the thesis by presenting a brief discussion of future prospects for the applications of femtosecond laser pulses.

Preface

This thesis is an interdisciplinary body of work that includes research topics in physics, engineering, cell biology and developmental biology. By combining engineering and physics principles with biological ones, this thesis attempts to demonstrate to engineers, physicists and biologists the importance of the reported engineering tool to a wide range of scientific disciplines. By definition, the term 'engineering' is an 'applied science.' Engineering tools, such as microscopes and macro/nano-manipulators, are often used to assist us in solving scientific problems with real world applications. In a similar fashion, in this thesis, engineering principles and tools, including femtosecond laser systems and various optical elements, were used to advance our understanding of biophysics and to solve relevant biomedical problems. Qualitative and especially quantitative analyses of experimental findings put the results into context and allowed for continuous improvements to the application of the femtosecond laser tool.

The goal of this work was to investigate the application of femtosecond laser pulses to cells, tissues and embryos. Specific applications that were pursued included the membrane surgery and dissection of living cells and the permeabilization of cells and embryos for the introduction of exogenous carbohydrates, fluorescent reporter molecules, quantum dots or DNA. While a large part of the results presented in this thesis have been discussed in a biological context, a firm foundation in engineering and physics principles was essential. For instance, to deliver the laser pulses, a microscope system was designed that could accurately focus the femtosecond lasers pulses to a location on or within the biological system studied. The choice of using femtosecond laser pulses over longer pulse durations (i.e. nanoseconds) required an understanding of the laser-tissue interaction process, including the non-linear multiphoton absorption process, the cascade/impact ionization process and an estimate of the electron density and the temperature rise after the pulse. In addition, the effect of cavitation bubble formation on the permeable state of the laser pulse generated pore and how these gas bubbles hindered passive diffusion were addressed. Estimates of the intracellular accumulation of an exogenous probe into cells and their respective kinetic responses were both analyzed using engineering insights.

Acknowledgements

Special thanks to my supervisor, Dr. A. Y. Elezzabi, for his continued support and motivation.

Thank you to Dr. D. Ali and his lab members for introducing me to the zebrafish. Your initial help in setting up our own zebrafish colony and the many hours discussing zebrafish care and development were greatly appreciated.

Thank you to Dr. A. Waskiewicz and his lab members for allowing me access to their zebrafish facility. Thank you to Patricia Gongal for preparing the plasmid construct and to Timothy Erickson and Laura Reaume for their assistance and training in microinjection. A special thanks to Dr. A. Waskiewicz for his time spent in educating me about plasmid constructs and zebrafish morphology, as well as his time spent reading manuscripts and providing helpful criticisms.

Thank you to Dr. G. Goss and his lab members for their assistance in performing heat shock analysis studies. A special thanks to Elizabeth Eorr for her preparation and analysis of the Western blots.

Thank you to Dr. L. McGann and his lab members for helping me understand cryopreservation and transport equations. A special thanks to Dr. H. Elmoazzen for her time spent teaching me aspects of mass transport.

Thank you to Dr. J. Acker and his lab members for their assistance in cell culture. A special thanks to Jelena Holovati and Kirby Scott for their continual support and encouragement.

Thank you to Dr. V. Robles and Dr. L. Cancela for their plasmid construct and the antifreeze protein. A special thanks to Dr. V. Robles for her countless hours spent assisting me in several of the published zebrafish studies and educating me in cryobiology.

Thank you to Rakesh Bhatnagar, Randy Mandryk and Jack Scott of the Biological Microscopy Facility for their advice, assistance and training in zebrafish SEM and TEM.

Thank you to the Electrical and Computer Engineering machine shop for their excellent workmanship.

Thank you to my lab members, John Holtzman, Scott Irvine, Ken Chau, Michael Quong, Corey Baron and Pouya Maraghechi for their general camaraderie. A special thank you to Michael Quong for his assistance in SEM imaging and the numerous hours spent discussing important physics and engineering principles with me. Your help was greatly appreciated.

Thank you to my committee members for their suggestions for improving the readability of this thesis.

Thank you to Mr.s. Nancy Anderson and Mr. Roger Marquis for their support and encouragement.

Thank you to my parents, without your love and support I would not be where I am today.

Lastly, to Ms. Jane Anderson, no words can express my gratitude. You stood by me throughout this endeavor. Without your constant support, encouragement and help, this thesis would not have been possible.

Table of Contents

1.0 FEMTOSECOND LASER PULSE INTERACTIONS WITH BIOLOGICAL MATERIALS

1.1 Introduction pg. 2-3

1.2 Laser-Tissue Interaction pg. 4-20

  Linear and nonlinear processes in laser-tissue interaction pg. 4-9

  Laser pulse ablation profile pg. 9-11

  Laser pulse induced heat stress pg. 11-13

  Shockwave and Cavitation bubble formation pg. 13-16

  Differences between 80 MHz and 1 KHz laser pulse ablation pg. 17

  Critical power for self-focusing and plasma formation pg. 18-20

2.0 CELL ISOLATION AND MEMBRANE SURGERY USING FEMTOSECOND LASER PULSES

2.1 Introduction pg. 22-30

  Mechanical Cell Manipulation Techniques pg. 24

  Ultraviolet and Near Infrared Laser Cell Manipulation Techniques pg. 24-27

  Purpose of this study pg. 28

  Cell line model systems pg. 28-29

  Potential applications pg. 29-30

2.2 Results and Discussion pg. 31-46
Experimental methodology pg. 31-37
Cell Isolation of V79-4 cells pg. 37-40
Membrane Surgery of MDCK cells pg. 40-42
Mechanism and action of femtosecond laser pulse surgery pg. 42-46

3.0 REVERSIBLE PERMEABILIZATION USING FEMTOSECOND LASER PULSES

3.1 Introduction pg. 48-59
Cryopreservation of biological materials pg. 50-52
A biological approach to cell permeabilization pg. 52-54
An electrical approach to cell permeabilization pg. 55-56
Femtosecond laser pulse induced cell permeabilization pg. 57
Purpose of this study pg. 58-59
3.2 Results and Discussion pg. 60-85
Experimental methodology pg. 60-62
Femtosecond laser pulse permeabilization of the plasma membrane pg. 62-64
Carbohydrate uptake into permeabilized cells pg. 65-68
Kinetic responses of laser pulse permeabilized cells pg. 68-72
Femtosecond laser pulse induced pore dynamics pg. 72-73
Reversible character of femtosecond laser pulse induced pores pg. 73-74
Survival analysis of femtosecond laser pulse porated cells pg. 74-78

Pore widening hypothesis pg. 78-83
Intracellular delivered carbohydrate concentration pg. 83-85

4.0 THE DELIVERY OF EXOGENOUS FOREIGN MATERIALS INTO DEVELOPING EMBRYONIC CELLS USING FEMTOSECOND LASER PULSES

4.1 Introduction pg. 87-103
The Zebrafish model system (*Danio rerio*) pg. 89-95
The manipulation of complex biological systems pg. 95-98
Laser manipulation of complex biological systems pg. 99-101
Purpose of this study pg. 101-103
4.2 Results and Discussion pg. 104-151
Experimental methodology pg. 104-111
The effect of femtosecond laser pulses on short-term zebrafish development pg. 111-115
Femtosecond laser pulse induced transient pore formation in dechorionated embryos pg. 115-118
The effect of blastomere patterning on fluorescence distribution pg. 119
Loading efficiency of FITC into dechorionated embryos pg. 119-123
Hypothesized mechanism of FITC uptake pg. 123-124
The chorion: a non-cellular embryonic barrier pg. 124-125

Transient pore formation at the blastomere-yolk interface in chorionated embryos pg. 125-129

Direct injection of FITC into developing blastomere cells pg. 129-130

Differences in FITC signal intensity for blastomere-yolk and blastomere injection pg. 130-134

The reactivity of FITC pg. 134

Delivery of exogenous quantum dots into developing blastomere cells pg. 134-138

Delivery of exogenous plasmid DNA into developing blastomere cells pg. 138-143

Femtosecond laser pulse excitation of the exogenous solution pg. 143-144

Transfection rates pg. 144-146

Femtosecond laser pulse poration pg. 146-147

Laser conditions for permeabilization pg. 147-148

Survivability of femtosecond laser pulse manipulated zebrafish embryos pg. 148-151

5.0 FEMTOSECOND LASER PULSE SURGERY AND DEVELOPMENT OF ZEBRAFISH EMBRYOS

5.1 Introduction pg. 153-156

Purpose of this study pg. 155-156

5.2 Results and Discussion pg. 157-194

Experimental methodology pg. 157-158
Note on figures pg. 158-159
Terminology defined pg. 159
Optimal laser parameters for the ablation of embryonic cells pg. 159-162
Cavitation bubble formation and surface scarring pg. 162-166
Qualititative assessment of blastomere-fluorescence as a function of beam dwell time pg. 166-173
Quantitative assessment of blastomere-fluorescence as a function of beam dwell time pg. 173-175
Developmental lag time pg. 175-176
Short-term effects of femtosecond laser pulse manipulation on morphological development pg. 176-183
Long-term effects of femtosecond laser pulse manipulation on morphological development pg. 183-194

6.0 CONCLUSION AND FUTURE PROSPECTS

6.1 Conclusion and future prospects pg. 196-203
A physiological study pg. 197-200
Future prospects pg. 200-203

APPENDIX A

A.1 Estimate of the pulse duration pg. 205-207
A.2 Sample calculations pg. 208-211

APPENDIX B

B.1 Calculation of the sucrose diameter pg. 213

APPENDIX C

C.1 Poration Injury: Induced pressure on the laser pulse induced pore pg. 215-216

APPENDIX D

D.1 Sucrose and water volume contribution pg. 218-219

APPENDIX E

E.1 Filter cube pg. 221-222
E.2 Fluorescence filters: Excitation and emission wavelengths pg. 223

APPENDIX F

Chapter 2 Materials and Methods pg. 226-230
- Preparing the Biosafety Cabinet pg. 226
- Preparation of culture media pg. 226
- Culture preparation pg. 226-227
- Media exchange pg. 227-228
- Preparation of a subculture pg. 228-229
- Harvesting and plating of cells pg. 229
- Laser pulse surgery of living cells pg. 229-230

Chapter 3 Materials and Methods pg. 232-239

Cell culture preparation pg. 232

Cell micropatterning pg. 232

Photolithography pg. 232-233

Preparation of the polydimethylsiloxane stamps pg. 233

Patterning of glass coverslips with agarose pg. 233

Preparation of SYTO 13™ and Ethidium bromide pg. 233-234

Cell viability assessment pg. 234

Cell volume measurements pg. 234

Preparation of sucrose pg. 235

Estimating the intracellular solute concentration pg. 235-237

Calculation of the diffusion coefficient pg. 237-238

Reversible permabilization of living cells pg. 238-239

Chapter 4 Materials and Methods

Zebrafish care pg. 241

Breeding process pg. 241

Embryo dechorionation pg. 241-242

Preparation of Fluorescein Isothiocyanate (FITC) pg. 242

Preparation of Streptavidin-Conjugated quantum dots pg. 242-243

Preparation of Simian-CMV-EGFP pg. 243

Fluorescence imaging pg. 243

Laser optical setup pg. 243-245

Laser pulse poration, exogenous material delivery and survival analysis pg. 245-246

Chapter 5 Materials and Methods

Zebrafish care pg. 248

Breeding and harvesting of embryo pg. 248

Embryo dechorionation process pg. 248-249

Preparation of Fluorescein Isothiocyanate (FITC) pg. 249

Fluorescence imaging pg. 249

Zebrafish development, survival and morphological integrity pg. 250

Zebrafish rearing media pg. 250-251

The fixing and mounting of embryos for SEM pg. 251-252

Sputtering and SEM imaging pg. 252-253

Optical system, laser pulse poration and delivery pg. 253-254

Image analysis pg. 254

REFERENCES pg. 256-277

CURRICULUM VITAE

Supplementary CD video list

CHAPTER 3.0

Additional File 1: A micropatterned MDCK laser pulse porated in the presence of 0.2 M sucrose.

Additional File 2: A micropatterned MDCK laser pulse porated in the presence of 0.5 M sucrose.

CHAPTER 4.0

Additional File 1: A laser pulse manipulated embryo that has developed to pec-fin stage.

CHAPTER 5.0

Additional File 1: Video depicting cavitation bubble formation and surface scarring of a blastomere cell. Embryo was chorionated and at the 2-cell stage.

Additional File 2: Video depicting the dorsal view of a laser-manipulated embryo developed to 5 dpf.

EXTRA VIDEOS NOT MENTIONED IN THE THESIS

Additional File 1: Video depicting zebrafish development from early 2-cell stage to hatch. The sequence of development was taken over a period of two days.

List of Tables

Table 4.1: Survival and loading assessment pg. 122

Table 5.1: Laser pulse surgical ablation of individual blastomere cells – Summary pg. 163

Table B.1: Common bond lengths. Values reproduced from [176]. pg. 213

List of figures

Figure 1.1: Diagram contrasting multiphoton absorption and single photon absorption. For multiphoton absorption, it is assumed that the energy per photon is 1.55 eV corresponding to a wavelength of 800 nm. The absorption of three simultaneous photons is required to elicit an electron transition from the lower state to the upper state. In single photon absorption, one photon excites the electron to the upper state. However, for this transition to occur, the excitation wavelength must be 266 nm (1/3rd of 800 nm) with a photon energy of 4.65 eV. pg. 5

Figure 2.1: Adherent junctions formed between two epithelial cells. In the intercellular space, transmembrane proteins of each cell connect and terminate at a linker protein on the intracellular side of the membrane. Attached to the linker protein are actin bundles, which extend throughout the cell. Through the interaction of actin with other linker-transmembrane proteins, an adherein belt is formed. Adjacent cells are mechanically coupled via actin and the junctional complex. An extracellular matrix (ECM) is located beneath the bastolateral surface of the cell. The above figure was adapted from [29]. pg. 22

Figure 2.2: Transparent front view of the modified upright Zeiss light microscope. Femtosecond laser pulses were coupled into the rear port of the microscope and reflected by the gold beam splitter towards the microscope objective lens, D. A – ocular imaging head, B – filter chamber, C – objective nose piece, D – microscope objective lens, E – *x-y-z* motorized stage, F – white light condenser and G – white light source. pg. 32

Figure 2.3: Rear view of the microscope shown in Figure 2.2. Femtosecond laser pulses were coupled into the rear port of the microscope, as shown above. A – ocular imaging head, B – filter chamber. pg. 33

Figure 2.4: Transparent side view of Figure 2.2. The femtosecond laser pulses were directed into the rear port of the microscope and were reflected by the gold beam splitter towards the microscope objective lens, D. Back reflected laser light and white light travel back up towards the filter chamber, B, and were captured at the imaging port (back reflected white light is not shown). A – ocular imaging head, B – filter chamber, C – objective nose piece, D – microscope objective lens, E – *x-y-z* motorized stage, F – white light condenser and G – white light source. pg. 35

Figure 2.5: Sub-10 femtosecond laser pulses produced from a modelocked titanium sapphire laser oscillator, with a center wavelength at 800 nm and a pulse repetition rate of 80 MHz, were coupled and focused onto the biological specimen by a 0.95 100X high numerical aperture air microscope objective. The biological sample was placed on a *x-y-z* motorized temperature controlled stage, cooled to 4 °C. White light illuminated the sample in the inverted position, where both the white light and the laser light were captured by a charge coupled device (CCD). The CCD was interfaced with a computer (not shown) allowing for the capture of still images and real time video. pg. 38

Figure 2.6: Live video observation of single cell isolation of living V79-4 cells. (a) Arrows indicate two fibroblast cells that are tethered together by a focal adhesion (width of the tethered region is ~ 1 μm) with the dotted line representing the dissection interface relative to which the cells are scanned for the removal of the focal adhesion. (b) The focused laser pulse was scanned along the dissection interface between the V79-4 cells,

resulting in the removal of the tethered region, (c). The dotted boxes in (c) and (d) depict the isolated curled fibroblast librated from its adjoining cell. Pulse energy used for single cell isolation was 5 nJ/pulse. pg. 39

Figure 2.7: (a) Depicts membrane surgery of a live MDCK cell. Three surgical incisions were made along the short axis of the 12 μm cell. The arrows in (a) represent the ablated extracellular matrix that is secreted by the cell. Scanning the cell along its long axis, (b) and (c), three additional membrane dissection cuts were made. Post-membrane surgery, the cell maintained its morphology without evidence of cell collapse, disassociation or bleb formation. It is suggested that single cell isolation of MDCK cells is realizable by tracing the exterior contour of the cell (see text for details). In (a), (b) and (c) the bright spot represents the focused laser pulse. Pulse energy used for membrane surgery was 5 nJ/pulse. pg. 41

Figure 3.1: Graphic depicting laser pulse induced permeabilization. (a) A cell is initially suspended in an exogenous solution containing a foreign molecule to be introduced. Focused femtosecond laser pulses are localized on the cell plasma membrane for creating a transient plasma membrane disruption, (b). Temporary disruption of the plasma membrane allows the foreign molecule to diffuse into the cell, (b). The membrane rapidly re-seals (c) with the delivered content localized in the intracellular space of the cell. pg. 49

Figure 3.2: The H5 hemolysin pore forming toxin. Alpha-hemolysin monomers secreted by the bacterium *Staphylococcus* oligomerize at the plasma membrane to create a transmembrane pore that extends into the intracellular environment. The transmembrane pore is hydrophilic and allows impermeable solutes to cross the plasma membrane to be

localized in the intracellular space. Figure adapted from Sigma-Aldrich, Canada. pg. 53

Figure 3.3: Electroporation. (a) A cell is suspended in an exogenous solution containing a foreign molecule to be introduced into the cell. Application of electrical pulses causes the cell plasma membrane to be disrupted, (b). Disruption to the cell membrane allows the foreign molecule to diffuse into the cell. (c) After the membrane has re-sealed, the desired foreign molecule is localized in the intracellular environment of the cell, (c). pg. 56

Figure 3.4: Brightfield and fluorescence image of micropatterned MDCK cells that were laser pulse targeted using a pulse energy of 5 nJ/pulse and a gated shutter time of ~ 10 ms. (a) Arrows indicate the cells that were selectively chosen for laser pulse permeabilization. Approximately 10 to 20 min post-laser pulse targeting, the cells underwent a dual fluorescence membrane integrity assay with SYTO 13 and EB. (b) After the addition and removal of SYTO 13/EB, the micropatterned cells were imaged under epi-fluorescence. Targeted cells (arrows) were positive for EB fluorescence indicating that the cells were successfully permeabilized. As expected, all non-targeted cells were positive for SYTO 13 only. pg. 63

Figure 3.5: Depicts the swelling response of MDCK cells laser pulse permeabilized in the presence of 1.0 M sucrose. (a) Three cells in close contact are shown at hypertonic volume. A single cell was selected for permeabilization with the arrow indicating the focused femtosecond laser spot. (b) Post-laser pulse targeting, the cell increased in cellular volume (arrow) towards a new hypertonic equilibrium volume. The change from hypertonic to equilibrium volume was found to be approximately 60 %. The cell was permeabilized using a pulse energy of 5 nJ/pulse and a gated shutter time of ~ 10 ms. pg. 66

Figure 3.6: Depicts the volumetric kinetic graph of a single cell permeabilized in 0.2 M sucrose. Before permeabilization the cell was initially at hypertonic volume. Following laser pulse poration, the volume of the cell quickly increased as a function of time plateauing at ~ 200 ms. V_{equil} was the measured volume at the new hypertonic state. Volume measurements were made using ImageJ analysis software. The single cell was permeabilized with a pulse energy of 3.3 nJ/pulse and a gated shutter time of ~ 10 ms. pg. 70

Figure 3.7: Brightfield and fluorescence images of micropatterned cells permeabilized in the presence of 0.2 M sucrose using a pulse energy of 3.3 nJ/pulse and a gated shutter time of ~ 10 ms. (a) The numbers indicate the selected cells that were permeabilized. (b) 30 to 40 min post-laser pulse poration, the cells were stained with a dual fluorescence membrane integrity assay composed of SYTO 13 and EB. Epi-fluorescence revealed that all porated cells had intact membranes as determined from the lack of EB fluorescence. Labeled cell number 5 detached from the well after the cells were rinsed with fresh culture media for removing the extracellular carbohydrate. Scale bars for (a) and (b) represent 40 and 100 μm, respectively. pg. 75

Figure 3.8: Brightfield and fluorescence images of micropatterned cells permeabilized in the presence of 0.5 M sucrose using a pulse energy of 3.3 nJ/pulse and a gated shutter time of ~ 10 ms. (a) The numbers indicate the selected cells that were permeabilized. (b) 30 to 40 min post-laser pulse poration, the cells were stained with a dual fluorescence membrane integrity assay composed of SYTO 13 and EB. Epi-fluorescence revealed that all porated cells had damaged permeable membranes as evidenced by the presence of intracellular EB fluorescence. Scale bar for (a) and (b) represent 40 and 100 µm, respectively. pg. 76

Figure 3.9: Depicts the trend in cell survival for cells laser pulse porated in increasing osmolarities of sucrose. Survival was assessed based on the SYTO 13/EB assay. Highest cell survival was observed for micropatterned cells permeabilized in 0.2 M sucrose. A progressive decrease in cell survival was observed as the concentration of sucrose increased. No cells survived in an extracellular osmolarity of 0.5 M sucrose. All cells permeabilized in their respective sucrose concentration were laser pulse porated with a pulse energy of 3.3 nJ/pulse and a gated shutter time of ~ 10 ms. pg. 77

Figure 3.10: Diffusion profile for micropatterned cells permeabilized in 0.2 M sucrose. The cell was permeabilized using a pulse energy of 3.3 nJ/pulse and a gated shutter time of ~ 10 ms. With the time for pore closure and the membrane thickness set to constant values of 200 ms and 5 nm, the estimated concentration on the inner intracellular side of the membrane was estimated to be 0.199 M. The inset shows the diffusion profile for long diffusion lengths. Setting the diffusion length to the average diameter of a MDCK cell, 14.85 µm, the estimated concentration was found to be 0.13 M. pg. 82

Figure 4.1: Adult zebrafish. Image was taken from www.fishbase.org. pg. 90

Figure 4.2: A 4-cell stage embryo developing within its chorion. Morphological structures that have been emphasized include the blastomere cells, the perivitelline space, the yolk cell and the chorion. The animal pole is located above the dividing blastomere cells, while the opposite side (bottom of the yolk cell) is the vegetal axis (i.e. vegetal pole). The dorsal-ventral axis cannot be defined in the above image. One would have to wait until epiboly, specifically when involution and convergence occurs, to define the dorsal-ventral axis [90]. pg. 92

Figure 4.3: A top view SEM image of an 8-cell stage dechorionated zebrafish embryo. The blastomere cells and the yolk cell have been indicated. Scale bar represents 100 μm. pg. 93

Figure 4.4: Sequence of images depicting zebrafish development from 2-cell stage to hatch. The barrier surrounding the developing embryo is the chorion. The embryo continues to differentiate within the chorion, until muscular activity frees the embryo from this barrier. Developed zebrafish larvae are shown in the last image. The above images were extracted from live video recordings of development. pg. 94

Figure 4.5: Microinjection of a cell. An injection pipette is brought in close contact with a cell. The pipette is mechanically forced through the cell membrane into the cell's cytoplasm. Through the application of pressurized air that is activated by a foot pedestal, the introduced molecule is forced through the injection tip into the cell. pg. 97

Figure 4.6: Depicts the microscope setup used to laser-manipulate zebrafish embryonic cells. The red lines indicate the optical beam path. See text for details. A1-A3 – dichroic mirrors, B – ocular imaging head, C – imaging block, D – fluorescence filter chamber, E – objective nose piece, F – objective lens, G – *x-y-z* motorized stage, H – motorized control shaft, I – white light chamber, J – stage controller and K – microscope aluminum support structure. pg. 105

Figure 4.7: Transparent front view of the microscope shown in Figure 4.6. Femtosecond laser pulses are directed through the imaging block, C, downwards towards the fluorescence filter chamber, D. If the carousel in the fluorescence filter chamber houses a blank filter, the femtosecond laser pulses pass through and are focused onto the biological specimen by the microscope objective lens, F. White light is shown illuminating the specimen in the inverted position. B – ocular imaging head, C – imaging block, D – fluorescence filter chamber, E – objective nose piece, F – objective lens, G – *x-y-z* motorized stage, H – motorized control shaft and I – white light chamber. pg. 107

Figure 4.8: Side view image of Figures 4.6 and 4.7. In this scenario a filter cube is placed in the optical beam path. Fluorescence light emitted from the fluorescence house is directed along the fluorescence filter chamber, D. The exciter region of the filter (see Appendix F for more information) transmits the fluorescence light, which is reflected towards the microscope objective lens, F. Back reflected light passes through the filter cube through the emitter and is reflected along the imaging block, C. A 45 ° mirror reflects the fluorescence light into the imaging port. In the above configuration, the filter cube blocks the femtosecond laser pulse. pg. 108

Figure 4.9: Side view image of Figures 4.6 and 4.7. In this scenario the carousel in the fluorescence filter chamber, D, houses a blank filter cube. In this configuration, the femtosecond laser pulse is transmitted by the beam splitter and through the fluorescence filter chamber, D. The laser pulse is then focused by the microscope objective lens, F, onto the sample. Back reflected laser light is captured through the same optical path, and is reflected by the beam splitter along the imaging block, C. A 45 ° mirror reflects the laser light into the imaging port. pg. 110

Figure 4.10: A simplified version of the experimental setup shown in Figures 4.6 through 4.9. Sub-10 femtosecond laser pulses were generated from a modelocked titanium sapphire laser oscillator. The pulse repetition rate and center wavelength were 80 MHz and 800 nm, respectively. Laser pulses were coupled to a 1.0 NA 60X water immersion microscope objective and focused to a location near the blastomere-yolk interface or directly onto the blastomere cell. A shutter (galvo) was inserted into the beam path to control the number of laser pulses irradiating the sample. Embryos of varying developmental stages, from early cleavage (2-cell stage) to early blastula (128-cell stage) were placed on a motorized *x-y-z* stage for laser poration. White light illuminated the embryos in the inverted position while fluorescence was collinearly coupled with the laser pulse in the forward direction. (The epi-fluorescence wavelength shown in the above image is that for FITC). The interaction of the femtosecond laser pulses with the embryonic cells was captured with a black and white CCD and with the Nikon DS-5M color camera. Cameras were interfaced with a computer for capturing still images and real time video. pg. 112

Figure 4.11: (a) An early 8-cell stage dechorionated embryo that was laser-targeted at the blastomere-yolk interface (arrow). Post-manipulation, (b) a cavitation bubble (arrow) was formed, which obscured the scarred blastomere-yolk surface. (c) 45 to 60 min following laser-manipulation, the embryo had developed to 64/128-cell stage with normal morphology as compared to control embryos and Westerfield images [126]. The arrow in (c) represents the location where the pore was formed in the original 8-cell stage embryo. The embryo was laser manipulated with a pulse energy of 2.7 nJ/pulse and a gated shutter time between 200 and 300 ms. B – blastomere; Y – Yolk. Scale bars for (a,c) and (b) represent 200 and 5 μm, respectively. pg. 114

Figure 4.12: High-resolution SEM image of the blastomere-yolk region in an 8-cell stage embryo. The area between the two lines was defined as the blastomere-yolk interface.

The dense region of the yolk, Y, is observed at the bottom of the image, while the less dense area of the blatstomeres, B, is seen at the top. Scale bar represents 5 µm. pg. 116

Figure 4.13: Brightfield and fluorescence images of (a,b) 32-, (c,d) 256- and (e,f) 512/1K-cell stage dechorionated embryos 30 min following laser pulse manipulation. The embryos in (a,b), (c,d) and (e,f) were laser pulse targeted at the 8-, 64- and 128-cell stage, respectively. Arrows in (a,c,e) depict the location where transient pores were formed in the original porated embryos. Delivery of exogenous FITC was clearly observable in the blastomere cells of (b), (d) and (f), where the introduction of the fluorescent molecule was found to be independent of the chosen developmental stage. Concentration of FITC in solution ranged from 0.02 to 0.03 mg/mL. All embryos were laser pulse porated with a pulse energy of 2.7 nJ/pulse and a gated shutter time between 200 to 300 ms. Scale bars represent 200 µm. pg. 118

Figure 4.14: An animal polar view of a 16-cell stage zebrafish embryo. The yolk, the blastodisc and the marginal and non-marginal blastomeres are indicated. The internalized blastomeres are the non-marginal cells that will form the epiblast and hypoblast in later development [90]. The figure was adapted from [90, 128]. pg. 120

Figure 4.15: Face view of a 32-cell stage embryo. Locations identified include the yolk, the YCL and the marginal and non-marginal cells. The YCL is the non-yolky cytoplasmic layer adjacent to the yolk. For embryos laser pulse manipulated at the blastomere-yolk interface, it was likely that the fluorescent probe was delivered into the YCL interface; marginal cells bridged to the yolk captured the localized dye and transported it to the non-marginal cells. The YCL surrounds the entire yolk, but is much thinner at the vegetal pole in comparison to the animal pole. Note that only two tiers of 8 blastomeres are shown in the above figure. Rotation of the embryo about an axis perpendicular to the animal-vegetal axis would reveal two addition 2x8 tiers of blastomere cells. The figure was adapted from [127]. pg. 121

Figure 4.16: Method used for targeting the blastomere-yolk interface in chorionated zebrafish embryos. Femtosecond laser pulses were focused beyond the structure of the chorion and localized to the region of interest (at the blastomere-yolk interface). With this targeting method, the chorion layer was undamaged. Pore formation and delivery occurred only at the laser focus by the non-linear mechanism described in Chapter 1. The embryo in the above figure is at the 4-cell stage. This image appeared on the cover of Biotechnology and Bioengineering, 98(6), December 2007. pg. 126

Figure 4.17: Fluorescence and brightfield images of (a,b,c) 32-cell, (d,e,f) 512/1K-cell and (g,h,i) 128/256-cell stage embryos 30 min post-laser pulse poration. The embryos were laser pulse manipulated at the 8-cell stage for (a,b,c), the 128-cell stage for (d,e,f) and the 32/64-cell stage for (g,h,i). Embryos were dechorionated to observe the pervitelline FITC delivered into the blastomere cells. As evidenced in (b,e,h), none of the embryos were compromised post-dechorionation. The uptake of pervitelline FITC via laser pulse induced transient pores was evident in (c,f,i), with the arrows indicating the exact locations were permeabilization occurred in the previously chorionated embryos. Individual nuclei of the blastomere cells in (i) were clearly visible. Concentration of FITC used in this study was 0.02 to 0.03 mg/ml. Laser parameters used for poration were 2.7 nJ/pulse with a gated shutter time rangimg from 200 to 300 ms. Scale bars represent 200 μm. pg. 128

Figure 4.18: Fluorescence and brightfield image of a (a,b) 16-cell stage dechorionated embryo imaged immediately after laser pulse poration. Laser pulses were localized onto the individual blastomere cells, with three to four transient pores created in each of four blastomere cells. Concentration of FITC used in this study was 0.02 to 0.03 mg/ml. The laser pulse energy for poration ranged from 0.5 to 0.6 nJ/pulse with a gated shutter time between 200 and 500 ms. Scale bars represent 200 μm. pg. 131

Figure 4.19: A Steptavidin-conjugated quantum dot. The core is composed of cadmium selenide, surrounded by a zinc sulfide shell. The outer layer is a polymer, which is conjugated to streptavidin. The diameter of the quantum dot is between 15 and 20 nm (Cedarlane Labs, ON, Canada). Figure was adapted from Invitrogen, US. pg. 136

Figure 4.20: (a) An early 2-cell stage dechorionated embryo that was laser pulse porated for introducing Streptavidin-conjugated quantum dots. The uptake of quantum dots in (a) is evidenced by the fluorescence localized in the dividing blastomere cells. The embryo in (a) was reared to just after germ-ring stage, (b), showing that quantum dot fluorescence was still observable during this developmental period. Each of the two blastomere cells were laser pulse porated three to four times per cell. The laser pulse energy used for poration was 1.5 and 1.9 nJ/pulse with a gated shutter time ranging from 200 to 500 ms. Concentration of the quantum dot solution was 0.4 μM. Scale bars represent 200 μm. pg. 137

Figure 4.21: Fluorescence and brightfield images of 24 hpf zebrafish expressing the sCMV-EGFP plasmid construct. (a) Expression was observed along the yolk sac extension, somites, notochord and floor plate. (b) In addition, EGFP expression was observed near the urinary duct and in many of the zebrafish tail cells. (c,d) Brightfield images of the same larva in (a,b) showing intact zebrafish development, indicating that expression was not due to autofluorescence from damaged cellular material. The concentration of the plasmid construct used in this study was 170 µg/mL. The developed embryos in (a,b,c,d) were laser pulse porated with a pulse energy ranging from 0.5 to 0.6 nJ/pulse and a gated shutter time between 200 and 500 ms. A total of three to four transient pores were made in each of 2, 2, 4 and 8 cells per 2-, 4-, 8- and 16-cell stage embryos. pg. 141

Figure 4.22: The sCMV-EGFP plasmid map. The EGFP gene was inserted into the Polylinker I site. Plasmid replication occurred in *E. coli*. The original plasmid map was provided by Patricia Gongal of Dr. Waskiewicz lab. pg. 142

Figure 4.23: Image depicting a larva reared to pec-fin stage that was laser pulse manipulated between early to mid cleavage (2-cell to 8/16-cell stage) stage. Developmental morphological structures that have been indicated include the pectoral fin, the ear, the otoliths, the yolk-sac, the location of the beating heart and the eye. Laser parameters chosen for embryo manipulation were 2.7 nJ/pulse with a gated shutter time ranging from 200 to 500 ms. pg. 151

Figure 5.1: A high magnification SEM image of the region near the blastomere-yolk interface of an 8-cell stage embryo. The less dense region, B, represents the blastomere cell while the dense area is the yolk, Y. Scale bar represents 5 µm. pg. 160

Figure 5.2: Cavitation bubble (Cb) formation and residual surface scarring (Ss) of blastomere cells post-femtosecond laser pulse manipulation. (a) The cavitation bubble (Cb) was produced using a pulse energy of 0.56 nJ/pulse with a gated shutter time of 100 ms and a single pulsing event of the shutter. A measurement of the cavitation diameter revealed a size of ~ 5 µm. (b) After pulsing the shutter a total of 3 times (total beam dwell time of 300 ms), surface scarring (Ss) of the blastomere cell was observed. The spatial extent of surface scarring was on the order of the cavitation bubble diameter, ~ 5 µm. (c) The cavitation bubble (Cb) was created using a pulse energy of 0.56 nJ/pulse with a gated shutter time of 500 ms and a single pulsing event of the shutter. The diameter of the cavitation bubble was measured to be ~ 10 µm. (d) After pulsing the shutter a total of 2 times (total beam dwell time of 1000 ms), surface scarring (Ss) of the blastomere cell was observed. Similar to (b), the scarring length in (d) was on the order of the cavitation bubble diameter, ~ 10 µm. The above figure was extracted from live video of the ablation process, which has been provided in the supplementary CD, Additional File 1 – Chapter 5. Scale bars for (a,b,c,d) represent 5 µm. pg. 164

Figure 5.3: Embryos laser pulse manipulated with a pulse energy of 0.56 nJ/pulse for introducing exogenous FITC into the blastomere cells. (a,b) Fluorescence and brightfield image of a post-laser pulse maniputed 8-cell stage embryo that was porated a total of 6 times in each of 2 blastomere cells (3 pores per blastomere cell with a maximum of 2 laser pulse treated cells; laser pulse treated at the 2-cell stage). Transient pores were formed using a beam dwell time of 100 ms and 3 pulsing events of the shutter. (c,d) Fluorescence and brightfield image of a post-laser pulse manipulated 4-cell stage embryo. The same number of pores were made in the blastomeres as in (a,b); however, the beam dwell time was set to 100 ms with the shutter pulsed once. The concentration of FITC used was 0.014 to 0.018 mg/ml, with the embryos exposed to the fluorescent probe for 10 to 15 min. Quantitative measurements of the mean blastomere-fluorescence intensity per unit area were (a) 53.9 and (c) 16.9. Scale bars for (a,b,c,d) represent 200 µm. pg. 167

Figure 5.4: Embryos laser pulse manipulated with a pulse energy of 0.56 nJ/pulse for introducing exogenous FITC into the blastomere cells. (a,b) Fluorescence and brightfield image of a post-laser pulse manipulated 8-cell stage embryo that was porated a total of 6 times in each of 2 blastomere cells (3 pores per blastomere cell with a maximum of 2 laser pulse treated cells; laser pulse treated at the 2-cell stage). Transient pores were formed using a beam dwell time of 50 ms and 3 pulsing events of the shutter. (c,d) Fluorescence and brightfield image of a post-laser pulse manipulated 8-cell stage embryo. Same number of pores were made in the blastomeres as mentioned in (a,b). The beam dwell time was set to 50 ms with the shutter pulsed a total of 2 times. The concentration of FITC used was 0.014 to 0.018 mg/ml, with the embryos being exposed to the fluorescent probe for 10 to 15 min. Quantitative measurements of the mean blastomere-fluorescence intensity per unit area were (a) 29.7 and (c) 15.4. Scale bars for (a,b,c,d) represent 200 μm. pg. 169

Figure 5.5: (a,b) Fluorescence and brightfield image of a post-laser pulse manipulated 8-cell stage embryo that was porated using a pulse energy of 0.56 nJ/pulse with a beam dwell time of 20 ms and a shutter pulse rate of 3. A total of 6 pores were made in each of 2 blastomere cells (3 pores per blastomere cell with a maximum of 2 laser pulse treated cells; laser pulse treated at the 2-cell stage) for introducing exogenous FITC. The concentration of FITC used was 0.014 to 0.018 mg/ml, with the embryos exposed to the fluorescent probe for 10 to 15 min. A quantitative measurement of the mean blastomere-fluorescence intensity per unit area was found to be 15.0. Scale bars for (a,b,c,d) represent 200 μm. pg. 171

Figure 5.6: Fluorescence and brightfield image of an 8-cell stage embryo that was not laser pulse manipulated, but was bathed and exposed to the FITC fluorescent probe at the same concentration (0.014 to 0.018 mg/ml) and time interval (10 to 15 min) as in Figures 5.3, 5.4 and 5.5. The embryo was rinsed several times in buffered reverse osmosis water and imaged with an imaging area and exposure time consistent with Figures 5.3, 5.4 and 5.5. No accumulation of blastomere-FITC was observed in the cells. (a) The weak fluorescence observed in the yolk was autofluorescence. A quantitative measurement of the mean blastomere-fluorescence intensity per unit area was found to be 4.4. Scale bars for (a,b) represent 200 μm. pg. 172

Figure 5.7: SEM images of control dechorionated embryos at the 2 and 8-cell stage. (a) Face view, (b) animal-vegetal axis rotated and (c) top view of a 2- and 8-cell stage control embryo. (d,e) High magnification SEM image of the blastomere-yolk region of an 8-cell stage embryo. B – Blastomere; Y – Yolk. Scale bar for (a,b,c) represent 100 μm and (d,e) 5 μm. pg. 177

Figure 5.8: SEM images of a laser pulse manipulated and a control larva reared to 2 dpf. (a,b) Lateral whole body mosaics and antero-lateral views of the laser pulse manipulated larva at 2 dpf. (c,d) Same larva in (a,b) illustrating key developmental morphological structures including the olfactory pit (OP), the yolk sac (YS), the yolk sac exstention (YSE), the caudal fin (CF) and the dorsal fin (DF). (e,f) Lateral whole body mosaics and antero-lateral views of the control larva at 2 dpf. (g,h) Same larva in (e,f) indicating the same developmental morphological structures observed in (c,d). Scale bars for (a,c,e,g) represent 200 μm and for (b,d,f,h) 100 μm. pg. 182

Figure 5.9: High magnification SEM images of the pectoral fin buds in a laser pulse manipulated and control larva reared to 2 dpf. (a) Pectoral fin bud of a laser pulse manipulated and (b) a control larva at 2 dpf. Orientation: anterior (left); posterior (right). Scale bar represents 10 µm. pg. 184

Figure 5.10: SEM images of laser pulse manipulated and control larvae reared to 7 dpf. (a,b,c,d) Dorso-lateral whole body mosaics and antero-dorsal views of laser pulse manipulated larvae at 7 dpf. (e,f,g,h) Lateral and dorso-lateral whole body mosaics and antero-dorsal views of control larvae at 7 dpf. Scale bars for (a,c,e,g) represent 200 µm and for (b,d,f,h) 100 µm. pg. 185

Figure 5.11: Illustration of key developmental morphological structures in a laser pulse manipulated and control larva reared to 7 dpf. (a,b) Dorso-lateral whole body mosaic and antero-dorsal view of a laser pulse manipulated larva at 7 dpf. (b) Same larva as (a). Developmental morphological structures that have been indicated include the protruding mouth (PM), the eye (E; cornea), the otic vesicle (OV), the pectoral fin (PF), the ventral fin (VF), the olfactory pit (OP), the otic capsule (OC) and the notochord (NC; depicting the location of where it would develop). (c,d) Lateral whole body mosaic and antero-lateral view of a control larva at 7 dpf. Same developmental morphological structures observed in (a,b) were also seen in (c,d). (d) Same larva as (c). Scale bars for (a,c) represent 200 µm and for (b,d) 100 µm. pg. 188

Figure 5.12: Magnified top and lateral views depicting key developmental morphological structures in laser pulse manipulated and control larvae reared to 7 dpf. (a,b,c) Magnified top and lateral views of (a) the olfactory pit, (b) the ear and (c) the neuromeres of the posterior forebrain and dorsal midbrain in laser pulse manipulated larvae. (d,e,f)

Magnified top and lateral views of (a) the olfactory pit, (b) the ear and (c) the neuromeres of the posterior forebrain and dorsal midbrain in control larvae. (g,h) Illustrated comparison of dorso-lateral views of the neuromeres in (g) a laser pulse manipulated and (h) control larva at 7 dpf. The dicephalon (D) and optic tectum (OT) shown in (g,h) represent the locations of the posterior part of the anterior forebrain and the dorsal midbrain. Also indicated are the locations of the eye (E) and the olfactory pit (OP). Orientation: anterior (left); posterior (right). Scale bars for (a,d) represent 20 μm and for (b,c,e,f,g) 50 μm. pg. 189

Figure 5.13: High magnification SEM images of the olfactory pit rim and the kinocilia projecting from the crista on the lateral wall of the inner ear in a laser pulse manipulated and control larva reared to 7 dpf. (a) Olfactory pit rim in a laser pulse manipulated and (b) a control larva showing kinocilia covering the inside wall of the olfactory pit. Kinocilia projecting from the lateral crista in (c) a laser pulse manipulated and (d) control larva. Scale bars for (a,b,c,d) represent 1 μm. pg. 190

Figure 5.14: LM image of a laser pulse manipulated larva reared to 2.5 dpf showing the dense otoliths of the zebrafish ear defining the location of the macula. The above figure is a cropped image of Figure 4.23 in Chapter 4. Orientation: anterior (left); posterior (right). pg. 192

Figure 5.15: Dorsal view of a laser pulse manipulated larva reared to 5 dpf. Developmental morphological structures that have been indicated include the protruding mouth, the eyes and the pectoral fins. The above image was extracted from live video, which has been provided in the supplementary CD, Additional File 2 – Chapter 5. pg. 194

Figure 6.1: Coupling of a femtosecond fiber laser to a microfluidic channel. Each channel can contain a different chemical compound or cell model system. The application of femtosecond laser pulses is localized to the irradiation zone for the intended application. pg. 202

Figure 6.2: Femtosecond fiber laser in an analogous experimental setup to those shown in Figures 2.2 through 2.5 in Chapter 2 and Figures 4.7 through 4.10 in Chapter 4, respectively. The entire laser oscillator is replaced with the femtosecond fiber laser depicted above. Biological samples placed on the motorized stage are cooled to a set temperature in the manner previously described in section 2.1 in Chapter 2. A stage controller allows for accurate positioning of the biological material under the fiber laser source. The bottom right corner of the image is a magnified view of the interacting region between the fiber and the model system studied (in this case a cell). Laser pulses could be localized onto the biological membrane, or into the intracellular space for sub-cellular ablation studies. pg. 203

Figure A.1: Diagram depicting the sequence of events involving laser pulse induced ionization. The diagram depicts the case where the Keldysh parameter, γ, is not greater than 1.5. Therefore, the band gap energy of water cannot be used to approximate the effective ionization potential. See text for description. Image adapted from [5, 7]. pg. 210

Figure B.1: Structure of a sucrose molecule. Red lines indicate the bond length calculation path used in estimating the sucrose diameter. pg. 213

Figure E.1: Graphic depicting the general layout and mechanism of the fluorescence filter cube. pg. 222

List of abbreviations

A	area of the pore
Δ	band gap energy (eV)
w_0	beam waist
B	blastomere
K_B	Boltzmann constant
BGP	bone gla protein
CF	caudal fin
cm	centimetre
CCD	charge coupled device
V79-4	Chinese hamster fibroblast cells
erfc	complementary error function
N_{crit}	critical electron density
P_{crit}	critical power for self-focusing
Da	daltons
dpf	days post-fertilization
°C	degrees centigrade
ρ_0	density of water
DNA	deoxyribonucleic acid
d_z	depth dimension of the irradiance profile
D	diencephalon

D_{sw}	diffusion coefficient of sugar in water
D_w	diffusion coefficient of water in solute and lipid
δ	diffusion range
DMSO	dimethyl sulfoxide
Δx	distance
DF	dorsal fin
ddH_2O	double distilled water
$\tilde{\Delta}$	effective ionization potential (eV)
m	effective mass
e	electron charge
m_e	electron mass
eV	electron volts
EGFP	enhanced green fluorescent protein
EtOH	ethanol
V_{equil}	equilibrium volume post-permeabilization
EB	ethidium bromide
EVA	ethylene vinyl acetate
$C^e_{electrolyte}$	extracellular electrolyte concentration
ECM	extracellular matrix
M^e_s	extracellular solute osmolarity
$C^e_{sucrose}$	extracellular sucrose concentration
E	eye; cornea

FITC	Fluorescein Isothiocyanate
J	flux
ω	frequency of light
F	frictional force
GPa	gigaPascal
g/mol	grams per mole
D	heat diffusivity
HSP	heat shock protein
Hz	hertz
HMDS	hexamethyldisilazane
hr	hours
hpf	hours post-fertilization
$n(\omega)$	index of refraction
C_0	initial solute concentration
$C^i_{electrolyte}$	intracellular electrolyte concentration
IIF	intracellular ice formation
M^i_s	intracellular solute osmolarity
$C^i_{sucrose}$	intracellular sucrose concentration
I	irradiance (W/cm^2)
1K-cell	K referring to 10^3
K	Kelvin
kbar	kilobar
kDa	kilodaltons

KHz	kilohertz
kW	kilowatts
LCM	laser capture microdissection
L	length of pore
$n_1(\omega)$	linear index of refraction
L	litre
MDCK	Madin-Darby Canine Kidney cells
ρ_{max}	maximum electron density
MHz	megahertz
MPa	megaPascal
L_p	membrane hydraulic conductivity
MeOH	methanol
m/s	metre/second
J	microJoule
μL	microlitre
mJ	milliJoule
mL	milliliter
mOsm	milli osmoles
ms	milliseconds
M	molar
molec	molecules
X_{elect}	mole fraction of electrolytes
nJ	nanoJoule

nm	nanometre
NIR	near-infrared
$n_2(\omega)$	nonlinear index of refraction
NC	notochord
k	number of absorbed photons
n_{cryo}	number of moles of cryoprotectants
n_{elect}	number of moles of electrolytes
n_w	number of moles of water
n	number of pores
NA	numerical aperture
OP	olfactory pit
OT	optic tectum
OC	otic capsule
OV	otic vesicle
I	peak intensity
P	peak power
PF	pectoral fin
P_f	permeability coefficient
ε_0	permittivity of free space
P_w	pressure due to water
PG	propylene glycol
PM	protruding mouth

τ_L	pulse duration
r	radius
(n =)	refers to the population size
RNA	ribonucleic acid
SEM	scanning electron microscopy
I_{sf}	self-focusing intensity
sCMV	simian cytomegalovirus
C_s	solute concentration
d_r	spatial dimension of the irradiance profile
C_p	specific heat capacity of water
ΔT	temperature
I_R	threshold irradiance (W/cm^2)
t	time
TEM	transmission electron microscopy
UV	ultraviolet
η	viscosity
VF	ventral fin
V	volume
ε	volumetric energy density
J_w	water flux
λ	wavelength
Y	yolk

YCL	yolk cytoplasmic layer
YSE	yolk sac extension
YS	yolk sac
YSL	yolk syncytial layer
Zn	zinc

CHAPTER 1

FEMTOSECOND LASER PULSE INTERACTIONS WITH BIOLOGICAL MATERIALS

1.1 Introduction

Recent interest in the use of laser pulses to manipulate biological materials makes understanding the laser-tissue interaction process increasingly important. By gaining insight into the various linear and nonlinear processes involved in tissue ablation, the application of laser pulses can be better tailored to the application of interest. However, much of what we understand about the mechanism of laser-tissue interaction and the lasers effect on biological materials is based on theoretical studies [1] using water as the model system [2-6]. While biological tissues are mostly composed of water, the effects of biomolecules (i.e. proteins, lipids and carbohydrates) and impermeable and permeable solutes on the tissue ablation parameters are unknown. Through the modeling of the ionized electron density, the temperature change in the focal volume, shockwave expansion and cavitation bubble formation in water, the goal has been to try to reconcile experimental work with theory [2, 4-13].

Pulse duration is an additional parameter that complicates knowledge of the laser-tissue interaction process. With the advent of femtosecond laser sources, the time scale of the pulse is significantly shorter than the shockwave and cavitation bubble events taking place on the picosecond, nanosecond and microsecond time scales [2-5, 10, 13]. To resolve the ablation dynamics on the order of the pulse duration, the response time of the detection system must be comparable if not faster than the duration of the applied laser pulse.

Despite the complexities underlying laser pulse ablation, as well as our incomplete understanding of its mechanism and influence on biological materials, laser-tissue interaction still remains an active area of research. This chapter provides a brief overview of our current understanding of the field, which is largely based on theoretical simulations and various assumptions. While this thesis focuses on the applications of the femtosecond laser to a variety of biological disciplines (and not on the laser-tissue interaction process), it is nevertheless instructive to provide a concise framework for the reasoning behind using these ultrashort laser pulses.

1.2 Laser-tissue interaction[1]

In biological studies, probing the internal working structures of cells with laser irradiation without inducing damage to the outer cellular surface requires that the incident wavelength of light be independent of the linear absorption coefficient of the system studied [8]. Macromolecules strongly absorb wavelengths of light in the ultraviolet (UV) (200 to 400 nm), limiting the usage of UV wavelengths to deep tissue studies [13]. In contrast, biological material is transparent to near-infrared (NIR) wavelengths (for instance 800 nm) [13], and the laser light can be focused beyond cellular structures and localized to a region of interest without disrupting cellular material above or below the laser focal spot. Only at the focus will biological material be laser pulse ablated, either for dissection, excision or permeabilization, through a linear or nonlinear process that is described below.

Linear and nonlinear processes in laser-tissue interaction

When laser irradiation is focused onto a biological structure, cellular material absorbs the irradiation either through single photon absorption or nonlinear absorption, depending on the excitation wavelength, the laser intensity and the laser pulse duration [5, 7]. In the case of nanosecond pulse durations, the peak power of the pulse is insufficient to elicit nonlinear absorption, where biological material absorbs laser photons through single photon absorption [5]. Single photon absorption refers to the excitation of the biological specimen by a single photon, as depicted in Figure 1.1. As the

---

[1] Portions of this chapter have been published in: Kohli *et al*. Prospects and developments in cell and embryo laser nanosurgery. Interdisciplinary Reviews: Nanomedicine. In press. (**Invited article**).

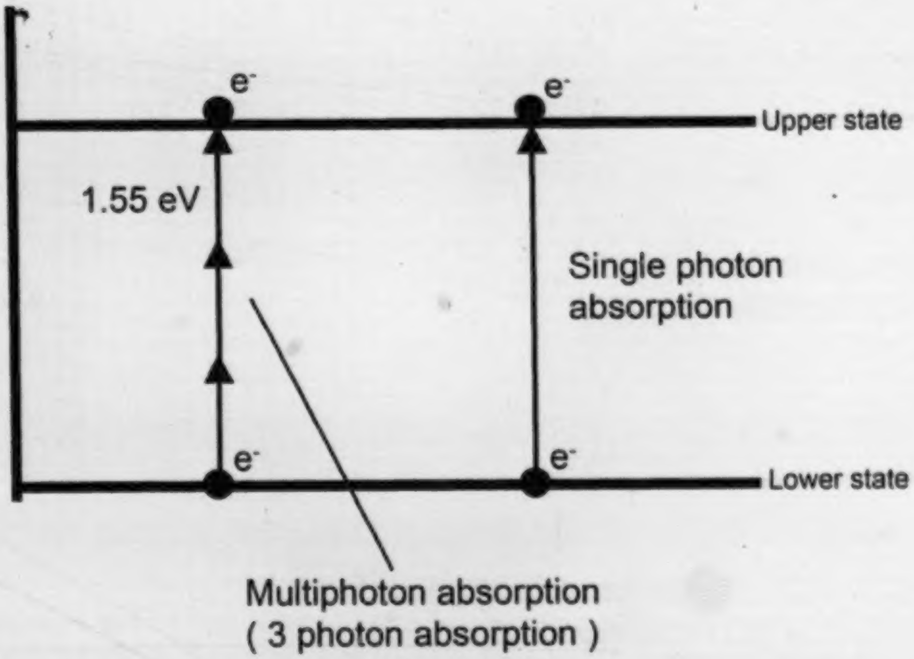
e⁻
e⁻
Upper state
1.55 eV
Single photon absorption
e⁻
e⁻
Lower state
Multiphoton absorption
(3 photon absorption)

Figure 1.1: Diagram contrasting multiphoton absorption and single photon absorption. For multiphoton absorption, it is assumed that the energy per photon is 1.55 eV corresponding to a wavelength of 800 nm. The absorption of three simultaneous photons is required to elicit an electron transition from the lower state to the upper state. In single photon absorption, one photon excites the electron to the upper state. However, for this transition to occur, the excitation wavelength must be 266 nm (1/3rd of 800 nm) with a photon energy of 4.65 eV.

pulse duration is shortened from nanoseconds to femtoseconds (while keeping the laser pulse energy constant), the peak power of the pulse increases to a value where multiphoton absorption[1] can occur. In the case of femtosecond laser pulse ablation, it is the multiphoton absorption process that initiates the ionization and chemical decomposition (i.e. bond-breaking or dissection) of the biological material [5]. The diagram in Figure 1.1 contrasts the multiphoton absorption and single photon absorption processes. In the figure, it is assumed that three photons with a photon energy of 1.55 eV (800 nm) are required to promote an electron from the lower energy state to the upper energy state for multiphoton absorption. For single photon absorption, a single photon with an energy equal to the difference in the energy states, 4.65 eV (266 nm) would be required to excite the electron.

The benefit of femtosecond laser pulses over longer pulse durations is inherent in the lower threshold energy required to elicit ablation [1, 5, 8] and the ability to localize the cellular and sub-cellular disruption to a high (typically on the order of sub-micron) spatial resolution [14, 15]. Both of these factors are intrinsically coupled, since the lower threshold energy means that less energy is available to be funneled into adverse side effects such as shockwave and cavitation bubble formation, which are known to increase the spatial extent of tissue damage [5, 16, 17].

Multiphoton absorption is the initiator of the laser pulse ablation of biological material. Through nonlinear absorption, the simultaneous absorption of 'k' photons excites a valence electron to the conduction band (Figure 1.1), leading to a quasi-ionized electron[1] [5, 7, 13]. Here, 'k' represents the number of absorbed photons required to excite the electron across the energy band gap of the material. In numerical simulations [5], water (represented as a semiconductor/insulator) has been the model system used to understand the laser-tissue interaction process with biological material. It has been suggested that 6.5 eV [5] be used as the band gap energy for water, a value that arises from experimental work performed by Boyle *et al.* [18] which examined the photolysis of pure distilled liquid water. If we assume a femtosecond laser pulse with an excitation wavelength centered at 800 nm (1.55 eV) that is focused with a high numerical aperture (NA) microscope objective (NA $\geq$ 0.9; here it is of interest to reduce the diffraction limited irradiance focal spot and consequently lower the input pulse energy), then the ionization of a single electron requires the simultaneous absorption of $k = 5$ photons. This excited electron, properly termed a 'lucky electron', provides the initial seed electron for the plasma (high density electron gas) mediated ablation process.

---

[1] To define if the laser-tissue interaction process is governed by multiphoton absorption and ionization, the Keldysh parameter, γ, must be estimated. The Keldysh parameter is related to the index of refraction, the band gap energy and the peak intensity [7]. If $\gamma > 1.5$, the laser-tissue interaction process is inititated by multiphoton absorption and ionization [7]. As will be seen throughout this thesis, γ is estimated to be greater than 1.5 based on the pulse energy and peak intensity used in each of the studies.

Having promoted an electron to the conduction band, the electron begins to absorb single laser photons within the lifetime of the laser pulse [5, 7, 13]. As a result, the seed electron increases in energy, achieving a higher energy state within the conduction band. Eventually a condition is reached where the electron has enough energy to impact ionize an additional electron, promoting a new seed electron to the conduction band [5]. These two seed electrons can than participate in impact ionization after achieving critical electron energy. The entire process of energy gain and electron impact increases the electron density, collectively defined as 'avalanche/cascade ionization,' to a critical value, N_{crit}[1], defined as the point where optical breakdown of the material occurs. N_{crit} follows the relation [7, 13]

---

[1] The electrons are not completely ionized, rather they occupy a higher energy state within the conduction band of the material.

$$N_{crit} = \frac{\omega^2 m_e \varepsilon_0}{e^2} \tag{1.1}$$

where $\omega, e, m_e, \varepsilon_0$ represent the frequency of light, electron charge, electron mass and permittivity of free space, respectively. For an excitation wavelength of 800 nm, $N_{crit} = 10^{21}\ \mathrm{cm}^{-3}$, where at this value the plasma becomes reflective [5, 13]. It is this large critical electron density that is referred to as the plasma at optical breakdown.

Femtosecond plasma mediated pulse ablation is a very efficient process that is statistically reproducible with defined ablation thresholds. This is in contrast to plasma mediated pulse ablation using longer pulse durations, where seed electrons are produced via thermionic emission of impurity electrons (also known as background or defect density) [7, 13]. Fluctuations in the impurity density result in varying ablation threshold values, making optical breakdown a statistically irreproducible process. In addition to the well defined ablation thresholds for femtosecond laser pulses, using NIR wavelengths increases the plasma formation efficiency, since both the plasma absorption coefficient and cascade ionization rate are proportional to the square of the excitation wavelength [5, 13]. Therefore, a shift in the excitation wavelength from the visible (i.e. 532 nm) to NIR (i.e. 800 nm) increases the production rate of ionized electrons. However, at the expense of shifting the wavelength to the NIR, a higher pulse energy is required to induce multiphoton absorption. This is due to the decrease in photon energy from 2.33 eV

---

[1] At N_{crit} the plasma frequency equals the laser frequency.

(532 nm) to 1.55 eV (800 nm) and a corresponding decrease in 'k' from 5 to 3. However, simulation results have shown that cascade ionization is the more dominant process for creating ionized electrons[1] [5]. As long as seed electrons are created via multiphoton absorption, cascade ionization will produce more 'lucky electrons' than multiphoton absorption alone. For longer pulse durations (i.e. nanoseconds), seed electrons for cascade ionization are produced through thermionic emission. A rapid rise in the electron density occurs only when the optical breakdown irradiance is reached[2] [5]. In contrast, for femtosecond laser pulses, seed electrons are produced for irradiance values less than I_R [5]. Under identical focusing, the requirement that $I = I_R$ and $I < I_R$ for nanosecond and femtosecond laser pulses for the generation of seed electrons, indicates that less energy is required to induce plasma mediated ablation with femtosecond laser pulses than with nanosecond pulses.

Laser pulse ablation profile

The spatial extent of tissue ablation is more confined using femtosecond laser pulses than longer pulse durations [5, 13, 19-21]. This originates from the nonlinear multiphoton absorption process that occurs within a small interaction volume. It is the electron density profile and not the irradiance profile that limits the spatial resolution of the ablation region [5], and knowledge of the electron density evolution as a function of space provides valuable information about the size of the ablated region. Simulations have shown that the electron density profile is narrower than the irradiance profile by a factor of $\sqrt{k}$ [5]. To place this in context, if we a assume a diffraction limited spot size with a radial dimension (d_r) and depth dimension (d_z) given by [4, 5]

---

[1] It is assumed that the pulse duration is ≥ 100 femtoseconds.

[2] Defined as the threshold irradiance (I_R) that produces $N_{crit} = 10^{21}$ cm^{-3} for a wavelength of 800 nm.

$$d_r = \frac{1.22\lambda}{NA} \quad \text{and} \quad d_z \approx 2\left(\frac{\pi w_0^2}{\lambda}\right) \tag{1.2}$$

where, for example, $NA = 1.0$, $\lambda = 800$ nm and $w_0 = 488$ nm $(d_r/2)$ are the numerical aperture, wavelength of light and radius of the beam waist, respectively, then $d_r = 976$ nm and $d_z = 1870$ nm. These values represent the dimensions of the irradiance profile with elliptical[1] type geometry. Using the above values, the electron density profile is smaller by $\sqrt{5}$ (assuming a wavelength of 800 nm (1.55 eV) and a band gap energy of 6.5 eV), with new dimensions of $d_r = 436$ nm and $d_z = 935$ nm. The ability to ablate biological material with a sub-diffraction limited spot size (i.e. less than d_r as calculated for the irradiance profile) has been experimentally observed [14, 19, 22, 23]. However, competing factors that extend the ablated region to above sub-diffraction size are shockwave and cavitation bubble formation (discussed later). This does not diminish the usefulness of femtosecond laser pulses for tissue ablation. For instance, using nanosecond pulses, the dominant process is single photon absorption, and the electron density profile is not narrowed by $\sqrt{k}$ as is the case for femtosecond laser pulses [5]. Therefore, the theoretical dimensions of the ablated region would be $d_r = 976$ nm and $d_z = 1870$ nm. Furthermore, optical breakdown is achieved only for irradiance values $I = I_R$ ($I < I_R$ for femtosecond pulses), resulting in more laser energy deposited into the tissue. This extra energy funnels into shockwave and cavitation bubble formation that have more disruptive effects on the material [3, 10] (due to the added energy deposition) than those generated by femtosecond laser pulses.

---

[1] The focused laser spot has a short and a long axis dimension.

Laser pulse induced heat stress

The accumulation of heat and the rise in temperature during femtosecond mediated plasma ablation has been an active area of research. Generally the temperature rise is smaller for femtosecond laser pulses (due to the lower threshold energy for ablation) than for longer pulse durations [5]; however, the exact value of the temperature rise is still unknown. Several studies have attempted to indirectly determine the contribution of thermal stress to the ablation process by examining ablated solids and tissue materials via scanning electron microscopy [9, 11]. Careful inspection of ablated regions revealed the presence of smooth crater walls with an absence of cracks or surface melting [11]. Neev *et al.* [9] used infrared camera observations to determine the temperature rise at the front surface of ablated dentin tissue irradiated with femtosecond laser pulses (350 femtoseconds) at a repetition rate of 10 Hz. The maximum observed temperature rise was 3.9 °C above room temperature (23 °C) [9]. In a study by Losel *et al.* [12], the authors claimed to have performed non-thermal ablation of neural tissue with femtosecond laser pulses (140 femtoseconds), yet observed thermal damage and structural changes to the tissue limited to a zone smaller than the focused laser spot size (5 μm). While it is unclear what the authors meant by non-thermal, it is possible that this referred to structurally induced changes via bond-breaking due to electron impact or to dissection through cavitation bubble formation.

As an alternative approach to the above methods, Vogel *et al.* [5] used numerical simulations to estimate the temperature rise after the application of a single femtosecond pulse (100 femtoseconds) in water. Since the pulse duration was shorter than the relaxation time (i.e. the time taken for the electrons to transfer energy to the ions), variously reported as 1 to 100 picoseconds [5, 24], the temperature rise is given by [5]

$$\Delta T = \frac{\varepsilon}{\rho_0 C_p} \tag{1.3}$$

where ε, ρ_0 and C_p are the volumetric energy density, the density of water (1 g/cm^3) and the specific heat capacity (4.184 J/K·g), respectively. This equation represents the temperature rise within the focal volume before any thermalization of the electrons has occurred. Both the density of water and the heat capacity are constants, while the change in temperature scales linearly with the deposited volumetric energy density. For large volumetric energy densities of 1 J cm^{-3}, the temperature rise, as calculated by (1.3), is ΔT = 0.2 K above room temperature [5]. This value represents the temperature rise after the application of a single femtosecond laser pulse. It is expected that the temperature would rise after multiple incident laser pulses in the case of femtosecond laser-tissue interactions performed with high repetition rate laser oscillators (i.e. 80 MHz). Each incident pulse effectively adds a heat source term at the interaction zone, raising the temperature within the focal volume. However, the temperature rise can be minimized by limiting the number of incident laser pulses and through a reduction in the laser pulse energy.

To accurately describe the temperature rise after a series of pulse trains (i.e. 1 KHz or 80 MHz) requires a more complex form of the temperature equation provided above and knowledge of the absorbed power, the heat diffusivity, the geometry of the electron density distribution and the number of absorbed laser pulses [5]. Considering that the pulse duration (i.e. femtoseconds) is shorter than the electron relaxation time (i.e. 1 to 100 picoseconds [5, 24]), the energy gain after a single pulse has a strong confinement factor with a small heat diffusion length. For instance, a 100 femtosecond laser pulse (τ_L) focused into water having a diffusion coefficient[1], D, equal to $1.38\text{x}10^{-7}$ m^2s^{-1}, has a thermal diffusion length (after the pulse and assuming no further input of energy) $\sim\sqrt{D\tau_L} = 0.12\,\text{nm}$ [13, 25]. The combination of the multiphoton absorption process, the lower threshold energy required for optical breakdown, the lower temperature rise in comparison to longer pulse durations and the strong confinement of energy in the focal volume are the main factors that make the femtosecond laser an attractive tool for tissue ablation.

Shockwave and Cavitation bubble formation

Two adverse effects that manifest from the plasma mediated ablation process are shockwave generation and cavitation bubble formation. The strength of each depends on the deposited laser energy, where an excess of energy deposition above threshold funnels into increasing the disruptive forces imparted by shockwave and cavitation [3, 5]. Laser-induced shockwaves originate from the kinetic energy of seed electrons. The high density of ionized electrons diffuses out of the focal volume, resulting in plasma expansion[2] [13].

---

[1] Also known as heat diffusivity

[2] Shockwaves initially expand with supersonic velocity, eventually slowing down to the speed of sound in the medium (~ 1500 m/s for water [13]]).

Together the supersonic and sonic shockwave expansion are referred to as acoustic transients [13]. If the energy of the electrons is high enough, bound ions may follow the escaping electrons, resulting in the movement of material [13]. The dynamics of shockwaves have been studied in corneal tissue and in water using nanosecond, picosecond and femtosecond laser pulses [2-4, 10]. A comparison of shockwave dynamics between nanosecond and picosecond pulses revealed that the initial pressure at the plasma rim was 17 kbar (1.7 GPa) for 30 picosecond pulses at a pulse energy of 50 μJ versus 21 kbar (2.1 GPa) for 6 nanosecond pulses at a pulse energy of 1 mJ [3]. These shockwaves were observed for pulse energies above the breakdown threshold energy (~ 3 times for 30 picoseconds; 5 times for 6 nanoseconds [3]) and do not represent the respective pressures at threshold. Despite the similar pressure values at the plasma border, the shockwave pressure for picosecond pulses decayed at a faster rate than that for nanosecond pulses[1] [3]. The faster decay time for picosecond laser pulses was attributed to the lower deposited laser energy, with the longer pressure decay time for nanosecond pulses imparting a larger spatial disruption [3]. Similar shockwave experiments have been performed using femtosecond laser pulses [2, 5]; however, only theoretical estimates of the pressure at the plasma rim have been reported [5]. When 100 femtosecond laser pulses were focused into water having a pulse energy ~ 10 times above the optical breakdown threshold, plasma expansion was observed 30 picoseconds after breakdown and continued for 200 picoseconds [2]. Theoretical predictions have revealed that the pressure amplitude at the plasma rim for a deposited volumetric energy density of 1 J cm^{-3} is 420 bar (42 MPa) [5]. This value is significantly lower than the pressure waves generated by picosecond or nanosecond laser pulses. While all of these analyses were performed using pulse energies well above threshold, the results, nevertheless, do provide conclusions that can be extrapolated to threshold pulse energies. As these various studies have shown, pressure amplitudes decrease with shorter pulse durations. Using a pulse energy closer to the threshold, the amount of energy contributing to shockwave formation decreases and this results in lower plasma rim pressure values. Since less funneled energy also indicates faster shockwave decay times, the pressure amplitude for shorter pulse durations decreases faster as a function of distance. Thus, the lower threshold energy and shorter pulse duration for femtosecond laser pulse ablation would lead to lower plasma rim pressure values and faster pressure decay rates, which would collectively decrease the spatial extent of tissue disruption.

---

[1] For picoseconds at a propagation distance of 50 μm the final pressure was 1 kbar; For nanoseconds at a propagation distance of 200 μm the final pressure was 1 kbar.

After shockwave formation following acoustic pressure waves, a cavitation bubble begins to form on the nanosecond time scale (~ 10 nanoseconds), which continues to expand for microseconds or even seconds depending on the deposited laser energy [2]. Cavitations originate from the ionization of the media or any liquid interface, forming a gaseous vapor that expands from the focal volume into the surrounding tissue or media [13]. According to Vogel *et al.* [5], the maximum radius of a cavitation bubble after a single 100 femtosecond laser pulse focused into water with an NA = 1.3 is 200 nm. The small radius reflects low energy conversion into the formation of a cavitation bubble and the lower threshold energy required to elicit plasma mediated ablation. As the cavitation bubble expands, the bubble wall thins and releases some of its energy into the surrounding environment [5]. Bubble collapse is followed by an increase in pressure and the generation of additional cavitation bubbles with smaller maximum radii and initial bubble pressure [5, 10]. While a single 100 femtosecond laser pulse produces a bubble radius of 200 nm (near threshold), cavitations become much larger, on the order of micrometers, after multiple incident femtosecond laser pulses [5, 16]. For instance, plasma mediated ablation with 100 femtosecond laser pulses at a repetition rate of 80 MHz, re-excites the cavitation bubble, depositing more energy into the bubble before its initial collapse. This is supported by the fact that it would take close to 10 nanoseconds for the cavitation to reach its maximum radius [5] and the time interval between each incoming pulse would be $\tau = 1/80\,\text{MHz} = 12.5$ nanoseconds. Therefore, within 12.5 nanoseconds, the bubble would still be close to its maximum radius and the next incoming pulse would deposit extra energy into the cavitation, increasing its overall radius. However, by selecting the appropriate number of laser pulses incident on the tissue, the maximum bubble radius of the cavitation can be minimized [16]. After the bubble has formed, it expands out of the focal volume with a pressure equaling or exceeding hundreds of MPa [5]. This pressure induces stress, disrupting tissue as the cavitation bubble expands [3]. To a good approximation, the maximum cavitation bubble diameter determines the spatial extent of tissue damage [16]. It has been experimentally found that cavitation bubbles formed in a tissue-media environment expand less than those generated in pure media alone [3, 10]. This observation is likely explained by the fact that tissues have mechanical strength, which can slow down the expanding cavitation minimizing its disruptive forces [3, 10].

Differences between 80 MHz and 1 KHz laser pulse ablation

In femtosecond laser-tissue interactions, it has been proposed that the mechanism of ablation differs for repetition rates of 80 MHz and 1 KHz [5]. For instance, for 80 MHz laser pulse ablation, the energy per pulse is well below the threshold energy for optical breakdown. Each pulse produces an electron density that is below the critical electron density N_{crit} ($N_{crit} = 10^{21}$ cm^{-3} for 800 nm), and the result is the formation of a low-density plasma [5]. Due to these below-threshold pulse energies, it is believed that laser pulse ablation of biological materials results from the free electron induced chemical decomposition of the material through bond-breaking [5]. This is in contrast to ablation performed using low repetition rate, i.e. 1 KHz, laser pulses. At this repetition rate value the pulse energies available for laser-tissue interactions are at or above the threshold energy required to elicit ablation. High density plasmas are formed in conjuction with cavitation bubbles, and it is suggested that it is the gas bubbles formed that are responsible for the dissection of the biological material [5].

An additional distinguishing feature between 80 MHz and 1 KHz repetition rates for laser-tissue interaction studies is that the plasma formed in 80 MHz laser pulse ablation is due to the interaction of multiple laser pulses arriving every 12.5 ns. This is in contrast to 1 KHz laser pulse ablation, where the next incoming pulse (every 1 ms) is well separated in time and does not influence the previous incident pulse. This distinguishing feature is particularly important in the formation of cavitation bubbles, where large gas bubbles and an accumulative temperature rise are formed through the interaction of multiple laser pulses in 80 MHz laser pulse ablation.

Critical power for self-focusing and plasma formation

Self-focusing is a nonlinear phenomenon that causes the laser beam diameter to decrease as it propagates through a material. The origin of spontaneous focusing arises from the dependence of the index of refraction on the laser intensity [26, 27],

$$n(\omega) = n_1(\omega) + n_2(\omega)I \qquad (1.4)$$

where $n(\omega)$, $n_1(\omega)$, $n_2(\omega)$ and I are the total refractive index, the index of refraction in the absence of self-focusing, the nonlinear index (units: m^2/W) and the peak intensity (units: W/m^2), respectively. If the peak intensity becomes sufficiently large, $n_2(\omega)I$ contributes to the linear index by increasing the value of the total refractive index. With self-focusing present in the laser pulse ablation process, the peak intensity, the ionized electron density and the temperature rise become difficult to define. This is due to the difficulty of measuring the beam diameter within the material and the degree of self-focusing induced in the sample as a function of the propagation distance. Therefore, in laser pulse ablation studies, avoiding nonlinear self-focusing becomes important.

When high NA microscope objectives are used, NA ≥ 0.9, self-focusing can be eliminated. This process can be understood through an analysis of the diffraction limited irradiance spot size, d_r. Higher NA microscope objectives produce smaller focal spots (from equation (1.2) $d_r \,\alpha\, \frac{1}{\mathrm{NA}}$), and a given peak intensity can be achieved with a peak power less than that required when using lower NA microscope objectives. To place this in context, consider two microscope objectives with NA values of 1.0 and 0.5. The diffraction limited irradiance spot sizes assuming an 800 nm wavelength, as calculated using equation (1.2), are 976 nm and 1.95 μm, respectively. For a given peak intensity of

10^{12} W/cm^2, the peak power required to produce this intensity would be 7.5 kW/pulse (NA = 1.0) and 30 kW/pulse (NA = 0.5). Therefore, for a NA = 0.5, the peak power would need to be four times higher to produce a peak intensity of 10^{12} W/cm^2 at the focus. Higher peak powers increase the likelihood of nonlinear self-focusing occurring since the intensity required for self-focusing is dependent on both the peak power and critical peak power [7, 28],

$$I_{sf} = \frac{I}{1 - \frac{P}{P_{crit}}} \quad \text{and} \quad P_{crit} = \frac{3.77\lambda^2}{8n_1n_2\pi} \qquad (1.5)$$

where I_{sf}, I, P, P_{crit}, λ, n_1 and n_2 are the self-focusing intensity[1], laser peak intensity, laser peak power, critical peak power for self-focusing, wavelength, linear and nonlinear refractive index, respectively.

Since water is used as the model system for laser pulse ablation, the critical power for self-focusing can be easily calculated. Assuming a wavelength of 800 nm and a nonlinear index equal to 10^{-20} m^2/W [27], P_{crit} = 7.2 MW. While ablation performed using both of the above mentioned microscope objectives yields a peak power below the critical power value, the peak power created using the lower NA objective approaches the critical power more quickly. This is particularly important in studies that examine shockwave and cavitation bubble formation, where pulse energies above threshold are often used to study their dynamics. Therefore, higher above threshold pulse energies can be used in conjuction with larger NA microscope objectives while avoiding nonlinear self-focusing.

---

[1] In equation (1.5) if P approaches P_{crit}, the equation suggests that I_{sf} approaches infinity, indicative of a singularity. However, before the collapse of the laser beam to a singularity, the generated plasma would cause defocusing likely stopping the self-focusing process.

Despite the fact that the peak power generated with lower NA microscope objectives (i.e. NA = 0.5, as above) is lower than the critical power for self-focusing, plasma formation has been observed to differ for higher NA objectives. Recently, through numerical simulation, Arnold *et al.* [28] showed that plasmas formed with 0.5 and 0.6 NA objectives are highly asymmetric. Interestingly, a high density plasma is created before the geometrical focus, with the high density region surrounded by a lower density area [28]. Plasma generation ahead of the the focus may distort the propagating pulse and cause a phenomena called plasma defocusing [28]. As a result, higher pulse energies may be required to achieve a particular breakdown irradiance. For NAs equal to or greater than 0.9, Arnold *et al.* [28] showed that plasma defocusing became weaker, and was accompanied by the formation of smaller, more symmetric plasmas.

CHAPTER 2

CELL ISOLATION AND MEMBRANE SURGERY USING FEMTOSECOND LASER PULSES

2.1 Introduction[1,2]

The ability to manipulate living cells for the analysis of cell structure and function, growth and differentiation and gene expression has important applications to cell and molecular biology. Presently, little is known about how individual cells in a complex tissue respond to stimuli and their mechanisms for transferring and interpreting external stresses. To understand the behavior of cells in their native environment, non-invasive tools are required whose function is to dissect, remove or impart tension to components of the intracellular and extracellular environments. For instance, in epithelial layers, individual cells are connected through adherent junctions (i.e. junctional complexes) that are composed of transmembrane proteins [29], as shown in Figure 2.1. The transmembrane proteins extend from linker proteins in the intracellular environment and connect in the intercellular space between the plasma membranes of adjacent epithelial cells [29], Figure 2.1. Connected to the linker proteins are actin filaments that extend through the cell and connect to other linker and transmembrane proteins. An adherein belt is formed [29], mechanically coupling cells connected through the actin filaments; any stress induced in a single cell can be transmitted to the entire tissue. An understanding of how a cell mechanically stimulated through the dissection of actin transmits this stress to adjacent cells would be important for elucidating the global behavior of cells in a tissue environment.

---

[1] Portions of this section have been published in Kohli *et al*. Laser Surg Med. 2005, 37:227-230.
[2] Portions of this section have been published in: Kohli *et al*. Prospects and developments in cell and embryo laser nanosurgery. Interdisciplinary Reviews: Nanomedicine. In press. (**Invited article**).

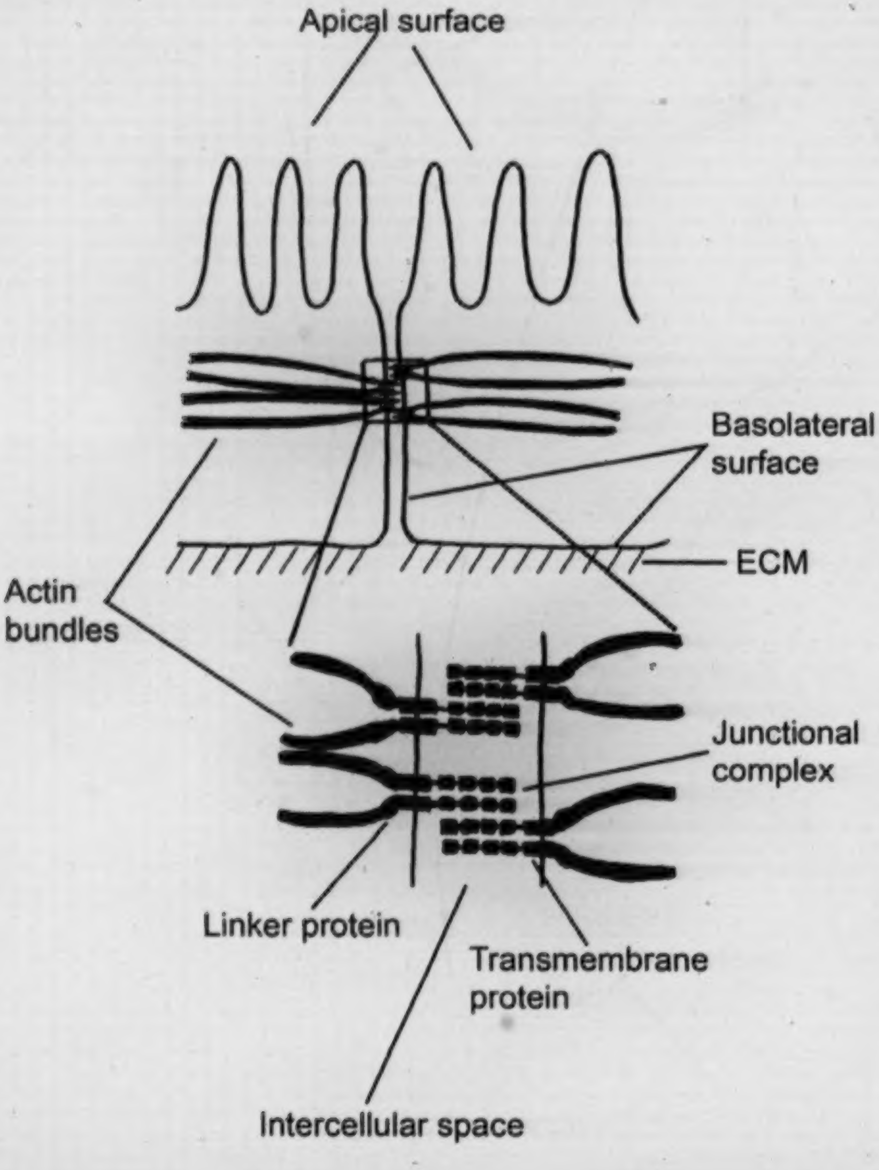
Apical surface
Basolateral surface
ECM
Actin bundles
Junctional complex
Linker protein
Transmembrane protein
Intercellular space

Figure 2.1: Adherent junctions formed between two epithelial cells. In the intercellular space, transmembrane proteins of each cell connect and terminate at a linker protein on the intracellular side of the membrane. Attached to the linker protein are actin bundles, which extend throughout the cell. Through the interaction of actin with other linker-transmembrane proteins, an adherein belt is formed. Adjacent cells are mechanically coupled via actin and the junctional complex. An extracellular matrix (ECM) is located beneath the bastolateral surface of the cell. The above figure was adapted from [29].

Mechanical Cell Manipulation Techniques

Several engineering techniques have been developed to study the structure and function of cells and tissues. Some of these techniques for manipulating both prokaryotic and eukaryotic cells include the use of needle probes, micromanipulators, magnetic tweezers, laser capture microdissection (LCM), UV and NIR light sources, [14, 19, 21-23, 30-35]. For instance, Maniotis *et al.* [36] demonstrated the use of ligand-coated microbeads bound to membrane receptors in bovine capillary endothelial cells to study the mechanical coupling of the cytoskeleton to the nuclear membrane. By pulling the bound microbeads away from the nucleus, a deformation was observed in the nuclear structure in the direction of the pulled bead. Utilizing this technique, the authors were able to identify the transmission of tensile stresses to the cytoskeleton and nucleoskeletal network, which induced changes in the intracellular environment of the cell [36]. In work by Alenghat *et al.* [37], protein coated microbeads bound to membrane receptors in mouse embryonic cells were also used to quantify mechanical stresses. In knock-down mice deficient in the interconnects between membrane receptors and the cytoskeleton, the authors observed an increase in bead displacement and a decrease in mechanical stiffness in comparison to wild type cells [37].

Ultraviolet and Near Infrared Laser Cell Manipulation Techniques

As an alternative to the mechanical stress studies mentioned above, LCM has been used as a technique for isolating cells for genomic and proteomic analysis [30-33]. To obtain cell isolates, an ethylene vinyl acetate (EVA) thermoplastic film is placed over the cells of interest [31, 33]. Using pulsed laser irradiation at infrared wavelengths, the

EVA polymer is thermally activated to 90 °C [30], melting and expanding the film over the targeted cells. As the EVA cools, the desired cells are impregnated in the solidified polymer, then biopsied after shearing from the surrounding tissue and substratum [32]. Isolated cells can then be transferred to a lysis buffer for DNA, RNA and protein analyses [38, 39].

Using UV laser pulses produced from a nitrogen gas laser, Roberts *et al.* [40] demonstrated the laser pulse ablation of the filamentous fungus *Aspergillus* for the purpose of measuring the activity of membrane bound ion channels. Before laser pulse ablation, Roberts and colleagues [40] exposed the fungus to a plasmolysing solution to detach the underlying plasma membrane from the overlying cell wall, except for a few remaining anchor points. UV laser pulses were then focused by a 0.8 to 1.3 NA 40X microscope objective onto *Aspergillus* for the creation of permanent holes in the cell wall [40]. After deplasmolysis, membrane-bound blebs formed within five to thirty minutes, which protruded from the UV ablated holes. Suction of the membrane-bound blebs in conjuction with patch-clamping was used to measure the ion channel activity in the extruded blebs [40].

In a study by Fuhr *et al.* [41], UV laser pulses were used to laser pulse ablate the sensory cells of the insect *Locusta migratoria L.* Laser pulses with a pulse duration 10 nanoseconds and a wavelength of 248 nm were directed onto the tympanal membrane in the ear drum for the creation of 20 µm x 20 µm sized square holes. Each hole was formed with a beam dwell time ranging from 1 to 10 microseconds and a pulse energy of 500 µJ [41]. Post-laser pulse ablation, the authors analysed the auditory threshold curves of the insects to determine if laser pulse ablation induced changes in the auditory responses of the left or right ears [41]. Depending on the location of ablation, asymmetries in the sensitivity of the ears to high frequencies were observed, indicating damage to certain auditory receptors [41].

In a recent article by Soustelle *et al.* [42], the UV-mediated pulse ablation of glial cells in *Drosophila melanogaster* was demonstrated to identify cell-cell interactions. Soustelle and colleagues [42] generated transgenic green fluorescent protein (GFP) labeled glial cells that were identified in the organism using confocal micrscopy. To excite the GFP labeled cell, UV laser sources at wavelengths of 351 and 364 nm were focused by a 1.4 NA 63X oil immersion microscope objective onto the nucleus of the cell. After twenty seconds of laser irradiation GFP expression from the glial cell faded, accompanying cell death [42]. To address whether the laser pulse ablated cells induced changes in adjacent cell layers, ventrally located cells in the fly wing epithelium were laser pulse irradiated using the same laser parameters and changes to dorsally located cells were monitored. The authors found that GFP labeled dorsal cells were unaffected by UV laser pulse ablation after cell death of the ventral cells had occurred [42].

NIR femtosecond laser pulses have recently emerged as an alternative laser source to study biological materials. The attractive features of this laser system are the lower threshold energy required to elicit laser pulse ablation and its applicability to deep tissue studies. Presently[1], femtosecond mediated pulse ablation has been used on several biological model systems including human metaphase chromosomes [14], plant chloroplasts [21], mitochondria in endothelial and HeLa cells [22, 34], yeast microtubules [35], hamster ovary cells [23] and the actin cytoskeleton in fixed 3T3 fibroblasts and Bovine endothelial cells [19, 22].

---

[1] A review article discussing the various applications of femotosecond laser pulses can be found in [43].

For instance, in work conducted by Konig *et al*. [14], the authors used femtosecond laser pulses with a pulse duration and wavelength of 170 femtoseconds and 800 nm, respectively, to nanodissect fixed air-dried human metaphase chromosomes. Dissection cuts were made by scanning the laser pulse across the chromosomal structure resulting in cuts 85 to 170 nm in width. More recently, Sacconi *et al*. [35] used 100 femtosecond laser pulses to laser ablate GFP-labeled microtubules in fission yeast cells. Individual mitotic spindles in anaphase B were irradiated with an average laser power of 4 mW for 150 ms [35]. Post-laser pulse ablation the spindles were found to bend and break into segments. In a study by Tirlapur *et al*. [21], lasers pulses similar to those used in the above studies were used to nanodissect plant cell walls and chloroplasts in *Elodea densa*. With an average laser power ranging from 30 to 50 mW, lesions were made in the plant cell wall and portions of targeted chloroplasts were removed.

Similar to the dissection of organelles in plants, Watanabe *et al*. [34] ablated a mitochondrion in a Human carcinoma cell line, HeLa, using a femtosecond laser pulse with an energy ranging 2 to 7 nJ/pulse and a laser exposure time of 250 ms. The authors used confocal imaging to confirm that the targeted mitochondrion was ablated, and that its absence was not due to its diffusion out of the focal plane [34].

Shen *et al*. [22] targeted a single fluorescently labeled mitochondrion in bovine adrenal capillary endothelial cells with femtosecond laser pulses. The purpose of the study was to identify the connective properties of this organelle. After stationary irradiation of the mitochondrion with a few hundred pulses at an energy of 2 nJ/pulse, removal of the mitochondrion from the endothelial cell was reported without affecting neighboring mitochondria [22].

Purpose of this study

This chapter explores the application of NIR femtosecond laser pulses as a tool to perform membrane surgery and cell isolation. The motivation for this study was to demonstrate that when focused femtosecond laser pulses were localized onto the plasma membrane of living cells, dissection cuts could be made in the membrane without inducing morphological changes in the cell. After multiple surgical incisions along the short and long axes of the cell membrane, it was shown that the cell maintained its membrane integrity without collapse or disassociation. By altering how the laser pulses were applied, single cell isolation through the removal of focal adhesions was demonstrated, again without affecting the morphology of adjacent cells. The experimental methods used for cell manipulation are detailed in section 2.2.

Cell line model systems

To achieve membrane surgery and cell isolation, two different cell model systems were used[1]. The selection of different cell types was to show that the application of this laser tool was independent of the chosen cell line. For membrane surgery, Madin-Darby Canine Kidney (MDCK) epithelial cells were chosen, while for single cell isolation Chinese Hamster fibroblast (V79-4) cells were used. Both of these model systems have been extensively used in cell biology [44-50], and the culture process for normal growth and adherence to the substratum are well known. MDCK and V79-4 cells both form tissues in cell culture; however, the mechanism of interaction between adjacent cells and their substrate is different [29]. For instance in MDCK epithelial cells, in addition to adherent junctions, Figure 2.1, tight junctions form between the plasma membranes of two closely spaced cells. Also located along the basolateral sides of the cells are desmosomes (another type of adherent junction) that attach adjacent cells and support intracellular intermediate filaments such as keratin [29]. Interactions of MDCK cells with the substrate occur through transmembrane proteins that bind to a thin extracellular matrix (ECM), Figure 2.1. In contrast, V79-4 fibroblast cells form adherent junctions between adjacent cells that are less reinforced than those between epithelial cells [29]. Fibroblast cells typically form connective tissue and attach to their substrate via a dense ECM rich in collagen [29].

---

[1] A detailed description of the cell culture processes can be found in Appendix F.

Potential applications

The membrane surgery and cell isolation techniques presented in this chapter have numerous applications to biological research. Similar to tissue biopsies performed with LCM, the scanning of femtosecond laser pulses for single or multiple cell isolation could be used as an alternative method for obtaining tissue isolates. With this technique, the need to procure cells using thermoplastic activated polymers could be eliminated. Tools such as LCM and protein coated microbeads are limited to the manipulation of the extracellular environment and cannot operate within the intracellular space of living cells.

Similar to studies by Alenghat *et al.* [37] on the cell mechanics of vinculin (linker protein) deficient mice embryonic cells, NIR femtosecond laser pulses could be used to selectively ablate the actin-linker protein region studied by the authors without inducing damage to the plasma membrane. For instance, in non vinculin-deficient cells, fluorescently labeled actin filaments and other intermediate filaments could be dissected to monitor mechanical and structural changes in single or multiple cells. As an analogous application, applied femtosecond laser pulses could be localized onto the biological membrane for permeabilizing and introducing exogenous foreign molecules into the intracellular environment. Such studies would be applicable to the discipline of cryobiology, for example, where the introduction of impermeable molecules (i.e. carbohydrates) into the cell acts to protect the viability of cells exposed to cryogenic temperatures (i.e. –196 °C). Successfully cryopreservation through the introduction of impermeable solutes would provide a resource bank of stored cells and tissues.

2.2 Results and Discussion[1]

Experimental methodology

Cell isolation and membrane surgery of living mammalian cells were performed using a modified Zeiss upright light microscope. Figure 2.2 presents a front view schematic of the upright light microscope. The microscope components indicated include the ocular imaging head, A, the filter chamber, B, the objective nose piece, C, microscope objective lens, D, *x-y-z* motorized stage, E, the white light condenser, F, and the inverted white light source, G. Located directly above the ocular imaging head is the imaging port that allows for image capture via a charge coupled device (CCD). At the rear of the light microscope the fluorescence lamp house was removed and this entrance port was used to couple the femtosecond laser pulses into the imaging setup, Figure 2.3. Excitation and emission filters housed in a filter cube for fluorescence imaging were replaced with a fabricated gold beam splitter (University of Alberta) mounted in the filter cube at an angle of 45 °. This beam splitter, shown in Figure 2.2, reflects the incoming laser light (the femtosecond pulse is coupled into the rear entrance port of the microscope as shown in Figure 2.3) towards the microscope objective lens, D.

The gold beam splitter was designed using a glass coverslip with a thickness of ~ 250 μm. A 22 mm diameter circle was cut from the glass coverslip using a waterjet[2]. Gold was sputtered onto the glass coverslip[3] with a sputtering time ranging from 50 to

---

[1] Portions of this section have been published in Kohli *et al.* Laser Surg Med. 2005, 37:227-230.

[2] Waterjet operated by the Electrical and Computer Engineering machineshop staff.

[3] Special thanks to Anthony Dechant for sputtering gold onto the coverslips. Sputtering was performed using the Kurt J. Lesker magnetron sputtering system #1 at the University of Alberta Nanofabrication facility. The power, pressure and voltage used in the sputtering of gold were 75 W, 7 mTorr and ~ 400 V, respectively.

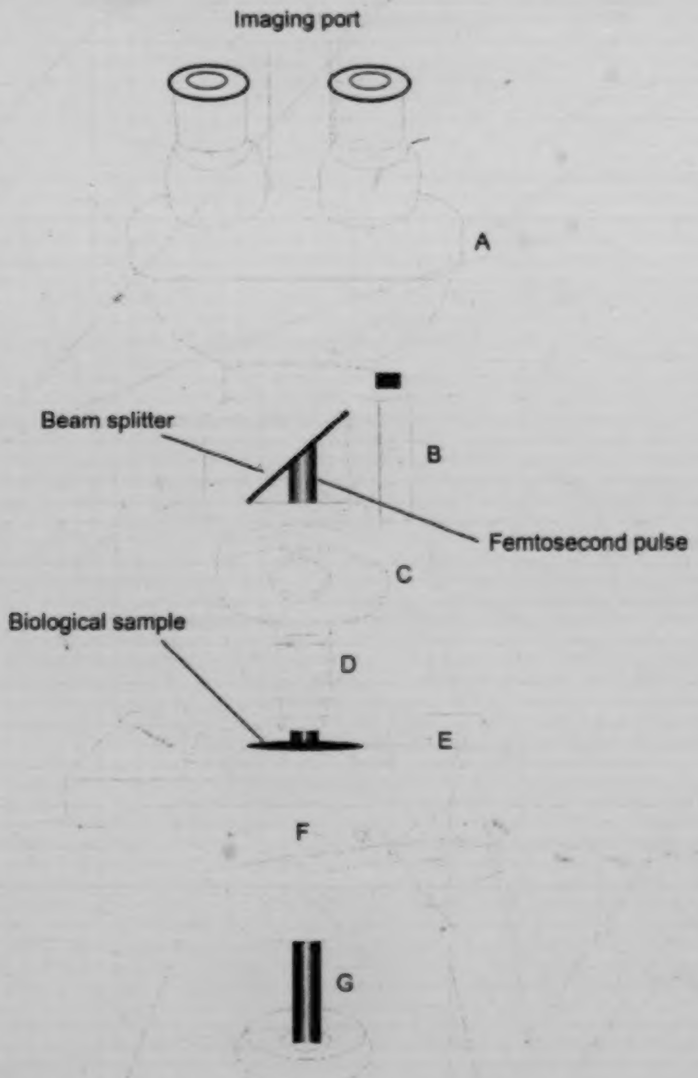
Imaging port
A
Beam splitter
B
Femtosecond pulse
C
Biological sample
D
E
F
G

Figure 2.2: Transparent front view of the modified upright Zeiss light microscope. Femtosecond laser pulses were coupled into the rear port of the microscope and reflected by the gold beam splitter towards the microscope objective lens, D. A – ocular imaging head, B – filter chamber, C – objective nose piece, D – microscope objective lens, E – *x*-*y*-*z* motorized stage, F – white light condenser and G – white light source.

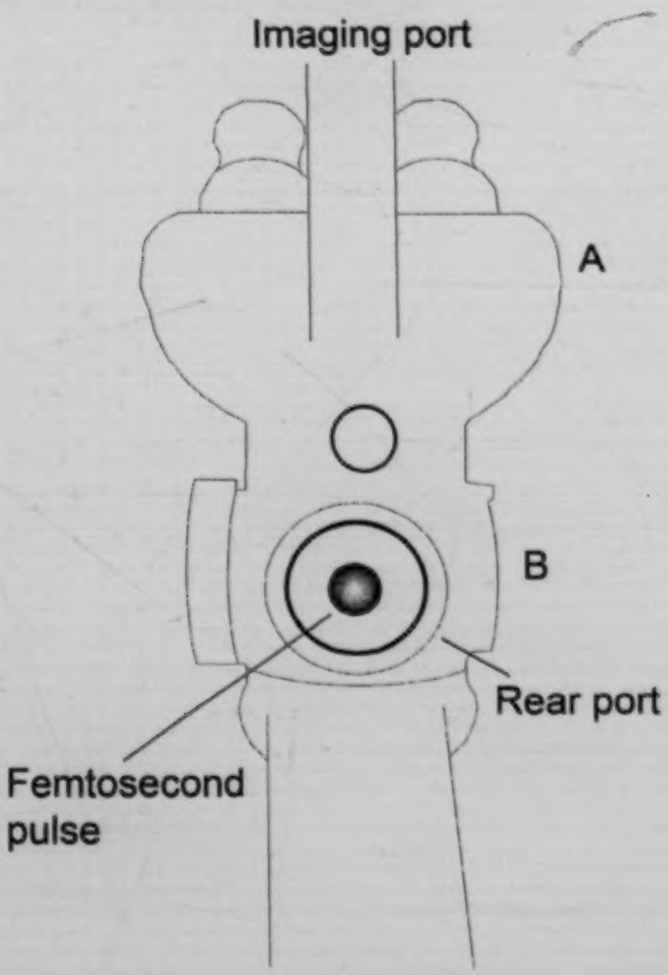
Imaging port
A
B
Rear port
Femtosecond pulse

Figure 2.3: Rear view of the microscope shown in Figure 2.2. Femtosecond laser pulses were coupled into the rear port of the microscope, as shown above. A – ocular imaging head, B – filter chamber.

100 seconds. Reflection and transmission measurements of the beam splitter were made by directing unfocused femtosecond laser light (700 to 900 nm, centered at 800 nm) at the beam splitter surface. With an average laser power of 389 mW incident on the beam splitter, the reflective and transmitted powers as measured by a power meter (Gentec-EO, Canada) ranged from 108 mW (27 % reflection) to 285 mW (73 % reflection) and from 92 mW (24 % transmittance) to 60 mW (15.4 % transmittance), respectively. The beam splitter with the largest reflective power was chosen for use in the optical setup to ensure maximum laser power delivery to the biological sample.

Figure 2.4 is a transparent side view of the microscope shown in Figure 2.2 with the beam splitter in place. The femtosecond laser pulse was first coupled into the rear entrance port of the filter chamber, B. Laser light was reflected by the fabricated gold beam splitter housed in the filter chamber and directed towards the microscope objective lens, D. Both back reflected laser light and white light traversed the filter chamber, B, and were captured at the imaging port shown in Figures 2.2 through 2.4.

Cultured MDCK and fibroblast cells (a detailed description of the cell culture process can be found in Appendix F) hydrated in fresh culture media (~ 10-20 μL) were placed on the *x-y-z* motorized stage, E. The collinearly coupled white light, G, was focused with a condenser, F, and parfocal imaging was set by observing the cells' image through the ocular imaging head, A. To minimize evaporation of the media covering the cells, the *x-y-z* motorized stage was temperature controlled to 4 °C. A controlled stage temperature was maintained by engineering a rectangular C-shaped copper block (not shown in Figures 2.2 and 2.4) machined to a maximum thickness of 37 mm and a length

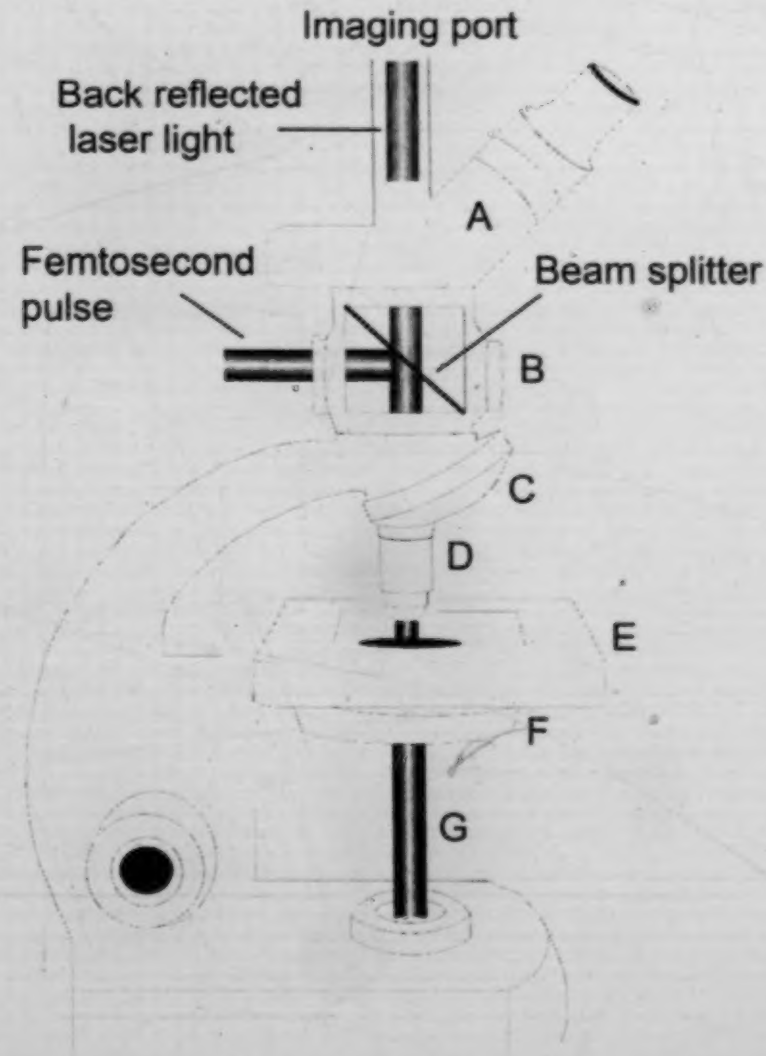
Imaging port
Back reflected laser light
A
Femtosecond pulse
Beam splitter
B
C
D
E
F
G

Figure 2.4 Transparent side view of Figure 2.2. The femtosecond laser pulses were directed into the rear port of the microscope and were reflected by the gold beam splitter towards the microscope objective lens, D. Back reflected laser light and white light travel back up towards the filter chamber, B, and were captured at the imaging port (back reflected white light is not shown). A – ocular imaging head, B – filter chamber, C – objective nose piece, D – microscope objective lens, E – *x*-*y*-*z* motorized stage, F – white light condenser and G – white light source.

of 125 mm. Inlet and outlet channels were milled along the length of the copper block to allow for circulating water flow. The inlet and outlet channels were connected to a water chiller set to 4 °C. After connecting the water channels, the underside of the block was coated with a conductive paste and the block was anchored to the microscope stage, E. Cells plated onto glass slides were mounted directly onto the stage adjacent to the cooling block. Temperature probes placed at various positions along the stage verified a stage temperature of 4 °C.

For membrane surgery and cell isolation, femtosecond laser pulses were directed through the rear port of the microscope (Figure 2.3) and reflected by the beam splitter (Figures 2.2 and 2.4) towards a 0.95 NA 100X air microscope objective. Femtosecond laser pulses were generated from a Titanium:Sapphire laser oscillator that produced sub-10 femtosecond laser pulses. The pulse repetition rate of the oscillator was 80 MHz, with a delay of 12.5 nanoseconds between consecutive pulses. The emitted wavelength spectrum ranged from 700 to 900 nm, centered at 800 nm (as measured by a spectrum analyzer). At the focus of the microscope objective, the diffraction limited irradiance spot size (diameter) as estimated using equation (1.2) in Chapter 1, was $d_r = 1027$ nm ($\lambda = 800$ nm). Biological samples were irradiated with a pulse energy of 5 nJ/pulse[1], resulting in a peak power at the focus of 17 kW/pulse (this value was calculated using an estimated broadened pulse duration of 291 femtoseconds; see Appendix A for details). The peak intensity at the focus, as calculated from the peak power and irradiance spot size, was estimated to be $2.1\text{x}10^{12}$ W/cm^2.

---

[1] The pulse energy represents the measured value entering the microscope objective lens. Fresnel's equations describing the reflection and transmission values through various index media can be used to approximate the amount of average laser power loss. From calculations (not presented in this thesis), the total average laser power loss was a few milliwatts.

Both the white light and laser light were collected by a monochrome CCD (WAT-902H Watec Monochrome Camera (Aegis Electronics, AZ) with horizontal and vertical pixel dimensions of 8.4 μm x 9.8 μm) and an attenuator filter (not shown in Figures 2.2 through 2.4) was placed in the beam path in front of the CCD to minimize the detected laser light. The CCD was interfaced with a computer for capturing video and still images. The magnification of the microscope was measured to ensure accurate measurements of biological cell sizes and laser pulse induced dissection cuts. Using a test sample consisting of a microscope slide with etched 10 μm divisional lines, each 1 μm line projected an image on the viewing screen of 2.5 mm in size. This yielded a total magnification of 2500X. A simplified version of the experimental setup shown in Figures 2.2 through 2.4 is presented in the schematic drawing of Figure 2.5.

Cell Isolation of V79-4 cells

Figure 2.6 depicts V79-4 cells cultured at low density. When these motile cells are plated, the cells spread and attach to their substratum via membrane integrins bound to the extracellular matrix (ECM). This binding is mediated by adhesive glycoproteins (i.e. fibronectin) [51]. Integrins are transmembrane proteins composed of two subunits (alpha and beta) that connect the cytoplasm to the extracellular environment [51]. At the outer membrane surface, integrin binds to fibronectin, which is found in the ECM. The ECM is a matrix secreted by the cells containing a meshwork of collagen, elastin, proteoglycan and fibronectin [51]. Binding interactions between integrins and the ECM form focal adhesions that anchor the cell to its substrate. These focal adhesions provide

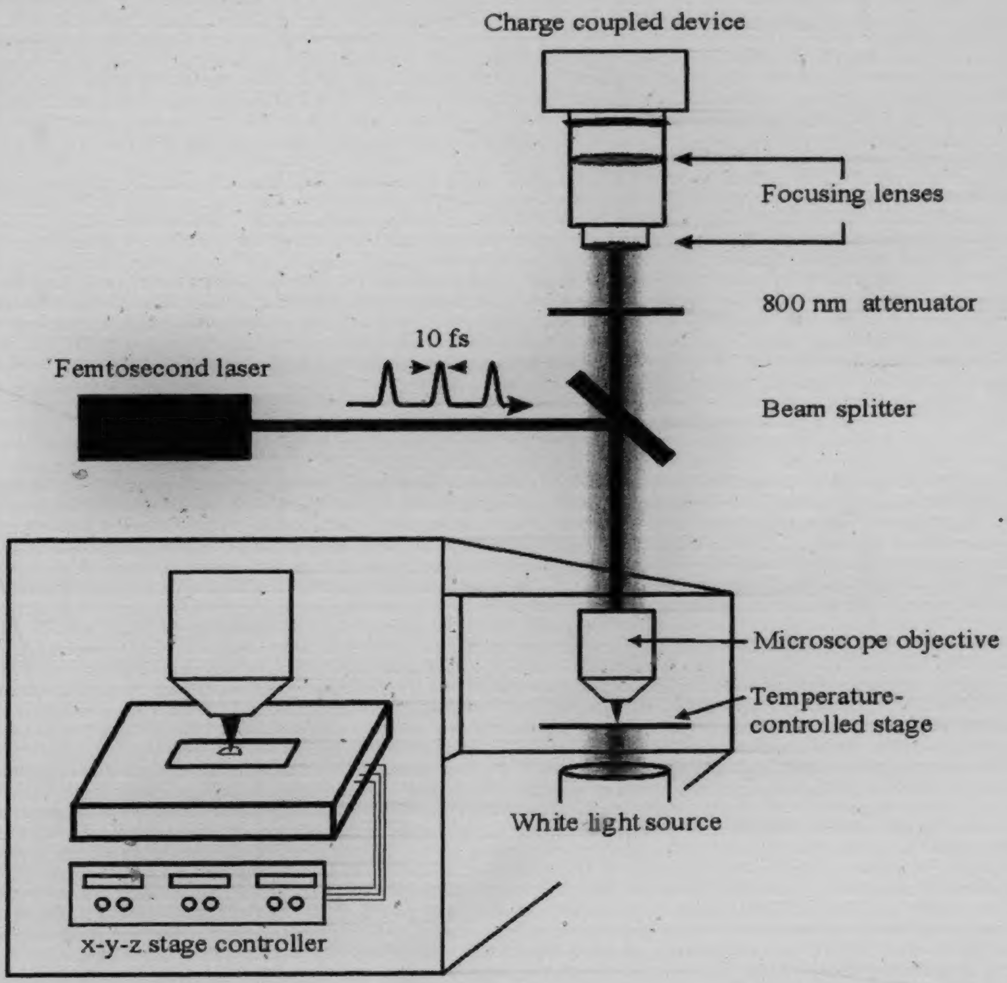
Charge coupled device
Focusing lenses
800 nm attenuator
10 fs
Femtosecond laser
Beam splitter
Microscope objective
Temperature-controlled stage
White light source
x-y-z stage controller

Figure 2.5: Sub-10 femtosecond laser pulses produced from a modelocked titanium sapphire laser oscillator, with a center wavelength at 800 nm and a pulse repetition rate of 80 MHz, were coupled and focused onto the biological specimen by a 0.95 100X high numerical aperture air microscope objective. The biological sample was placed on a *x-y-z* motorized temperature controlled stage, cooled to 4 °C. White light illuminated the sample in the inverted position, where both the white light and the laser light were captured by a charge coupled device (CCD). The CCD was interfaced with a computer (not shown) allowing for the capture of still images and real time video.

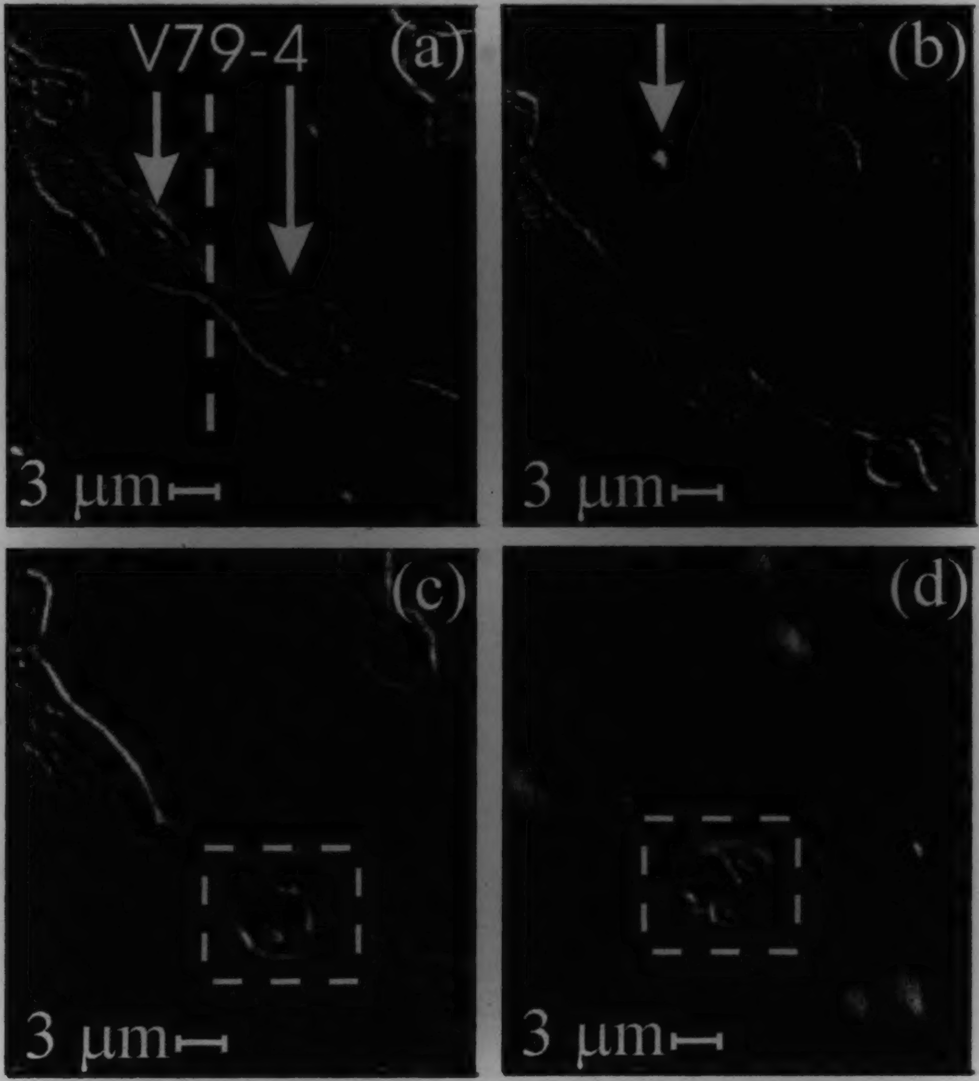

Figure 2.6: Live video observation of single cell isolation of living V79-4 cells. (a) Arrows indicate two fibroblast cells that are tethered together by a focal adhesion (width of the tethered region is ~ 1 μm) with the dotted line representing the dissection interface relative to which the cells are scanned for the removal of the focal adhesion. (b) The focused laser pulse was scanned along the dissection interface between the V79-4 cells, resulting in the removal of the tethered region, (c). The dotted boxes in (c) and (d) depict the isolated curled fibroblast librated from its adjoining cell. Pulse energy used for single cell isolation was 5 nJ/pulse.

tension, which when disrupted releases the cell from the substratum, resulting in the cells folding into circular form.

The tethering of two V79-4 cells with focal adhesions is observed in Figure 2.6(a), where the arrows indicate the individual cells. In this figure, the dashed line represents the dissection interface relative to which the cells were scanned for the removal of the focal adhesion and the isolation of an individual cell. Scanning of the focused laser spot, Figure 2.6(b) (arrow), along the dissection interface resulted in the removal of the tethered connection joining the fibroblast cells. The single isolated cell is depicted in Figure 2.6(c), which has curled into circular form, resulting from the release of tension that was sustained by the focal adhesions. An image of the folded cell separated from its adjoining partner and the substrate is observed in Figure 2.6(d). Only morphological assessments of cell viability by visual inspection were performed and included the absence of membrane re-orientation, bleb formation or cell collapse.

Membrane Surgery of MDCK cells

Unlike fibroblasts, MDCK cells are devoid of focal adhesions [51]. Cell-substrate interactions are mediated by adhesive glycoproteins such as laminin, which is present in the basal lamina (underlying the cell, see Figure 2.1). Similar to the ECM secreted by fibroblast cells, the basal lamina contains collagen and proteoglycans [51]. Laminins in the basal lamina bind to integrins [51]; together these provide an anchor for binding the cell to its substratum.

Figure 2.7 depicts a 12 μm MDCK cell plated and bound to its substrate. When the cell was scanned along its short axis relative to the focused femtosecond laser spot,

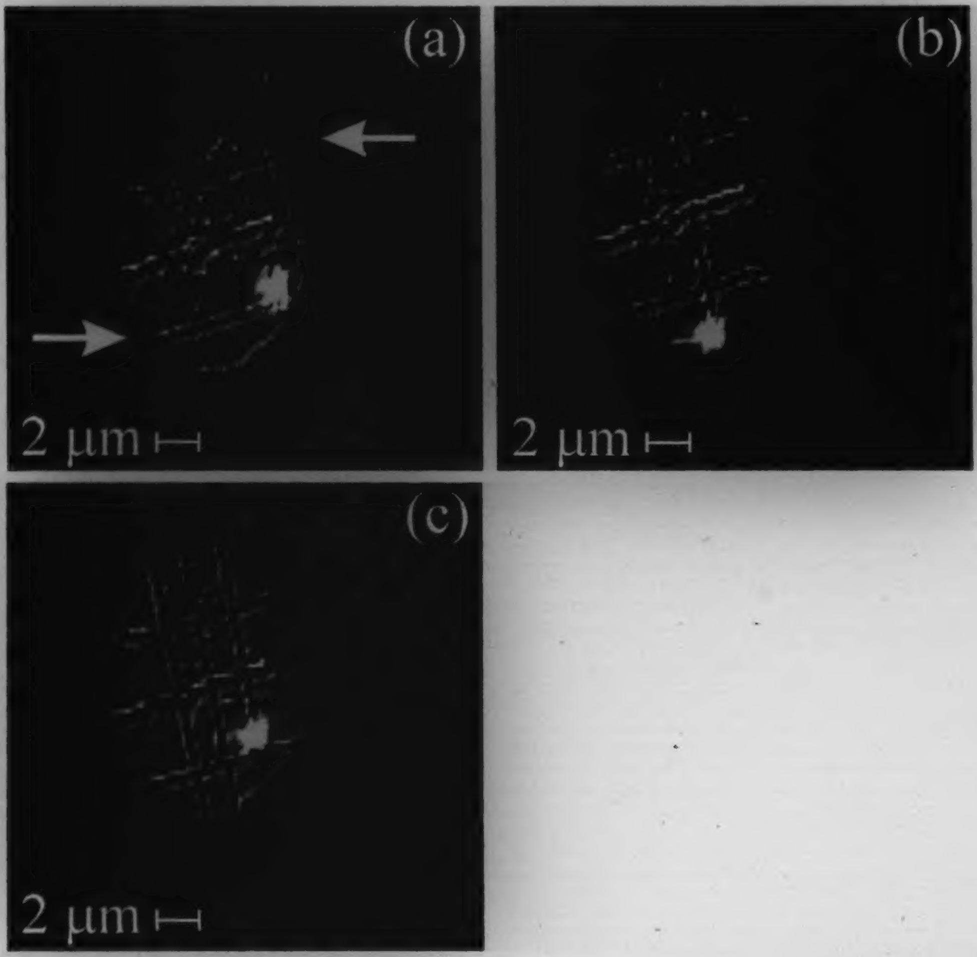

Figure 2.7: (a) Depicts membrane surgery of a live MDCK cell. Three surgical incisions were made along the short axis of the 12 µm cell. The arrows in (a) represent the ablated extracellular matrix that is secreted by the cell. Scanning the cell along its long axis, (b) and (c), three additional membrane dissection cuts were made. Post-membrane surgery, the cell maintained its morphology without evidence of cell collapse, disassociation or bleb formation. It is suggested that single cell isolation of MDCK cells is realizable by tracing the exterior contour of the cell (see text for details). In (a), (b) and (c) the bright spot represents the focused laser pulse. Pulse energy used for membrane surgery was 5 nJ/pulse.

three surgical dissection cuts were made in the biological membrane, Figure 2.7(a). Traversing the cell along its long axis, Figures 2.7(b) and 2.7(c), three additional surgical incisions were made. The arrows in Figure 2.7(a) and the bright spots in Figures 2.7(a), 2.7(b) and 2.7(c) represent the removed adhesive matrix and the focused femtosecond laser spot respectively. Similar to the fibroblast study, only morphological assessments of cell viability were performed[1].

Mechanism and action of femtosecond laser pulse surgery

The mechanism responsible for the removal of focal adhesions and the dissection of the biological membrane can be attributed to the laser-tissue interaction process mentioned in Chapter 1. Through nonlinear multiphoton absorption and ionization, ablation of the biological tissue occurs, resulting in the removal of cellular material contained within the focused laser spot. The spatial extent of tissue removal depends on the interplay between the laser spot size, the pulse energy and the beam dwell time. Decreasing the focused laser spot size (achieved by using higher NA microscope objectives) localizes the nonlinear absorption process to a smaller focal volume. In addition, a proper balance between pulse energy and beam dwell time must be established in order to reduce the amount of energy deposition and the formation of large cavitation bubbles. Both of these parameters could increase the spatial extent of tissue disruption and decrease the precision of laser dissection.

From Figures 2.6 and 2.7, it was found that living cells were quite resilient to the applied femtosecond laser pulses. Post-laser pulse treatment, the cells remained morphologically intact without membrane re-orientation, bleb formation or cell collapse. Figure 2.7 further supports these observations, showing that the MDCK cell remained intact after multiple dissection cuts along both axes of the cell. It was hypothesized that the lack of cell collapse and disassociation following membrane surgery was likely attributed to the coalescence of the dissected plasma membrane. Permanent incisions in the membrane without resealing of the lipid bilayer would compromise cell viability leading to eventual cell death. However, if the bilayer had resealed, closing the incision, no evidence of membrane surgery would have been observed. Since none of these two cases was observed, it was likely that fusion of the dissected plasma membrane prevented cell disassociation. Further experimentation is required to justify this hypothesis.

---

[1] A more rigorous assessment of cell viability would be to perform a membrane integrity assay on the dissected cell, or to culture the laser-manipulated cell and observe cell division.

As with the demonstrated isolation of fibroblast cells, single cell isolation of MDCK cells is realizable. The arrows in Figure 2.7(a) indicate portions of the removed ECM. By scanning the focused laser spot around the contour of the cell, the entire adhesive matrix could be removed, liberating the cell from its substrate. The precision of cell isolation would depend on the laser spot size, laser pulse energy, laser scanning precision and beam dwell time.

As mentioned in Figures 2.6 and 2.7 and in Appendix F, the pulse energy used for cell isolation and membrane surgery was 5 nJ/pulse with a peak power at the focus of 17 kW/pulse. The irradiance profile, as given by equation (1.2) in Chapter 1, has a theoretical elliptical geometry with radial and depth dimensions of $d_r = 1027$ nm and $d_z = 2071$ nm. However, the ablation profile is governed by the electron density profile and not the irradiance profile, and both d_r and d_z need to be divided by $\sqrt{5}$ to account for the multiphoton absorption process. The theoretical geometric ablation profile (electron density profile) then becomes $d_r = 460$ nm and $d_z = 926$ nm. From Figure 2.7(c), the width of the dissection cut was measured to be ~ 800 nm, as determined from calibrated measurements of the microscope magnification[1]. Comparing the dissection cut to the theoretical radial dimension of the ablation profile (i.e. the irradiance profile that is reduced by $\sqrt{k}$), the incision made in the biological membrane was 1.74 times larger. The increased width was likely attributable to many factors, including the microscope objective not being index matched with the media (an air microscope objective and not a water immersion objective was used), the spot size at the focus not being diffraction limited and the formation of cavitation bubbles that induced disruptive forces as they expanded, increasing the spatial extent of cell damage.

The ionized electron density after a single femtosecond laser pulse can be theoretically estimated using Vogel *et al.* [5] simulation results on the maximum evolution of the electron density as a function of the normalized irradiance (I/I_R; $I_R = 6.5\text{x}10^{12}$ W/cm^2 for $N_{crit} = 10^{21}$ cm^{-3} [5]). The ratio of $I/I_R = 0.32$ ($I = 2.1\text{x}10^{12}$ W/cm^2 as previously calculated in the experimental methodology section), yields an approximate maximum electron density of 10^{18} cm^{-3}. A density of 10^{18} cm^{-3} represents an overestimate of the true value, as Vogel *et al.* [5] simulations were performed using a pulse duration of 100 femtoseconds and not 291 femtoseconds (see Appendix A). For 100 femtoseconds the peak power would be higher (assuming the same pulse energy of 5 nJ/pulse; 17 kW/pulse vs. 50 kW/pulse) and the electron density would also be larger. Despite this, the exponent value would be within two orders of magnitude (50 kW/pulse; 100 femtoseconds; $I/I_R = 0.93$; $\rho_{max} = 10^{20}$ cm^{-3}) for pulse durations between 100 and 291 femtoseconds. It should be noted that the estimated electron density after a single femtosecond laser pulse is 1000 times smaller than the breakdown density ($N_{crit} = 10^{21}$ cm^{-3} [5]). This result indicates that it is the cumulative interaction of many laser pulses that leads to the optical breakdown of the material. Therefore, each applied laser pulse is below the threshold for breakdown, yet each pulse results in an electron density of 10^{18} cm^{-3} that is produced from the nonlinear multiphoton absorption and cascade ionization processes. These calculated values confirm that a lower irradiance (or consequently a lower pulse energy) can initiate the ablation process without reaching the breakdown irradiance value, as is required for longer pulse durations (i.e. nanoseconds).

---

[1] See the experimental methodology section.

With knowledge of the electron density, the temperature rise within the focal volume after a single femtosecond laser pulse can also be estimated. From equation (1.3) in Chapter 1 the temperature rise scales linearly with the volumetric energy density. According to [5], the volumetric energy density is related to the electron density, the average gain in energy of the ionized electrons for impact ionization and the effective ionization potential of water (different from the band gap of water; see appendix A for more detail) [5],

$$\varepsilon = \rho_{\max}(9/4)\tilde{\Delta} \tag{2.1}$$

where $\rho_{\max}$ and $\tilde{\Delta}$ are the maximum electron density and the effective ionization potential [5]. The factor 9/4 originates from the average gain in kinetic energy of the impact electron plus the effective ionization potential (5/4 (average kinetic of the impacting electron) $+\tilde{\Delta}$ [5]; see Appendix A for more detail). The effective ionization potential depends on the Keldysh parameter, γ, which describes whether ablation results from tunneling ionization ($\gamma < 1.5$), multiphoton ionization ($\gamma > 1.5$) or a combination of both ($\gamma \sim 1.5$) [7]. The Keldysh parameter is related to the peak intensity and the band gap energy [7],

$$\gamma = \frac{\omega}{e}\sqrt{\frac{cm\varepsilon_o n\Delta}{I}} \qquad (2.2)$$

where $\omega, e, c, m, \varepsilon_o, n, \Delta$ and I are the frequency of light, electron charge, speed of light, effective mass ($\frac{1}{2}m_e$ [52]), permitivity of free space, index of refraction (1.33 for water), band gap energy of water (6.5 eV [18]) and the peak intensity, respectively. For $\gamma > 1.5$, the effective ionization potential reduces to the band gap energy [5]. With the peak intensity equaling $2.1\text{x}10^{12}$ W/cm^2, γ, as calculated from equation (2.2), is 4.15. Therefore, the effective ionization potential in equation (2.1) can be approximated as the band gap energy of water. With $\rho_{max} = 10^{18}$ cm^{-3}, $\varepsilon = 2.34$ J/cm^3 and $\Delta T = 0.56$ K (ΔT is the temperature rise after a single 291 femtosecond laser pulse). This result may seem surprising; however, considering that the electron density created after the laser pulse is 1000 times smaller than N_{crit}, the temperature rise per pulse would be expected to be small since the peak intensity is well below the breakdown threshold irradiance, I_R. As a comparison, if we assume that after a single laser pulse an electron density of $1.8\text{x}10^{20}$ cm^{-3} was created, then $\varepsilon = 420.5$ J/cm^3 and $\Delta T = 100.5$ K after 291 femtoseconds. After the application of multiple incident femtosecond laser pulses it is expected that the temperature within the focal volume would rise.

CHAPTER 3

REVERSIBLE PERMEABILIZATION USING FEMTOSECOND LASER PULSES

3.1 Introduction[1]

In chapter 2, cell isolation and membrane surgery of V79-4 and MDCK cells was shown. To further demonstrate the multifunctional use of the femtosecond laser, this chapter addresses whether transient pores can be induced in the biological membrane of living cells for the purpose of introducing foreign materials into the intracellular environment. By creating laser pulse induced pores in the cell, a direct pathway is created that allows for extracellular material to diffuse and accumulate within the intracellular space. The importance of such an application is that it provides biomedical engineers and biologists with an alternative tool that allows foreign molecules including proteins, DNA, and fluorescent probes to be delivered into the cell.

Figure 3.1 provides a visual description of the laser pulse induced transient pore formation process. In (a) the cell is suspened in an impermeable exogenous solution (i.e. foreign molecule that cannot penetrate the cell membrane) and femtosecond laser pulses are focused onto the plasma membrane to induce a transient disruption. After disruption of the cell membrane, (b), the foreign substance diffuses into the cell. Shortly after, (c), the transient pore seals with the delivered impermeable molecule localized in the intracellular space.

An example of a particular discipline that may directly benefit from laser pulse induced permeabilization is the field of cryobiology. The purpose of cryobiology is to improve the integrity and functionality of living cells, tissue and organs following *ex vivo* storage at ultra low temperatures (i.e. –80 °C to –196 °C; cryogenic temperatures) [53]. However, to ensure cell viability after thawing, the cellular material is first exposed to

---

[1] Portions of this section have been published in Kohli *et al*. Biotechnol. Bioeng. 92:7, 889-899.

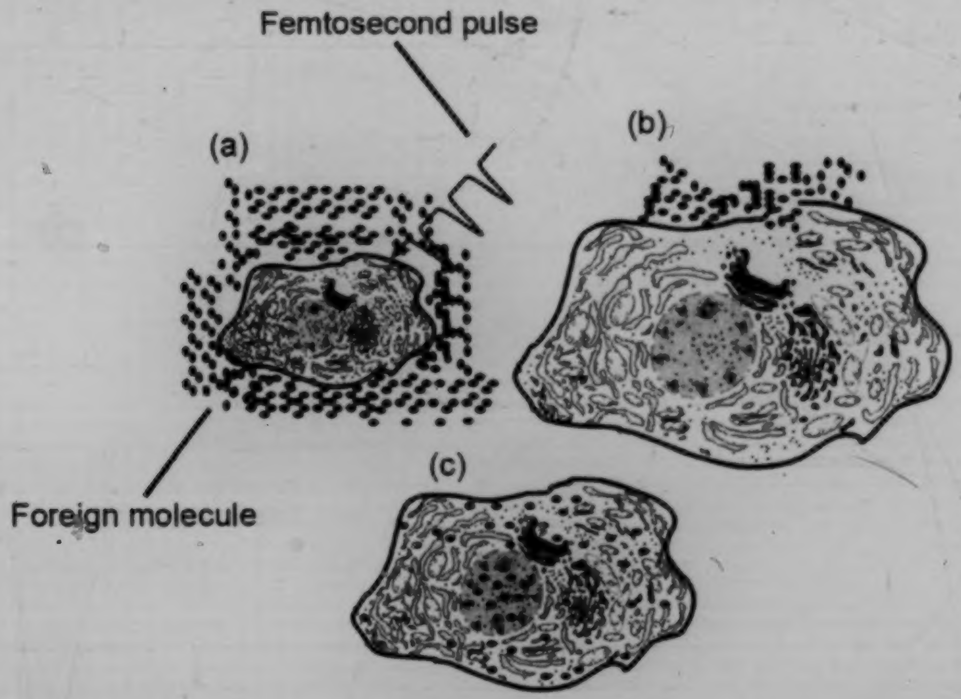

Figure 3.1: Graphic depicting laser pulse induced permeabilization. (a) A cell is initially suspended in an exogenous solution containing a foreign molecule to be introduced. Focused femtosecond laser pulses are localized on the cell plasma membrane for creating a transient plasma membrane disruption, (b). Temporary disruption of the plasma membrane allows the foreign molecule to diffuse into the cell, (b). The membrane rapidly re-seals (c) with the delivered content localized in the intracellular space of the cell.

permeable or impermeable cryoprotective molecules [46, 48-50, 54-58] that act to protect the cells when frozen. It is conceivable that femtosecond laser pulse induced permeabilzation can be used to introduce impermeable cryoprotectant molecules into living cells and improve their survival. If successful non-invasive permeabilization and delivery of exogenous cryprotectants is shown, then it is foreseeable that the femtosecond laser may become an integral tool to be used in cryobiology. In this chapter, the demonstration of permeabilization and delivery is discussed within the context of cryobiology. An in depth discussion of this field is provided below for the purpose of describing the relevance of the femtosecond laser to the discipline.

Cryopreservation of biological materials

Cryopreservation has been the main technique used for the long-term preservation of biological materials [59]. In cryopreservation, cells are progressively frozen to cryogenic temperatures using slow or fast cooling methods and stored at these low temperatures for weeks to years. To ensure that the cells, tissues or organs maintain viability post-thaw, a proper balance between cooling rates and thawing rates must be established [53, 60]. Since cells vary in size and have differing water permeability coefficients[1] [53], osmosis will transport water from the intracellular space to the extracellular environment due to the increased extracellular solute fraction originating from the homogenous freezing of water. In addition to optimizing cooling and thawing rates, low weight membrane permeable cryoprotective molecules such as glycerol and dimethyl sulfoxide (DMSO) [61] are routinely added to the cell suspension during cryopreservation to increase cell survival post-thaw.

---

[1] Defined as the membrane hydraulic conductivity, L_p, with units of $\mu m^3/\mu m^2 \cdot atm \cdot min$ [44, 45]. The hydraulic conductivity is a phenomenological coefficient that describes the rate of water movement with L_p related to the permeability coefficient P_f(cm/s) and the molar volume of water.

While the mechanism of cryoprotectant protection on cellular material is unknown, the hypothesis is that it may protect cryopreserved cells from 'solution effects' [53, 62]. When cells are cooled and the extracellular environment is either spontaneously nucleated or seeded by an ice crystal (i.e. initiating the freezing of extracellular water), the extracellular electrolyte concentration increases, resulting in the efflux of water from the intracellular space. The movement of water dilutes the electrolyte concentration, and increases the intracellular electrolyte osmolarity. Both the movement of water and its freezing eventually stabilize when the intracellular and extracellular osmolarities are equal. At this point, both the extracellular and intracellular environments contain a high concentration of electrolytes, which is believed to induce changes in the membrane structure (also known as solution effects)[1] [53, 62]. Upon thawing, the cells undergo osmotic shock, compromising their viability [53, 62]. By the addition of permeable cryoprotectants, the mole fraction of the electrolytes is reduced, X_{elect} to $\frac{n_{elect}}{n_{elect} + n_{cryo}}$ [64] where n_{elect} and n_{cryo} are the number of moles of electrolytes and cryoprotectants, respectively[2]. The reduction in the electrolyte mole fraction is believed to reduce the solution effects and increase cell viability [53].

More recently, cryopreservation protocols have been developed using carbohydrates (i.e. trehalose and sucrose) as potential cryoprotectants. Carbohydrates are believed to have similar protective effects to permeable cryoprotectants. Crowe *et al.* [65] further hypothesizes the important role of carbohydrates in cell survival by claiming that sugars prevent the fusion of the lipid bilayer and can bind to proteins for stabilization. Alternatively, Eroglu *et al.* [46] suggested that intracellular sugars increase the viscosity of the cytoplasm and decrease the growth of intracellular ice. Regardless of the mechanism of action, the protective effects of carbohydrates have been demonstrated [46, 48-50].

---

[1] Meryman *et al.* has suggested an alternative mechanism for membrane damage, which involves osmotic stresses. See reference [63].

[2] It is assumed that the number of moles of water (n_w) is small, which should be true since water is in the frozen state.

The challenge of using carbohydrates as intracellular protective agents is that sugars are impermeable to the plasma membrane. Therefore, a method is required to permeabilize the cell for intracellular uptake without affecting cell viability. A few techniques have been developed for permeabilizing cells for cytoplasmic delivery and include the engineered metal-actuated pore-forming toxin, H5, derived from *Staphylococcus aureus* hemolysin [46, 48-50, 66, 67], electroporation that involves the application of square wave and exponential decay electrical pulses [68-73] and NIR laser pulses [74-76].

A biological approach to cell permeabilization

In the H5 pore forming toxin method, the bacterium *Staphylococcus* secretes alpha-hemolysin monomers that oligomerize at the surface of the plasma membrane to create a mushroom shaped hydrophilic pore. Figure 3.2 shows a graphical representation of H5 hemolysin bound to the extracellular leaflet of the biological membrane. The hydrophilic pore extends through the membrane into the intracellular space. H5 forms several 2 nm transmembrane pores [46, 49, 66, 67] in the cell plasma membrane that can

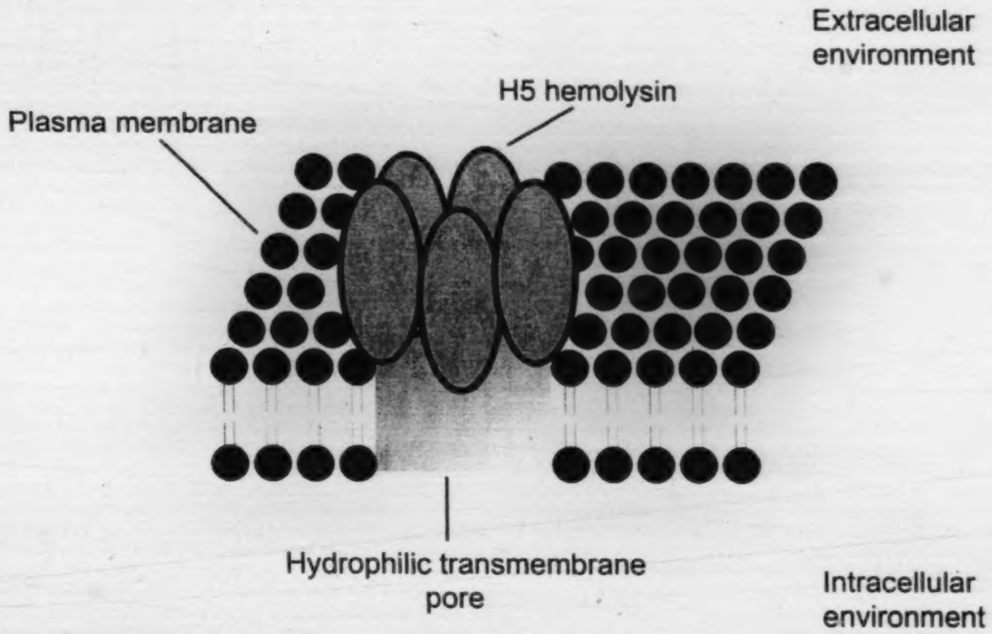
Extracellular
environment
H5 hemolysin
Plasma membrane
Hydrophilic transmembrane
pore
Intracellular
environment

Figure 3.2: The H5 hemolysin pore forming toxin. Alpha-hemolysin monomers secreted by the bacterium *Staphylococcus* oligomerize at the plasma membrane to create a transmembrane pore that extends into the intracellular environment. The transmembrane pore is hydrophilic and allows impermeable solutes to cross the plasma membrane to be localized in the intracellular space. Figure adapted from Sigma-Aldrich, Canada.

be toggled between an open and closed state by the addition of Zn^{2+} ions (micromolar concentrations) [46, 49, 66]. When carbohydrates are placed in the extracellular environment of the cell in the presence of H5, sugar can diffuse through the toxin pores into the intracellular environment. For cryopreservation purposes, Russo *et al.* [49] used the H5 engineered Zn^{2+} switchable pore to efflux fluorescent dye (carboxycalcein blue) and introduce sucrose into 3T3 mouse fibroblast cells. It was found that when 3T3 fibroblast cells were exposed to H5 in the absence of Zn^{2+}, the intracellular fluorescence intensity of carboxycalein blue decreased, indicative of transmembrane pores being formed. When 3T3 fibroblast cells were permeabilized in 0.75 M sucrose with 20 μg/ml of H5, the cells initially shrank due to the hyperosmotic solution, followed by a slow increase in cell volume resulting from the passage of sucrose into the cell via the H5 pore [49]. Cells were observed to reach equilibrium with the extracellular solution within 35 mins [49].

In a similar study by Eroglu *et al.* [46] the switchable H5 toxin was used to permeabilize 3T3 fibroblast cells and human keratinocytes in the presence of trehalose. Pre-freeze survival results of H5 porated fibroblast cells in increasing osmolarities revealed a cell survival ranging from 98.1 % to 60.6 % for trehalose concentrations ranging from 0.2 M to 1.0 M [46]. Fibroblasts cryopreserved after H5 treatment and trehalose uptake, yielded a cell survival approaching 80 % in comparison to a survival of < 20 % for untreated cryopreserved cells [46]. Similar results were found for human keratinocytes.

An electrical approach to cell permeabilization

Electroporation has found many interesting applications, specifically in the electrotransfection of DNA into embryonic cells. Figure 3.3 depicts a graphical representation of electroporation where (a), cells suspended in an exogenous solution (i.e. foreign molecule) are placed between negative and positive electrodes. The application of an electrical pulse, (b), transiently disrupts the cell plasma membrane allowing for the accumulation of the foreign substance inside the cell, (c).

Using this technique, Buono *et al.* [70] applied electrical pulses to zebrafish embryos in the presence of 800 μL of plasmid DNA. It was found that 62 % of the embryos survived, and that expression of the introduced construct ranged from 20 % to 80 % [70]. Interestingly, despite the benefits of electroporation, several authors have tried to replicate the Buono *et al.* result with little success [70]. Reasons for variations in the number of positively expressing animals and for findings of inconsistent or no results using identical electroporation parameters are unknown [70].

Golzio *et al.* [71] used electroporation as a technique for understanding gene delivery into single cells. Using Chinese hamster ovary cells as the animal model system, a plasmid encoding GFP was intercalated with the dye TOTO-1 and electrotransfected into the cell. Golzio and colleagues monitored the interaction of the DNA with the permeabilized interface, and used fluorescence assessment to examine the localization and transport of the DNA into the cell [71].

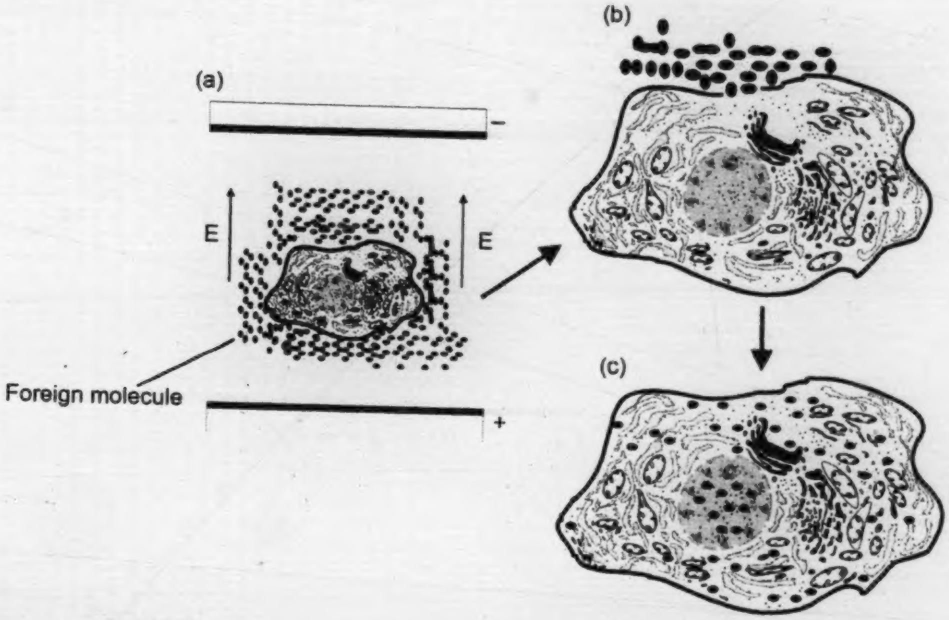

Figure 3.3: Electroporation. (a) A cell is suspended in an exogenous solution containing a foreign molecule to be introduced into the cell. Application of electrical pulses causes the cell plasma membrane to be disrupted, (b). Disruption to the cell membrane allows the foreign molecule to diffuse into the cell. (c) After the membrane has re-sealed, the desired foreign molecule is localized in the intracellular environment of the cell, (c).

Femtosecond laser pulse induced cell permeabilization

The use of NIR laser pulses for permeabilization and immobilization of human spermatozoa was recently demonstrated by Montag *et al*. Using 1.48 μm laser pulses produced from a semiconductor diode laser coupled to an inverted microscope, human sperm were laser pulse irradiated in the tail region. Depending on the laser energy, which ranged from 0.25 mJ to 2.0 mJ, temporary immobilization, permanent immobilization or complete permeabilization of spermatozoa was observed.

NIR femtosecond laser pulses with a center wavelength at 800 nm were recently used by Tirlapur *et al*. [74] to introduce plasmid DNA into Chinese hamster ovarian cells (CHO) and rat-kangaroo kidney epithelial cells. For cell peremabilization, a pulse energy ranging from 0.63 nJ/pulse to 1.25 nJ/pulse was focused onto the cell plasma membrane for 16 ms in the presence of the DNA construct [74]. Expression in the cells was verifed by two-photon fluorescence imaging. Despite claims of 100 % transfection efficiency, no expression efficiency values were reported. In similar work, Stevenson *et al*. [75] transfected CHO cells with femtosecond laser pulses using a pulse energy and beam dwell time ranging from 50 to 225 mW and 10 to 250 ms, respectively. Contrary to the 100 % transfection efficiency reported by Tirlapur and colleagues [74], Stevenson measured an average transfection rate of 50 ± 10 % in 4,000 laser pulse treated CHO cells [75]. The non-fluorescent dye, trypan blue, was used to confirm cell membrane viability.

Purpose of this study

This chapter explores the application of femtosecond laser pulses as an alternative tool for transiently disrupting the plasma cell membrane. The motivation of this study was to demonstrate that when focused femtosecond laser pulses are localized onto the cell membrane, a temporary pathway can be created, allowing for the cytosolic accumulation of an impermeable solute. As an initial test for laser pulse induced permeabilization, a dual fluorescence membrane integrity assay was used, composed of SYTO 13 and ethidium bromide (EB). This fluorescent assay for quantifying cell membrane integrity has been widely used [47, 77]. SYTO 13 functions by staining intact cells (i.e. cells whose membranes have not been compromised) with a green fluorescent complex, with the dye readily transported across the cell plasma membrane (i.e. SYTO 13 is a membrane permeable stain). In contrast, EB is an impermeable dye that forms a red/orange fluorescent complex and is excluded from the intracellular environment. For EB to accumulate within the cell, the cell plasma membrane must be disrupted either through permanent damange or through transient pore formation via the femtosecond laser. Using this dual fluorescence stain in conjunction with laser pulse induced permeabilization, epi-fluorescence imaging can be used to quantify the poration process. Following poration, laser pulse treated cells positive for EB would be indicative of cell membranes that were permeabilized.

For applications to cryopreservation, the cytoplasmic delivery of sucrose was also examined. Cells were placed in varying hyperosmotic concentrations of sucrose, and the volumetric kinetics of the cells from hypertonic volume to a new hypertonic equilibrium volume following laser pulse permeabilization was evaluated. Shrink-swell analysis provided direct evidence of permeabilization, and volumetric kinetics graphs were used to estimate the longevity of the laser pulse induced pore. To confirm that the pores were transient, the SYTO 13/EB assay was used. A cell survival curve was developed based on the SYTO 13/EB stain, providing a general trend for laser pulse permeabilized cell survival in increasing osmolarities of sugar. An estimate of the delivered sucrose concentration is also presented.

The model system chosen to demonstrate the permeabilization and delivery of exogenous material was Madin-Darby Canine Kidney (MDCK) epithelial cells. This cell line was used for the reasons stated in section 2.1 of Chapter 2. However, in contrast to the patterning of MDCK cells onto sterile coverslips as in the previous study in Chapter 2, these cells were cultured in 30 x 30 μm square wells with a well separation of 60 μm (see Appendix F for details). Patterning of cells in the wells allowed each cell to be easily identified and targeted for permeabilization and imaging. A detailed description of the cell culture process is found in Appendix F.

3.2 Results and Discussion[1]

Experimental methodology

The permeabilization of micropatterned MDCK cells was performed using the previously mentioned experimental setup detailed in Chapter 2 (see Figures 2.2 through 2.5 in Chapter 2). A simplified schematic diagram of the setup is found in Figure 2.5 of Chapter 2. Similar to the studies detailed in Chapter 2, MDCK cells were cultured in fresh culture media and patterned onto sterile micropatterned glass slides. Patterned cells were hydrated with a small volume (~ 10-20 μL) of fresh culture media. The cells were placed on an *x-y-z* temperature controlled (4 °C) stage, and the femtosecond laser pulses were focused by a 0.95 100X high NA air microscope objective onto the plasma membrane of the cell. Pulse energies for laser pulse induced permeabilization ranged from 2 nJ/pulse to 5 nJ/pulse[2]. Using equation (1.2) in Chapter 1, the diffraction limited irradiance spot size (diameter) was estimated to be $d_r = 1027$ nm at the focus, with the peak power ranging from 6.9 kW/pulse (2 nJ/pulse) to 17 kW/pulse (5 nJ/pulse). (These values (peak power and peak irradiance) were calculated using an estimated broadened pulse duration of 291 femtoseconds; see Appendix A for details). From the irradiance spot size and the peak power values, the estimated peak intensity at the focus was $8.3\text{x}10^{11}$ W/cm^2 to $2.1\text{x}10^{12}$ W/cm^2. Using equation (2.2) in Chapter 2, γ ranges from 4.15 ($2.1\text{x}10^{12}$ W/cm^2) to 6.60 ($8.3\text{x}10^{11}$ W/cm^2) and the effective ionization potential in equation (2.1) in Chapter 2 can be approximated as the band gap energy of water. With knowledge of the irradiance profile and the peak intensity, the maximum electron density and the temperature rise after a single femtosecond laser pulse were estimated to be $\rho_{max} = 10^{16}$ cm^{-3} to 10^{18} cm^{-3} ($I/I_R = 0.13$ to 0.32) and $\Delta T = 0.006$ to 0.56 K (the temperature would be expected to rise after multiple incident femtosecond laser pulses), respectively. These values were calculated using the equations developed in Chapters 1 and 2.

---

[1] Portions of this section have been published in Kohli *et al.* Biotechnol. Bioeng. 92:7, 889-899.

[2] These pulse energies represent the values measured entering the microscope objective lens. Fresnel's equations describing the reflection and transmission values through various index media can be used to approximate the amount of average laser power loss. From calculations (not presented in this thesis), the total average laser power loss was a few milliwatts.

For permeabilization, the laser pulses were gated with a mechanical shutter at a gated shutter time of ~ 10 ms (Note: the mechanical shutter is not shown in Figure 2.5 of Chapter 2). The mechanical shutter was placed in the optical beam path ahead of the beam splitter, which functioned to reduce the delivered laser energy to the cells. Based on the gated shutter time, the pulse energy and the oscillator repetition rate (80 MHz), the total delivered energy and the number of laser pulses irradiating the micropatterned cells were estimated to be 1.6 mJ to 4 mJ and $800\text{x}10^3$ pulses, respectively.

To monitor laser pulse induced permeabilization, white light illuminated the sample in the inverted position. A CCD mounted at the imaging port of the modified Zeiss upright microscope (see the Experimental methodology section of Chapter 2 for more information regarding the microscope modifications; see Figures 2.2 through 2.5 in Chapter 2) was used to capture both the laser light and the white light. Still images and real time video of the permeabilization process were captured and processed using commercial video software. Epi-fluorescence imaging of MDCK cells was conducted using a standard upright Zeiss epi-fluorescence microscope[1,2] equipped with the

---

[1] Epi-fluorescence imaging of the cells was conducted in Dr. McGann's laboratory in the department of Laboratory Medicine and Pathology at the University of Alberta.

[2] Special thanks to Dr. McGann for allowing access to his fluorescence microscope.

DAPI/TRITC/FITC filter set (Chroma Technologies Corp, Rockingham, VT). A detailed description of the cell culture process can be found in Appendix F.

Femtosecond laser pulse permeabilization of the plasma membrane

Before demonstrating the delivery of exogenous cryoprotective carbohydrates into the intracellular environment of cells, it was shown that the plasma membrane could be permeabilized using focused femtosecond laser pulses. By definition, successful permeabilization exposed the intracellular space to the extracellular environment, allowing solutes access to the interior of the cell. Figure 3.4 depicts micropatterned MDCK cells that were targeted for laser-pulse induced permeabilization. In Figure 3.4(a), the arrows indicate cells that were chosen for laser pulse targeting. Using a pulse energy of 5 nJ/pulse gated with a ~ 10 ms mechanical shutter, the femtosecond laser pulses were focused onto the cell membrane. The brightfield image of the targeted cells (arrows) is presented in Figure 3.4(a).

A SYTO 13/EB membrane integrity assay was used to assess the permeability of the targeted cells. The dual fluorescence stain was added to the micropatterned cells ~ 10 to 20 min following laser pulse manipulation. After removing the background fluorescence, the cells were imaged under epi-fluorescence to verify permeabilization. Figure 3.4(b) depicts the fluorescence image of the micropatterned cells (same cells as in Figure 3.4(a)), showing the targeted cells positive for the uptake of EB. Since SYTO 13 is readily permeable to the cell plasma membrane while EB is excluded, intact cells should fluoresce green (indicative of SYTO 13), while cells with damaged membranes will fluoresce red (indicative of EB). The results obtained indicated that focusing

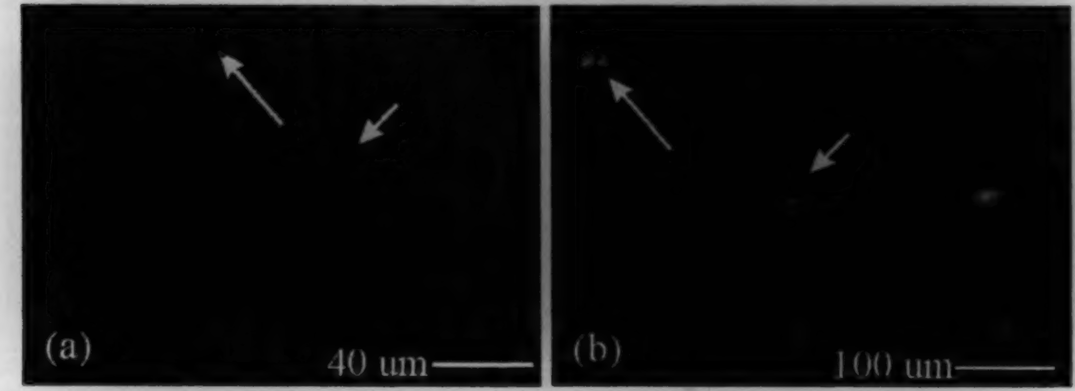

Figure 3.4: Brightfield and fluorescence image of micropatterned MDCK cells that were laser pulse targeted using a pulse energy of 5 nJ/pulse and a gated shutter time of ~ 10 ms. (a) Arrows indicate the cells that were selectively chosen for laser pulse permeabilization. Approximately 10 to 20 min post-laser pulse targeting, the cells underwent a dual fluorescence membrane integrity assay with SYTO 13 and EB. (b) After the addition and removal of SYTO 13/EB, the micropatterned cells were imaged under epi-fluorescence. Targeted cells (arrows) were positive for EB fluorescence indicating that the cells were successfully permeabilized. As expected, all non-targeted cells were positive for SYTO 13 only.

femtosecond laser pulses onto the structure of the membrane induced a permeabilized state that allowed the impermeable EB to diffuse into the intracellular space of the cell through the laser pulse induced pore. The ability to localize pore formation to a single cell was observed in Figure 3.4(b), where only the cells selected for permeabilization were positive for EB. However, it remained to be determined whether the permeabilized state of the cells was reversible.

Before permeabilizing cells in the presence of sucrose, the appropriate pulse energy and energy absorption were defined. Through a series of experiments, individual cells were permeabilized with varying pulse energies from 2 to 5 nJ/pulse, gated with a shutter time of ~ 10 ms. In order to avoid irreparable cell damage, the optimum pulse energy was defined as the maximum value that resulted in maximal membrane integrity as determined by the SYTO 13/EB assay. Post-laser pulse permeabilization, the cells were allowed to recover for ~ 20 min before the addition of the fluorescence stains. Based on the ratio of SYTO 13 positive cells over the total number of cells, cell survival was determined. It should be noted that the membrane integrity assay did not provide an absolute measure of cell viability; however, it has been widely used to characterize cell death [48]. As determined by the assay, ~ 3.3 nJ/pulse was the optimum pulse energy yielding maximum cell survival. Unless otherwise stated, for all subsequent experiments a pulse energy of 3.3 nJ/pulse was used with the femtosecond pulse train gated at ~ 10 ms.

Carbohydrate uptake into permeabilized cells

Having demonstrated the permeabilization of individual cells, the ability of the permeabilized cell to uptake carbohydrates was evaluated. For this study, sucrose was chosen as the molecule of interest. Micropatterned MDCK cells were suspended in a 1.0 M sucrose solution and laser pulse porated with a pulse energy and gated shutter time of 5 nJ/pulse and ~ 10 ms, respectively. Figure 3.5 depicts micropatterned cells pre- and post-laser pulse permeabilization. In Figure 3.5(a), three micropatterned cells in close contact are shown, with the arrow representing the focused laser pulse. An individual cell was selected for the permeabilization and introduction of the exogenous carbohydrate. Since sucrose is impermeable to the plasma membrane, the concentration difference between the extracellular and intracellular environments is thought to elicit a dehydration response in the cell. Water exits the cell by osmosis to dilute the extracellular sucrose osmolarity. The cells in Figure 3.5(a), therefore, are those in a shrunken state due to their suspension in a hyperosmotic (or hypertonic[1]) solution.

Following laser pulse induced permeabilization, the targeted cell was observed to increase in volume, Figure 3.5(b), with this volume change occurring only in the targeted cell. An increase in cell volume is a well characterized response [49], indicating the occurrence of permeabilization and the intracellular accumulation of an impermeable solute. The change in volume from hypertonic to equilibrium was measured to be $V/V_{equil} = 0.578 \pm 0.085$ at hypertonic and $V/V_{equil} = 1.000 \pm 0.055$ at equilibrium (the cell was assumed to be spherical in geometry; see Appendix F for further details on how

---

[1] Defined as a cell state where the extracellular concentration is higher than the intracellular concentration. As a result, water diffuses out of the cell to dilute the extracellular osmolarity. This causes the cell to shrink.

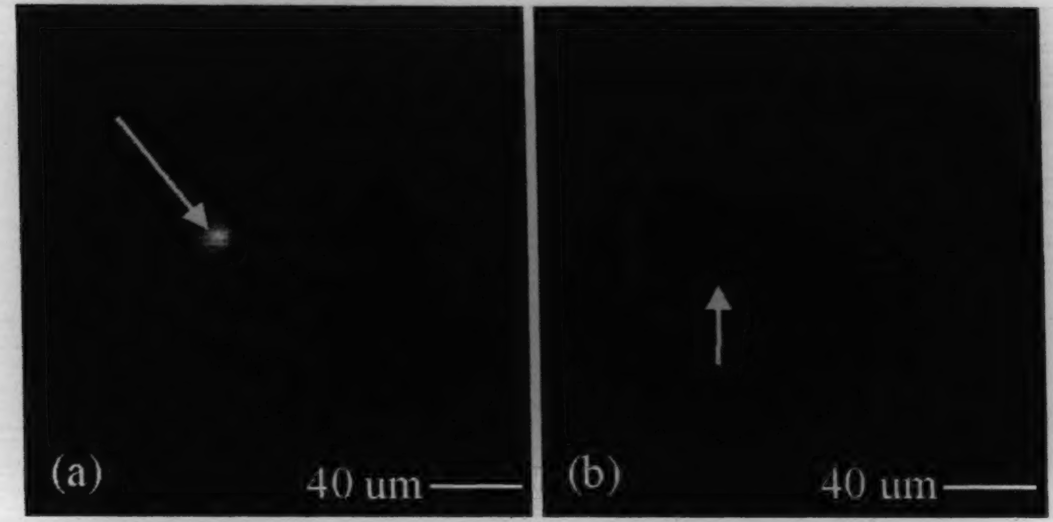

Figure 3.5: Depicts the swelling response of MDCK cells laser pulse permeabilized in the presence of 1.0 M sucrose. (a) Three cells in close contact are shown at hypertonic volume. A single cell was selected for permeabilization with the arrow indicating the focused femtosecond laser spot. (b) Post-laser pulse targeting, the cell increased in cellular volume (arrow) towards a new hypertonic equilibrium volume. The change from hypertonic to equilibrium volume was found to be approximately 60 %. The cell was permeabilized using a pulse energy of 5 nJ/pulse and a gated shutter time of ~ 10 ms.

the cell volume was calculated). Therefore, an approximate 60 % change in cell volume was observed post-poration for cells permeabilized in 1.0 M sucrose.

Figure 3.5 shows the increase in cellular volume of a cell porated in 1.0 M sucrose. A quick change in the cell volume was observed (~ 60 %), from hypertonic to a new equilibrium volume following permeabilization. It should be noted that the new equilibrium volume does not represent the isotonic[1] volume of the cell. The new equilibrium volume represents a new hypertonic state, with the delivered intracellular sucrose osmolarity less than the initial (i.e. 1.0 M) extracellular osmolarity. Toplace this in context, if an impermeable 0.2 M sucrose solution is placed in the extracellular environment of the cell, the cell shrinks as water moves out of the cell to dilute the solute concentration. However, just before the cell begins to dehydrate, the molar fraction of the solute is equal to one. As intracellular water begins to dilute the extracellular sucrose, the molar fraction of the solute decreases due to an increase in the number of moles of water. Eventually the volume of the cell stabilizes (i.e. the flux of water driven by the solute gradient becomes zero), with the intracellular electrolyte fraction increasing (i.e. the number of moles of water is reduced due to the efflux of water) to a point where the solute concentrations of the extracellular and intracellular environments become equal. When the cell is permeabilized, a solute flux is established, with sucrose diffusing into the cell, followed by water. The movement of water is required to dilute the increasing solute concentration within the intracellular environment. An increase in the molar fraction of the extracellular solute occurs together with a decrease in the molar fraction within the intracellular environment. Again, the cell stabilizes its volume when the concentrations are balanced across the cell membrane. Despite equal concentrations between the intra- and extracellular spaces, the amount of intracellularly delivered sucrose does not equal the value in the extracellular space. While the total concentration in the extracellular environment is due to sucrose plus other extracellular solutes (i.e. electrolytes) ($C^{e}_{sucrose} + C^{e}_{electrolytes}$), the intracellular environment is the sum of the delivered sucrose concentration and electrolytes ($C^{i}_{sucrose} + C^{i}_{electrolytes}$). Therefore, while $C^{e}_{sucrose} + C^{e}_{electrolytes} = C^{i}_{sucrose} + C^{i}_{electrolytes}$ post-laser pulse permeabilization, $C^{e}_{sucrose} \neq C^{i}_{sucrose}$ ($C^{e}_{sucrose} > C^{i}_{sucrose}$) and the cell is still in a hyperosmotic solution, with the new cell volume representing a new hypertonic state. Post-laser pulse poration, then, the extracellular sucrose concentration still represents an infinite solute source. For equilibrium to occur (i.e. when the extracellular and intracellular sucrose concentrations are equal), the time required to balance the solute concentration would be much longer than the laser pulse induced pore kinetics (to be discussed later). The electrolyte concentration represents the cells initial concentration, ~ 300 mOsm [78], at isotonic volume.

---

[1] Defined as a cell state where the extracellular and intracellular concentrations are equal. Water diffuses in and out of the cell at the same rate, and no change in cell volume is observed.

Kinetic responses of laser pulse permeabilized cells

Despite the similar molecular weights of EB and sucrose, the kinetic responses of permeabilized MDCK cells in various hypertonic solutions of sucrose were also measured. Using video microscopy, the change in volume of the cells porated with femtosecond laser pulses was measured as a function of time. All measurements of the volume were normalized to the new hypertonic equilibrium volume post-laser pulse poration. Knowledge of the volume change allowed for cell kinetic profiles to be developed. From the kinetic profiles, the time taken for the cell to reach a new hypertonic equilibrium volume could be determined. Figure 3.6 depicts the kinetics of a single micropatterned cell laser pulse porated in the presence of 0.2 M sucrose. The cell was initially at hypertonic volume, V/V_{equil} = 62.9 %, which quickly increased after poration (Figure 3.6). The volume of the cell plateaued at ~ 200 ms, after which it remained constant. Similar kinetics profiles (for a single cell) were observed for cells permeabilized in 0.3 and 0.5 M sucrose (kinetics profiles for cells suspended in 0.4 M sucrose were not analyzed). The time taken for a single cell to reach the new equilibrium volume for these osmolarities was ~ 130 ms. It should be noted that the time intervals to reach hypertonic equilibrium volume approximated the longevity of the transient pore, as the pore provided the only mode of sugar uptake[1]. As sugar accumulated in the intracellular environment, water was osmotically driven towards the inside of the cell to dilute the increasing sugar concentration. When the pore closed, sugar no longer accumulated in the intracellular environment and the water flux went to zero, resulting in a stabilized volume. The differing equilibrium times determined, ~ 200 ms versus ~ 130 ms, were likely attributable to differences in the volume of the cells (to be discussed later). For a live observation of permeabilization and cellular volume increase, Additional Files 1 and 2 show micropatterned MDCK cells laser pulse porated in the presence of 0.2 and 0.5 M sucrose (0.2 M, Additional File 1-Chapter 3; 0.5 M, Additional File 2-Chapter 3). Particular attention should be directed to the change in cell volume post-laser pulse poration.

---

[1] Sucrose is impermeable to the plasma membrane and can only accumulate within the cell via diffusion through the laser pulse induced pore.

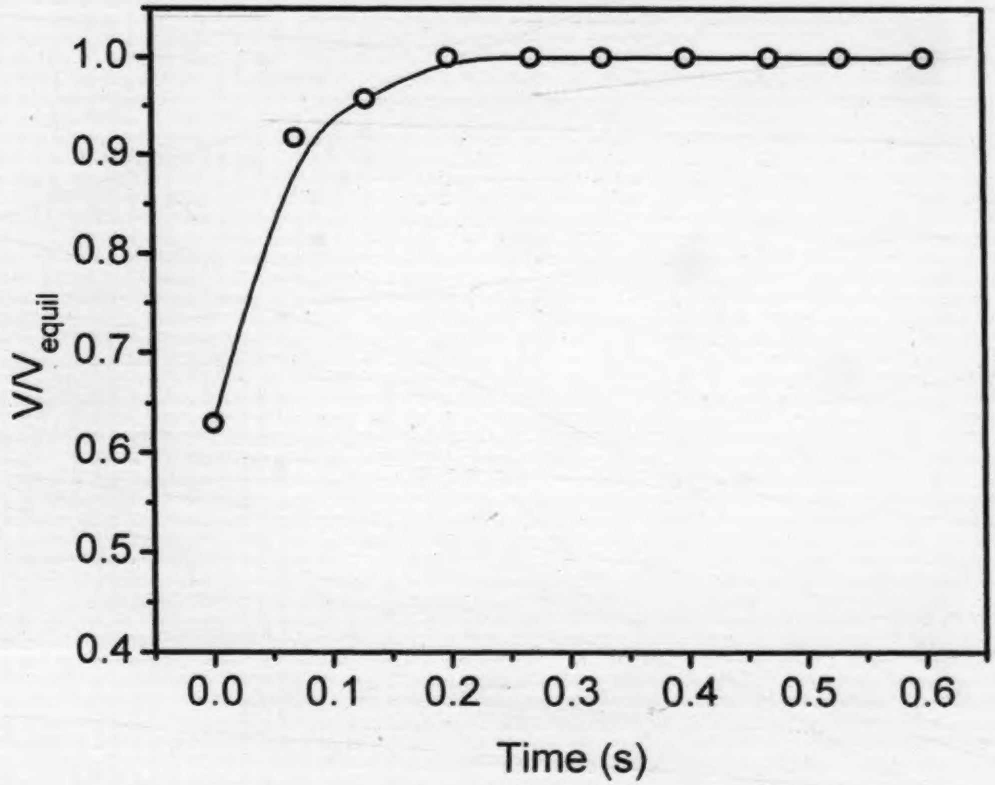

Figure 3.6: Depicts the volumetric kinetic graph of a single cell permeabilized in 0.2 M sucrose. Before permeabilization the cell was initially at hypertonic volume. Following laser pulse poration, the volume of the cell quickly increased as a function of time plateauing at ~ 200 ms. V_{equil} was the measured volume at the new hypertonic state. Volume measurements were made using ImageJ analysis software. The single cell was permeabilized with a pulse energy of 3.3 nJ/pulse and a gated shutter time of ~ 10 ms.

In Figure 3.6, no error bars are shown as the plot is only valid for a single cell. The inclusion of error bars would only be valid for a volumetric kinetics graph obtained from a cell size distribution representing the laser pulse permeabilization of many cells. This requirement stems from the fact that cells have varying cell size distributions (to be discussed later), as evidenced by Elmoazzen *et al.* [78], and each cell responds to an osmotic gradient differently due to differences in cell surface area and volume. Ideally, to obtain a reasonable statistical representation of the cell volume change depicted in Figure 3.6, a sample size of thirty would be required. However, this statistical requirement assumes that the randomly selected cells (the sample population) from the entire cell distribution could accurately represent the parent population. Examination of brightfield micropatterned MDCK cells exposed to sucrose reveals that the statistically mandated two-thirds of cells in the population do not fall within the required one standard deviation of the mean cell size[1]. Therefore, a sample size much larger than thirty (i.e. several hundred cells) would be required to produce a statistically accurate cell kinetics curve.

Figure 3.6 illustrated the volumetric kinetics of a cell permeabilized in the presence of 0.2 M sucrose. Similar kinetic plots showing an increasing cell volume were observed for single cells laser pulse porated in 0.3 and 0.5 M sucrose. From Figure 3.6, the volume of the cell was found to quickly swell from its initial hypertonic volume to a new hypertonic equilibrium volume. The upward trend towards a new larger equilibrium volume is a well characterized response indicative of the diffusion of both sucrose and water into the intracellular environment [46, 49, 50]. In fact, Russo *et al.* [49]

---

[1] Evidence of this is apparent in the brightfield images of Figures 3.7 and 3.8. The widely varying cell sizes of cells in hyperosmotic sucrose solutions are evident, and the statistical requirement that two-thirds of the cells be nearly identical in size (i.e. within one standard deviation) is not satisfied.

demonstrated the volumetric response of 3T3 mouse fibroblast cells permeabilized in 0.75 M sucrose with the H5 hemolysin pore forming toxin. Before permeabilization, the fibroblast cells decreased in volume, followed by an increase due to the presence of transmembrane pores facilitating sucrose accumulation. The kinetic response illustrated in Figure 3.6 is therefore consistent with the Russo *et al*. study.

Femtosecond laser pulse induced pore dynamics

As previously mentioned, knowledge of the cell kinetics provides information regarding the longevity of the laser pulse induced transient pore. The time taken for the cell to reach the new hypertonic equilibrium volume (defined as the point where the cell volume as a function of time plateaus) would represent a reasonable estimate of the pore closure dynamics. For cells permeabilized in 0.2 M, 0.3 M and 0.5 M sucrose, the estimated time for pore closure was found to be ~ 200 ms and ~ 130 ms, respectively. Since sucrose is impermeable to the plasma membrane, the change in volume must be due to the passage of the solute through the transient pore, as was observed in the Russo *et al*. study. Immediately after a pore is created in the plasma membrane, the solute concentration gradient drives the sucrose molecules into the intracellular environment of the cell. The pore provides a diffusion pathway for introducing the impermeable solute, which also carries water into the cell. The solvent diluting the accumulating intracellular sucrose must be transported through the laser pulse induced pore, since the kinetics in Figure 3.6 are much faster than the typical transit time for water influx or efflux through a cell membrane [44]. Once the pore seals, sucrose and water no longer accumulate within the intracellular environment. As a result, the cell reaches a constant volume, defined in Figure 3.6 as the point where V/V_{equil} plateaus, with the plateau time representing the time for pore closure.

The difference between the estimated pore duration times (~ 200 ms and ~ 130 ms) for cells permeabilized in 0.2 M, 0.3 M and 0.5 M sucrose was likely attributable to fluctuations in the cell size distribution. In fact, Elmoazzen *et al.* [78] showed that MDCK cells have broad cell size distributions, which change as a function of time when the cell shrinks when suspended in a hyperosmotic solution. Since the osmotic response of cells depends on the surface area and volume of the cell [78], it is expected that the volumetric kinetics vary from cell to cell. Therefore, each cell chosen from the same sample pool would respond differently to the solute driven osmotic change. As a result, kinetic responses between individual cells cannot be accurately compared. However, this fact does not negate the kinetic measurements made in Figure 3.6. As seen from the kinetic plots, the times taken to reach equilibrium volume, 200 ms (0.2 M) and 130 ms (0.3 and 0.5 M), do not represent the mean time for the entire cell sample, but times accurate for a single cell. However, these times can provide an initial starting value to estimate the pore kinetics. A more rigorous experiment would require permeabilizing several hundred cells and averaging the kinetic responses over the entire sample size.

Reversible character of femtosecond laser pulse induced pores

To verify that laser pulse induced permeabilization was a reversible process, individual cells were porated in 0.2 (n = 6 samples), 0.3 (n = 7 samples), 0.4 (n = 15 samples) and 0.5 M (n = 8 samples) sucrose and stained 30 to 40 min post-laser pulse permeabilization with SYTO 13/EB to test for membrane integrity. The time delay between poration and staining was to allow for cell membrane recovery. Figures 3.7 and 3.8 depict brightfield and fluorescence images of micropatterned cells permeabilized in 0.2 and 0.5 M sucrose (fluorescence assessment for 0.3 and 0.4 M not shown). Fluorescent cells positive for EB were considered irreversibly compromised by permanent membrane damage. In Figures 3.7 and 3.8, the numbers indicate the cells that were selectively chosen for poration and delivery of the exogenous solute. From the membrane integrity assay presented in Figure 3.7(b), all of the laser pulse targeted cells had membranes that were intact, with an absence of permanent damage. This observation differed from cells permeabilized in 0.5 M sucrose. The fluorescence assay presented in Figure 3.8(b) showed that all targeted cells in 0.5 M sucrose were positive for EB. These cells had plasma membranes that were irreversibly compromised.

Survival analysis of femtosecond laser pulse porated cells

Figure 3.9 presents the survival analysis (based on the SYTO 13/EB assay) of post-laser pulse permeabilized cells as a function of the extracellular sucrose osmolarity. All cells were porated using a constant pulse energy and gated shutter time (3.3 nJ/pulse; ~ 10 ms gated shutter time). A trend in decreasing cell survival was found as the extracellular osmolarity increased. The highest cell survival was achieved using 0.2 M sucrose, 91.5 ± 8 %, with 75 ± 5 %, 30 ± 10 % and 0 % survival for 0.3 M, 0.4 M and 0.5 M sucrose, respectively. These pre-freeze survival results are consistent with the Eroglu *et al.* [46] study which observed cell survival of 98.1 ± 6.4 % and 84.1 ± 3.3 % for

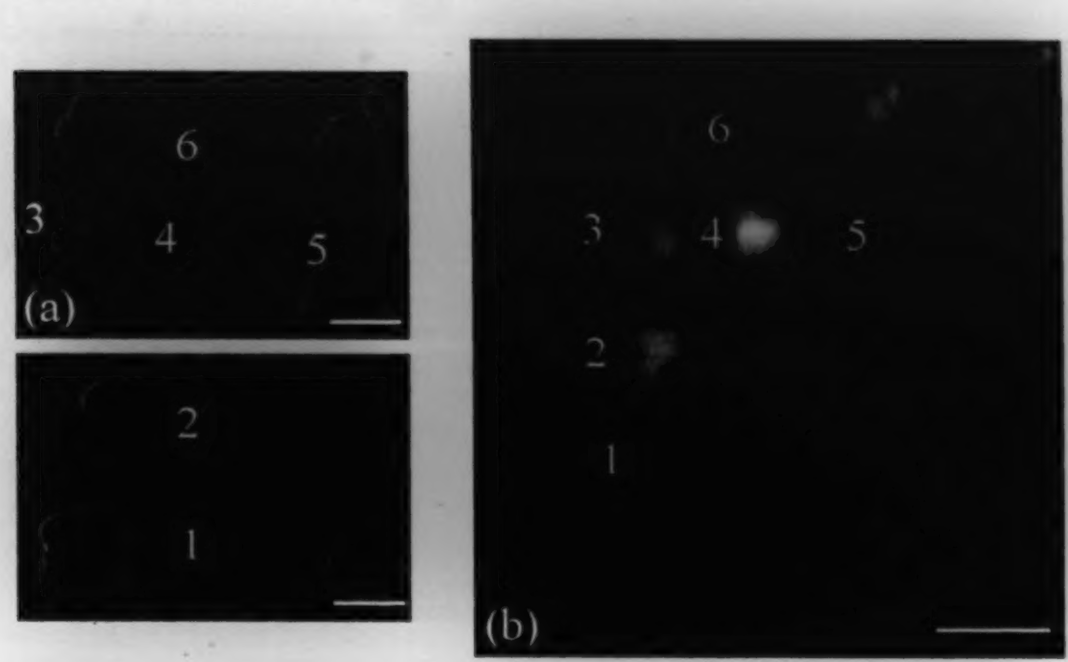

Figure 3.7: Brightfield and fluorescence images of micropatterned cells permeabilized in the presence of 0.2 M sucrose using a pulse energy of 3.3 nJ/pulse and a gated shutter time of ~ 10 ms. (a) The numbers indicate the selected cells that were permeabilized. (b) 30 to 40 min post-laser pulse poration, the cells were stained with a dual fluorescence membrane integrity assay composed of SYTO 13 and EB. Epi-fluorescence revealed that all porated cells had intact membranes as determined from the lack of EB fluorescence. Labeled cell number 5 detached from the well after the cells were rinsed with fresh culture media for removing the extracellular carbohydrate. Scale bars for (a) and (b) represent 40 and 100 μm, respectively.

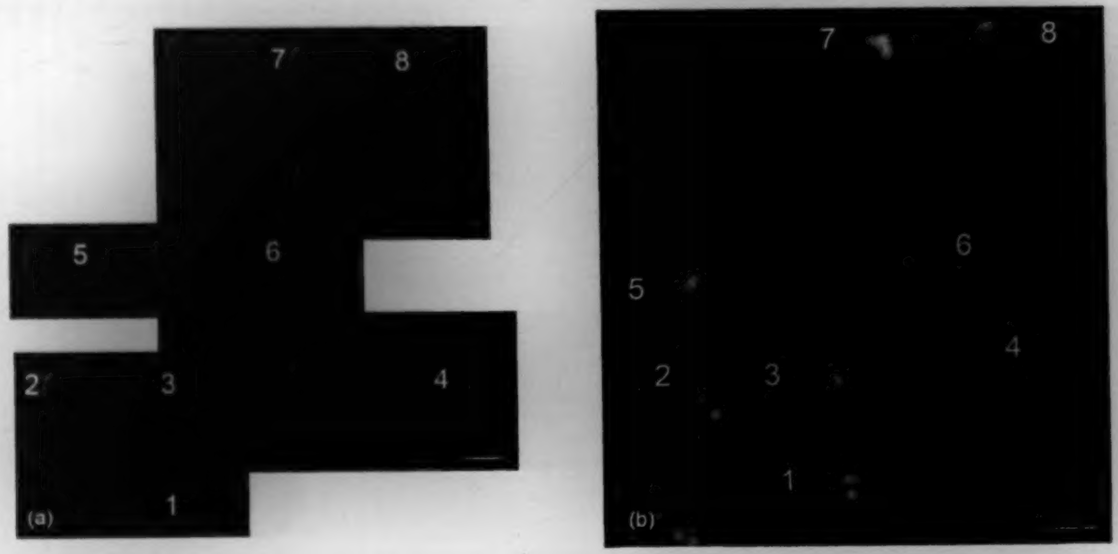

Figure 3.8: Brightfield and fluorescence images of micropatterned cells permeabilized in the presence of 0.5 M sucrose using a pulse energy of 3.3 nJ/pulse and a gated shutter time of ~ 10 ms. (a) The numbers indicate the selected cells that were permeabilized. (b) 30 to 40 min post-laser pulse poration, the cells were stained with a dual fluorescence membrane integrity assay composed of SYTO 13 and EB. Epi-fluorescence revealed that all porated cells had damaged permeable membranes as evidenced by the presence of intracellular EB fluorescence. Scale bar for (a) and (b) represent 40 and 100 μm, respectively.

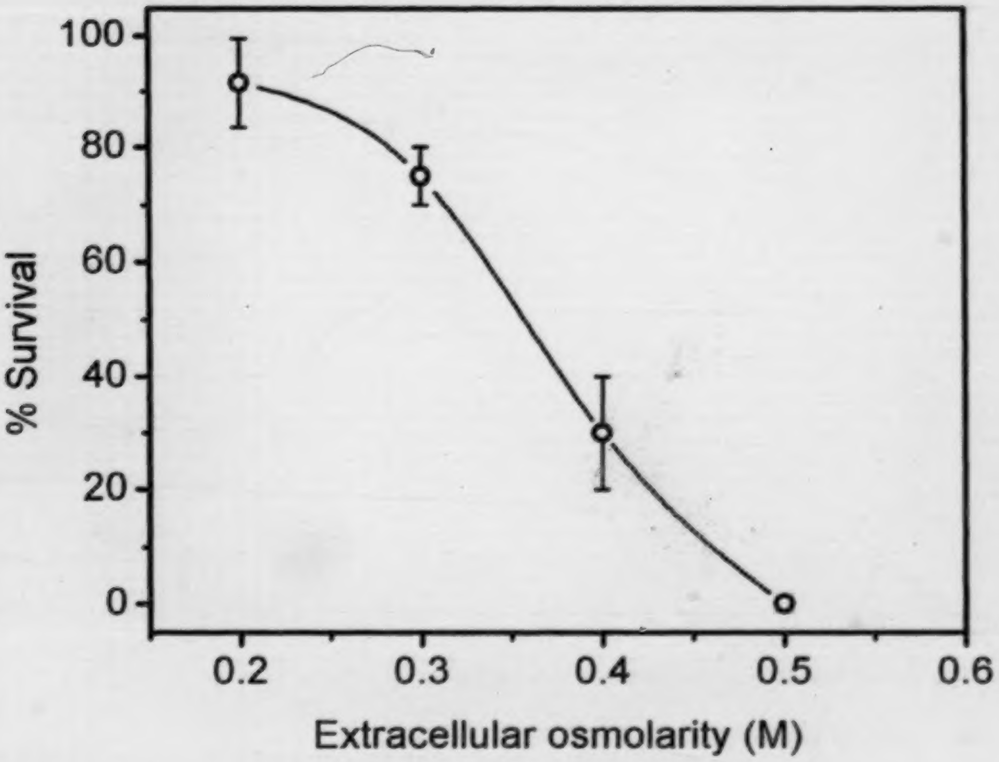

Figure 3.9: Depicts the trend in cell survival for cells laser pulse porated in increasing osmolarities of sucrose. Survival was assessed based on the SYTO 13/EB assay. Highest cell survival was observed for micropatterned cells permeabilized in 0.2 M sucrose. A progressive decrease in cell survival was observed as the concentration of sucrose increased. No cells survived in an extracellular osmolarity of 0.5 M sucrose. All cells permeabilized in their respective sucrose concentration were laser pulse porated with a pulse energy of 3.3 nJ/pulse and a gated shutter time of ~ 10 ms.

H5 permeabilized 3T3 mouse fibroblast cells in 0.2 and 0.4 M trehalose[1]. It is conjectured that the decrease in cell survival with increasing hyperosmotic solutions of sucrose may be explained by the osmotic poration injury hypothesis described by Muldrew and McGann *et al.* [45].

Pore widening hypothesis

In cryopreservation protocols, when cells are cooled to sub-zero temperatures the water in the extracellular environment freezes. This results in an increase in the solute concentration in the extracellular space, with the cells responding by dehydration through the efflux of water[2]. According to the hypothesis of Muldrew and McGann [45], it is believed that cell damage during freezing arises from the osmotic response elicited by the cell due to the increasing extracellular solute fraction (the extracellular solute fraction increased due to the freezing of extracellular water). Through experiments and mathematical modelling, Muldrew and McGann were able to infer that the pressure induced on the cell membrane by water increased as a function of cooling rate, and that the membrane could be sufficiently stressed, leading to its rupture. Damage to the cell membrane would allow extracellular ice to propagate into the intracellular environment, leading to intracellular ice formation. Therefore, according to Muldrew and McGann, cell death during freezing is likely attributable to osmotic stresses which result in cell damage and intracellular ice nucleation.

---

[1] The choice of using trehalose or sucrose is arbitrary, as both cryoprotectants have been shown to produce similar survival rates [79].

[2] The osmotic response elicited by the cells is important since it reduces the volume of water available in the intracellular environment that can form ice. It is important to note that the intracellular space does not immediately freeze after water freezes in the extracellular environment since the biological membrane is believed to act as a barrier preventing intracellular freezing [53]. While intracellular ice formation (IIF) is known to be lethal to cells, the exact cause of cell damage or death is unknown (various hypotheses have been presented, see [80] for an excellent review).

It is hypothesized that a water pressure stress similar to that proposed in Muldrew and McGann's study might be responsible for the increasing cell death observed in Figure 3.9 as the solute concentration was increased. When micropatterned cells were initially placed in a hyperosmotic solution of sucrose, the cells shrank due to the efflux of water. Varying the extracellular osmolarity from a lower concentration to a higher concentration resulted in an increase in the water flux across the cell membrane. A larger volume of water across the cell membrane in response to extracellular sucrose was not expected to rupture the cell membrane. This was supported by data from Figures 3.7 and 3.8, where non-laser pulse targeted cells exhibited intact cell membranes as determined by the absence of EB fluorescence. When cells were permeabilized in the hyperosmotic solution, the biological membrane was disrupted by the creation of a pore that exposed the extracellular environment to the intracellular space. Sucrose as well as water diffused through the pore, accumulating within the cell. It was hypothesized that the frictional force and pressure induced on the cell membrane in Muldrew and McGann's study [45] would be the same force and pressure generated along the length of the laser pulse induced pore. This force, driven by the water flux, might lead to pore widening, thereby compromising the viability of the cell and leading to increased membrane damage. The amount of pressure generated would increase as a function of the solute concentration difference (the derivation can be found in Appendix C),

$$P_w = (1\mathrm{x}10^{-3}) \frac{n6\pi A D_w \eta R}{\delta n_w} \frac{\Delta C_s}{\Delta x} \qquad (3.1)$$

resulting in increased pore widening and cell damage. In equation (3.1), $P_w, n, A, D_w, \eta, R, \delta, n_w$ and $\frac{\Delta C_s}{\Delta x}$ represent the water pressure, the number of pores, the area of the pore, the diffusion coefficient of water in the presence of sugar and lipids, the viscosity of the solution within which water is diffusing, the radius of the water molecule, the distance over which the diffusion is calculated, the number of moles of water and the solute concentration difference as a function of distance, respectively (the factor of 1×10^{-3} arises from the conversion of mol/L to mol/cm^3 with 1 mL = 1 cm^3). It was expected that the pressure generated by the laser pulse permeabilization method would be higher than the pressure observed in Muldrew and McGann's study [45], as the main mode of water transport would be through the pore (the least resistive path to water movement). Therefore, the pressure would be confined to the area of the pore, and not distributed over the membrane, as with Muldrew and McGann's study [45].

The assumption that the pore represents the least resistive path for water movement can be justified by the analysis of permeabilized cells suspended in an impermeable solute. The rate of water influx or efflux through a cell membrane is governed by the hydraulic conductivity coefficient, L_p, or the osmotic water permeability coefficient, P_f, (P_f describes the net volume flow across a cell membrane [44]) with the typical transit time for water movement ranging from seconds to minutes [44]. Transit times depend on the solute concentration and temperature of the cell media, with equilibrium dehydration occurring more quickly (seconds) for higher osmolarities and temperatures (i.e. 22 °C vs. 4 °C) [44]. From Figure 3.6, it is noted that the cell reaches a new hypertonic equilibrium volume post-laser pulse permeabilization within ~ 200 ms at a temperature of 4 °C. Passive diffusion of water through the membrane (seconds to minutes [44]), facilitated by the solute concentration difference, cannot account for the observed cellular volume increase within the defined temperature and time. Therefore, for the cell to reach equilibrium volume within 200 ms would require water to be predominately transported through the laser pulse induced pore. The pressure induced by water would then be confined to the area of the pore, potentially resulting in pore widening. The degree of widening would increase with the extracellular osmolarity (solute flux increases with concentration difference) due to the dependence of the pressure on concentration. The above analysis may explain the results observed in Figure 3.9[1].

In addition to the potential force induced by the water flux on the pore, sucrose diffusion through the pore may also impart a force. However, it is assumed that the pressure contribution of sucrose would be minimal in comparison to the water pressure, with the cell volume change post-laser pulse permeabilization mainly due to water. To justify this assumption, the volume contribution of both sucrose and water can be estimated (the calculation can be found in Appendix D). Using Figures 3.6 and 3.10, and assuming that the isotonic volume of the cell in the absence of sucrose was 1753 μm^3 [78], the change in volume of the cell after the addition of 0.2 M was assumed to be 40 % that of isotonic volume. An ~ 60 % change in volume occured post-laser pulse permeabilization, and the relative contributions of water and sucrose to the new hypertonic volume were estimated to be 92 and 8 % respectively (see Appendix D for the detailed calculation). The estimated number of water molecules that diffused per sucrose

---

[1] It is important to mention that in equation (3.1) only the sucrose concentration was considered as the driving force for the water flux. This is the case as sucrose is impermeable to the plasma membrane and no other permeable or impermeable solutes were added to the cells that would contribute to water movement.

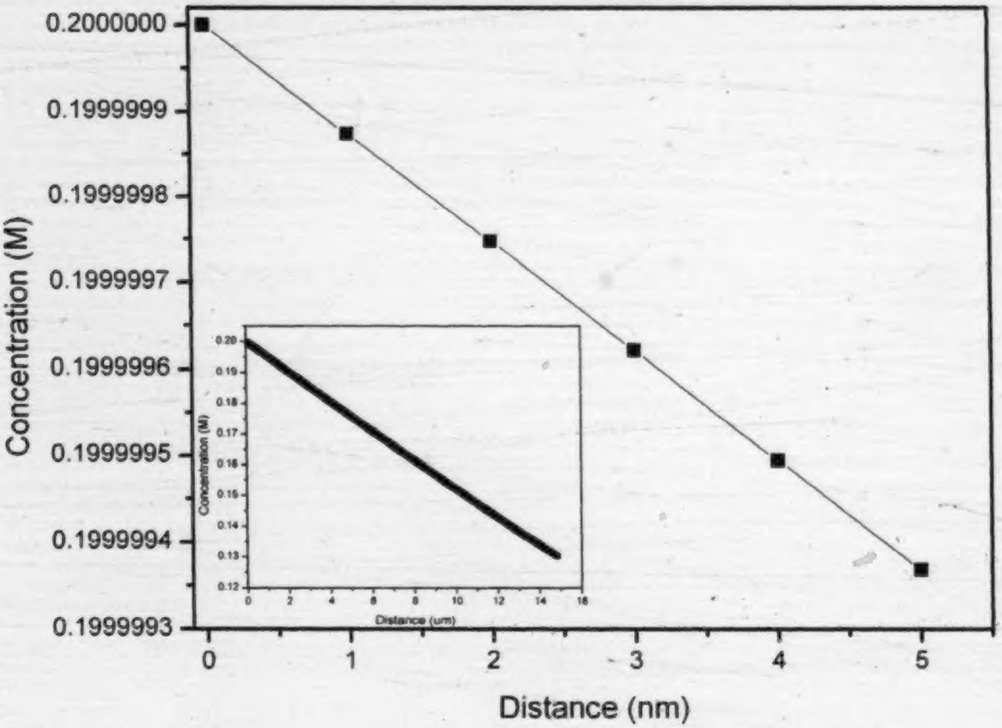

Figure 3.10: Diffusion profile for micropatterned cells permeabilized in 0.2 M sucrose. The cell was permeabilized using a pulse energy of 3.3 nJ/pulse and a gated shutter time of ~ 10 ms. With the time for pore closure and the membrane thickness set to constant values of 200 ms and 5 nm, the estimated concentration on the inner intracellular side of the membrane was estimated to be 0.199 M. The inset shows the diffusion profile for long diffusion lengths. Setting the diffusion length to the average diameter of a MDCK cell, 14.85 µm, the estimated concentration was found to be 0.13 M.

molecule was 135. Therefore, the overall contribution of sucrose to the new volume was negligible in comparison to the volume of water. Considering that 135 water molecules traverse the pore per sucrose molecule, it is reasonable to assume that any pressure generated on the pore would be predominantly due to the water flux.

Intracellular delivered carbohydrate concentration

Figure 3.10 shows theoretical estimates of the intracellularly delivered sucrose concentration for a cell permeabilized in 0.2 M sucrose[1]. In equation (F.5) of Appendix F, t represents the equilibrium time required for the cell to reach constant volume, as determined from the volumetric response plots (0.2 M, $t = 200$ ms). As previously mentioned, the equilibrium time estimates the longevity of the transient pore, and using $t = 200$ ms in equation (F.5) of Appendix F provides a theoretical value for the solute concentration just after pore closure. The area of the pore, A, was assumed to be the area of the laser spot (i.e. the irradiance spot size), with the spot diameter equaling ~ 1 μm. D_{sw} and δ are the diffusion coefficient of the solute in water, $2.536\text{x}10^{-6}$ cm^2/s, and the distance over which diffusion occurred, taken as 14.85 μm (14.85 μm represents the average diameter of a MDCK cell at isotonic volume [78]). The method used for calculating the diffusion coefficient is detailed in Appendix F. The length of the pore, L, was assumed to be equal to the thickness of the plasma membrane, 5 nm [29]. Using these values, with the number of laser pulse induced pores, n, equal to one, the intracellular sucrose concentration as a function of distance within the cell was plotted, Figure 3.10 (for both short and long (inset) diffusion lengths). From the plot, the theoretical concentration at the inner side of the membrane (the side facing the intracellular environment) was found to be 0.199 M. However, this value does not represent the final intracellular concentration since the accumulated solute at the inner face of the membrane will diffuse and equilibrate over the entire length of the cell, resulting in a much lower solute concentration. At a larger diffusion length of 14.85 μm (inset in Figure 3.10), the theoretical concentration was estimated to be 0.130 M. Similar theoretical concentration values and diffusion plots were found for cells suspended in 0.3 M and 0.5 M sucrose. At the inner face of the membrane, the calculated sucrose concentration was found to be 0.299 M and 0.499 M for 0.3 M and 0.5 M sucrose, and 0.128 M and 0.213 M for 0.3 M and 0.5 M sucrose at a diffusion length of 14.85 μm (no data analysis was performed for 0.4 M sucrose).

---

[1] The equations used to estimate the intracellular sucrose concentration are found in Appendix F.

The diffusion curves presented in Figure 3.10 are valid only for the specific permeabilized cell studied, but do provide a general trend in the delivered concentration that can be extrapolated to larger sample sizes. To generate the plot shown in Figure 3.10, it was assumed that the hyperosmotic extracellular solute concentration represented an infinite source. Figures 3.6 and 3.10 provide justification of this assumption. If the volume of the cell in Figure 3.6 reached equilibrium volume (i.e. extracellular and intracellular sucrose concentrations are equal) before closure of the pore, then using the equilibrium time in equation (F.5) in Appendix F would yield a concentration value equal to the extracellular sucrose osmolarity (i.e. 0.2 M). Considering that for a diffusion length of 14.85 μm (diameter of a typical MDCK cell at isotonic volume [78]), the concentration was estimated to be 0.13 M and not 0.2 M, and the plateau in the cell volume in Figure 3.6 could not have occurred through cell equilibrium, but only through closure of the transient pore. With the intracellular concentration (0.13 M) less than 0.2 M, after permeabilization the cell was still at hypertonic volume (a new hypertonic volume) and the extracellular sucrose concentration must necessarily be considered an infinite source.

In this chapter, the application of femtosecond laser pulses to permeabilize individual cells was demonstrated. With this reported technique, permeabilization occurs without the need for metal ions or toxins, as required in the hemolysin method [46, 48-50]. Through the analysis of the volumetric kinetics, it was found that laser pulse induced permeabilization elicited a rapid response in both the movement of solutes and water across the pore, with the cell reaching a new equilibrium volume within milliseconds. This is in contrast to a time of > 5 min for a 10 % change in volume using H5 hemolysin [49]. This long permeabilization time increases the exposure time of the cell to the toxin, potentially leading to detrimental effects. Therefore, reversible permeabilization using femtosecond laser pulses offers the advantage of faster cytoplasmic uptake of exogenous molecules, with each laser pulse induced pore delivering a substantial concentration of the desired foreign substance into the intracellular environment of the cell.

CHAPTER 4

THE DELIVERY OF EXOGENOUS FOREIGN MATERIALS INTO DEVELOPING EMBRYONIC CELLS USING FEMTOSECOND LASER PULSES

4.1 Introduction[1]

Throughout Chapters 2 and 3 the benefits of using femtosecond laser pulses to study biological material were reported. By altering how the laser pulses were applied, it was shown that femtosecond laser pulses could be used to both dissect and permeabilize individual cells. Both of these studies demonstrated the multiple applications for this applied tool. Building from the study in Chapter 3, this chapter further explores the versatility of the femtosecond laser by demonstrating its application to more complex biological systems such as embryos. Embryos represent a class of multicompartmental biological organisms that undergo embryogenesis, with the accompanying distinct formation of organs and a circulatory system. As the embryo progresses through its complex development, manipulation of the embryonic cells becomes increasingly difficult as a result of the barriers created by its multicellular layers. However, if the successful non-invasive manipulation of embryos via femtosecond laser pulses was demonstrated, this would make the applied femtosecond laser an important device for biomedical engineers and biologists in a wide range of disciplines including pharmacy, toxicology, the aquaculture industry, and medical and biological research.

In Chapter 3, the permeabilization and delivery of exogenous carbohydrates was discussed in the context of cryopreservation. The localization of femtosecond laser pulses to the biological membrane allowed extracellular solutes to quickly accumulate within the intracellular environment of the cell. A dual fluorescence membrane integrity assay verfied the transient nature of the laser pulse induced pore, and showed the survivability of the laser-treated cells. To extend this application, this chapter focuses on using the femtosecond laser to permeabilize individual embryonic cells in developing embryos. Transient pores formed in the embryonic membrane could be used as a delivery method for introducing DNA for the analysis of gene expression, for example, or the development of transient or stable transgenic organisms. Alternatively, the identification of cell lineage maps in embryos using traceable markers could benefit from laser pulse induced permeabilization. Knowledge of how individual cells contribute to the overall development of organisms is essential to the field of developmental biology. Femtosecond laser pulses in conjunction with fluorescent probes may prove to be an invaluable tool for labeling dividing cells and monitoring their eventual fate. By restricting the transport of the probe through cell division (based on the size of the fluorescent molecule), progeny cells derived from the parent can be traced as a function of development. However, before such applications are pursued and laser pulse induced permeabilization can be evaluated, an understanding of embryonic development is required.

---

[1] Portions of this section have been published in Robles V., Herraez E., **Kohli V**., Cabrita P. Aquaculture Research Trends: Prospects and Developments in sperm and fish embryo cryopreservation. Nova Science Publisher Inc. In press. 2008. **(Invited book chapter)**

In Chapters 2 and 3, V79-4 and MDCK cells were used to demonstrate cell isolation, membrane surgery and permeabilization. However, these do not represent true *in vivo* model systems as the cells were extracted and cultured from hamsters and the kidney tissues of canines, respectively. The isolation of these cells to an *ex vivo* environment has likely changed their characteristic behaviours and responses so as to no longer mimic those of cells in a tissue setting. Therefore, the cells' responses to femtosecond laser pulses must also take into account effects induced by the external environment. This is in contrast to embryonic model systems, in particular the zebrafish, in which embryos are externally fertilized. The eggs are laid by the female fish and externally fertilized by the males and develop outside the organism within their normal developmental surroundings. As a consequence, the manipulation of the embryos takes place in normal *in vivo* conditions. This particular feature makes the embryo a useful model system to study. Furthermore, since embryos progress through a series of developmental stages, continually dividing from a single cell into multiple cells, this model system is ideal for tracking the effect of an applied stimulus on the overall development of the organism. As an example, if femtosecond laser pulses are used to permeabilize individual embryonic cells, an assessment of how the laser-manipulated cell responds, divides and changes the entire morphological development of the organism can be readily evaluated.

The Zebrafish model system (*Danio rerio*)

Among the various mammalian and non-mammalian vertebrate and invertebrate embryonic model systems, the zebrafish (*Danio rerio*) has received particular attention. The zebrafish, Figure 4.1, is a non-mammalian vertebrate freshwater fish belonging to the family of Cyprinidae [81], indigenous to the rivers of northeastern India [82]. This organism has been extensively studied since the 1930s [81] and was recognized by G. Streisinger in the 1980s as an important model organism for genetic analysis [82]. Presently, zebrafish are actively studied worldwide, and have received attention from vertebrate embryologists, zoologists and developmental biologists.

The zebrafish is genetically and developmentally closer to humans than the common invertebrates *Drosophila melanogaster* (fruit fly) and *Caenorhabditis elegans*

Figure 4.1: Adult zebrafish. Image was taken from www.fishbase.org.

(C. elegans) [83, 84]. Key developmental morphological structures that distinguish this organism from others include: the size of the fish (3 to 4 cm; 1 to 1.5 inches; Figure 4.1) [81, 85], the large quantity of laid eggs (150 to 400 eggs per spawning[1]) [81], the transparency of the developing embryo within its proteinaceous membrane (chorion), the formation of organs clearly observable throughout embryogenesis, the short developmental time from fertilization to hatching (between 48 and 96 hrs[2]) [81] and the rapid progression to sexual maturity within 2 to 3 months [82]. An image of an early 4-cell stage zebrafish embryo is presented in Figure 4.2, identifying key structures, including the developing embryonic cells (i.e. blastomere cells; Figure 4.2), the embryo axes (i.e. animal and vegetal poles; Figure 4.2) and a non-cellular barrier (i.e. chorion; Figure 4.2). Figures 4.3 and 4.4 further show a scanning electron microscopy image (SEM)[3] of an animal pole view of an 8-cell stage embryo and a sequence of zebrafish development from 2-cell stage to hatching. Embryo transparency is evident in Figure 4.4, and the patterning of key developmental morphological structures can be readily identified as the embryo ages.

Currently, zebrafish are being used to investigate the chemical toxicity of metals, pesticides and aromatic compounds during development [85], hematopoietic disorders[4] [86, 87], blood coagulation [88] and cardiac function [89]. In all of these studies (except

---

[1] The number depends on various factors including the water quality, the pH, the temperature and the health of the fish.

[2] The large variation in hatching time likely depends on the strength and thickness of the chorion as well as the muscular activity of the developing embryo inside the chorion.

[3] The preparation of embryos for SEM imaging is presented in Appendix F of Chapter 5.

[4] Hematopoiesis is the study of blood cell (erythrocyte) formation in the body.

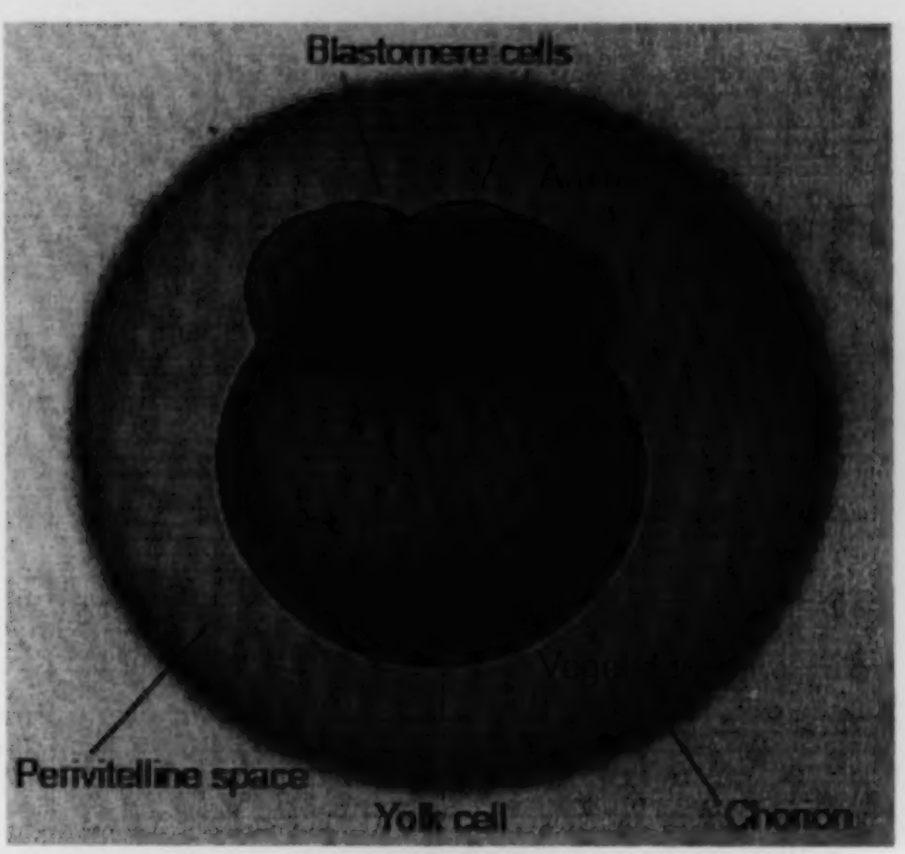

Figure 4.2: A 4-cell stage embryo developing within its chorion. Morphological structures that have been emphasized include the blastomere cells, the perivitelline space, the yolk cell and the chorion. The animal pole is located above the dividing blastomere cells, while the opposite side (bottom of the yolk cell) is the vegetal axis (i.e. vegetal pole). The dorsal-ventral axis cannot be defined in the above image. One would have to wait until epiboly, specifically when involution and convergence occurs, to define the dorsal-ventral axis [90].

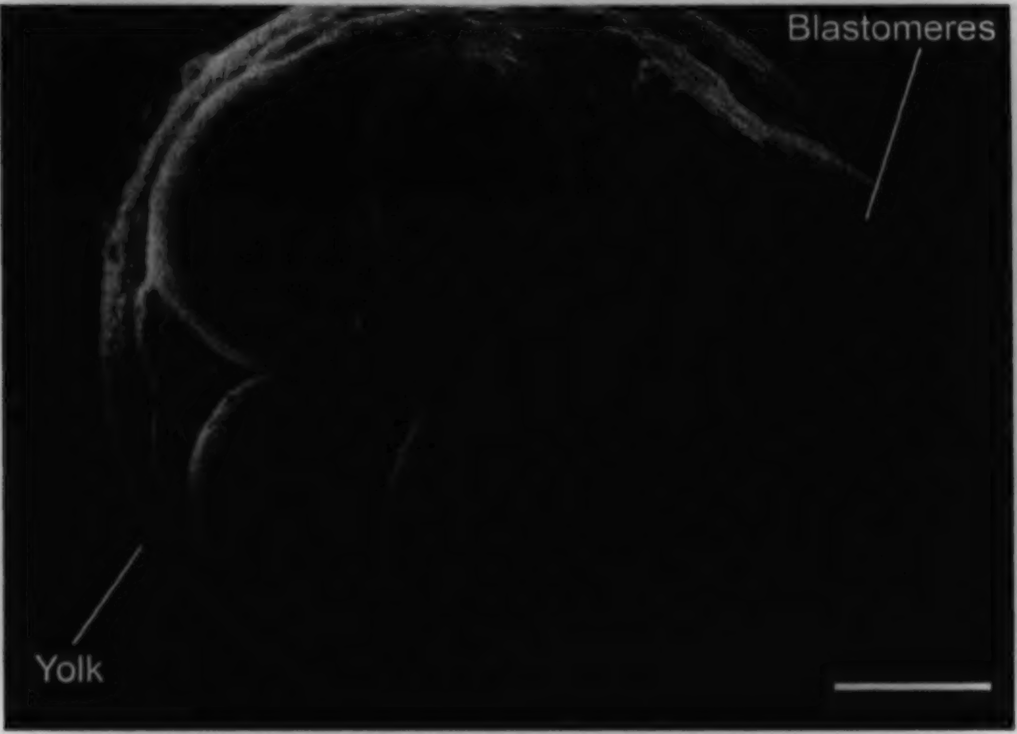

Figure 4.3: A top view SEM image of an 8-cell stage dechorionated zebrafish embryo. The blastomere cells and the yolk cell have been indicated. Scale bar represents 100 μm.

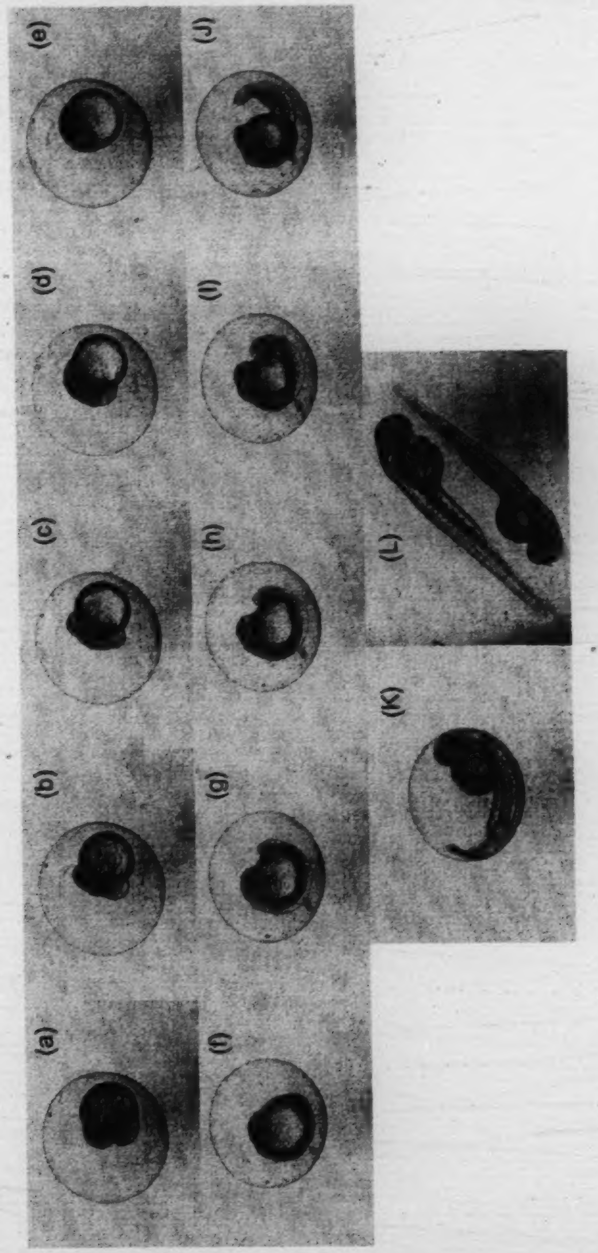

Figure 4.4: Sequence of images depicting zebrafish development from 2-cell stage to hatch. The barrier surrounding the developing embryo is the chorion. The embryo continues to differentiate within the chorion, until muscular activity frees the embryo from this barrier. Developed zebrafish larvae are shown in the last image. The above images were extracted from live video recordings of development.

for [88]), zebrafish mutants[1] were created to identify the chemical pathways and genes responsible for these disorders, which also affect humans. Ideally, a resource bank of stored zebrafish mutants would improve the progress and development of human health research.

Despite the benefits of using the zebrafish as a model organism for understanding human disease, the manipulation of this species has been difficult. For instance, to establish a resource bank of mutant zebrafish, cryobiologists have attempted to cryopreserve this organism [91-103]. However, the blastoderm, yolk syncytial layer (YSL), yolk cell and chorion[2] provide barriers (some of these morphological structures are shown in Figures 4.2 and 4.4) to both water and cryoprotectant influx and efflux. The large overall size of the embryo (~ 800 μm), its low surface to volume ratio, its sensitivity to chilling and relatively large osmotically inactive volume and the differing permeability properties of the aforementioned compartments [95, 96, 99, 101, 103, 105-108] have prevented the successful cryopreservation of the zebrafish (for a review of fish cryopreservation see reference [109]).

The manipulation of complex biological systems

To date several techniques have been used for the manipulation of complex biological systems, including the use of microinjection [56, 102, 103, 110-112], electroporation [69, 70, 72, 113, 114], UV [115-121] and NIR laser pulses [17, 20, 122-124].

---

[1] Zebrafish exhibiting a particular phenotype such as a hypothropic mutant (a mutant with an abnormal sized ventricle and normal atrium [92]), or delayed erythroid maturation (a mutant where red blood cell production is delayed potentially leading to anemia [89]).

[2] Blastoderm refers to the collection of blastomere cells that forms a cap on top of the yolk [90]. The YSL is an additional barrier that forms from the collapse of marginal blastomere cells into the yolk cytoplasmic layer [104]. Two types of YSLs form, the external YSL (E-YSL) and internal YSL (I-YSL) [90]. The E-YSL progresses downwards toward the vegetal pole (a process known as epiboly), with blastomere cells riding on the E-YSL. In contrast, the I-YSL develops between the blastoderm and yolk. It is believed that the role of the I-YSL is to transport nutrients to the blastomere cells from the yolk [90].

For instance, the prevalent method of microinjection uses pulled hollow glass needles to perforate cells for the cytoplasmic delivery of materials such as DNA, Figure 4.5. The injection pipette is first loaded with the desired molecule to be delivered (e.g. fluorescent probe or DNA) and brought into contact with the cell. Mechanical force is used to perforate the cell membrane and through the application of pressure controlled by a foot pedestal, material is forced through the microinjection tip into the cytoplasm, Figure 4.5. While microinjection has been an invaluable technique used in various biological disciplines, it also represents a tedious and repetitive method requiring superior manual dexterity. For instance, as an embryo ages, blastomere divisions decrease the size of the embryonic cells, making microinjection of individual cells at later developmental stages increasingly difficult.

Using the technique shown in Figure 4.5, Stuart *et al.* [110] microinjected DNA into the cytoplasm of 1-, 2-, or 4-cell stage zebrafish embryos and monitored the fate of the introduced DNA as a function of embryonic development. The authors [110] found that the survival of the embryos depended on the injected DNA concentration, and that the introduced construct rapidly degraded at the onset of gastrulation. Higashijima *et al.* [111] also used microinjection to produce transgenic zebrafish using DNA with an actin promoter from the organism. Linearized DNA constructs were introduced into 1-cell stage chorionated embryos, and the expression of GFP in 24 hour post-fertilized (hpf) embryos was assessed. Embryos exhibiting strong EGFP fluorescence were raised to

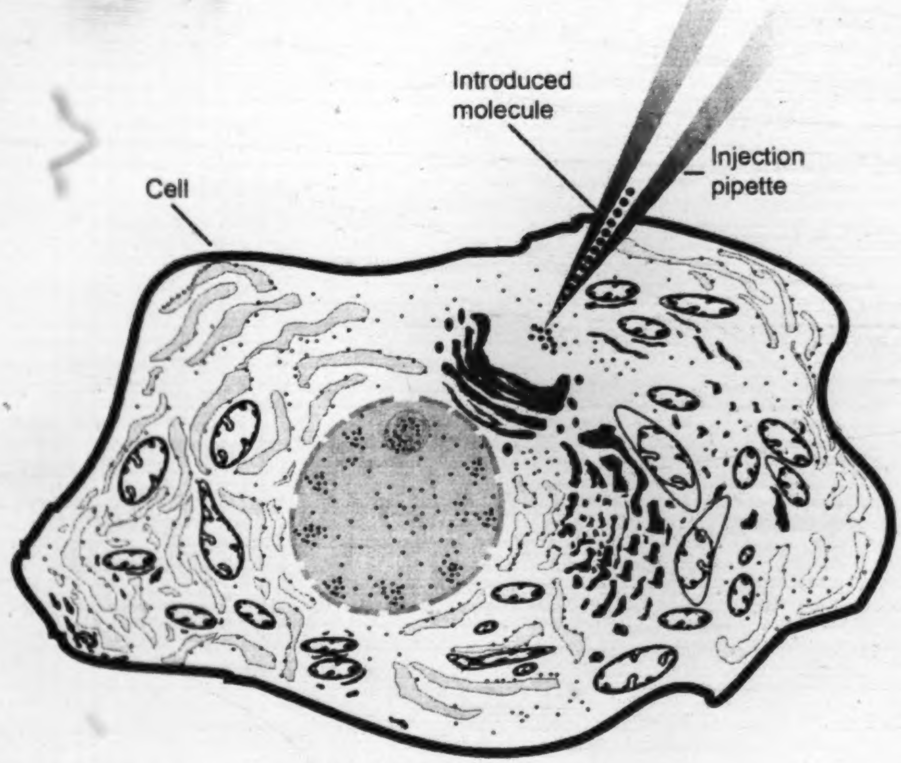

Figure 4.5: Microinjection of a cell. An injection pipette is brought in close contact with a cell. The pipette is mechanically forced through the cell membrane into the cell's cytoplasm. Through the application of pressurized air that is activated by a foot pedestal, the introduced molecule is forced through the injection tip into the cell.

sexual maturity and mated with wild-type zebrafish. The percentage of offspring with GFP expression was observed to range from 2 to 50 % [111].

In similar studies by Linney *et al.* [112] and Culp *et al.* [56] microinjected DNA was introduced into zebrafish for the purpose of determining germ-line transmission. Linney *et al.* [112] compared a retroviral vector method to DNA injection to determine the level of transgene expression. The authors observed a higher percentage of transgenic progeny with microinjected embryos than with the viral vector method [112]. Culp and colleagues [56] microinjected dechorionated 1-cell stage zebrafish embryos and contrary to the Higashijima *et al.* study, observed a frequency of transmission between 7 and 25 % [56]. Differences in the percentage of positive founders were likely due to the chosen DNA construct.

Similar to the Buono *et al.* [70] study mentioned in section 3.1 of Chapter 3, Cerda *et al.* [72] used electroporation (see diagram, Figure 3.3) to introduce DNA, RNA and morpholinos into the neural, retinal and somitic tissue of dechorionated zebrafish embryos. For material delivery into 13 to 48 hpf embryos and 3 to 5 day post-fertilized (dpf) embryos, electrodes were positioned outside the embryo and inserted into the tissue near the injection site [72]. Through the application of an electrical pulse, the authors reported the successful introduction of DNA into the midbrain, somites and eye and of RNA and morpholinos into the eye, minbrain and trunk of the fish [72]. It should be noted, however, that electroporation represents a technique that cannot be applied to study the intracellular environment of cells deep within an organism. Moreover, as stated in section 3.1 of Chapter 3, identical electroporation protocols often yield inconsistent or no results [70]. This has been discussed in the pioneering work of Buono *et al.* [70]

Laser manipulation of complex biological systems

UV laser pulses at a wavelength of 488 nm were used by Liu *et al.* [119] to laser ablate the Mauthner cells and motorneurons in 4 dpf zebrafish. The motivation of the study was to indentify if laser-induced lesions in the cells lead to changes in the escape response of stimulated zebrafish [119]. Cells selected for laser ablation were labeled with calcium green dextran and were identified using confocal microscopy. Depending on the chosen cells, the irradiation time required to completely ablate and induce cell death was 1 min for motorneurons in the spinal cord and 10 to 12 min for Mauthner cells in the hindbrain [119]. Interestingly, animals that were laser pulse ablated showed a change in their behavioral escape response. Specifically, the time it took the fish to respond to stimuli was 40 ms slower than before laser-treatment. Very little difference in the swimming turning angle was observed post-laser pulse ablation; however, the angular velocity and the length of the response were different [119].

In addition to the Liu *et al.* study [112] and other investigations involving the laser pulse ablation of neurons [121], the laser pulse ablation of sensory hair cells associated with neuromasts of the lateral line organ and melanocytes has been recently shown. For the ablation of sensory hair cells, Jones *et al.* [118] directed 337 nm 175 μJ laser pulses from a nitrogen gas laser onto the nuclei of hair cells in zebrafish. Laser pulses were focused onto the cell by a 1.25 NA 100X glycerin immersion microscope objective. The authors used time-lapse video to track the lineages that gave rise to the replacent of the laser pulse ablated hair cells [118]. Using laser pulses in the visible spectrum (532 nm) with a pulse duration of 5 to 7 nanoseconds, Yang *et al.* [117] laser irradiated dorsal melanocytes in 60 hpf zebrafish and monitored the regeneration of the pigment cells. The authors [117] hypothesized that the mechanism of melanocyte laser pulse ablation arose from heat-induced death due to the absorption of laser light by the light absorbing pigment melanin.

Recently, NIR femtosecond laser pulses have been used to laser-manipulate model organisms such as *Caenorhabditis elegans* (C. elegans) [20, 123], *Drosophila melanogaster* (fruit fly) [17] and Sprague-Dawley rats. For instance, in a study by Yanik *et al.* [123] 200 femtosecond laser pulses at a pulse energy of 40 nJ/pulse were used for the laser axotomy of D-motor neurons in L4 larval-stage *C. elegans*. It was shown that femtosecond laser pulses could sever the D-motor neuron, preventing backward locomotion. In a similar study by Chung *et al.* [20], 100 femtosecond laser pulses at a pulse energy of 3 nJ/pulse were used to study AFD neurons in C. elegans. Chung and colleagues severed individual dendrites within a bundle of amphid dendrites without inducing damage to adjacent dendrites [20]. Interestingly, contrary to the Yanik *et al.* study [123], ablated sensory neurons were not found to repair, indicating that the cuts were permanent [20].

Nishimura *et al.* [124] used 100 femtosecond laser pulses with a pulse energy ranging from 0.03 to 0.5 μJ/pulse to study the photodisruption of microvessels in the parenchyma of rat brains. Depending on the laser pulse energy, laser induced hemorrhaging, extravasation and intravascular clot formation were observed [124]. The authors also measured the changes in adjacent and downstream blood flow in obstructed vessels following laser pulse induced clot formation [124].

Recently, Supatto *et al.* [17], applied 130 femtosecond laser pulses to induce morphogenetic movements in *Drosophila* embryos. Embryos were laser pulse ablated at a location below the vitelline membrane. Laser pulse ablation was achieved without affecting cytoskeletal dynamics adjacent to the laser-targeted area [17]. In addition to laser pulse ablation, the authors [17] also examined the *in vivo* modulation of cellularization front invagination (CFI) in laser-treated embryos [17].

Purpose of this study

Expanding on the study presented in Chapter 3, this chapter demonstrates the application of focused femtosecond laser pulses as a tool for transiently permeabilizing embryonic cells. A schematic representation of laser pulse induced permeabilization was previously shown in Chapter 3, Figure 3.1. The motivation of this study was to show that embryonic cells could be successfully permeabilized for the delivery of exogenous foreign material without compromising the development of the organism. The animal model system chosen in this chapter was the zebrafish (*Danio rerio*), a rapidly dividing animal that is externally fertilized and appears transparent until hatching, Figure 4.4. The transparent development of the zebrafish is a feature unique to this organism, allowing the targeted region to be visualized during laser pulse manipulation.

To laser-manipulate zebrafish embryos, focused femtosecond laser pulses were localized either at the blastomere-yolk interface or on individual blastomere cells (disscused in section 4.2). A range of cell stages were chosen for permeabilization, from 2-cell stage to 128-cell stage, and both dechorionated and chorionated embryos were investigated for laser pulse permeabilization and delivery. The molecules chosen for cytoplasmic introduction were the fluorescent reporter molecule fluorescein isothiocyanate (FITC), Streptavidin-conjugated quantum dots and plasmid DNA. Loading efficiencies of introduced FITC into both dechorionated and chorionated embryos were investigated, and the survival of laser pulse manipulated embryos to the developmental endpoint of pec-fin stage was evaluated. A detailed explanation of the experimental design for the laser pulse manipulation of zebrafish embryonic cells is presented in section 4.2, and the handling and harvesting of fertilized embryos can be found in Appendix F.

The results presented in this chapter have important applications to biology. For instance, in the discipline of cryobiology, femtosecond laser pulses could be used for the cytoplasmic introduction of membrane impermeable carbohydrates such as trehalose or maltose for the purpose of generating a resource bank of preserved embryos. However, to date, the zebrafish has not been successfully cryopreserved [109]. Difficulties inherent in the cryopreservation of this organism include a low permeability to permeable cryoprotectants resulting from the multiple barriers of the chorion, yolk-syncitial layer and yolk (see Figures 4.2 through 4.4 for the locations of some of these barriers) [91-97, 99-103, 106-108]. It is also conceivable that femtosecond laser pulses could be used to transiently permeabilize the zebrafish embryonic membrane in the presence of permeable cryoprotectants. Pores formed in the cells could increase the solute permeability of the cryoprotect agent, leading to a larger intracellular accumulation of the delivered molecule.

More recently, other protective agents such as antifreeze protein have been suggested as additional molecules that may help in cryopreserving embryos. In fact, Robles *et al*. [57, 58, 125] recently demonstrated the protective action of microinjected antifreeze protein in vitrified winter flounder and the chilling response of turbot and seabream embryos. In a similar study, the author of this thesis introduced FITC labeled antifreeze protein into dechorionated zebrafish blastomere cells with femtosecond laser pulses (unpublished data[1]). Preliminary experiments on the chilling sensitivity of embryos cooled to 0 °C revealed that intracellular antifreeze protein did not protect the embryos upon warming. It is unknown whether the introduced protein concentration was too low to confer protection or if the thermal hysteresis range was insufficient to avoid chilling sensitivity.

---

[1] Work was conducted in collaboration with Dr. V. Robles from CCMAR, Center for Marine Sciences, University of Algarve, Faro, Portugal.

4.2 Results and Discussion[1]

Experimental methodology

The experimental method used for manipulating dechorionated and chorionated zebrafish embryos is presented in Figure 4.6. To permeabilize embryos for exogenous delivery of FITC, quantum dots or DNA, sub-10 femtosecond laser pulses were generated from a Ti:Sapphire laser oscillator with an emitted wavelength spectrum ranging from 700 to 900 nm, centered at 800 nm. The repetition rate of the oscillator was 80 MHz. In Figure 4.6, femtosecond laser pulses were directed and coupled into an upright Nikon 80i microscope (Nikon, Japan). The red lines in this image represent the optical beam path, which was manipulated via dichroic mirrors labeled as optical elements A1 through A3. At element A3, the laser pulse is shown reflected into the ocular imaging head, B, however, this imaging head was removed during laser-manipulation. The ocular imaging head was replaced when visual assessment of blastomere-fluorescence was performed. Removal of the ocular head during the experiment was to avoid additional pulse broadening at the focal plane, caused by the large glass element housed at the base of the ocular imaging head. With the ocular imaging head removed, the femtosecond laser pulses were coupled directly into the imaging block, C. At the entrance of the imaging block a 45 ° mounted 45:55 (reflection:transmission) beam splitter transmitted the laser light into the fluorescence filter chamber, D, down through the objective nose piece, E, and into the objective lens, F. To ensure that a filter cube[2] in the fluorescence chamber did not block the laser pulse, the carousel housing the filter cubes was rotated to a blank filter holder.

---

[1] Portions of this section have been published in Kohli *et al.* Biotechnol. Bioeng. 98(6), pg. 1230-1241.

[2] A detailed explanation of how the filter cube works is presented in Appendix E.

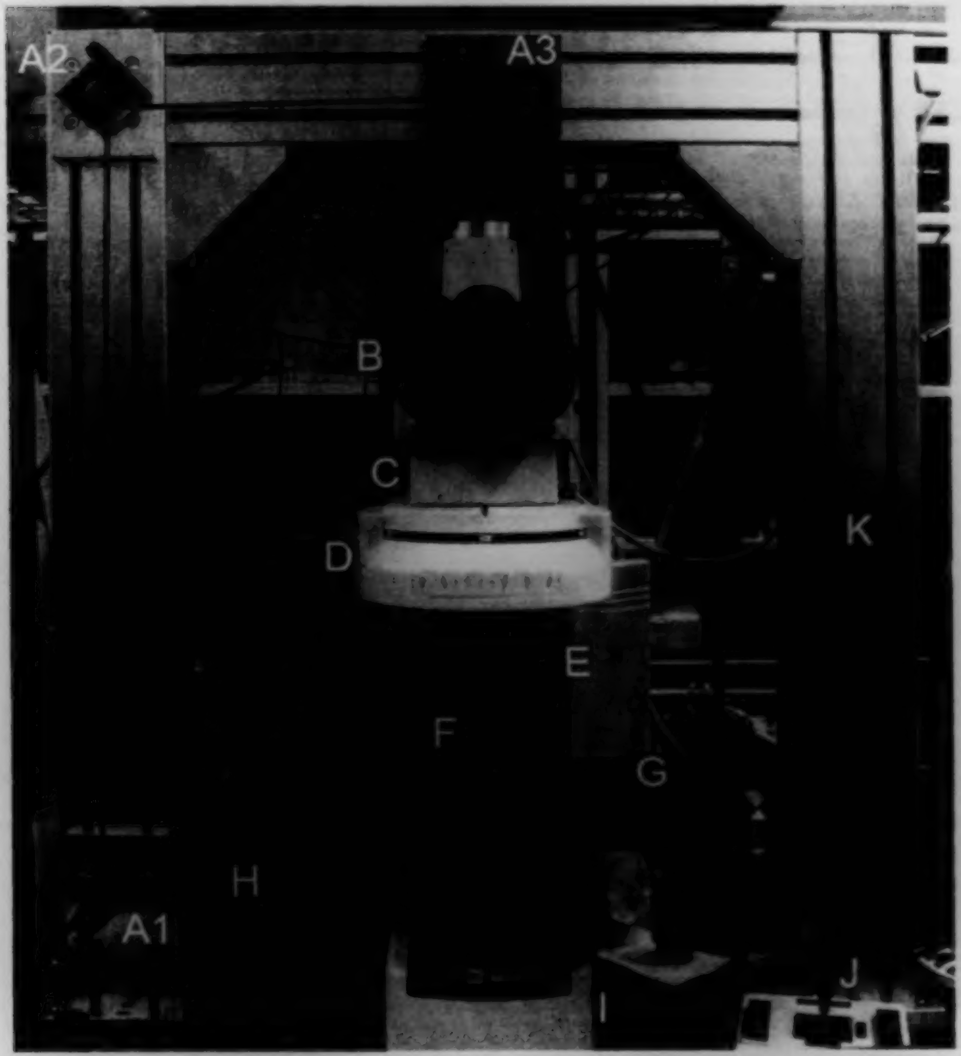

Figure 4.6: Depicts the microscope setup used to laser-manipulate zebrafish embryonic cells. The red lines indicate the optical beam path. See text for details. A1-A3 – dichroic mirrors, B – ocular imaging head, C – imaging block, D – fluorescence filter chamber, E – objective nose piece, F – objective lens, G – *x-y-z* motorized stage, H – motorized control shaft, I – white light chamber, J – stage controller and K – microscope aluminum support structure.

With the femtosecond laser pulses coupled into the objective lens, the laser light was focused onto the embryo, either at the blastomere-yolk interface or directly on the blastomere cell. Embryos were placed on a motorized *x-y-z* stage, G, and stage movements were controlled (for accurate positioning of the embryo) by the motorized shaft and stage controller, H and J. The embryos were illuminated with white light in the inverted position in the same imaging plane as the objective lens through adjustments of the condenser located directly below the stage, G. Reflected and transmitted laser light and white light for image capture traveled back through the objective lens and fluorescence filter chamber, and were reflected by the 45:55 beam splitter along the length of the imaging block. Located at the rear of the imaging block, a 45 ° mirror reflected the light out through an imaging port (the port is located just behind the ocular imaging head; it cannot be seen in Figure 4.6). A monochrome (WAT-902H Watec Monochrome Camera (Aegis Electronics, AZ); horizontal and vertical pixel dimensions of 8.4 μm x 9.8 μm; ½ inch sensor) or a color CCD (DS5-M color camera, Nikon, Japan; pixel size of 3.4 μm; 4:3 aspect ratio sensor) was mounted at the exit of the imaging port and interfaced with a computer for the capture of still images and real time video. An attenuator filter was placed between the camera and exit port to minimize the detected laser light.

A transparent front view of Figure 4.6 is presented in Figure 4.7. As seen in the image, the femtosecond laser pulse traverses the beam splitter located in the imaging block, C. Provided that the carousel in the fluorescence filter chamber, D, is rotated to a blank filter cube, the femtosecond laser pulse passes through towards the objective lens, F. An illustrated side view of Figures 4.6 and 4.7 is shown in Figure 4.8. This figure

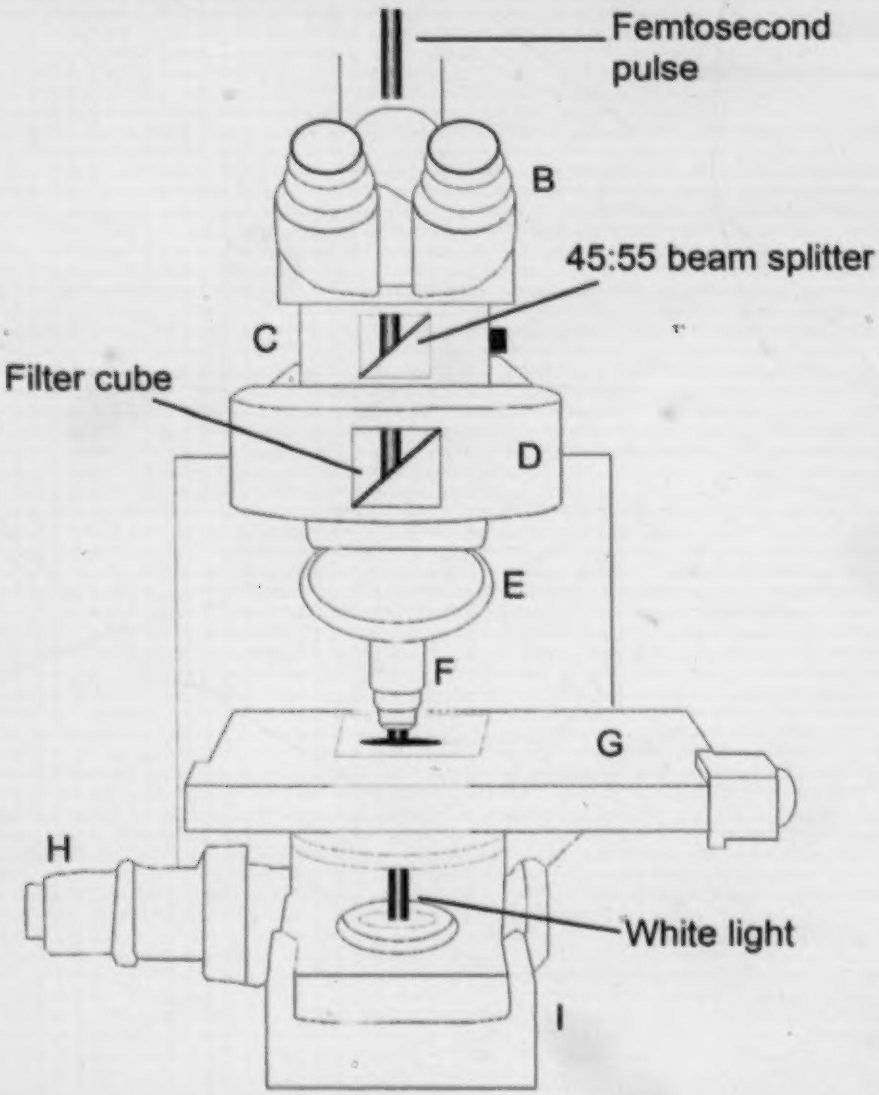

Figure 4.7: Transparent front view of the microscope shown in Figure 4.6. Femtosecond laser pulses are directed through the imaging block, C, downwards towards the fluorescence filter chamber, D. If the carousel in the fluorescence filter chamber houses a blank filter, the femtosecond laser pulses pass through and are focused onto the biological specimen by the microscope objective lens, F. White light is shown illuminating the specimen in the inverted position. B – ocular imaging head, C – imaging block, D – fluorescence filter chamber, E – objective nose piece, F – objective lens, G – *x-y-z* motorized stage, H – motorized control shaft and I – white light chamber.

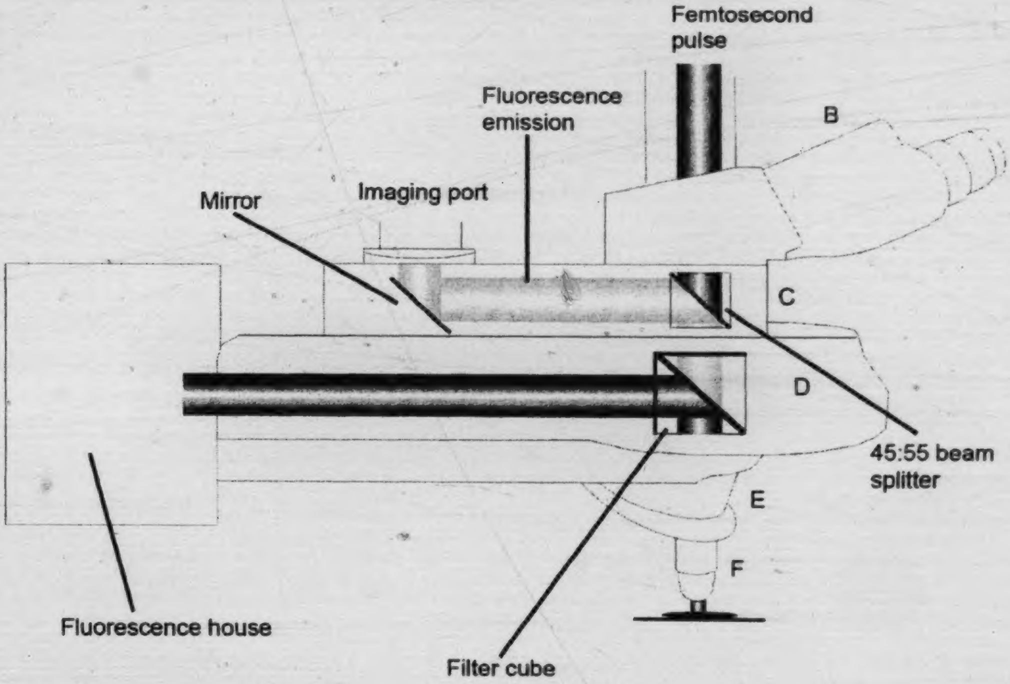
Femtosecond pulse
Fluorescence emission
B
Mirror
Imaging port
C
D
45:55 beam splitter
E
F
Fluorescence house
Filter cube

Figure 4.8: Side view image of Figures 4.6 and 4.7. In this scenario a filter cube is placed in the optical beam path. Fluorescence light emitted from the fluorescence house is directed along the fluorescence filter chamber, D. The exciter region of the filter (see Appendix F for more information) transmits the fluorescence light, which is reflected towards the microscope objective lens, F. Back reflected light passes through the filter cube through the emitter and is reflected along the imaging block, C. A 45 ° mirror reflects the fluorescence light into the imaging port. In the above configuration, the filter cube blocks the femtosecond laser pulse.

illustrates the scenario where the filter cube is placed in the optical beam path, preventing the femtosecond laser pulse from reaching the objective lens, F. Fluorescence light is produced from the fluorescence house and travels along the fluorescence filter chamber, D. The filter cube exciter region (see appendix E for a detailed explanation of the filter cube) reflects fluorescence towards the objective lens, F, and emitted fluorescence is transmitted through the filter cube emitter region and is detected through the imaging port. When the filter cube is removed, the femtosecond laser pulse passes through the fluorescence filter chamber and down towards the objective lens, F, Figure 4.9. Back reflected laser light is collected via the same pathway as for fluorescence detection (Figure 4.8), and imaged through the imaging port.

To laser-manipulate zebrafish embryos, a pulse energy ranging from 0.5 nJ/pulse to 2.7 nJ/pulse was used[1]. The laser pulses were gated with a galvo (subsequently referred to as a shutter), located in front of the dichroic mirror A1 (the shutter is not shown in Figures 4.6 and 4.7) to control the amount of laser energy deposited at the targeted interface. The maximum shutter gating time was less than one second. Femtosecond laser pulses were focused by a 1.0 NA 60X water immersion microscope objective (F in Figures 4.6 through 4.9). An estimate of the diffraction limited irradiance spot size (diameter) from equation (1.2) in Chapter 1 was calculated to be $d_r = 976$ nm ($\lambda = 800$ nm). The peak power at the focus for laser-poration was between 1.7 kW/pulse (0.5 nJ/pulse) and 9.3 kW/pulse (2.7 nJ/pulse) (these values were calculated using an estimated broadened pulse duration of 291 femtoseconds; see Appendix A for details).

---

[1] These pulse energies represent the values measured entering the microscope objective lens. Fresnel's equations describing the reflection and transmission values through various index media can be used to approximate the amount of average laser power loss. From calculations (not presented in this thesis), the total average laser power loss was a few milliwatts.

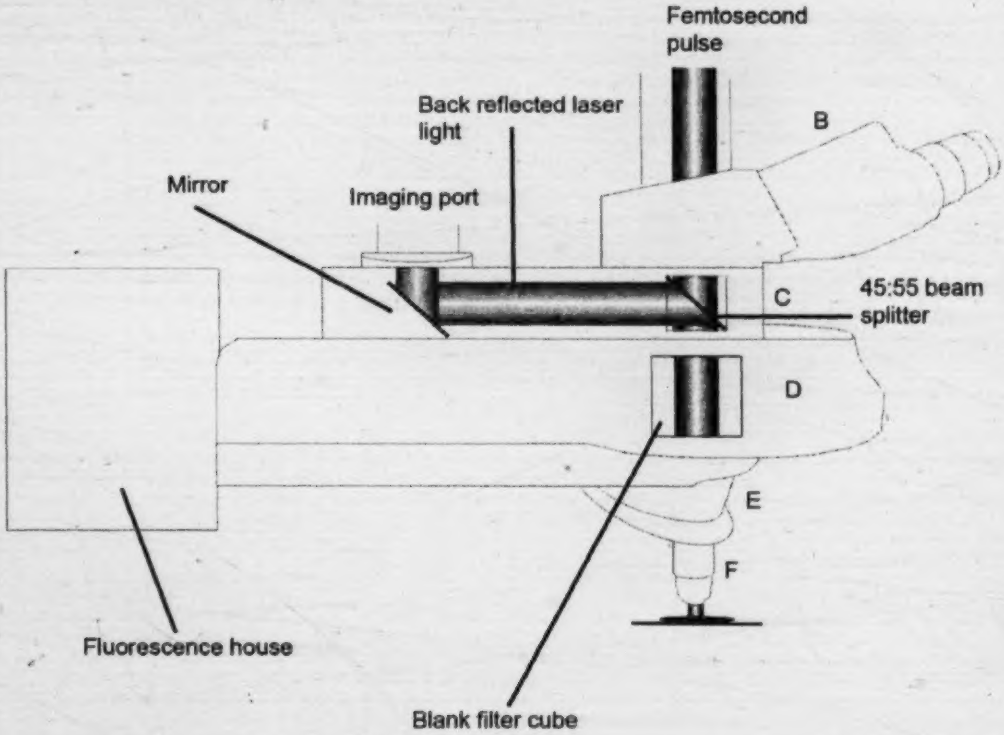
Femtosecond pulse
Back reflected laser light
B
Mirror
Imaging port
C
45:55 beam splitter
D
E
F
Fluorescence house
Blank filter cube

Figure 4.9: Side view image of Figures 4.6 and 4.7. In this scenario the carousel in the fluorescence filter chamber, D, houses a blank filter cube. In this configuration, the femtosecond laser pulse is transmitted by the beam splitter and through the fluorescence filter chamber, D. The laser pulse is then focused by the microscope objective lens, F, onto the sample. Back reflected laser light is captured through the same optical path, and is reflected by the beam splitter along the imaging block, C. A 45 ° mirror reflects the laser light into the imaging port.

Based on the irradiance spot size and peak power, the peak intensity at the focus was estimated to be between 2.3×10^{11} W/cm^2 and 1.2×10^{12} W/cm^2. With the peak intensity defined, the equations developed in Chapter 1 and 2 were used to estimate the maximum electron density and the temperature rise at the focus after a single femtosecond laser pulse. From equation (2.2) in Chapter 2, γ ranges from 4.76 (1.2×10^{12} W/cm^2) to 12.5 (2.3×10^{11} W/cm^2), and the effective ionization potential in equation (2.1) in Chapter 2 can be approximated as the band gap energy of water. The calculated values for $\rho_{\max}$ and ΔT after a single femtosecond laser pulse were estimated to be $\rho_{\max} = 10^{12}$ to 10^{17} cm^{-3} ($I/I_R = 0.04$ for 0.5 nJ/pulse; $I/I_R = 0.18$ for 2.7 nJ/pulse) and $\Delta T = 5.60\times10^{-7}$ to 0.06 K (the temperature would be expected to increase after multiple incident femtosecond laser pulses), respectively.

An assessment of blastomere-fluorescence was performed through epi-fluorescence imaging using the same setup shown in Figures 4.6 through 4.9. A standard FITC filter (Chroma Technology Corp., Rockingham, VT), qdot 605 filter (Chroma Technology Corp., Rockingham, VT) or long-pass GFP filter (Chroma Technology Corp., Rockingham, VT) was used for fluorescence detection.

As observed in Figure 4.6, the entire microscope was anchored to the optical table and to the aluminum rectangular blocks, K. A simplified version of the experimental setup shown in Figures 4.6 through 4.9 is presented in Figure 4.10.

The effect of femtosecond laser pulses on short-term zebrafish development

A preliminary study was performed to examine the laser's effect on short-term embryonic development. Before demonstrating the permeabilization and introduction of

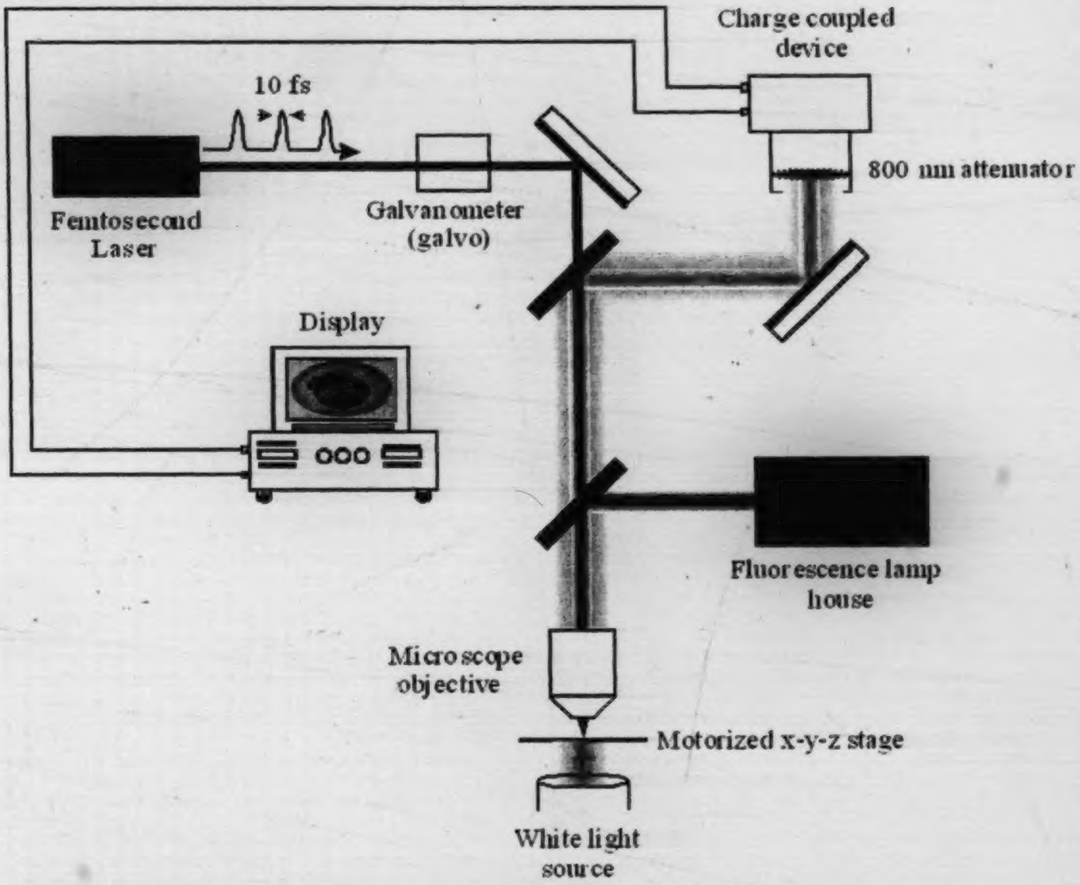
Charge coupled device
10 fs
800 nm attenuator
Femtosecond Laser
Galvanometer (galvo)
Display
Fluorescence lamp house
Microscope objective
Motorized x-y-z stage
White light source

Figure 4.10: A simplified version of the experimental setup shown in Figures 4.6 through 4.9. Sub-10 femtosecond laser pulses were generated from a modelocked titanium sapphire laser oscillator. The pulse repetition rate and center wavelength were 80 MHz and 800 nm, respectively. Laser pulses were coupled to a 1.0 NA 60X water immersion microscope objective and focused to a location near the blastomere-yolk interface or directly onto the blastomere cell. A shutter (galvo) was inserted into the beam path to control the number of laser pulses irradiating the sample. Embryos of varying developmental stages, from early cleavage (2-cell stage) to early blastula (128-cell stage) were placed on a motorized *x-y-z* stage for laser poration. White light illuminated the embryos in the inverted position while fluorescence was collinearly coupled with the laser pulse in the forward direction. (The epi-fluorescence wavelength shown in the above image is that for FITC). The interaction of the femtosecond laser pulses with the embryonic cells was captured with a black and white CCD and with the Nikon DS-5M color camera. Cameras were interfaced with a computer for capturing still images and real time video.

foreign materials into developing embryonic zebrafish cells, individual dechorionated embryos at early cleavage to early blastula stage (2-cell to 128-cell stage) (n = 5 to 10 embryos) were laser pulse targeted for ablation in the absence of exogenous solution.

Figure 4.11 depicts the ablation and subsequent development of an 8-cell stage dechorionated embryo that was targeted at the blastomere-yolk interface, indicated by the arrow in Figure 4.11(a). A cavitation bubble, Figure 4.11(b), was formed at the interface, which obscured the scarred blastomere-yolk surface. Forty-five to 60 minutes following laser pulse targeting, the embryo continued to develop normally, Figure 4.11(c), relative to control embryos and standard Westerfield images [126] at the same developmental stage. The embryo in Figure 4.11(c) developed to 64/128-cell stage (late cleavage/early blastula) with normal developmental morphology. Other ablated embryos at various developmental stages (8-, 16-, 32- and 128-cell stage) were also found to develop in a manner consistent with control and Westerfield images [126] (data not shown). All dechorionated embryos from early cleavage to early blastula stage (2-cell to 128-cell stage), including Figure 4.11, were laser pulse manipulated at the blastomere-yolk interface with a pulse energy of 2.7 nJ/pulse and a gated shutter time between 200 to 300 ms.

In Figure 4.11, the blastomere-yolk interface of the 8-cell stage dechorionated embryo was intentionally targeted due to the geometry of the blastomere cells in relation to the yolk cell. The blastomere-yolk interface represents the region delineating the blastomeres from the yolk, where the curved blastomere cells pinch off. Between the blastomeres and the beginning of the dense yolk area, the interface represented a relatively smooth, flat region that could be accurately targeted under high magnification

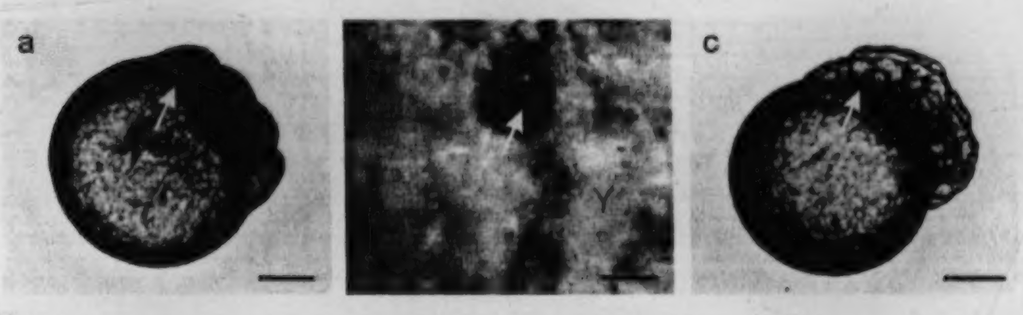

Figure 4.11: (a) An early 8-cell stage dechorionated embryo that was laser-targeted at the blastomere-yolk interface (arrow). Post-manipulation, (b) a cavitation bubble (arrow) was formed, which obscured the scarred blastomere-yolk surface. (c) 45 to 60 min following laser-manipulation, the embryo had developed to 64/128-cell stage with normal morphology as compared to control embryos and Westerfield images [126]. The arrow in (c) represents the location where the pore was formed in the original 8-cell stage embryo. The embryo was laser manipulated with a pulse energy of 2.7 nJ/pulse and a gated shutter time between 200 and 300 ms. B – blastomere; Y – Yolk. Scale bars for (a,c) and (b) represent 200 and 5 μm, respectively.

(60X)[1]. Figure 4.12 presents an SEM image of the blastomere-yolk region of an 8-cell stage dechorionated embryo showing the denser and less dense areas of the yolk (Y) and the blastomeres (B) respectively. As seen in the image, adjacent to the yolk the fixed cellular surface was smooth but quickly increased in curvature further away. This change in the curvature was observed as a reduction in the image sharpness, Figure 4.12. The space between the solid lines in Figure 4.12 was defined as the blastomere-yolk interface. It should be noted that the pinched-off blastomere cells were not completely separated from the yolk cell. In fact, between early and mid cleavage stage (2-cell to 16-cell stage), blastomere divisions are meroblastic in nature (i.e. cleavages are incomplete) [82, 90, 127] with the cells in syncytium with the yolk cell. Beyond 16-cell stage, the more central blastomeres become completely cleaved from the yolk, representing the first cells that lose cytoplasmic connections to the yolk cell and more marginal cells (to be discussed) [82, 90, 127]. Before fertilization, the yolk granules and the cytoplasm are mixed [128], but become separated at the time of fertilization when the cytoplasm streams towards the animal pole, defining the blastomere cells. Cytoplasmic streaming, however, subsides by the 3rd or 4th cleavage (8/16-cell stage) [81].

Femtosecond laser pulse induced transient pore formation in dechorionated embryos

Having established that early stage dechorionated embryos continued to divide normally 45 to 60 min post-laser manipulation, the state of the scarred blastomere-yolk region was assessed. To verify that the laser pulse ablated region led to the formation of a

---

[1] It is easier to focus the laser beam onto a flat surface than a curved surface.

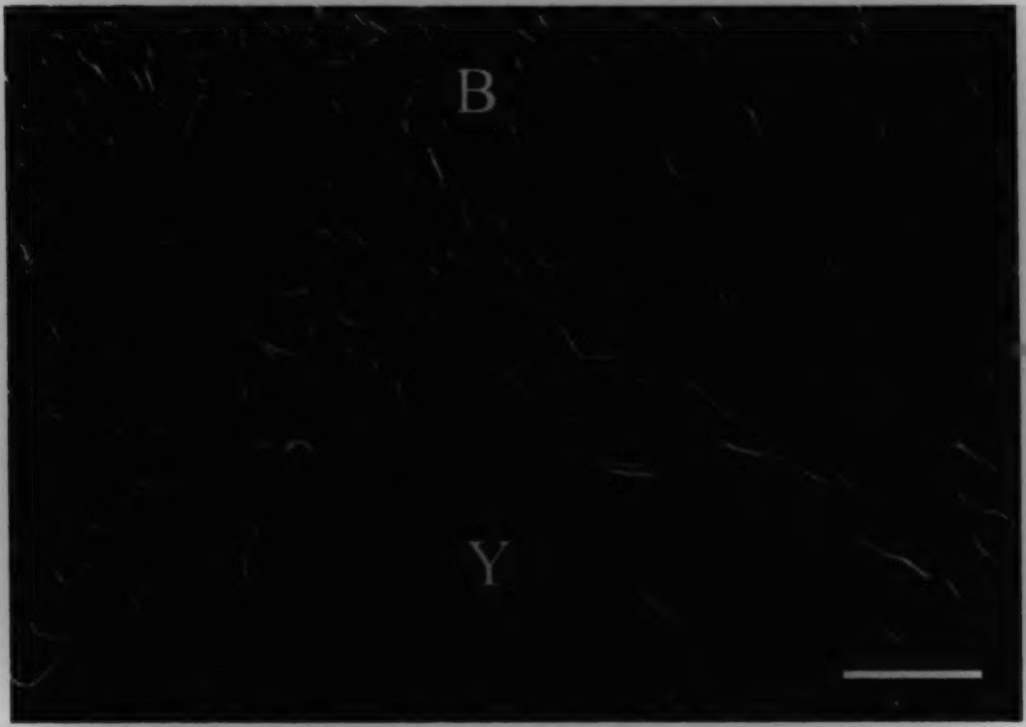

Figure 4.12: High-resolution SEM image of the blastomere-yolk region in an 8-cell stage embryo. The area between the two lines was defined as the blastomere-yolk interface. The dense region of the yolk, Y, is observed at the bottom of the image, while the less dense area of the blatstomeres, B, is seen at the top. Scale bar represents 5 μm.

transient pore, individual dechorionated embryos (n = 39 embryos) at mid cleavage to early blastula stage (8-cell to 128-cell stage) were laser pulse targeted (2.7 nJ/pulse; 200 to 300 ms gated shutter time) at the blastomere-yolk interface in the presence of a fluorescent reporter molecule, FITC. The final concentration of FITC in solution was 0.02 to 0.03 mg/ml.

Figure 4.13 depicts dechorionated zebrafish embryos at varying developmental stages: Figures 4.13(a,b) at 32-cell stage, Figures 4.13(c,d) at 256-cell stage and Figures 4.13(e,f) at 512/1K-cell stage. These above stages represent the developmental progress of the embryos 30 min following laser pulse manipulation at the blastomere-yolk interface. Therefore, considering that early cleavage divisions occur fairly synchronously approximately every 15 min [90], then Figures 4.13(a,b), 4.13(c,d) and 4.13(e,f) were laser permeabilized at 8-cell, 64-cell and 128-cell stage, respectively. Verification of permeabilization (i.e. pore formation) for FITC delivery into the dividing embryonic cells is demonstrated in Figures 4.13(b,d,f). The arrows in Figures 4.13(a,c,e) represent the location where femtosecond laser pulses were localized, namely at the blastomere-yolk interface. In Figures 4.13(b,d,f), FITC fluorescence was observed and was found to be distributed throughout the blastomere cells. This distributed pattern of fluorescence, which varied between embryos, was likely due to differences in blastomere patterning. This was clearly observable by noting that FITC fluorescence was less uniformly distributed in Figures 4.13(d) and 4.13(f) than in Figure 4.13(b). It was hypothesized that blastomere patterning may affect the spatial distribution of FITC.

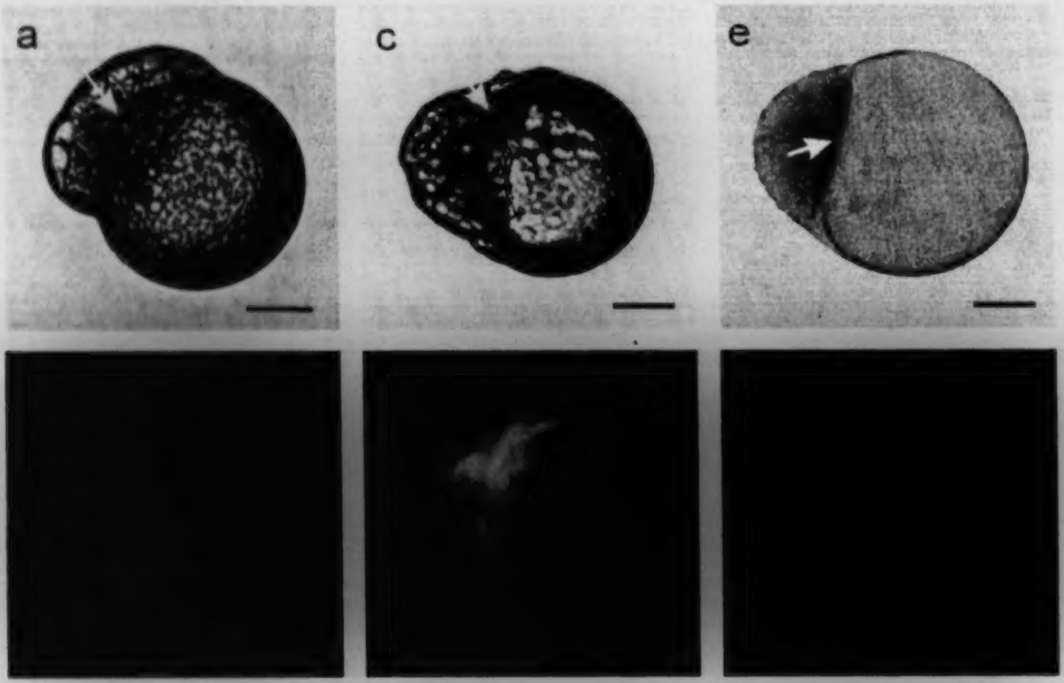

Figure 4.13: Brightfield and fluorescence images of (a,b) 32-, (c,d) 256- and (e,f) 512/1K-cell stage dechorionated embryos 30 min following laser pulse manipulation. The embryos in (a,b), (c,d) and (e,f) were laser pulse targeted at the 8-, 64- and 128-cell stage, respectively. Arrows in (a,c,e) depict the location where transient pores were formed in the original porated embryos. Delivery of exogenous FITC was clearly observable in the blastomere cells of (b), (d) and (f), where the introduction of the fluorescent molecule was found to be independent of the chosen developmental stage. Concentration of FITC in solution ranged from 0.02 to 0.03 mg/mL. All embryos were laser pulse porated with a pulse energy of 2.7 nJ/pulse and a gated shutter time between 200 to 300 ms. Scale bars represent 200 μm.

The effect of blastomere patterning on fluorescence distribution

The pattern of FITC fluorescence seen in Figures 4.13(d,f) was less uniform than that observed in Figure 4.13(b). This result was likely attributable to the patterning of the blastomere cells as the embryo aged. For instance, at 8-cell stage, all blastomere cells are located at the edge of the blastodisc and are considered marginal cells (all of the cells were bridged to the yolk [127]). Increased cleavage divisions, however, produce more central non-marginal cells, Figures 4.14 and 4.15, that are not connected to the yolk cell. As more non-marginal cells form, these cells begin to lose blastomere-blastomere bridges to the more marginal cells [82, 127], yet gap junctions between the cells likely still exist [127]. Therefore, the number of blastomeres participating in the uptake of the fluorescent probe via cytoplasmic bridges to the yolk remains fairly constant. Cell divisions increase the complexity of blastomere patterning as the embryo ages. At the 64-cell stage, blastomere cells begin to cover other cells located at a lower plane within the blastodisc [90]. As a result, the distribution of FITC would be different for Figures 4.13(b) and 4.13(d,f), which were laser pulse manipulated at the 8-, 64- and 128-cell stage respectively.

Loading efficiency of FITC into dechorionated embryos

To determine whether pore formation and exogenous FITC delivery was a reproducible process, an analysis of the FITC loading efficiency was performed, Table 4.1. Loading efficiency was defined as the percentage of embryos positive for blastomere FITC fluorescence. Based on 39 laser-porated embryos at developmental

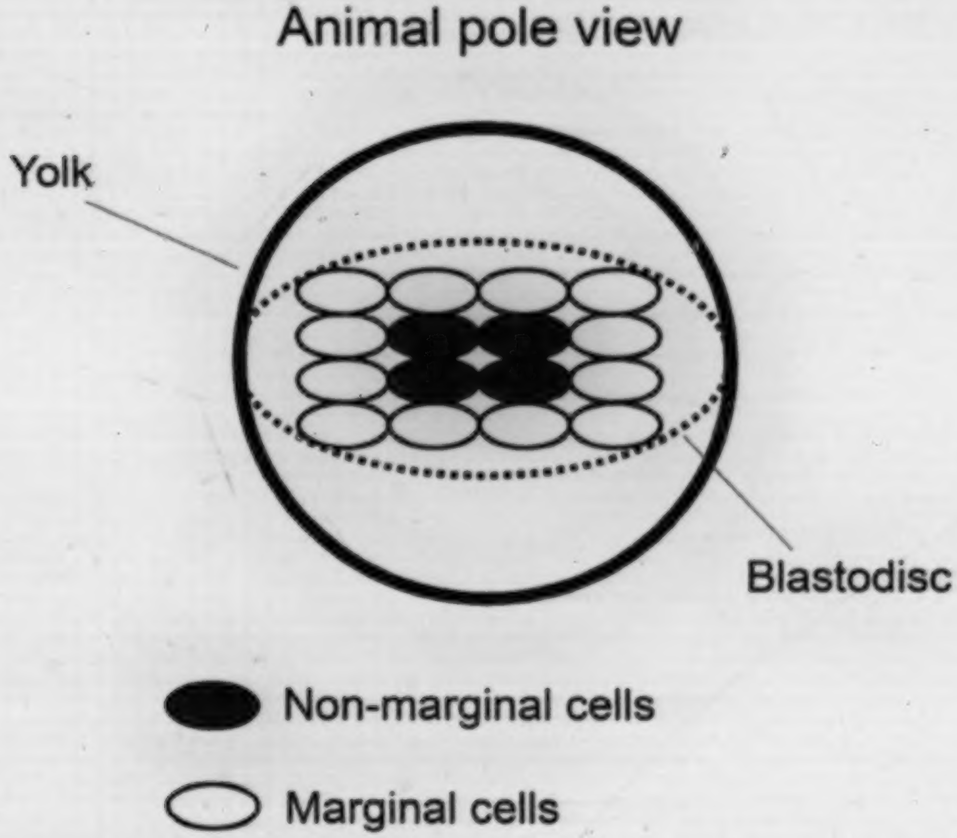
Animal pole view
Yolk
Blastodisc
Non-marginal cells
Marginal cells

Figure 4.14: An animal polar view of a 16-cell stage zebrafish embryo. The yolk, the blastodisc and the marginal and non-marginal blastomeres are indicated. The internalized blastomeres are the non-marginal cells that will form the epiblast and hypoblast in later development [90]. The figure was adapted from [90, 128].

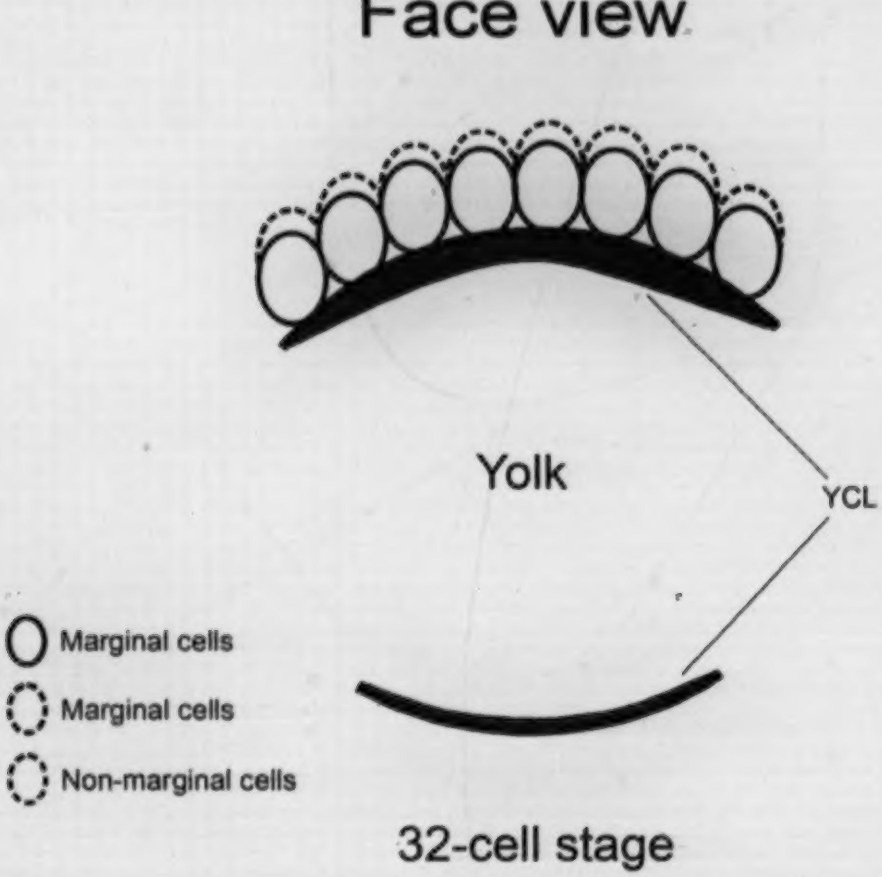

Figure 4.15: Face view of a 32-cell stage embryo. Locations identified include the yolk, the YCL and the marginal and non-marginal cells. The YCL is the non-yolky cytoplasmic layer adjacent to the yolk. For embryos laser pulse manipulated at the blastomere-yolk interface, it was likely that the fluorescent probe was delivered into the YCL interface; marginal cells bridged to the yolk captured the localized dye and transported it to the non-marginal cells. The YCL surrounds the entire yolk, but is much thinner at the vegetal pole in comparison to the animal pole. Note that only two tiers of 8 blastomeres are shown in the above figure. Rotation of the embryo about an axis perpendicular to the animal-vegetal axis would reveal two addition 2x8 tiers of blastomere cells. The figure was adapted from [127].

Table 4.1: Survival and loading assessment

	N	Cell stage	FITC loading (%)
Dechorionated[1]	39	2-cell to 128-cell	87
Chorionated[1]	27	2-cell to 128-cell	78
Control (dechorionated)[2]	20	2-cell to 128-cell	0
			Survival (%)
Dechorionated[3]	23	2-cell to 8/16-cell	89
Chorionated[3]	26	2-cell to 8/16-cell	100
Control (chorionated)[4]	20	2-cell to 8/16-cell	90

[1] Embryos were porated in the presence of exogenous FITC.

[2] Embryos were suspended in FITC. These embryos were not laser porated. Embryos were dechorionated to prevent perivitelline-FITC from obscuring blastomere-FITC fluorescence.

[3] Embryos were laser porated in tank water only

[4] Embryos were not laser porated. Embryos were only exposed to tank water.

stages ranging from 2-cell to 128-cell stage, 87 % of the embryos were found to be positive for FITC fluorescence. The impermeability of FITC to the blastomere cells in the absence of pore formation was also verified. When control dechorionated embryos (n = 20 embryos) (2-cell to 128-cell stage) were incubated in FITC (0.02 to 0.03 mg/ml) none of the embryos were positive for blastomere FITC fluorescence, Table 4.1.

Hypothesized mechanism of FITC uptake

As evidenced in Figure 4.13, localizing femtosecond laser pulses to the blastomere-yolk interface resulted in the formation of pores and the uptake of FITC into the blastomere cells. Figures 4.13(b,d,f) show blastomere-fluorescence in each of the targeted embryos, indicating that poration and delivery were independent of the chosen embryonic stage. While the delivery of FITC was localized to the blastomere-yolk interface, the fluorescent probe was found to spread among the dividing blastomeres, as seen in Figures 4.13(b,d,f). It was hypothesized that in early developmental stages (from 2-cell stage until 16-cell stage) the dye would be captured by the blastomere cells through cytoplasmic bridging with the yolk cell. At later developmental stages, the marginal cells remain connected to the yolk cell, but the more internally located (or non-marginal) cells lose cytoplasmic connections to the yolk cell and become completely cleaved from adjacent cells [127]. Figure 4.14 is an animal pole view of a 16-cell stage embryo showing the marginal and non-marginal cells. The entire 4x4 row of cells is termed the blastodisc [90], with vertical and horizontal cleavages planes dividing the individual cells. The blastomere cells on the edge of the blastodisc are termed the marginal cells and remain bridged to the yolk cell, while the more centrally located non-marginal cells are completely cleaved from the yolk and surrounding cells[1]. When individual blastomere cells are completely cleaved from each other, gap junctions[2] still exist between the cells. The existence of gap junctions, ~ 1 kDa in size [29], was verified by Kimmel *et al.* [127] by injecting low molecular weight Lucifer yellow dye (457 Da) into non-marginal cells. The dye was found to spread among adjacent blastomere cells [127]. From Figures 4.13, 4.14 and 4.15 it was conjectured that the likely pathway followed by the introduced fluorescent probe was: (i) FITC was delivered into the non-yolky cytoplasmic layer (blastomere-yolk interface), Figure 4.15, (ii) irrespective of the embryonic developmental stage the probe was captured by the marginal cells (Figures 4.13, 4.14 and 4.15) that were bridged to the yolk, (iii) FITC was then transported to adjacent cells via blastomere bridges in cells of developmental stages up to mid cleavage (16-cell stage) or via gap junctions for embryos beyond 16-cell stage and (iv) as the embryo developed, cells with intracellular FITC transfered the dye to daughter cells through cell division.

The chorion: a non-cellular embryonic barrier

When zebrafish eggs are laid by the females and fertilized by males, a non-cellular barrier termed the chorion inflates and surrounds the developing embryo. The embryo continues to divide and grow within the chorion, until the embryo hatches at a developmental time ranging from 48 to 96 hpf [81]. The chorion that surrounds the embryo acts as a selectively permeable barrier for the transport of materials, as well as a physical membrane protecting the embryo from its environment [129]. Embedded in the chorion are pores, termed chorion pore canals, that vary in diameter from 500 to 700 nm [129]. These corkscrew shaped pores have an outer diameter larger than the inner diameter (the inner side is the side facing the perivitelline space, Figure 4.2), as observed under field emission scanning electron microscopy [129]. The spacing between each of the pores, as observed by Rawson *et al.* [129] was between 1.5 and 2 µm. Covering the outer surface of the chorion was an uneven granular layer (not to be confused with the yolk granules) that acted to plug the chorion pores[1] [81, 129]. Figure 4.2 shows a labeled image of a 4-cell stage embryo growing within its chorion, locating the position of the chorion, the perivitelline space, the blastomere cells and the yolk cell.

---

[1] It is interesting to note that the marginal cells are not always connected to the yolk cell. At mid blastula (512-cell stage) the marginal cells collapse into the non-yolky region of the YCL (the YCL is adjacent to the yolk cell; see Figure 4.15) forming the yolk syncytial layer [104].

[2] Gap junctions are channels providing cytoplasmic connections between cells [29, 51].

Transient pore formation at the blastomere-yolk interface in chorionated embryos

Following the demonstration that transient pores could be formed at the blastomere-yolk interface of dechorionated embryos for FITC upake, Figure 4.13, the creation of transient pores at the same interface in chorionated embryos was also assessed. Figure 4.16 depicts the method used to focus femtosecond laser pulses (2.7 nJ/pulse, 200 to 300 ms gated shutter time) onto chorionated embryos for transient pore formation. The laser pulses were focused beyond the structure of the chorion and localized to a region on or near the blastomere-yolk interface. With this focusing method, the chorion remained undamaged.

When mid cleavage to early blastula stage (8-cell to 128-cell stage) chorionated zebrafish embryos were suspended in FITC (0.02 to 0.03 mg/ml), the fluorescent probe

---

[1] It is interesting to note that Rawson *et al.* [129] measured a chorion thickness ranging from 1.5 to 2.5 µm while Laale *et al.* [81] mentions a thickness of 10 µm. While the disparity between these values is unknown, the quoted value by Laale *et al.* [81] may have considered the thickness of the granular layer in addition to the thickness of the chorion.

Figure 4.16: Method used for targeting the blastomere-yolk interface in chorionated zebrafish embryos. Femtosecond laser pulses were focused beyond the structure of the chorion and localized to the region of interest (at the blastomere-yolk interface). With this targeting method, the chorion layer was undamaged. Pore formation and delivery occurred only at the laser focus by the non-linear mechanism described in Chapter 1. The embryo in the above figure is at the 4-cell stage. This image appeared on the cover of Biotechnology and Bioengineering, 98(6), December 2007.

was found to diffuse through the chorion pores into the pervitelline space (FITC was verified to be impermeable to the blastomere cells, see Table 4.1). With FITC localized in the pervitelline region, femtosecond laser pulses were focused in the manner shown in Figure 4.16 to introduce pervitelline FITC into the blastomere cells. Figure 4.17 shows laser pulse manipulated chorionated embryos (n = 27 embryos) at varying developmental stages 30 min post-laser targeting. The embryos in Figures 4.17(a,b,c), 4.17(d,e,f) and 4.17(g,h,i) were laser pulse treated at 8-cell, 128-cell and 32/64-cell stage and have developed to 32-cell, 512/1K-cell and 128/256-cell stage, respectively. Perivitelline FITC is readily observed in Figures 4.17(a,d,g), with the strong fluorescence signal obscuring the developing embryo. To observe the uptake of blastomere-FITC, the embryos were dechorionated, Figures 4.17(b,e,h), to remove the interfering fluorescence signal originating from the perivitelline space. Epi-fluorescence images of the dechorionated embryos, Figures 4.17(c,f,i), revealed that transient pores were created near the blastomere-yolk interface, resulting in the delivery of pervitelline FITC[1]. The mode of FITC transport into the cells was expected to occur through the same mechanism previously described.

The arrows in Figures 4.17(c,f,i) represent the locations where transient pores were formed in the chorionated embryos. Pore formation and delivery into chorionated embryos, as shown in Figure 4.17, was a reproducible result, as evidenced by a high FITC loading efficiency of 78 %, Table 4.1. This result indicated that the presence of the chorion did not hinder successful pore formation near or at the blastomere-yolk interface. Transient pore formation at the interface occured without damage induced to the chorion,

---

[1] The nuclei of the blastomere cells are faintly visible.

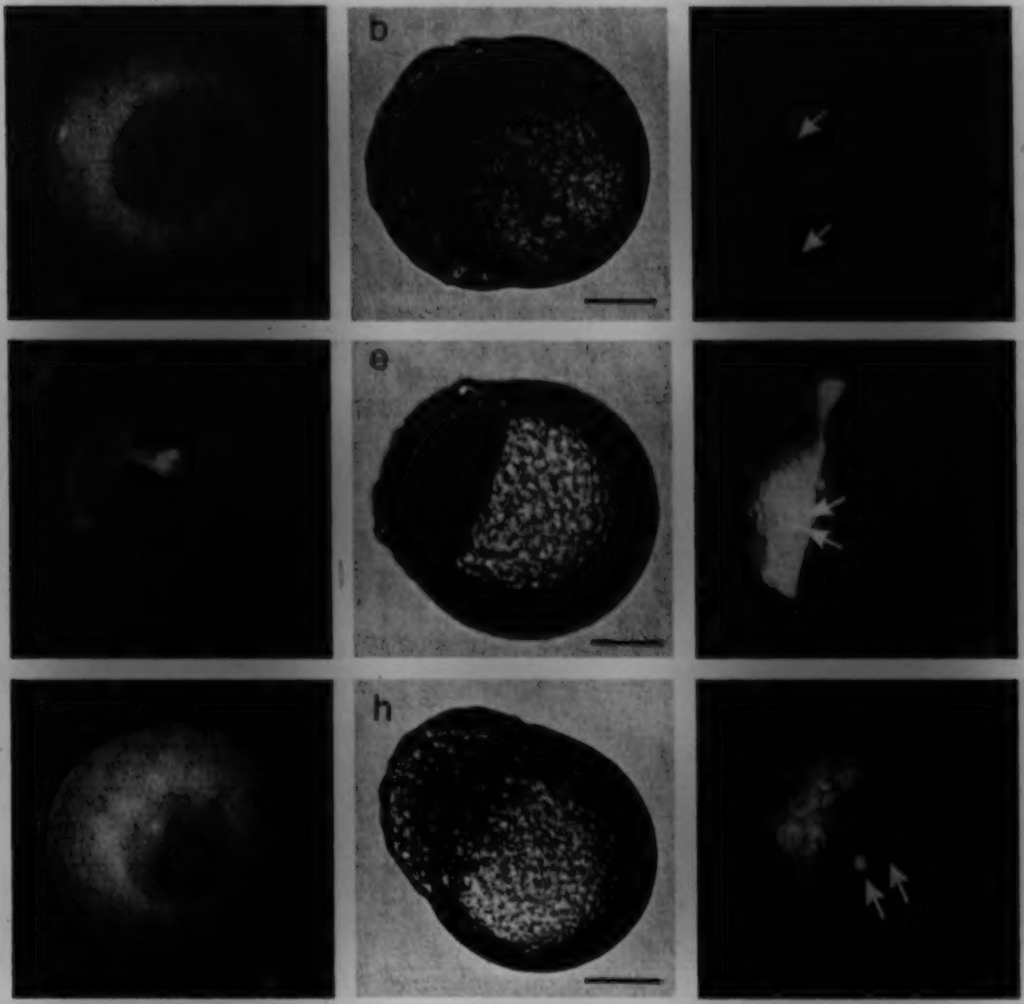

Figure 4.17: Fluorescence and brightfield images of (a,b,c) 32-cell, (d,e,f) 512/1K-cell and (g,h,i) 128/256-cell stage embryos 30 min post-laser pulse poration. The embryos were laser pulse manipulated at the 8-cell stage for (a,b,c), the 128-cell stage for (d,e,f) and the 32/64-cell stage for (g,h,i). Embryos were dechorionated to observe the pervitelline FITC delivered into the blastomere cells. As evidenced in (b,e,h), none of the embryos were compromised post-dechorionation. The uptake of pervitelline FITC via laser pulse induced transient pores was evident in (c,f,i), with the arrows indicating the exact locations were permeabilization occurred in the previously chorionated embryos. Individual nuclei of the blastomere cells in (i) were clearly visible. Concentration of FITC used in this study was 0.02 to 0.03 mg/ml. Laser parameters used for poration were 2.7 nJ/pulse with a gated shutter time rangimg from 200 to 300 ms. Scale bars represent 200 μm.

Figures 4.17(a,d,g), with the membrane visibly inflated around the embryo without deformation. This is in contrast to the formation of invasive boring holes in chorionated embryos during microinjection. Since the chorion is a non-cellular membrane, large holes in its structure cannot be repaired.

Interestingly, the ability to focus femtosecond laser pulses beyond the structure of the chorion, as illustrated in Figure 4.16, makes targeting cellular sites within the embryo possible. If the embryos are reared to later developmental stages, developing organs can be selectively laser pulse targeted without affecting adjacent cellular tissues. For example, in zebrafish larvae, the notochord[1] could be severed using focused femtosecond laser pulses to identify behavioral changes in the fish. The severing of the notochord would be achieved without inducing damage to epithelial cell layers and muscle cells surrounding the notochord. Performing the same study using electroporation or microinjection would result in damage not only to the notochord, but also to surrounding tissues.

Direct injection of FITC into developing blastomere cells

In Figures 4.11, 4.13, 4.16 and 4.17, femtosecond laser pulses were focused to a location on the embryo near or at the blastomere-yolk interface. The goal was to address whether this interface represented a unique laser pulse induced pore forming region or whether successful pore formation could be induced directly in individual blastomere cells. Using a pulse energy ranging from 0.5 to 0.6 nJ/pulse, with a gated shutter time of 200 to 500 ms, individual dechorionated embryos were suspended in FITC

---

[1] The notochord is a rod-like supportive structure that develops along the midline of the zebrafish body [90].

(0.02 to 0.03 mg/ml) and laser pulse targeted on the blastomere cells for introducing the reporter molecule. Figure 4.18 depicts a mid cleavage stage (16-cell stage) dechorionated embryo that was laser pulse porated in 3 to 4 locations per cell, with a maximum of four laser pulse treated blastomeres per embryo. Epi-fluorescence imaging of the embryo immediately following poration revealed the successful creation of transient pores with the introduced FITC probe distributed among all dividing blastomere cells. This result indicated that the blastomere-yolk interface was not a unique location for transient pore formation. Interestingly, it was found that when exogenous material was introduced into the blastomere-yolk interface, a lower blastomere-fluorescence signal was observed versus introduction into the cytoplasm of the blastomere cells. This disparity likely arose from both the diffusion of the introduced FITC molecules into the YCL and the impermeability of the yolk globules to the dye. Both factors would hinder the probe's diffusion and accumulation in the blastomere cells.

Differences in FITC signal intensity for blastomere-yolk and blastomere injection

Comparing the FITC signal intensity of embryos laser pulse manipulated at either the blastomere-yolk interface or the blastomere cells, the latter were found to have a higher blastomere-FITC signal intensity. It was hypothesized that the lower fluorescence intensity for blastomere-yolk injection was likely due to the impermeability of the yolk platelets to FITC. As a result, the yolk inhibits uptake of FITC by the marginal cells, hindering diffusion. Laser injection of the probe further away from the interface, towards the vegetal pole (i.e. deeper within the yolk cell), would further complicate FITC diffusion due to an increased amount of yolk for the FITC to travel through.

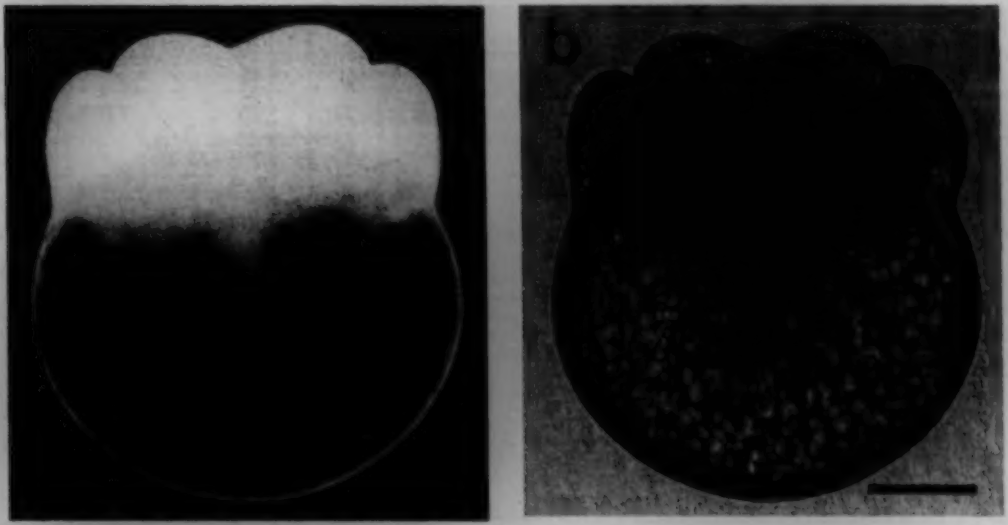

Figure 4.18: Fluorescence and brightfield image of a (a,b) 16-cell stage dechorionated embryo imaged immediately after laser pulse poration. Laser pulses were localized onto the individual blastomere cells, with three to four transient pores created in each of four blastomere cells. Concentration of FITC used in this study was 0.02 to 0.03 mg/ml. The laser pulse energy for poration ranged from 0.5 to 0.6 nJ/pulse with a gated shutter time between 200 and 500 ms. Scale bars represent 200 μm.

This hypothesis was supported by work investigating the introduction of FITC into the yolk cell (unpublished work). It was found that independent of the chosen injection site, the dye could not be delivered into the yolk. Whether the fluorescent probe was unable to diffuse through the laser pulse induced pore or was prevented by the outward pressure of the yolk granules was unknown. Possibly, both the impermeability of the yolk to the dye and the outward pressure prevented the successful uptake of FITC[1]. Interestingly, Kimmel *et al*. [127] also observed the impermeability of the yolk platelets to dye. The diffusion of microinjected fluorescein-dextran was limited in the yolk cell owing to the yolk platelets. Therefore, the observed decrease in fluorescence intensity (in this study) for embryos porated at the blastomere-yolk interface was expected.

Chorionated embryos were laser pulse targeted at the blastomere-yolk interface, Figures 4.17(c,f,i), with the arrows indicating the positions where laser poration occurred. From the figures, it can be noted that poration was not perfectly localized to the blastomere-yolk interface. As shown in Figures 4.17(c) and 4.17(i), the transient pores were often formed further into the yolk rather than directly at the interface[2]. Generally, under 60X magnification, the flat region of the interface could be easily observed; however, the defined boundary of the blastomere-yolk interface was difficult to discern (this was further complicated by the fact that the interface would appear slightly different in each embryo). While an increased amount of yolk surrounding the introduced dye would hinder FITC diffusion, blastomere fluorescence was still observed. Another potential factor that could have lead to a lower blastomere-fluorescence signal for blastomere-yolk injected embryos was the loss of dye in the YCL. Laser injection of FITC into or near the blastomere-yolk interface localized the dye to the YCL. Since marginal cells were bridged to the yolk, the dye was likely captured from the YCL and transported to adjacent blastomeres [90, 127]. However, some of the dye may have diffused along the YCL which surrounds the entire yolk, extending from the animal pole to the vegetal pole [128], Figure 4.15.

---

[1] While it was a possibility that laser pulse induced pores were not properly formed in the yolk cell, this hypothesis was disproven. At large pulse energies, ~ 6 nJ/pulse, the yolk was successfully porated, with the observance of yolk globules being shed from the yolk cell (unpublished data). The release of yolk globules indicated that laser poration exposed the yolk intracellular space to the extracellular environment.

[2] It is interesting to point out that the ability to identify the exact location of poration was likely a result of FITC's amino reactivity (Sigma-Aldrich, St. Louis, MO). During poration, while majority of the dye diffused into the cell, some of the molecules would be bound to proteins at the permeabilized interface. This binding provided visual cues to identify the spatial location and frequency of the pores. In the fluorescence images of Figure 4.13, no poration indicators could be observed. The lack of these identifiers was a result of imaging the embryo on the opposite face.

Evidence of dye loss along the YCL was observed in Figures 4.13(d,f) and 4.17(f,i) with fluorescence seen on the side and bottom layer surrounding the yolk. Interestingly, embryos that were porated in the blastomere cells also showed fluorescence in the YCL, Figures 4.18(a)[1]. This might be attributable to the back transfer of dye from the marginal cells to the underlying YCL. In fact Kimmel *et al.* [127] found that when fluorescein-dextran was injected into a marginal cell at the 32-cell stage, the dye was found to leak into the YCL and was taken up by the more distant marginal cells. This likely also occurred in Figures 4.18(a)[2], with the marginal cells leaking the dye to YCL. In Figure 4.18(a)[3] all of the blastomere cells were bridged to the yolk cell, participating in the transfer of dye to the YCL. (In Figure 4.18(a) the cell was nearing 16-cell stage with the four most central cells starting to lose their cytoplasmic connections to the yolk [90, 127].) It was also expected that the amount of fluorescence found in the YCL would also depend on the developmental stage. When fertilization occurs, a cytoplasmic stream develops, forming the blastomere cells. This rapid streaming reduces the fraction of the cytoplasm surrounding the yolk, thinning out the YCL [128]. Why some embryos show YCL fluorescence and others do not is not known.

---

[1] In studies involving quantum dots as the exogenous molecule (discussed later), quantum dot fluorescence was also observed in the YCL (see Figure 4.20(a)).

[2] Also true for Figure 4.20(a).

[3] Also for Figure 4.20(a).

The reactivity of FITC

Throughout Figures 4.13, 4.17 and 4.18 FITC was used as the reporter molecule to verify laser pulse peremabilization and exogenous delivery. However, FITC is known to be an amine reactive dye (Sigma-Aldrich, St. Louis, MO). Since no proteins were added to the tank water, no unfavorable reactions between FITC and the solution or the embryonic membrane (in the absence of laser poration) were expected. If FITC was found to bind to the embryo surface, epi-fluorescence would have revealed the entire embryo fluorescing. Considering the non-uniform blastomere-FITC fluorescence observed in Figures 4.13(b,d,f), Figures 4.17(c,f,i) and the well spaced poration indicators (arrows in Figures 4.17(c,f,i)), it can be noted that no undesired FITC reactivity was detected. Nevertheless, to confirm that the observed blastomere-fluorescence originated from pore formation and exogenous delivery, each embryo was inspected under 4X, 10X and 60X magnification to verify the existence of intracellular blastomere-fluorescence.

Delivery of exogenous quantum dots into developing blastomere cells

In addition to the delivery of FITC into the blastomere cells of dechorionated and chorionated zebrafish embryos, the introduction of other exogenous foreign molecules was examined. In this study, Streptavidin-conjugated quantum dots, composed of a semiconductor material, were used. The structure of the quantum dot is shown in

Figure 4.19. The core of the quantum dot is made from cadmium selenide (CdSe) and the shell is zinc sulfide (ZnS). The entire quantum dot is capped with a polymer and conjugated to the biomolecule streptavidin[1], resulting in a quantum dot ranging from 15 to 20 nm in diameter (Cedarlane Labs, ON, Canada).

Quantum dots have multiple applications in cell biology. As mentioned in section 4.1, these fluorescent probes can be used in developmental biology as cell tracing molecules. Provided that the quantum dots do not pass through cell-cell junctions (i.e. gap junctions), the probes will remain in the cell and are transferred to adjacent cells through cell division. Quantum dots introduced into a few blastomere cells of the late cleavage period (32/64-cell stage), for example, could be used to determine cell lineage tracing in order to identify the fate maps of individual cells.

To deliver the fluorescent probe, early cleavage stage (2-cell stage) dechorionated embryos (n = 10 embryos) were suspended in a 0.4 μM solution of Streptavidin-conjugated quantum dots. Femtosecond laser pulses, with a pulse energy ranging from 1.5 to 1.9 nJ/pulse and a gated shutter time between 200 and 500 ms, were localized on the blastomere cells. A maximum of two blastomere cells were laser pulse treated, with the creation of three to four transient pores per cell (at different locations on the blastomere cell). As shown in Figure 4.20(a), conjugated quantum dots were introduced into the dividing cells, with quantum dot fluorescence subsequently found within each of the two blastomere cells. Rearing the embryo to just after germ-ring stage (~ 6 hr of development at a temperature of 28.5 °C [90]), Figure 4.20(b), the quantum dot

---

[1] Streptavidin is a protein that is found in the bacterium *Streptomyces avidinii* and strongly binds to biotin.

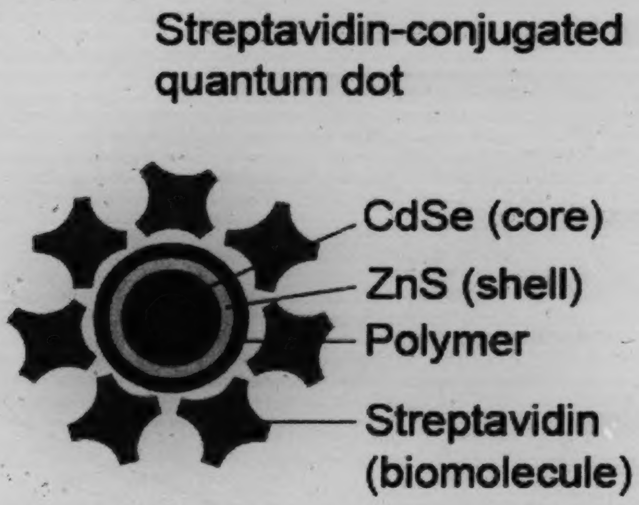
Streptavidin-conjugated quantum dot
CdSe (core)
ZnS (shell)
Polymer
Streptavidin (biomolecule)

Figure 4.19: A Steptavidin-conjugated quantum dot. The core is composed of cadmium selenide, surrounded by a zinc sulfide shell. The outer layer is a polymer, which is conjugated to streptavidin. The diameter of the quantum dot is between 15 and 20 nm (Cedarlane Labs, ON, Canada). Figure was adapted from Invitrogen, US.

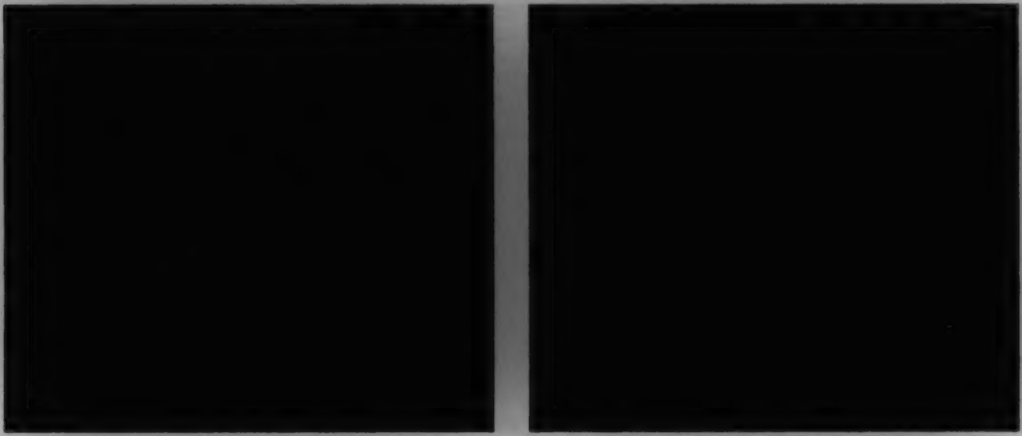

Figure 4.20: (a) An early 2-cell stage dechorionated embryo that was laser pulse porated for introducing Streptavidin-conjugated quantum dots. The uptake of quantum dots in (a) is evidenced by the fluorescence localized in the dividing blastomere cells. The embryo in (a) was reared to just after germ-ring stage, (b), showing that quantum dot fluorescence was still observable during this developmental period. Each of the two blastomere cells were laser pulse porated three to four times per cell. The laser pulse energy used for poration was 1.5 and 1.9 nJ/pulse with a gated shutter time ranging from 200 to 500 ms. Concentration of the quantum dot solution was 0.4 μM. Scale bars represent 200 μm.

fluorescence was still observed throughout the developing cells[1]. Early introduction of the quantum dots when the blastomere cells were syncytium with the yolk cells was required for the nearly uniform distribution of this reporter molecule in later developmental stages. For instance, as the embryo aged, the more central blastomere cells (i.e. non-marginal cells [90, 127]; see Figures 4.14 and 4.15) lost cytoplasmic connections to the yolk cell, where both marginal (see Figures 4.14 and 4.15) and non-marginal cells were bridged by gap junctions[2] [127]. Since the size of the conjugated quantum dots, ~ 15 to 20 nm (Cedarlane Labs, ON, Canada) restricted their diffusion through gap junctions [130], their overall distribution was limited to transfer through cell division. Restriction of the fluorescent probe's mode of cell-to-cell movement to cell division only makes the Streptavidin-conjugated quantum dot an ideal probe for studying cell lineage tracing in the zebrafish.

Delivery of exogenous plasmid DNA into developing blastomere cells

In developmental biology, the need to differentially label developing cellular structures has become increasingly important. To differentiate specific developing cells from a cluster of cells, DNA is often used as the fluorescent reporter construct [56, 110-112, 131-135], with microinjection being the prevalent method for introducing the DNA marker [56, 110-112, 131-135]. Here, it was addressed whether the application of femtosecond laser pulses could be used as an alternative method for introducing plasmid DNA into developing zebrafish embryos.

---

[1] No loading efficiency studies were performed using quantum dots.

[2] Gap junction size is ~ 1 kDa [29].

In the studies mentioned above, both FITC and quantum dots were successfully introduced into the dividing blastomere cells via femotsecond laser pulse poration. FITC and quantum dots are naturally fluorescing molecules (under UV excitation), and their fluorescence provides a visual indication of their location within the cell after cytoplasmic introduction by the laser pulse. In contrast, DNA encoding a reporter gene requires active transcription and translation before the fluorescence of the gene product can be observed. For this to occur, the introduced DNA must migrate into the nucleus of the cell to be transcribed, and the transcribed product is then translated outside of the nucleus in the cytoplasm. It is the translated product (i.e. protein) that is detected by fluorescence. As a result of the cell's requirement to actively produce the gene product, a delay in the production of fluorescence from the encoded gene occurs, and fluorescence is usually observed several hours[1] after its introduction, with maximum expression occuring at 24 hours.

The introduction of DNA can be used to produce transient or stable transgenic organisms, an essential process central to modern biology. Transgenic organisms are genetically modified for the purpose of creating a functional change in the model system that would not naturally be produced. For instance, to generate a resource bank of preserved fish embryos, DNA encoding a protein that protects the embryo against the cold could be introduced into the organism. If the DNA was integrated into the genome of the fish, exposure to the cold would elicit a production of the protective protein, allowing the embryo to survive in a low temperature environment. Therefore, the ability to non-invasively introduce DNA that encodes specific products would be invaluable for medical and biological research.

---

[1] In reality, the strength of the DNA promoter and how the organism responds to the introduced foreign DNA all determine when the construct will be expressed.

In this study, early to mid cleavage stage (2-cell to 8/16-cell stage) dechorionated embryos (n = 20 embryos) were suspended in a 170 µg/ml DNA solution composed of an upstream simian cytomegalovirus immediate early promoter (sCMV) fused with the downstream-enhanced green fluorescent protein (EGFP). The dechorionated embryos were laser pulse permeabilized directly in the blastomere cells with a pulse energy of 0.5 to 0.6 nJ/pulse and a gated shutter time ranging from 200 to 500 ms. Each cell was permeabilized a total of three times (at three different locations) with a maximum of 2, 2, 4 and 8 cells targeted per 2-, 4-, 8- and 16-cell embryo. Post-laser treatment, the embryos were incubated at 26 ± 1 °C and expression of the foreign DNA was checked at 24 hpf.

Figure 4.21 represents a brightfield and fluorescence image of a 24 hpf larva expressing the sCMV-EGFP construct. In Figure 4.21(a), EGFP expression was observed along the yolk sac extension, somites, notochord and floor plate. Figure 4.21(c) depicts the brightfield image of Figure 4.21(a), showing intact tissue and indicating that expression was not due to the autofluorescence known to accompany damaged cells. Expression was also observed in many tail cells and a few cells near the urinary duct (just above the yolk sac extension), Figure 4.21(b). As seen with the intact tissue in Figure 4.21(c), the fluorescence seen in Figure 4.21(b) was not due to autofluorescence from damaged cells, as evidenced by the brightfield image in Figure 4.21(d). These results confirm the introduction of the plasmid construct[1] via laser pulse induced transient

---

[1] A diagram of the sCMV-EGFP plasmid map is presented in Figure 4.22. From this map, it is noted that the origin of replication is from *E. coli* and not from the zebrafish. Therefore, *in vivo* amplification of the construct is not expected. Expression of the sCMV-EGFP construct in the zebrafish would depend on the number of plasmid copies introduced and how the organism treats foreign DNA.

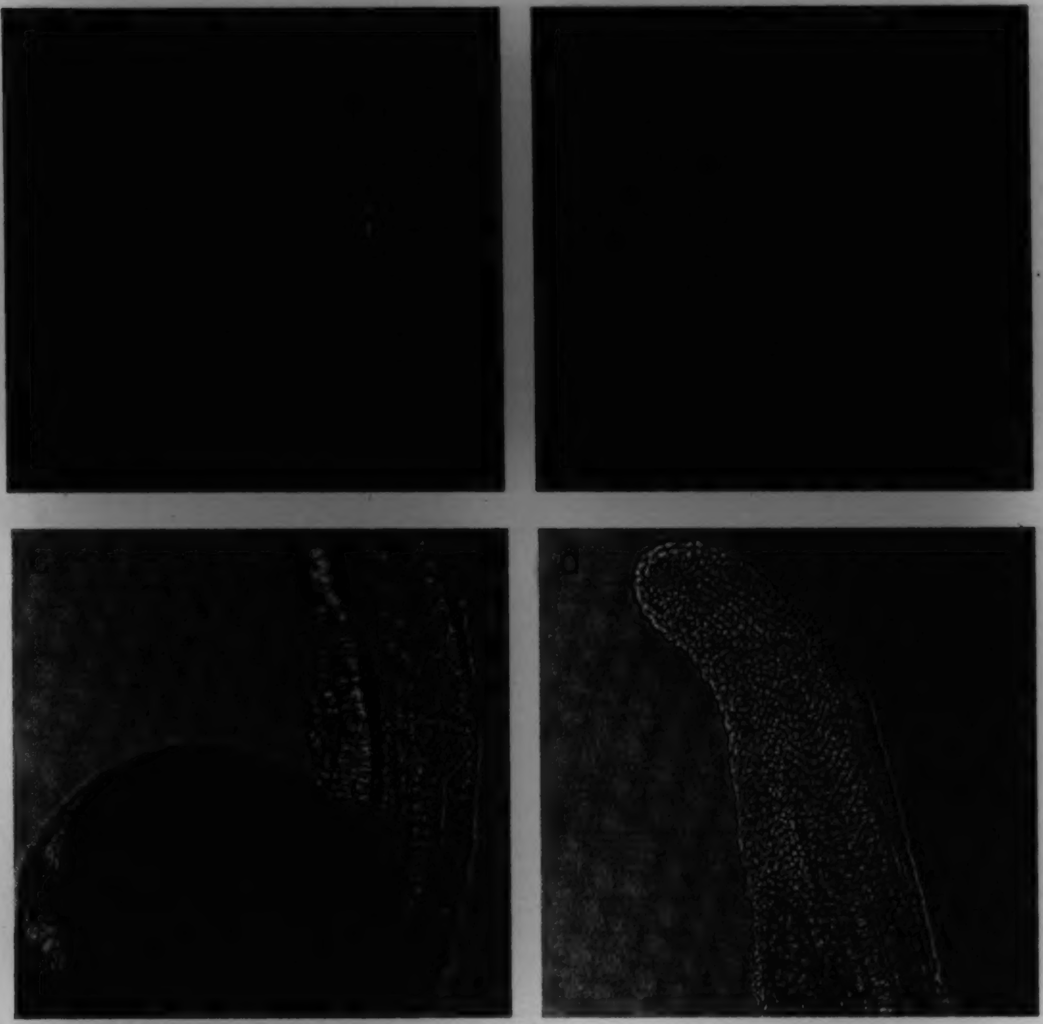

Figure 4.21: Fluorescence and brightfield images of 24 hpf zebrafish expressing the sCMV-EGFP plasmid construct. (a) Expression was observed along the yolk sac extension, somites, notochord and floor plate. (b) In addition, EGFP expression was observed near the urinary duct and in many of the zebrafish tail cells. (c,d) Brightfield images of the same larva in (a,b) showing intact zebrafish development, indicating that expression was not due to autofluorescence from damaged cellular material. The concentration of the plasmid construct used in this study was 170 μg/mL. The developed embryos in (a,b,c,d) were laser pulse porated with a pulse energy ranging from 0.5 to 0.6 nJ/pulse and a gated shutter time between 200 and 500 ms. A total of three to four transient pores were made in each of 2, 2, 4 and 8 cells per 2-, 4-, 8- and 16-cell stage embryos.

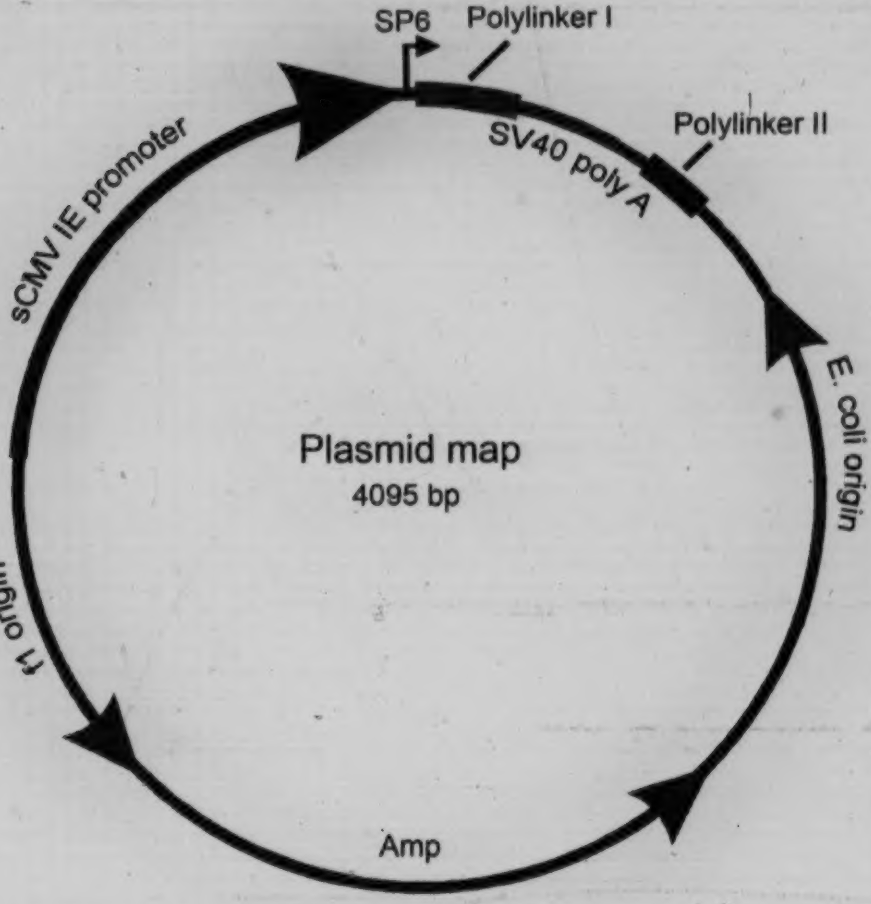
SP6
Polylinker I
Polylinker II
SV40 poly A
sCMV IE promoter
E. coli origin
Plasmid map
4095 bp
f1 origin
Amp

Figure 4.22: The sCMV-EGFP plasmid map. The EGFP gene was inserted into the Polylinker I site. Plasmid replication occurred in *E. coli*. The original plasmid map was provided by Patricia Gongal of Dr. Waskiewicz lab.

pores and the survivability of laser pulse manipulated embryos reared to 24 hpf. The pattern of plasmid expression observed in Figure 4.21 does not correlate to the properties of the plasmid construct. sCMV-EGFP does not differentially tag specific cells in the zebrafish, rather, expression is ubiquitous. However, generally it was not expected that the entire zebrafish would be expressing EGFP, since many factors, including the strength of the plasmid promoter, the number of DNA molecules entering the nucleus for transcription and eventual translation to EGFP, the response of the zebrafish to foreign DNA (i.e. degradation or perhaps silencing) and, potentially, genomic methylation could affect the level of expression [136, 137]. Expression in only 1 % of the cells is not unexpected [138].

Femtosecond laser pulse excitation of the exogenous solution

In Figures 4.20 and 4.21, introduced quantum dots and plasmid DNA were shown in the dividing blastomere cells. This result showed that exogenous material delivery via laser pulse induced poration was successful and independent of the chosen molecule. Smaller sized molecules[1] would naturally migrate along the length of the pore more easily than larger structures. Despite the fact that the quantum dots used in Figure 4.20 were 8 to 10 times larger in diameter than FITC, both molecules were still introduced into the blastomere cells. It is important to mention that since blastomere-fluorescence from FITC, quantum dots or DNA was observed in the dividing cells, the laser intensity at the focus did not damage the FITC fluorophore, the conjugated quantum dot or the DNA molecule. Therefore, no adverse effects of the focused femtosecond laser pulse on the exogenous solution could be detected.

---

[1] Compare FITC with a long axis diameter of 1.85 nm (diameter calculated in a manner similar to that done for sucrose in Appendix B) to Streptavidin-conjugated quantum dots ~ 15 to 20 nm (Cedarlane Laboratories Ltd., Burlington, ON, Canada).

Transfection rates

DNA transfection rates were not measured for the study shown in Figure 4.21, nor was the expression efficiency compared to values obtained using microinjection. To accurately compare the two techniques, the injected construct and the model organism must be the same, the constructs must be injected at the same developmental stage and the plasmid copy number introduced into the cells must also be identical. In this study, the sCMV-EGFP construct was used to evaluate the laser pulse induced transfection and expression of the plasmid DNA. The promoter, sCMV is known to drive the overexpression of the gene of interest [137] (in this case EGFP), producing more transcriptional and translational products in the cell than plasmid constructs with weaker promoters. For instance, in unpublished results, the expression efficiency of microinjected sCMV-EGFP was compared to the CMV-BGP-EGFP plasmid[1]. With nearly identical promoters, the latter construct had the extra fusion product bone gla protein (BGP) [137]. Using identical plasmid preparation procedures (constructs prepared in Milli-Q water at a final concentration of 200 μg/ml and microinjected into chorionated 1 to 8-cell stage zebrafish embryos), very different expression efficiencies were observed. The percentage of 24 hpf embryos expressing the CMV-BGP-EGFP construct was 25 % versus greater than 70 % for the sCMV-EGFP plasmid (expression was categorized as weak to moderate using epi-fluorescence imaging). Differences in the expression level likely arose from the slightly different promoters employed in the construct as well the lengths of the plasmid (a full analysis of how the promoter strength and construct length might effect the expression is beyond the scope of this thesis). More experimentation is required to justify the above assumptions.

---

[1] Dr. L. Cancela at CCMAR, Center for Marine Sciences, University of Algarve, Faro, Portugal provided the plasmid construct.

As reported by Collas *et al*. [136], zebrafish embryos possess a methylation cycle that begins at 6 hpf. Methylation is a process by which the organism begins to add methyl groups to certain DNA bases (i.e. cytosine). The addition of these groups is a protective mechanism in bacteria and controls gene regulation in vertebrates and mammals, preventing DNA replication and cleavage[1] [139]. Collas *et al*. [136] showed that when methylated DNA was microinjected into zebrafish embryos, the DNA became quickly de-methylated within 2 hours following fertilization. In contrast, de-methylated DNA became re-methylated after 6 hours of development. This transient methylation/de-methylation cycle in zebrafish could also affect the level of plasmid expression. Since methyl groups prevent the steric interactions of enzymes with the DNA chain, transcription factors cannot bind to DNA to produce transcriptional products (in this study, EGFP). Therefore, depending on the stage of injection, the zebrafish might methylate the introduced DNA construct, resulting in a decrease in gene expression. A further complication that arises when comparing laser pulse induced transfection and microinjection is the number of plasmid copies introduced into the cell (ideally more DNA molecules increases the expression efficiency). Contrary to the volumetric kinetics performed in Chapter 3, determining the change in embryo volume pre- and post-permeabilization, as well as the pore kinetics, was not possible (discussed in the next section). As a result, the number of DNA molecules introduced into the developing blastomere cells by laser pulse poration was unknown. This is in contrast to microinjection where knowledge of the needle diameter and the concentration of DNA can lead to a fairly reasonable estimate of the DNA copy number.

---

[1] In DNA replication certain enzymes are required to bind to the double helix. With methyl groups present, methylated bases prevent the steric interactions of the enzymes with the DNA chain.

Femtosecond laser pulse poration

The extent to which fluorescent probes and DNA accumulated within the blastomere cells depended on the longevity of the laser pulse induced pore. Alternatively, increasing the number of transient pores per cell may increase the volume of the delivered exogenous molecule, since more delivery pathways are created. In Chapter 3, estimates of the pore duration were made by analyzing the volumetric kinetics of cells permeabilized in the presence of impermeable carbohydrates. Upon pore formation, the cells were found to swell, attaining a new hypertonic equilibrium volume. The same analysis of zebrafish embryos would be difficult owing to the embryo's low surface-to-volume ratio, low membrane permeabilities, the differing osmotic properties of the blastomderm and yolk and the large sizes of the yolk and cells [91, 101, 102, 106, 107]. Further complicating a volumetric response measurement is the relatively large osmotically inactive volume fraction of the embryo, which has been found to approach 80 % [101, 106]. Therefore, any dehydration response of the embryo in the presence of FITC, quantum dots or DNA would be unobservable due to the above aforementioned properties and the low concentration (micromoles) of the exogenous solutions used in this study[1]. As a result, laser pulse poration would not lead to an observable increase in embryo volume, which is a necessary requirement for a volumetric analysis. Despite these difficulties, the value of 200 ms found in Chapter 3 may represent a starting point for estimating the laser pulse induced pore dynamics in zebrafish embryonic cells. And while the model systems used in this study and Chapter 3 differed, it was conjectured that the bulk molecular structure would be substantially the same (i.e. phospholipid bilayers). However, further work is required to justify the above hypotheses.

Laser conditions for permeabilization

In the above studies, various laser pulse energies were used to introduce exogenous foreign materials into the developing zebrafish embryonic cells. To establish a more well-defined range of pulse energies for laser pulse induced poration, individual dechorionated embryos (n = 10 to 15 embryos) at the early to mid cleavage stage (2-cell to 8/16-cell stage) were laser pulse targeted at the blastomere-yolk interface using a wide range of laser pulse energies. The criteria used to determine the ideal laser parameters for transient pore formation were the size and decay time of the laser pulse generated cavitation bubble, and more importantly, the observance of positive maximum blastomere FITC fluorescence. Laser pulse energies and beam dwell times were varied from 0.3 nJ/pulse to 2.75 nJ/pulse and from 5 ms to 1 sec. All dechorionated embryos were laser pulse porated in the presence of a 0.02 to 0.03 mg/ml FITC-tank water solution. Based on epi-fluorescence imaging, transient pores could not be formed for pulse energies below 0.38 nJ/pulse. This result was independent of the chosen beam dwell time. However, at a slightly higher pulse energy of 0.56 nJ/pulse, poration and blastomere FITC fluorescence was observed for the entire beam dwell range. Larger cavitation bubbles, in excess of 10 µm, were found when beam dwell times longer than 500 ms were chosen. In contrast, between 200 and 500 ms, cavitation bubbles were relatively short-lived, decaying within a few seconds. Cavitation bubble sizes for this beam dwell time range were observed to be larger than 5 µm. For pulse energies in excess of 0.56 nJ/pulse, poration and FITC delivery were still observed; however, cavitation bubbles became quite large. Interestingly, longer beam dwell times resulted in lower observed blastomere fluorescence. This decrease in blastomere fluorescence was hypothesized to originate from the outward expansion of the cavitation bubble, which likely hindered the diffusion of the FITC probe through the transient pore[1]. Based on the previously stated criteria and the above results, a pulse energy ranging from 0.5 to 0.56 nJ/pulse and a beam dwell time between 200 and 500 ms were considered optimum parameters for permeabilization.

---

[1] Dehydration studies on zebrafish embryos have been performed [103]. However, to elicit a shrinking response, the extracellular osmolarity must be higher than the isotonic concentration of ~ 300 mOsm [103]. Interestingly, zebrafish embryos exposed to hypotonic solutions do not swell (this was also observed in this study), indicating that the embryos appear to be osmoconformers [103].

Survivability of femtosecond laser pulse manipulated zebrafish embryos

Having demonstrated an alternative method for introducing fluorescent reporter molecules and DNA into zebrafish embryonic cells, it was important to assess the short-term survival of the laser treated embryos. The manipulated embryos in Figures 4.11, 4.13 and 4.17, 4.20 and 4.21 were found to develop normally, when observed 30 and

---

[1] No analysis of the FITC signal intensity as a function of pulse energy and beam dwell time was performed.

60 min, and 6 and 24 hpf post-poration. To further refine the above results, individual chorionated (n = 26 embryos) and dechorionated (n = 23 embryos) embryos at the early to mid cleavage stage (2-cell to 8/16-cell stage) were laser pulse porated using a pulse energy of 2.7 nJ/pulse with a gated shutter time ranging from 200 to 500 ms in the absence of exogenous foreign material. A pulse energy of 2.7 nJ/pulse was chosen over the previously defined optimum pulse energy of 0.5 to 0.56 nJ/pulse to better reflect the laser parameters used in Figures 4.11, 4.13 and 4.17[1]. Based on the survival results using an energy of 2.7 nJ/pulse, it was assumed that a lower pulse energy would result in a higher (if not equal) embryo survival rates. In addition, the choice of assessing survival in the absence of exogenous foreign material was to eliminate external factors that may have influenced survival. For instance, the cytotoxicity induced by FITC, quantum dots or DNA may have affected the short-term morphological development of the embryo, resulting in skewed results.

For this study, chorionated and dechorionated embryos were laser pulse porated two to three times at the blastomere-yolk interface with a maximum of 2, 2, 4 and 8 cells targeted per 2-, 4-, 8- and 16-cell stage embryo respectively. Post-poration, all embryos were reared at 26 ± 1 °C until pec-fin stage (arbitrarily defined as the developmental endpoint for determining survival in this study). Control chorionated (n = 23 embryos) and dechorionated (n = 32 embryos) embryos were also reared to pec-fin stage at the same temperature, providing reference embryos to compare hatching rates and general developmental morphologies. Throughout embryonic development, no significant differences in the developmental morphologies or hatching rates of the laser pulse manipulated embryos were observed in comparison to the control embryos. Specifically, at pec-fin stage, the hatched laser pulse treated embryos looked developmentally similar to the controls, with straight bodies, and well-formed symmetric yolk sacs. Figure 4.23 depicts one of the laser pulse manipulated embryos reared to pec-fin stage. Developmental morphological structures that have been emphasized include the ear, the calcified otoliths, the eye, the beating heart, the yolk-sac and the pectoral fin. This image was extracted from live video of the developed hatched larva, which has been included in the supplementary CD (Additional File 1 – Chapter 4). Based on comparisons of hatching rates and developmental morphologies between laser pulse manipulated and control embryos, as well as standard Westerfield [126] images, survival percentages of 89 and 100 % were measured for dechorionated and chorionated embryos respectively, Table 4.1. These values, as well as Figure 4.23, indicated that the application of femtosecond laser pulses did not adversely affect short-term embryonic survival.

---

[1] 2.7 nJ/pulse was the highest pulse energy used in the aforementioned studies.

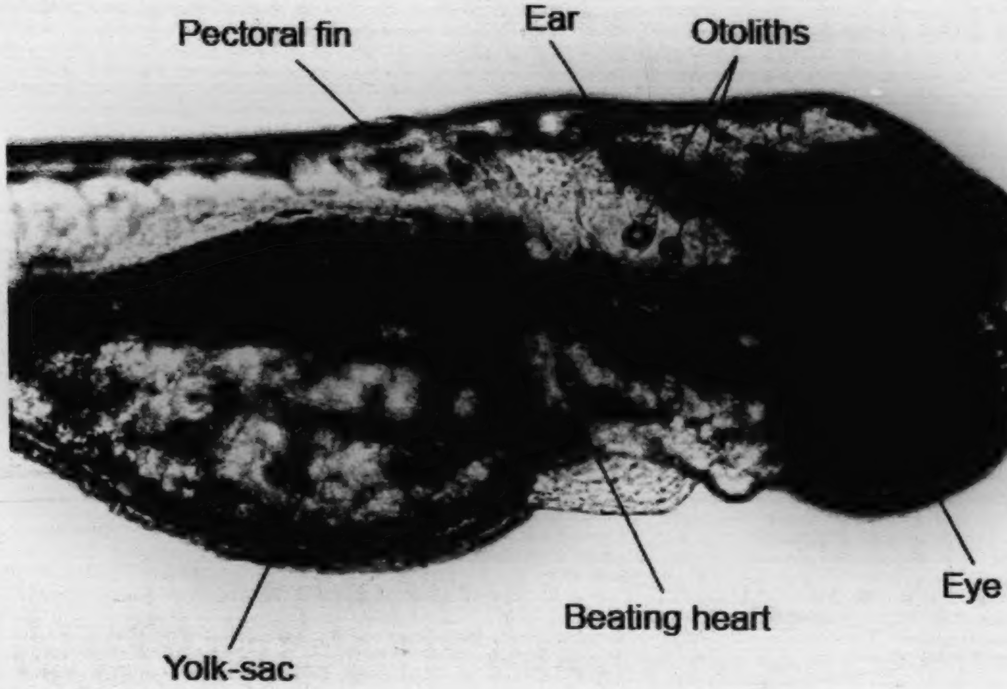

Figure 4.23: Image depicting a larva reared to pec-fin stage that was laser pulse manipulated between early to mid cleavage (2-cell to 8/16-cell stage) stage. Developmental morphological structures that have been indicated include the pectoral fin, the ear, the otoliths, the yolk-sac, the location of the beating heart and the eye. Laser parameters chosen for embryo manipulation were 2.7 nJ/pulse with a gated shutter time ranging from 200 to 500 ms.

CHAPTER 5

FEMTOSECOND LASER PULSE SURGERY AND DEVELOPMENT OF ZEBRAFISH EMBRYOS

5.1 Introduction

In Chapter 4, a novel method for the creation of laser pulse induced transient pores in developing zebrafish embryos was demonstrated. When focused femtosecond laser pulses were localized to the blastomere-yolk interface or on individual blastomere cells, a pathway was formed that allowed for the accumulation of an impermeable exogenous solution into embryonic cells. A short-term morphological study was presented, which revealed that the laser pulse manipulated embryos continued to develop normally, with cleavage divisions in early stage embryos occuring in nearly identical fashion to Westerfield images [126]. Despite the importance of this survival analysis study, the results could not be extrapolated to later developmental stages (i.e. past pec-fin stage). If the femtosecond laser is to be used by biomedical engineers, biophysicists and biologists, for an intended application, then it must be demonstrated that the tool is non-invasive to the development of the organism studied. For instance, how femtosecond laser pulses affect both the short- and long-term morphological development of the embryo is a question that has not been answered.

The technique used for assessing embryonic survival in Chapter 4 was light microscopy (LM) imaging, a method that is valid for analyzing the general body plan of the developing fish. However, if the femtosecond laser is to be integetrated into lifesciences as a tool to manipulate a variety of animal model systems, then a more rigorous definition of survival must be made. The zebrafish represents the ideal biological system for studying laser pulsed induced effects on embryo development. This is due to the transparency of the developing embryo, which was discussed in detail in Chapter 4 section 4.1. As a result of this transparency, laser pulse treated blastomere cells can be monitored as a function of development to identify adverse morphological changes. However, to ensure that the manipulation tool is non-invasive, the developed embryos must be examined with sub-micron resolution

Building on the study presented in Chapter 4, a more rigorous analysis of zebrafish embryo development would require key developmental morphological structures to be examined. In this chapter, developmental morphological structures that were examined for morphological abnormalities included the pectoral fin buds that develop into the elaborate pectoral fins, the otic capsule (outer ear) [140, 141], the otic vesicle (inner ear) [140, 141], the olfactory pit [142, 143], the sensory epithelium (crista) and projecting kinocilia of the inner ear [140, 141], the pectoral fins, the neuromeres of the fore- and midbrain [90, 128] and the neuromast patterning[1]. Such morphological structures were not resolvable in the study described in Chapter 4 using standard LM imaging. Provided that zebrafish embryos at various developmental stages can be properly prepared for characterization, scanning electron microscopy (SEM) imaging represents an ideal tool for observing the aforementioned developmental morphological structures with sub-micron resolution. Therefore, a comparative study between control and laser pulse manipulated embryos using SEM analysis would represent an ideal morphological assay to confirm the non-invasiveness[2] of the laser based on normal embryonic development.

---

[1] Sensory epithelium with projecting kinocilia located along the lateral line organ [141].

[2] It is important to mention that the term 'non-invasive' applies only to morphological development and not to a physiological one. In Chapter 6, a physiological study is hypothesized that would complement the results presented in this chapter. Together, both the morphological and physiological studies would provide a global understanding of the laser's effect on the biological system studied.

In addition to a morphological study, the effect of laser pulse energy and beam dwell time on the intracellular accumulation of a delivered foreign molecule was of interest. With the demonstration in Chapter 4 that femtoseocond laser pulses could successfully permeabilize embryonic cells, it was important to elucidate the general trend in the intracellular accumulation of the introduced molecules as a function of the laser parameters. Knowledge of the intracellular fluorescence intensity with changing laser parameters would be particularly important to biomedical engineers and cell biologists to allow for the proper identification of the ideal laser conditions for maximum delivery.

Purpose of this study

The motivation for the studies in this chapter was to address the above concerns. Using the zebrafish (*Danio rerio*) as the animal model system, Chapter 5 begins by examining in further detail the ideal laser conditions for ablating zebrafish embryonic cells. Specific emphasis was placed on the formation of cavitation bubbles and residual surface scarring of the blastomere surface. By monitoring how the cavitation bubble diameter changes as a function of laser pulse energy and beam dwell time, the ideal laser conditions for ablation could be defined. Ideal conditions were defined as the laser parameters that produced short-lived cavitation bubbles (bubbles that decayed within a few seconds) and those that produced minimal surface scaring on the blastomere interface. Refining the above results, the predetermined laser parameters were used to permeabilize dechorionated zebrafish embryos in the presence of fluorescein isothiocyanate (FITC). Permeabilization was evaluated as a function of beam dwell time, by examining the change in the accumulated intracellular fluorescence intensity. Two methods were used to analyze the fluorescence intensity. The first method involved qualitative observations, while the second analysis was a quantitative measurement of the intracellular blastomere fluorescence intensity per unit area of the blastomere cells. Through a comparison of the fluorescence intensities emanating from blastomere cells for each chosen beam dwell time, the laser parameters were refined to reflect the ideal permeabilization conditions that lead to maximum intracellular material delivery.

With knowledge of the appropriate laser pulse permeabilization conditions, chorionated zebrafish embryos were laser pulse ablated using the refined parameters in the absence of exogenous solution. The embryos were cultured to 2 and 7 days post-fertilization (dpf) and were individually examined for normal morphology using LM and SEM imaging. LM imaging provided an analysis of general zebrafish body plan, while SEM was used to characterize the morphology of key developmental structures. Together both assays provided an assessment of the effect of the laser pulses on zebrafish development. The morphological study presented in this chapter represents the first literature report documenting in detail the effects of applied focused femtosecond laser pulses on embryonic development. This work also provides the basis for future studies of femtosecond laser interactions with multicellular biological systems.

The experimental method used to laser pulse manipulate zebrafish embryos was identical to the experimental methodology detailed in Chapter 4, section 4.2. Zebrafish handling and care as well as the embryo harvesting procedure can be found in Appendix F. Details of the fixing and mounting of zebrafish embryos for SEM imaging can also be found in Appendix F. The various tools that have been used to manipulate embryos were previously discussed in detail in Chapter 4, section 4.1.

5.2 Results and Discussion[1]

Experimental methodology

The experimental method used for the laser pulse manipulation of zebrafish embryos was identical to the setup described and shown in Figures 4.6 through 4.10 of Chapter 4. Sub-10 femtosecond laser pulses with a wavelength bandwidth from 700 nm to 900 nm (centered at 800 nm) were directed (red lines in Figure 4.6 of Chapter 4) into the upright Nikon 80i microscope with dichroic mirrors, labeled A1 through A3. The laser pulses were coupled into a 1.0 NA 60X water immersion microscope objective, F. Zebrafish embryos were placed on a motorized stage, G, and the stage was controlled either by the motorized shaft, H, or hand controller, J. Embryos were laser pulse targeted at the blastomere-yolk interface with a pulse energy ranging from 0.3 to 0.63 nJ/pulse[2]. Laser pulses were gated with a galvo (subsequently referred to as a shutter) located in front of dichroic mirror A1 (not shown in Figure 4.6 of Chapter 4). The beam dwell time for laser pulse manipulation ranged from 5 to 500 ms. At the focus of the 1.0 NA water immersion microscope objective, the diffraction limited irradiance spot size was estimated to be $d_r = 976$ nm ($\lambda = 800$ nm), as calculated from equation (1.2) in Chapter 1. The peak power at the focus was estimated to be between 1 kW/pulse (0.3 nJ/pulse) to 2.2 kW/pulse (0.63 nJ/pulse) (these values were calculated using an estimated broadend pulse duration of 291 femtoseconds; see Appendix A). From the peak power and irradiance spot size, the peak intensity at the focal plane ranged from

---

[1] Portions of this section have been published in Kohli *et al.* BMC Biotechnol. 8:7, pg. 1-20, 2008.

[2] These pulse energies represent the values measured entering the microscope objective lens. Fresnel's equations describing the reflection and transmission values through various index media can be used to approximate the amount of average laser power loss. From calculations (not presented in this thesis), the total average laser power loss was a few milliwatts.

$1.3\text{x}10^{11}$ W/cm^2 to $2.9\text{x}10^{11}$ W/cm^2. To estimate the maximum electron density and temperature rise within the focal spot after a single femtosecond laser pulse the equations developed in Chapter 1 and 2 were used. From equation (2.2) in Chapter 2, γ ranges from 11.2 ($2.9\text{x}10^{11}$ W/cm^2) to 16.7 ($1.3\text{x}10^{11}$ W/cm^2) and the effective ionization potential in equation (2.1) in Chapter 2 can be approximated as the band gap energy of water. The maximum electron density and temperature rise after a single femtosecond laser pulse were found to be between $\rho_{max} = 10^{11}$ cm^{-3} to 10^{12} cm^{-3} ($I/I_R = 0.02$ for 0.3 nJ/pulse; $I/I_R = 0.04$ for 0.63 nJ/pulse) and $\Delta T = 5.6\text{x}10^{-8}$ to $0.56\text{x}10^{-7}$ K (the temperature would be expected to rise after multiple incident femtosecond laser pulses), respectively.

The uptake of blastomere-fluorescence was assessed using the setup shown in Figure 4.8 of Chapter 4. A fluorescence lamp house located at the rear of the microscope (see Figure 4.8 of Chapter 4) and the filter cubes in the fluorescence filter chamber, D, allowed for epi-fluorescence imaging. To capture fluorescence, a Nikon DS-5M (Nikon, Japan) color CCD was used, which was mounted at the rear exit port of the microscope (i.e. imaging port of Figure 4.8 of Chapter 4). A standard FITC filter (Chroma Technology Corp., Rockingham, VT) allowed for the detection of FITC fluorescence. A more detailed explanation of the experimental setup can be found in Chapter 4, section 4.2.

Note on figures

The fluorescence, LM and SEM images presented in this chapter represent a subset of the images taken of the experimental specimens that clearly demonstrated the observations discussed. All observations and conclusions were based on the entire sample group.

Terminology defined

Throughout the text, the phrase 'laser pulse manipulated larva' refers to an embryo that was laser pulse treated at the early to mid cleavage stage (2-cell to 4/8-cell stage) and was subsequently allowed to hatch into a larva and mature to the indicated developmental endpoint (2 or 7 dpf).

Optimal laser parameters for the ablation of embryonic cells

Before addressing the short- and long-term morphological development of laser pulse manipulated larvae, the optimal laser parameters for embryo ablation were determined. To define the ideal laser parameters, individual dechorionated embryos (n = 30 embryos) at the early to mid cleavage stage (2-cell to 4/8-cell stage) were laser pulse ablated with a pulse energy and beam dwell time ranging from 0.3 to 0.63 nJ/pulse and 5 to 500 ms, respectively[1]. For each pulse energy and beam dwell time chosen, dechorionated embryos were ablated near the blastomere-yolk interface with a maximum of 4 to 5 spatially separated ablation spots made in each of 2 to 4 blastomere cells per embryo. A high magnification SEM image of the blastomere-yolk interface is presented in Figure 5.1, where B and Y designate the blastomere and the yolk, respectively. The transition between the dense region of the yolk and the less dense area of the blatomere is clearly evident in the figure, and is defined as the blastomere-yolk interface

---

[1] Each ablation spot at a given beam dwell time was induced with a single pulsing event of the shutter. For instance, at 500 ms, the shutter was left in the 'open state' for 500 ms.

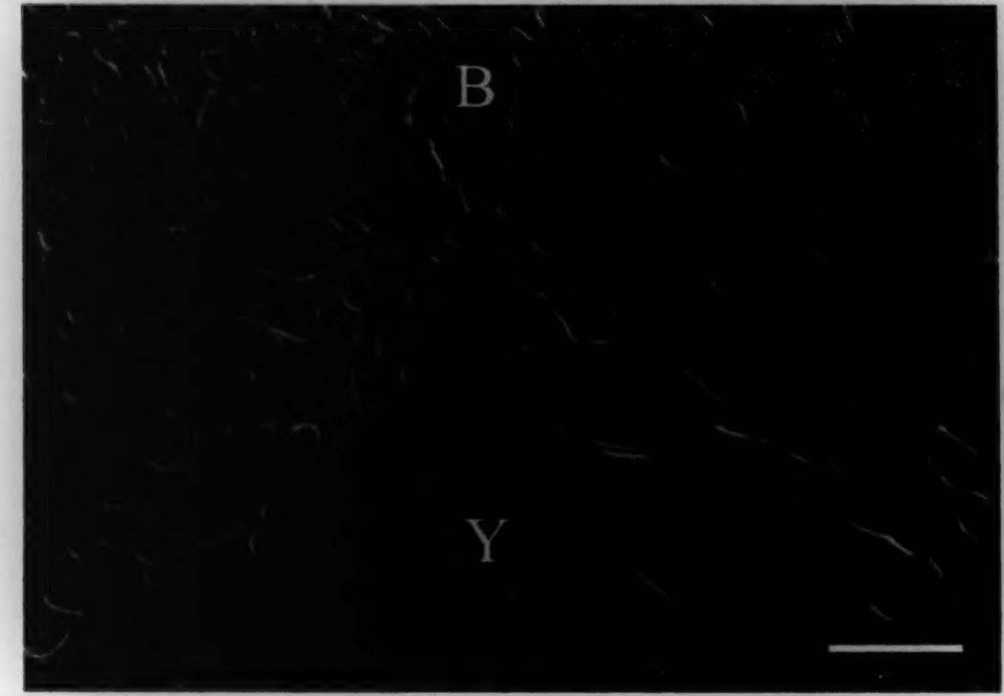

Figure 5.1: A high magnification SEM image of the region near the blastomere-yolk interface of an 8-cell stage embryo. The less dense region, B, represents the blastomere cell while the dense area is the yolk, Y. Scale bar represents 5 μm.

(also see Figure 4.12 in Chapter 4).

To assess embryonic surgical pulse ablation, visual inspection of the ablated region was performed, with specific emphasis on the formation of cavitation bubbles and residual surface scarring of the interface. Based on the size of the cavitation bubble, as well as the spatial extent of surface scarring, the ideal laser parameters for surgical pulse ablation were defined. The lowest pulse energy and shortest beam dwell time producing short-lived cavitation bubbles with minimal surface scarring were the criteria used to define the optimal laser conditions. At a pulse energy of 0.3 nJ/pulse and a gated shutter time of 5 to 500 ms, the region near the blastomere-yolk interface could not be laser pulse ablated. This result was independent of the chosen beam dwell time. Increasing the pulse energy to 0.38 nJ/pulse with a beam dwell time of 50 to 200 ms, ablation of the interface occurred occasionally. At beam dwell times in excess of 200 ms, specifically at 500 ms, surgical pulse ablation of the blatomere-yolk region was observed with high reproducibility[1]. A further increase in the pulse energy to 0.5-0.56 nJ/pulse resulted in ablated blastomeres irrespective of the chosen beam dwell time. However, at gated shutter times ≤ 100 ms, laser pulse generated cavitation bubbles were short-lived, decaying within a few seconds. Above 100 ms, cavitation bubbles became quite large, greater than 5 μm in diameter, which resulted in increased tissue scarring of the blastomere surface. For laser pulse energies above 0.56 nJ/pulse, surgical pulse ablation of the blastomere-yolk region persisted over the entire beam dwell range from 5 to 500 ms. Cavitation bubbles were observed to be large in diameter, often exceeding 10 μm, with the residual surface scarring length on the order of the cavitation diameter. Based on the previously defined criteria (lowest pulse energy for surgical pulse ablation; fast decaying cavitation bubbles with small diameters; minimal blastomere surface scarring), a pulse energy of 0.5 to 0.56 nJ/pulse with a beam dwell time of ≤ 100 ms[1] was considered the ideal laser condition for embryo surgical pulse ablation. Table 5.1 presents a summary of the results of this study.

---

[1] High reproducibility was defined as surgical-ablation occurring continuously at every chosen spatial location on the cell.

Cavitation bubble formation and surface scarring

Cavitation bubble formation and residual surface scarring in the region near the blastomere-yolk interface of a chorionated 2-cell stage embryo is shown in Figure 5.2[2]. In Figure 5.2(a), the cavitation bubble (Cb) was formed using a pulse energy of 0.56 nJ/pulse with the shutter pulsed once at 100 ms. Measurements showed the cavitation bubble diameter to be ~ 5 μm. After pulsing the shutter an additional two times (total beam dwell time duration of 300 ms) and waiting for the collapse of the cavitation, residual tissue surface scarring (Ss) of the blastomere cell post-laser pulse manipulation could be seen, Figure 5.2(b). The spatial extent of the tissue scarring was estimated to be ~ 5 μm, equivalent to the diameter of the cavitation bubble. Under constant pulse energy, larger cavitation bubbles were generated when the beam dwell time was increased from 100 to 500 ms. Figure 5.2(c) depicts the expanded cavitation bubble (Cb) after a single pulsing event of the shutter at 500 ms. The diameter of the cavitation bubble was estimated to be ~ 10 μm and the length of surface scarring (Ss) after 1000 ms (two pulsing events of the shutter) was found to be equal to the cavitation diameter,

---

[1] While it is true that beam dwell times shorter than 100 ms produce smaller cavitation bubbles and less tissue scarring, it is unknown which beam dwell time ≤ 100 ms yields maximum uptake of a fluorescent probe into the blastomere cells.

[2] The chorion did not prevent tissue scarring or hinder surgical pulse ablation. This result was verified in Chapter 4 with the delivery of pervitelline FITC into the dividing chorionated blastomere cells.

Table 5.1: Laser pulse surgical ablation of individual blastomere cells – Summary

Average laser power	Beam dwell time	Observations
0.31 nJ/pulse	5 to 500 ms	Region near the blastomere-yolk interface could not be laser ablated. This result was independent of the chosen beam dwell time.
0.38 nJ/pulse	50 to 200 ms	Region near the blastomere-yolk interface was occasionally laser ablated.
	> 500 ms	Laser ablation near the blastomere-yolk region occurred with high reproducibility.
0.50-0.56 nJ/pulse	5 to 500 ms	Surgical-ablation near the blastomere-yolk region occurred for the entire beam dwell range. Cavitation bubbles were short lived for beam dwell times ≤ 100 ms. Above 100 ms, cavitation bubbles were large, with increased blastomere-surface damage.
> 0.56 nJ/pulse	5 to 500 ms	Surgical-ablation persisted for the entire beam dwell range. Laser induced cavitation bubbles were large. A large area of blastomere-surface damage was observed.

Note: The center wavelength of the femtosecond laser pulses was at 800 nm, and the repetition rate of the laser oscillator was 80 MHz. As stated in the text, the laser pulses were focused by a 1.0 NA 60X water immersion microscope objective. The estimated diffraction limited irradiance spot size (diameter) was 976 nm.

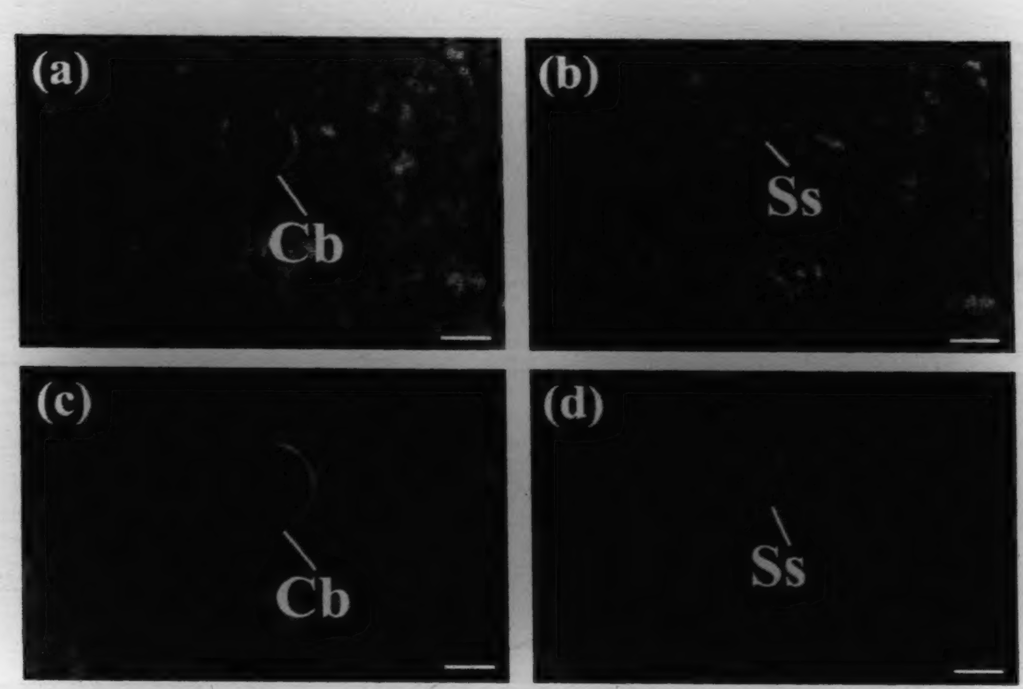

Figure 5.2: Cavitation bubble (Cb) formation and residual surface scarring (Ss) of blastomere cells post-femtosecond laser pulse manipulation. (a) The cavitation bubble (Cb) was produced using a pulse energy of 0.56 nJ/pulse with a gated shutter time of 100 ms and a single pulsing event of the shutter. A measurement of the cavitation diameter revealed a size of ~ 5 μm. (b) After pulsing the shutter a total of 3 times (total beam dwell time of 300 ms), surface scarring (Ss) of the blastomere cell was observed. The spatial extent of surface scarring was on the order of the cavitation bubble diameter, ~ 5 μm. (c) The cavitation bubble (Cb) was created using a pulse energy of 0.56 nJ/pulse with a gated shutter time of 500 ms and a single pulsing event of the shutter. The diameter of the cavitation bubble was measured to be ~ 10 μm. (d) After pulsing the shutter a total of 2 times (total beam dwell time of 1000 ms), surface scarring (Ss) of the blastomere cell was observed. Similar to (b), the scarring length in (d) was on the order of the cavitation bubble diameter, ~ 10 μm. The above figure was extracted from live video of the ablation process, which has been provided in the supplementary CD, Additional File 1 – Chapter 5. Scale bars for (a,b,c,d) represent 5 μm.

Figure 5.2(d). It is important to mention that the cavitation bubble and surface scarring in Figures 5.2(a,b) were formed in one of the two blastomere cells, while those in Figures 5.2(c,d) occured in the second cell. The above quoted values for the tissue scarring length represent the maximum estimated length along the long axis of the scar. The images in Figure 5.2 were extracted from live video of the ablation process, which has been included in the supplementary CD, Additional File 1 – Chapter 5.

Differences in the cavitation diameters in Figures 5.2(a) and 5.2(c) were readily discernable in the images, with the bubble diameter and surface scarring length for Figures 5.2(c,d) observed to be two times larger than those seen in Figures 5.2(a,b) This result, while interesting, was expected[1]. With increased energy deposition for ablation, it was expected that the cavitaiton bubble would be larger and more spatially disruptive due to excess energy being funneled into cavitation formation. To place this in context, if it is assumed that the tissue absorbs each incident laser pulse in the pulse train, then the total absorbed energy by the biological material can be estimated. For Figures 5.2(a) and 5.2(c) the femtosecond pulse train was gated at 100 and 500 ms respectively. Therefore, the number of incident pulses at the interface was $8x10^6$ and $4x10^7$ pulses, respectively, for 100 and 500 ms beam dwell times. Since the pulse energy was set to 0.56 nJ/pulse, the total deposited energy was estimated to be 4.48 mJ and 22.4 mJ for 100 and 500 ms, respectively. In relation to Figure 5.2, the 5-fold increase in laser energy deposition for 500 ms versus 100 ms likely resulted in a 2-fold increase in cavitation diameter and surface scarring length, as seen in Figure 5.2(c). It was hypothesized that limiting the number of laser pulses delivered to the interface could decrease the energy deposition, the cavitation diameter and the surface scarring length. The overall results presented in Figure 5.2 indicated that the spatial resolution of ablation was limited by the size of the cavitation diameter, which could be accurately controlled by the appropriate choice of laser parameters.

---

[1] As addressed in Chapter 1, cavitation bubbles impart a pressure force as the bubble expands away from the focus into the surrounding tissue. An expanding cavitation bubble induces tissue disruption, which increases the spatial extent of cellular damage.

Qualititative assessment of blastomere-fluorescence as a function of beam dwell time

Having established the ideal laser parameters for embryonic surgical pulse ablation, and having demonstrated transient pore formation in zebrafish embryonic cells as described in Chapter 4, the laser conditions were further refined to elucidate the relationship between beam dwell time and blastomere-fluorescence intensity. In this study, individual early cleavage stage (2-cell stage) dechorionated embryos (n = 10 embryos) were surgically pulse ablated on the blastomere cells with a pulse energy of 0.56 nJ/pulse. Three different beam dwell times of 100, 50 and 20 ms were chosen to examine the change in the fluorescence intensity originating from the permeabilized blastomere cells. For each ablation event, the shutter was pulsed 1 to 3 times per pore (with < 20 sec between each pulsing event). Dechorionated embryos were bathed in 0.014 to 0.018 mg/mL FITC solution and were laser pulse porated three times per blastomere cell (at different locations), with a maximum of two laser pulse treated cells (a total of 6 pores created per 2-cell stage embryo). At the time of transient pore formation, the embryo was at the 2-cell stage.

Figures 5.3(a,b) depict a post-laser pulse manipulated 8-cell stage dechorionated embryo that was porated with a pulse energy of 0.56 nJ/pulse and a beam dwell time of 100 ms. Each of the 6 pores were created with 3 pulsing events of the shutter at 100 ms

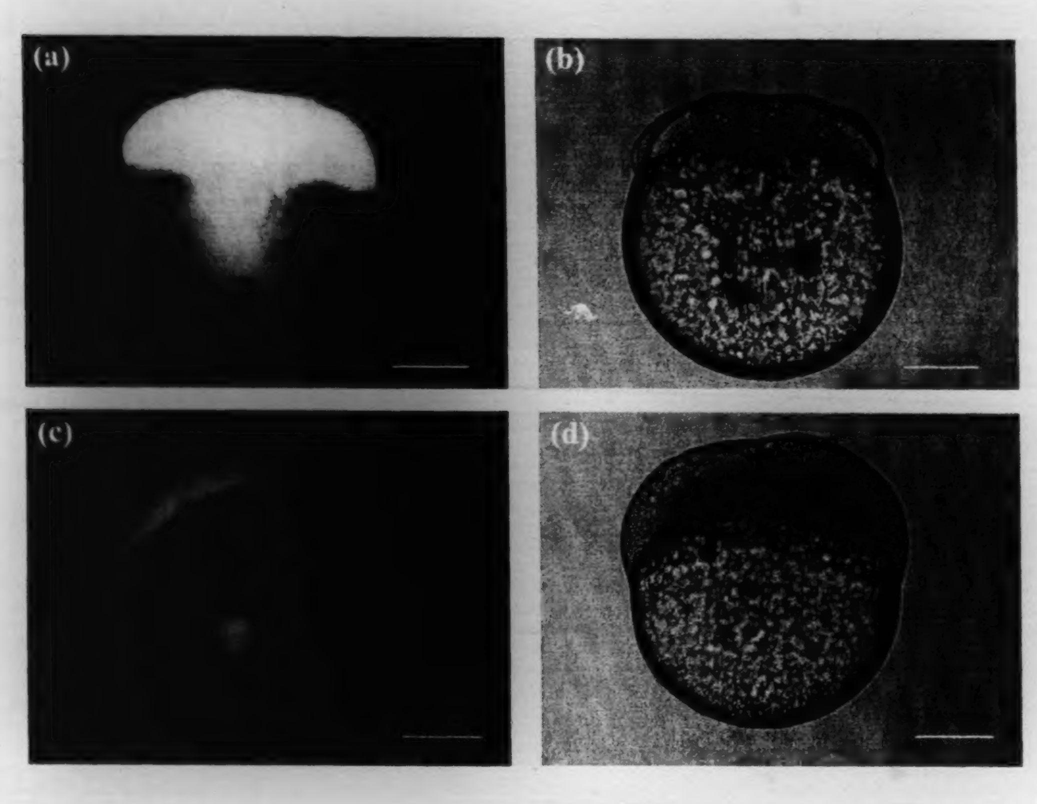

Figure 5.3: Embryos laser pulse manipulated with a pulse energy of 0.56 nJ/pulse for introducing exogenous FITC into the blastomere cells. (a,b) Fluorescence and brightfield image of a post-laser pulse maniputed 8-cell stage embryo that was porated a total of 6 times in each of 2 blastomere cells (3 pores per blastomere cell with a maximum of 2 laser pulse treated cells; laser pulse treated at the 2-cell stage). Transient pores were formed using a beam dwell time of 100 ms and 3 pulsing events of the shutter. (c,d) Fluorescence and brightfield image of a post-laser pulse manipulated 4-cell stage embryo. The same number of pores were made in the blastomeres as in (a,b); however, the beam dwell time was set to 100 ms with the shutter pulsed once. The concentration of FITC used was 0.014 to 0.018 mg/ml, with the embryos exposed to the fluorescent probe for 10 to 15 min. Quantitative measurements of the mean blastomere-fluorescence intensity per unit area were (a) 53.9 and (c) 16.9. Scale bars for (a,b,c,d) represent 200 μm.

(total beam dwell time of 300 ms). In Figure 5.3(a), FITC fluorescence was observed in the blastomere cells, indicating the creation of laser pulse induced pores. Post-manipulation, the embryo maintained normal morphology as compared to Westerfield images [126], and the pore was observed to be transient, as evidenced by the lack of cytoplasmic leakage of cellular material into the extracellular environment, Figure 5.3(b). Decreasing the number of shutter pulsing events to 1 (total beam dwell time of 100 ms; 0.56 nJ/pulse) resulted in a lower accumulation of blastomere-FITC, Figure 5.3(c). Despite the creation of pores in each of the 2-cells at the time of laser pulse manipulation, the 4-cell stage dechorionated embryo in Figure 5.3(c) exhibited higher fluorescence in the leftmost blastomere. This was in contrast to the uniform blastomere-FITC fluorescence observed in all of the dividing cells of Figure 5.3(a). Similar to Figure 5.3(b), the embryo maintained normal morphology post-laser pulse manipulation with no observable leakage of cytoplamic material. A visual comparison of the blastomere-fluorescence intensity between Figures 5.3(a) and 5.3(c) revealed that longer beam dwell times resulted in increased intracellular accumulation of the FITC probe. This result was likely due to the kinetics of the laser pulse induced pore, where it was hypothesized that additional shutter pulsing events (3x100 ms vs 1x100 ms) would make subsequent pore formation easier and increase the time the intracellular space was exposed to the extracellular environment (to be discussed).

In Figures 5.4(a,b) the post-laser pulse manipulated 8-cell stage dechorionated embryo was laser pulse porated using a pulse energy of 0.56 nJ/pulse with a beam dwell time of 50 ms. Each of the 6 pores (3 pores per blastomere with a maximum of 2 laser pulse treated cells) were formed with three pulsing events of the shutter at 50 ms (total

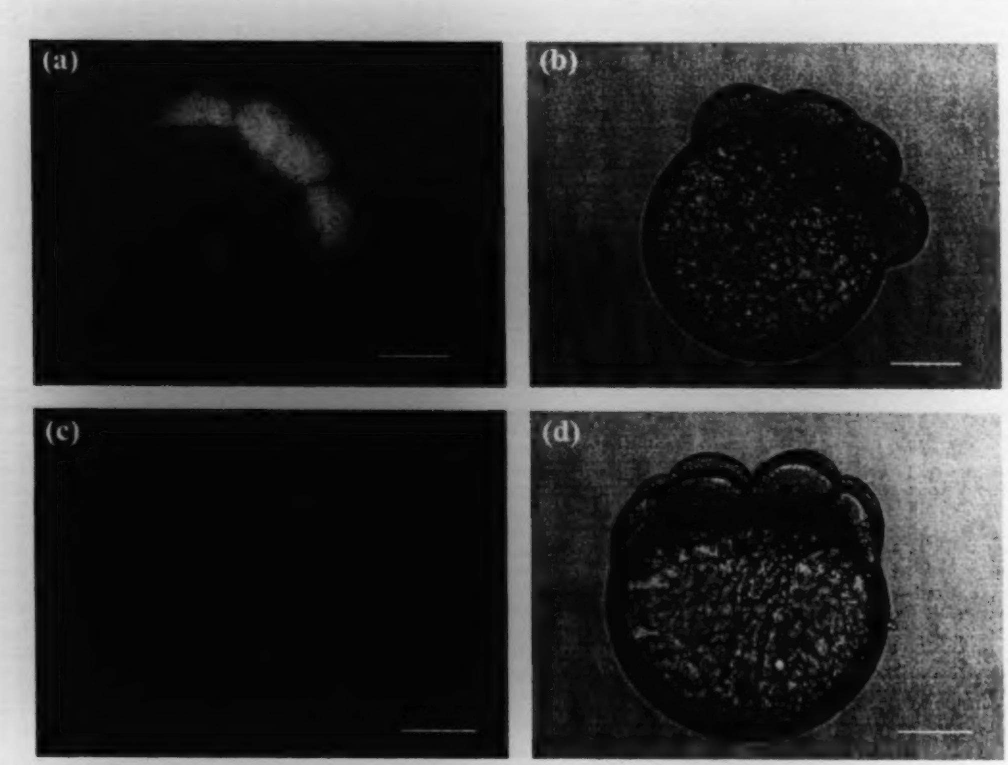

Figure 5.4: Embryos laser pulse manipulated with a pulse energy of 0.56 nJ/pulse for introducing exogenous FITC into the blastomere cells. (a,b) Fluorescence and brightfield image of a post-laser pulse manipulated 8-cell stage embryo that was porated a total of 6 times in each of 2 blastomere cells (3 pores per blastomere cell with a maximum of 2 laser pulse treated cells; laser pulse treated at the 2-cell stage). Transient pores were formed using a beam dwell time of 50 ms and 3 pulsing events of the shutter. (c,d) Fluorescence and brightfield image of a post-laser pulse manipulated 8-cell stage embryo. Same number of pores were made in the blastomeres as mentioned in (a,b). The beam dwell time was set to 50 ms with the shutter pulsed a total of 2 times. The concentration of FITC used was 0.014 to 0.018 mg/ml, with the embryos being exposed to the fluorescent probe for 10 to 15 min. Quantitative measurements of the mean blastomere-fluorescence intensity per unit area were (a) 29.7 and (c) 15.4. Scale bars for (a,b,c,d) represent 200 μm.

beam dwell time of 150 ms). Fluorescence was observed in all dividing blastomere cells, Figure 5.4(a), with the embryo maintaining normal morphology, Figure 5.4(b). Comparing Figure 5.4(c) with 5.4(a), the 8-cell stage embryo in Figure 5.4(c) showed noticeably lower blastomere-fluorescence intensity. This embryo was porated with two shutter pulsing events at 50 ms (total beam dwell time of 100 ms). Despite the differing fluorescence intensities between Figure 5.4(a) and 5.4(c) all blastomere cells were positive for FITC fluorescence. Similar to the normal development observed in Figure 5.4(b), this result was also found for Figure 5.4(d).

At a beam dwell time of 20 ms (pulse energy remained constant at 0.56 nJ/pulse) the blastomere-fluorescence intensity signal was observed to be the lowest from among all of the previously mentioned parameters (i.e. 100 and 50 ms; 3, 2 and 1 shutter pulsing events). Figure 5.5(a) depicts a post-laser pulse manipulated 8-cell stage dechorionated embryo with blastomere-fluorescence localized in all of the developing cells. Poration was induced with three shutter pulsing events at 20 ms (total beam dwell time of 60 ms). The embryo was not compromised following laser pulse manipulation, as evidenced by Figure 5.5(b)[1].

To confirm that the blastomere-fluorescence observed in Figures 5.3, 5.4 and 5.5 originated from the diffusion of FITC through laser pulse generated transient pores, non-laser pulse porated embryos were exposed to the FITC flurophor and imaged. Figure 5.6 represents an 8-cell stage dechorionated embryo that was bathed in FITC (0.014 to

---

[1] It is important to mention that the embryo in Figure 5.5(b) was nearing 8-cell stage. Furrow cleavage formation has already occurred in the front and rear blastomere cells resulting in two sets of four blastomeres.

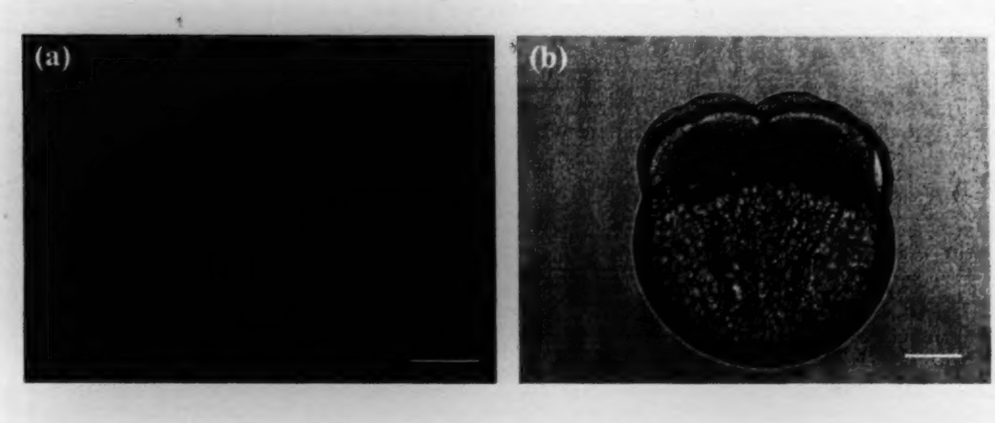

Figure 5.5: (a,b) Fluorescence and brightfield image of a post-laser pulse manipulated 8-cell stage embryo that was porated using a pulse energy of 0.56 nJ/pulse with a beam dwell time of 20 ms and a shutter pulse rate of 3. A total of 6 pores were made in each of 2 blastomere cells (3 pores per blastomere cell with a maximum of 2 laser pulse treated cells; laser pulse treated at the 2-cell stage) for introducing exogenous FITC. The concentration of FITC used was 0.014 to 0.018 mg/ml, with the embryos exposed to the fluorescent probe for 10 to 15 min. A quantitative measurement of the mean blastomere-fluorescence intensity per unit area was found to be 15.0. Scale bars for (a,b,c,d) represent 200 μm.

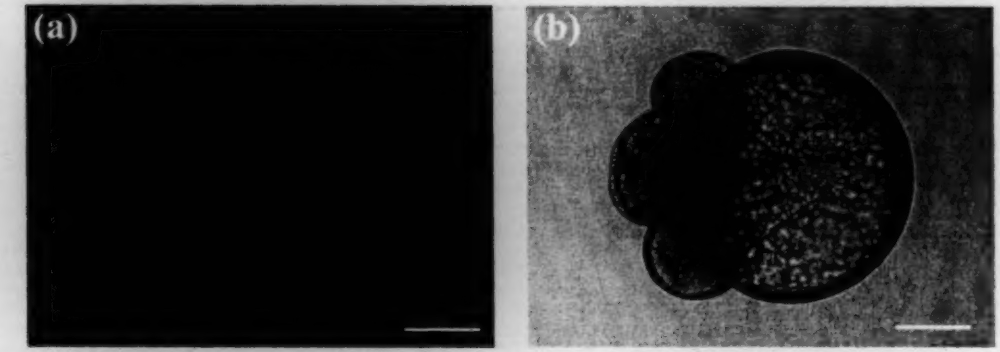

Figure 5.6: Fluorescence and brightfield image of an 8-cell stage embryo that was not laser pulse manipulated, but was bathed and exposed to the FITC fluorescent probe at the same concentration (0.014 to 0.018 mg/ml) and time interval (10 to 15 min) as in Figures 5.3, 5.4 and 5.5. The embryo was rinsed several times in buffered reverse osmosis water and imaged with an imaging area and exposure time consistent with Figures 5.3, 5.4 and 5.5. No accumulation of blastomere-FITC was observed in the cells. (a) The weak fluorescence observed in the yolk was autofluorescence. A quantitative measurement of the mean blastomere-fluorescence intensity per unit area was found to be 4.4. Scale bars for (a,b) represent 200 μm.

0.018 mg/mL) without pore formation. This embryo was exposed and imaged using the same parameters used in Figures 5.3, 5.4 and 5.5 (see Appendix F for the details). No accumulation of blastomere-fluorescence was observed in the embryo, Figure 5.6(a), confirming that delivery of FITC in Figures 5.3, 5.4 and 5.5 must have occurred through the transient pores. Furthermore, Figure 5.6 also verifies that no unfavourable interactions of the dye with the embryo membrane, resulting from FITC's amino reactivity, could have lead to the blastomere-fluorescence observed in Figures 5.3, 5.4 and 5.5 (all embryos were also inspected under 4X, 10X and 60X magnification to verify blastomere-fluorescence). If FITC had reacted with the entire cellular membrane, strong fluorescence would be observed emanating from the embryo, and qualitative analysis of the blastomere-fluorescence intensity would reveal a relatively large fluorescence signal comparible to embryos that were laser pulse manipulated for pore formation and delivery. The weak fluorescence observed in the yolk of Figure 5.6(a) was autofluorescence. Figure 5.6(b) is the brightfield image of the embryo seen in Figure 5.6(a).

Quantitative assessment of blastomere-fluorescence as a function of beam dwell time

Comparing Figures 5.3, 5.4, 5.5 and 5.6 reveals a general trend towards decreasing blastomere-fluorescence as both the beam dwell time and the number of shutter pulsings decreased. This observation was based on visual inspection of the fluorescence intensity originating from the blastomere cells and represented a qualititative analysis. Such an analysis was sufficient to elucidate the general trend in blastomere-fluorescence as a function of beam dwell time and shutter pulsing rate. However, to provide a more quantitative analysis of the blastomere-fluorescence, and to confirm the qualitative conclusions, the mean fluorescence intensity per unit area originating from the blastomeres cells in Figures 5.3, 5.4, 5.5 and 5.6 was measured. The respective mean intensities per unit area were 53.9 (100 ms; 3 pulsings of the shutter), 16.9 (100 ms; 1 pulsing of the shutter), 29.7 (50 ms; 3 pulsings of the shutter), 15.4 (50 ms; 2 pulsings of the shutter), 15.0 (20 ms; 3 pulsings of the shutter) and 4.4 (autofluorescence; non-laser-manipulated) for Figures 5.3, 5.4, 5.5 and 5.6. From these values, the blastomere-fluorescence decreased with beam dwell time and shutter pulsing rate, confirming the qualitative assessment. The strongest signal intensity (53.9 mean intensity/area) was found for embryos porated with a pulse energy of 0.56 nJ/pulse using a beam dwell time of 100 ms and a shutter pulsing rate of 3. It is interesting to note that both the qualitative and quantitative analyses of fluorescence showed that the FITC intensity for 50 ms and 3 shutter pulsing events (29.7 mean intensity/area) was higher than that for 100 ms and 1 shutter pulsing event (16.9 mean intensity/area). This result was expected, despite the decreased beam dwell time, as the total laser exposure time for Figures 5.4(a,b) was 150 ms versus 100 ms for Figures 5.3(c,d).

However, the beam dwell time is not the only parameter contributing to blastomere-fluorescence, and the number of shutter pulsing events must also be taken into consideration. For laser pulse induced pores created with multiple pulsing events of the shutter, it was expected that the competency of the pore would increase, since each pulsing event would weaken the tensile strength of the membrane, making subsequent pore formation easier[1]. Higher blastomere-fluorescence signals, as determined through the quantitative analysis, would define pores with higher compentency. Together the pulse energy, beam dwell time and the number of shutter pulsing events all determine the degree of competency. However, there would be an upper limit on the number of shutter pulsing events that would increase pore competency. Since laser pulse poration is accompanied by the formation of cavitation bubbles, it was also found (data not shown) that as the cavitation bubble diameter increased (approaching if not exceeding 10 µm), either through an increase in pulse energy or through an increased number of shutter events, there was an observed decrease in blastomere-fluorescence. It was hypothesized that this observation resulted from the outward expansion of the cavitation, driving the exogenous solute away from the pore and effectively reducing the efficency of passive diffusion into the cell.

---

[1] Pore compentency is the ability of the pore to transport exogenous molecules into the developing blastomere cells.

Developmental lag time

In Figures 5.3, 5.4 and 5.5, the embryos are shown developed to 4/8-cell stage after being laser pulse porated at the 2-cell stage. This development (1 to 2 cleavage divisions) occurred during the time it took to laser pulse manipulate each sequence of embryos, including rinses to remove the fluorescent probe and re-mounting the specimens for imaging. Furthermore, these differences in development should have no effect on the quantitative measurements of the blastomere-FITC signal due to the method used to analyze the blastomere-FITC fluorescence (see Appendix F for details). At the time of epi-fluorescence imaging, a complete image of each whole embryo was photographed with a constant exposure time of 1.5 sec. Upon assessing the blastomere-fluoresecence signal, the respective area of the blastomere cells were defined, and the mean intensity was determined by dividing the signal value by the blastomere area.

Irrespective of the developmental stage differences for the embryos seen in Figures 5.3, 5.4 and 5.5, the total volume occupied by the fluorescent probe remained the same, since each cleavage division of the embryo divided the cell volume in half. For instance in the SEM image in Figure 5.7, the 2-cell stage embryo in Figure 5.7(a) originated from the cleavage of a single blastomere cell and would have approximately the same total blastomere volume as at the one-cell stage. Increased cleavage cuts along the blastodisc would divide each blastomere cell in Figure 5.7(a) in half, resulting in a 4- or 8-cell stage embryo later in development. In the animal-vegetal axis rotated or top view of the 8-cell stage embryo in Figures 5.7(b,c), the total volume occupied by all blastomere cells would be approximately the same as the volume occupied in earlier developmental stages. Therefore, cleavages divisions would continue to reduce the volume of the cells, increasing the number of blastomeres while maintaining a constant total volume of all cells. As a further note, all embryos in Figures 5.3, 5.4 and 5.5 were imaged in the face view orientation. At the 4/8-cell stage (the developmental stages shown in Figures 5.3, 5.4 and 5.5), all blastomeres lie within the same plane and none of the cells cover adjacent blastomeres as is the case at the 64-cell stage [90].

Short-term effects of femtosecond laser pulse manipulation on morphological development

In disciplines like cryopreservation and developmental biology, achieving the highest intracellular concentration of a desired exogenous compound (i.e. cryoprotective molecule or gene of known function) is important. Based on Figures 5.3, 5.4, 5.5 and 5.6, as well as the qualitative and quantitative analyses of the blastomere-fluorescence

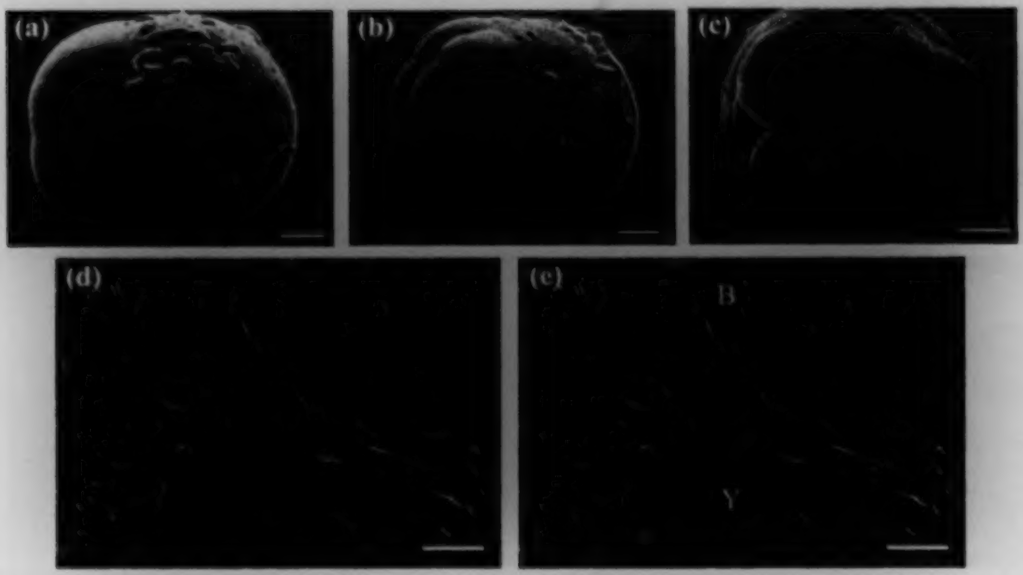

Figure 5.7: SEM images of control dechorionated embryos at the 2 and 8-cell stage. (a) Face view, (b) animal-vegetal axis rotated and (c) top view of a 2- and 8-cell stage control embryo. (d,e) High magnification SEM image of the blastomere-yolk region of an 8-cell stage embryo. B – Blastomere; Y – Yolk. Scale bar for (a,b,c) represent 100 μm and (d,e) 5 μm.

intensity, a pulse energy of 0.56 nJ/pulse with a beam dwell time of 100 ms and a shutter pulse rate of 3 represented the optimally refined laser parameters for poration and exogenous delivery. However, it remained to be determined whether these laser conditions induced any short-term effects on the morphological development of the zebrafish embryo.

To address the short-term morphological development of the zebrafish, control (n = 30 embryos) and laser pulse porated (n = 30 embryos) early cleavage stage (2/4-cell stage) chorionated embryos were reared at 27 ± 1° C until 2 dpf. All laser pulse manipulated embryos were porated near the blastomere-yolk interface using a pulse energy of 0.56 nJ/pulse and a beam dwell time of 100 ms. A total of 3 transient pores were made in each blastomere cell, with a maximum of two laser pulse treated cells (total number of pores created per embryo was 6). Each transient pore was formed with a shutter pulsing rate of 3, which was chosen to reflect the previously determined optimal laser parameters. Control and laser pulse manipulated embryos remained chorionated and were raised in rearing media (see Appendix F) in the absence of exogenous solution or proteolytic enzyme for dechorionation. This was done to avoid any cytotoxic or enzymatic affects that may have hindered an accurate assessment of embryo survival. For laser pulse manipulated embryos, femtosecond laser pulses were focused beyond the structure of the chorion in a manner identical to that shown in Figure 4.16 of Chapter 4. Similar to the observations made on the chorionated embryos in Chapter 4, the presence of the chorion did not prevent the successful laser pulse ablation of the embryo, indicating that energy loss through the chorion was minimal. (It is important to mention that the laser parameters used in this short-term survival analysis study were identical to the previously defined optimal conditions (0.56 nJ/pulse; 100 ms; 3 shutter pulsing events) stated above. Since it was already shown that the embryos could be successfully porated for FITC introduction[1], the pores formed in this study must necessarily have been competent for exogenous material delivery as well.)

Short-term embryo survival was determined in two distinct phases. The first phase involved using LM imaging observations of the developing zebrafish. Survival was defined as laser pulse manipulated larvae exhibiting normal hatching rates and developmental morphologies as compared to control larvae at the same stage. Specific morphological structures that were examined under LM were the yolk sac, the dorsal curvature and the general body axis. Laser pulse manipulated larvae displaying asymmetric yolk sacs, curved dorsals and malformation of the body axis, relative to the controls, were considered morphologically compromised and non-viable. Based on compared morphology between control and laser pulse manipulated samples, the first phase of short-term survival revealed a survival percentage of 93 % (28/30). These laser pulse manipulated larvae showed no differences in hatching rates as compared to the controls, and the developmental morphological structures looked very similar to those of the control larvae.

While LM analysis of zebrafish development did provide a reasonable assessment of survival, this imaging technique was limited to the observation of macroscopic structures. To refine the above results, SEM imaging was performed on viable larvae for a more thorough investigation of short-term survival. In order to accurately compare SEM images of control and laser pulse manipulated larvae, the fixing and graded alcohol steps were carefully performed to minimize differential shrinkage. For instance, embryos and larvae exposed to the fixative and alcohol solutions could undergo a dehydration response, preventing an accurate assessment of morphological development. Embryos and larvae that had undergone differential shrinkage would appear morphologically compromised in relation to samples that had been properly fixed. In the survival analysis study, the addition and removal of the fixative and alcohol solutions were performed slowly, allowing each solution to equilibrate with the sample. Evidence of normal fixing is shown in Figure 5.7, depicting SEM images of control embryos. The face view, animal-vegetal axis rotated and top view of the 2- and 8-cell stage embryos (Figures 5.7(a,b,c)) exhibited symmetrically shaped blastomeres, with no evidence of tissue tearing along the furrow cleavage or asymmetry in the yolk mass. In Figures 5.7(d,e), the delineation between the dense and less dense regions of the yolk and blastomeres was clearly observable, indicative of proper fixation. It is important to mention that the yolk mass in Figures 5.7(a,b) shows slight signs of improper fixation[1]. However, this result was expected, as the yolk mass was more difficult to fix than cellular tissue, as the yolk globules likely hindered the permeation of the fixative solution throughout the yolk. Longer exposure times of the yolk to the fixative would decrease the amount of improper fixation; however, the increased exposure time could compromise the fixing of cellular material. Adverse effects resulting from the longer exposure time would be less evident in SEM images, but would be observable in transmission electron microscopy (TEM). In unpublished results, TEM analysis of control zebrafish embryos exposed overnight to a fixative solution showed disrupted cellular membranes and missing membrane infoldings in organelles (specifically mitochondria)[1].

---

[1] See Figure 5.3(a,b); mean fluorescence intensity per unit area for Figure 5.3(a) was 53.9 (100 ms; 3 pulsings of the shutter).

---

[1] This observation would not affect the short- and long-term survival analysis study, since the yolk mass progressively gets smaller as the embryo ages.

All embryos and larvae that were fixed for SEM imaging were mounted on carbon tape stubs. Embryos were mounted in the face view and top view orientations, while larvae were mounted in the dorso-lateral and lateral orientations. Despite all attempts to accurately mount all embryos and larvae in the same orientation, slight differences in the projected views occurred. Once the embryos and larvae were mounted on the stubs and partially dried, further manipulation of the samples was avoided in order to minimize induced damage.

Figure 5.8 depicts SEM images of a laser pulse manipulated larva (n = 10 embryos; Figures 5.8 (a,b,c,d)) and a control larva (n = 8 embryos; Figures 5.8(e,f,g,h)) at 2 dpf. Figures 5.8(a,c,e,g) and Figures 5.8(b,d,f,h) represent lateral views of the whole body and magnified antero-lateral views of the zebrafish head. Specific developmental morphological structures that have been emphasized for comparison include the olfactory pit (OP), the yolk sac (YS), the yolk sac extension (YSE; also known as the zebrafish gut), the caudal fin (CF) and the dorsal fin (DF). A comparison of lateral whole body views of the laser pulse manipulated and control samples revealed that the developmental morphologies of both samples were very similar. In Figure 5.8(a,c) and 5.8(e,g), both larvae exhibited a slight curvature of the head about the yolk sac pointing ventrally[2].

---

[1] There are slight differences between SEM and TEM fixing procedures. In contrast to the single fixing step in SEM, TEM requires pre- and post-fixing, with the pre-fixing step identical to that performed in SEM. The post-fixing involves incubating the embryos in an additional fixative called osmic acid (osmium) for a few hours. Osmium is used to increase the contrast of cellular material.

[2] Other developmental patterning not indentified in Figure 5.8 includes the muscle cells (mytomes; derived from the somites [90]) that are found along the midlateral line of the developing zebrafish body, Figures 5.8(a,c,e,g). The notochord is located in a plane deep within the mytomes [90], which cannot be observed in either of the experimental samples.

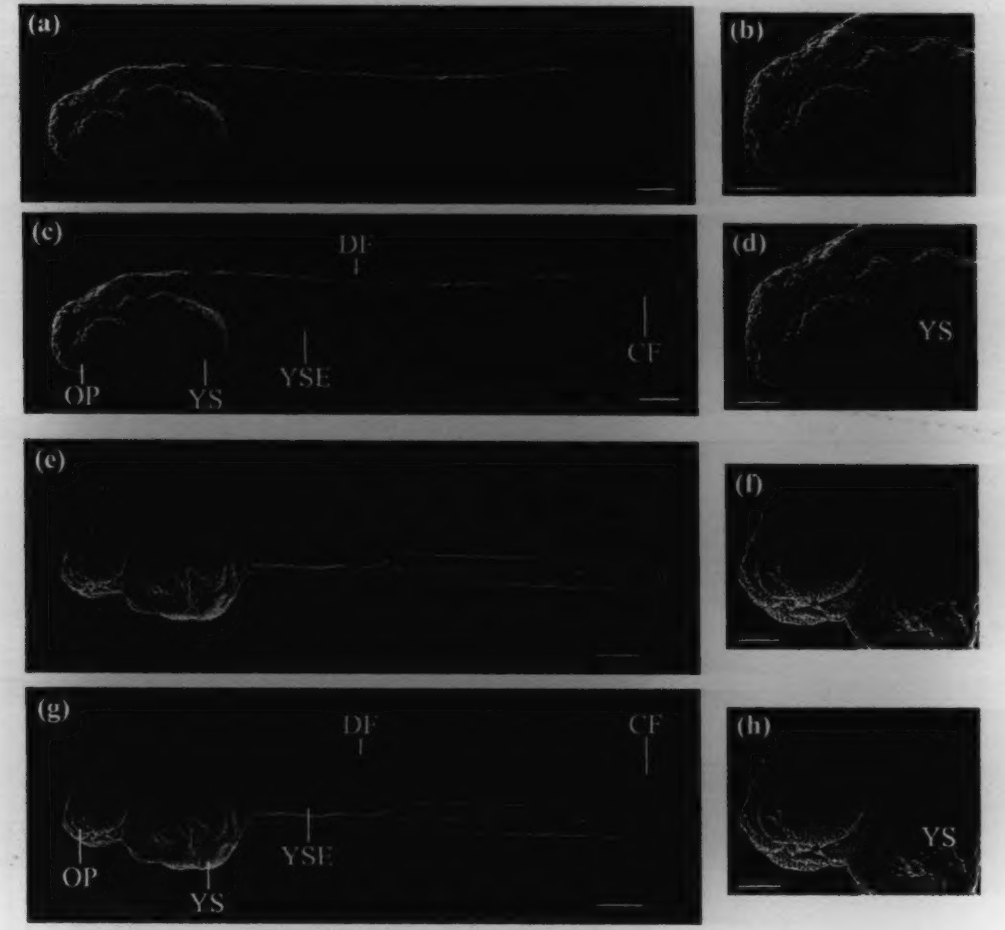

Figure 5.8: SEM images of a laser pulse manipulated and a control larva reared to 2 dpf. (a,b) Lateral whole body mosaics and antero-lateral views of the laser pulse manipulated larva at 2 dpf. (c,d) Same larva in (a,b) illustrating key developmental morphological structures including the olfactory pit (OP), the yolk sac (YS), the yolk sac exstention (YSE), the caudal fin (CF) and the dorsal fin (DF). (e,f) Lateral whole body mosaics and antero-lateral views of the control larva at 2 dpf. (g,h) Same larva in (e,f) indicating the same developmental morphological structures observed in (c,d). Scale bars for (a,c,e,g) represent 200 μm and for (b,d,f,h) 100 μm.

Additionally, the developing pectoral fin bud was found slightly posterior to the eye above the yolk sac, Figures 5.8(b,d,f,h), and developed along the lateral sides of each larva as it aged. While the pectoral fin buds were difficult to resolve in Figures 5.8(b,d,f,h), Figure 5.9 depicts a magnified view of the fin buds in a laser pulse manipulated (Figure 5.9(a)) and control larva (Figure 5.9(b)) developed to 2 dpf. As seen in Figure 5.9, both fins have begun to lift away from the underlying yolk and will develop into the elaborate fins observed in Figures 5.10(a,c). Comparing the pectoral fin buds in Figure 5.9 to the pectoral fins in Figure 5.10, it was observed that development from immature fin to mature fin had ccurred normally. All developmental morphological structures examined in the laser pulse manipulated larvae (n = 10 embryos) were observed to be morphologically similar to those in the control larvae (n = 8 embryos). Together, the 93 % survival rate determined by LM imaging and the SEM mosaics depicted in Figures 5.8 and 5.9, indicated that the laser did not induce any significant short-term effects on the development of the zebrafish embryo.

Long-term effects of femtosecond laser pulse manipulation on morphological development

While the short-term survival analysis study revealed that laser pulse manipulated larvae developed normally in comparison to control larvae, the laser's effect on embryonic development may not be apparent until later developmental stages. To assess long-term development, control (n =12 embryos) and laser pulse manipulated larvae (n = 10 embryos) at the early cleavage stage (2/4-cell stage) were raised in rearing media at

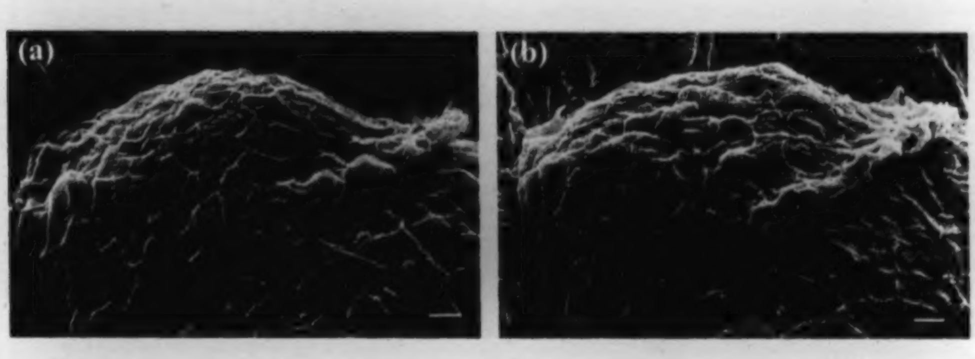

Figure 5.9: High magnification SEM images of the pectoral fin buds in a laser pulse manipulated and control larva reared to 2 dpf. (a) Pectoral fin bud of a laser pulse manipulated and (b) a control larva at 2 dpf. Orientation: anterior (left); posterior (right). Scale bar represents 10 μm.

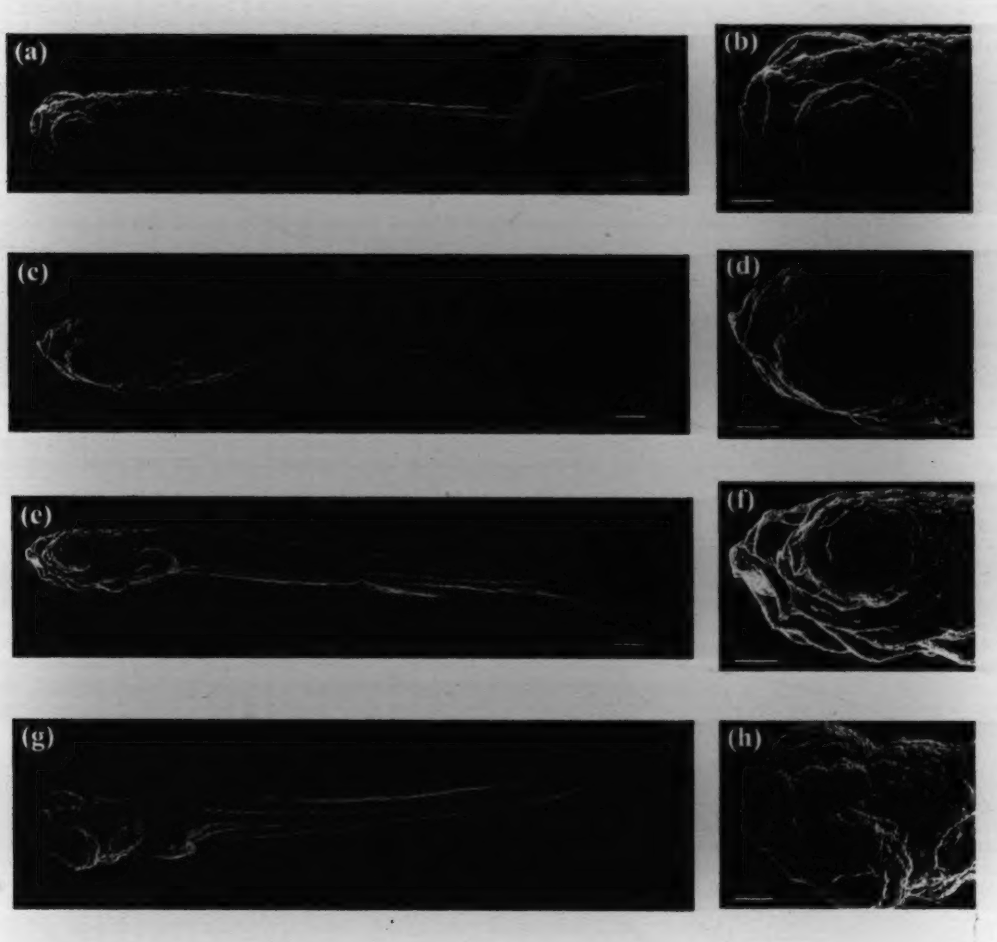

Figure 5.10: SEM images of laser pulse manipulated and control larvae reared to 7 dpf. (a,b,c,d) Dorso-lateral whole body mosaics and antero-dorsal views of laser pulse manipulated larvae at 7 dpf. (e,f,g,h) Lateral and dorso-lateral whole body mosaics and antero-dorsal views of control larvae at 7 dpf. Scale bars for (a,c,e,g) represent 200 μm and for (b,d,f,h) 100 μm.

27 ± 1 °C until 7 dpf. Similar to the laser parameters used in the short-term survival analysis study, all embryos were laser pulse manipulated near the blastomere-yolk interface with a pulse energy of 0.56 nJ/pulse and a beam dwell time of 100 ms. A total of 3 transient pores were made in each of the blastomere cells with a maximum of two laser pulse treated cells. For each pore, the shutter was pulsed 3 times at 100 ms. Embryos remained chorionated (to avoid cytotoxicity and exposure to the proteolytic enzyme) and the laser pulses were focused beyond the chorion as depicted in Figure 4.16 of Chapter 4. As with the short-term survival, long-term survival was assessed in two phases using both LM and SEM imaging. Developmental morphological structures that were examined in control and laser pulse manipulated samples using LM imaging included the protruding mouth, the olfactory pits, the pectoral fins, the otic capsule (outer ear) and the otic vesicle (inner ear). No significant differences in the developmental morphologies of these morphological structures were observed between the samples.

Evidence of this is provided in Figure 5.10, which depicts dorso-lateral, lateral and dorsal views of laser pulse manipulated (n = 10 embryos; Figures 5.10(a,b,c,d)) and control larvae (n = 9 embryos; Figures 5.10(e,f,g,h)) at 7 dpf. Whole body dorsal-lateral and lateral mosaics are shown in Figures 5.10(a,c,e,g), while Figures 5.10(b,d,f,h) represent magnified dorsal and lateral views of the zebrafish head. The general whole body plans of laser pulse manipulated larvae were found to be similar to those of the control larvae. Specifically, in laser pulse manipulated larvae, Figures 5.10(a,b,c,d), the pectoral fins developed normally along the zebrafish body, the zebrafish ear was patterned slightly posterior to the eye and dorsal to the pectoral fins, the olfactory pit was symmetrically placed adjacent to the eye, the mouth was in a protruding state and the muscle cells were observed patterned along the midline of the zebrafish body. These observations were very similar to those made for control larvae, Figures 5.10(e,f,g,h). Figure 5.11 presents an illustrated comparison of a laser pulse manipulated larva, Figures 5.11(a,b), and a control larva, Figures 5.11(c,d). Indicated developmental morphological structures include the protruding mouth (PM), the eye (E; cornea), the otic vesicle (OV), the pectoral fin (PF), the ventral fin (VF), the olfactory pit (OP), the otic capsule (OC) and the notochord (NC). (The notochord cannot be directly observed in the figure as it is located in a deeper plane below the myotome muscle cells [90].) No differences in the indicated developmental morphological structures were observed between the control and laser pulse manipulated samples.

Further evidence of normal developmental morphology is shown in Figure 5.12. Figures 5.12(a,b,c,g) are magnified dorsal and lateral views of the olfactory pit (Figure 5.12(a)), the ear (Figure 5.12(b)) and the structures overlying the posterior forebrain and dorsal midbrain [90, 128] (Figures 5.12(c,g)) in laser pulse manipulated larvae. Figures 5.12(d,e,f,h) depict the same developmental morphological structures in control larvae. Comparing Figures 5.12(a) and 5.12(d) it was found that the olfactory pit in the laser pulse manipulated larva developed similarly to the control. In both samples, dense hair- like projections (termed kinocilia [142]) were found covering the rim of the olfactory pit[1] adjacent to the eye. A high magnification SEM image of the olfactory pit rim in a laser pulse manipulated larva and a control larva is shown in Figures 5.13(a,b).

---

[1] As a side note, the olfactory organ is responsible for detecting and discriminating thousands of ordorants [143]. Courtship depends on the chemosensitivity of the organ, where specific pheromones act as attractants [143]. Interestingly, zebrafish that are rendered anosmic are unable to reproduce [143], indicating that this organ is functionally essential.

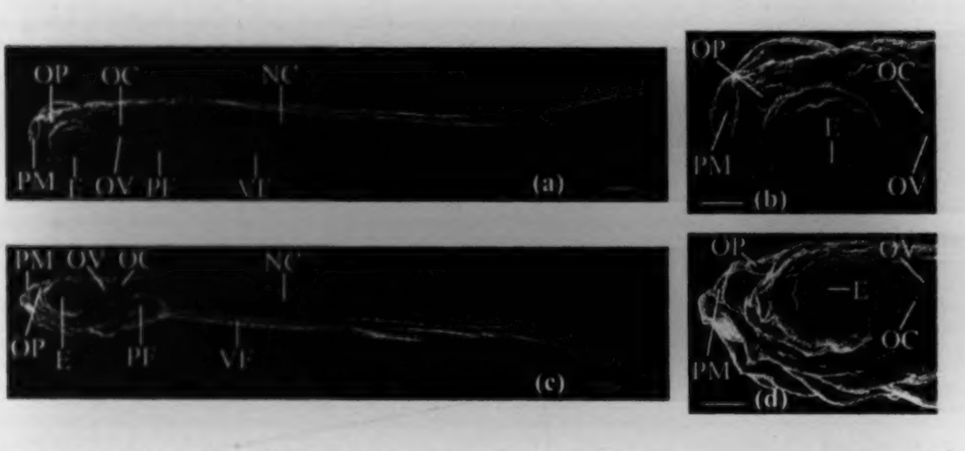

Figure 5.11: Illustration of key developmental morphological structures in a laser pulse manipulated and control larva reared to 7 dpf. (a,b) Dorso-lateral whole body mosaic and antero-dorsal view of a laser pulse manipulated larva at 7 dpf. (b) Same larva as (a). Developmental morphological structures that have been indicated include the protruding mouth (PM), the eye (E; cornea), the otic vesicle (OV), the pectoral fin (PF), the ventral fin (VF), the olfactory pit (OP), the otic capsule (OC) and the notochord (NC; depicting the location of where it would develop). (c,d) Lateral whole body mosaic and antero-lateral view of a control larva at 7 dpf. Same developmental morphological structures observed in (a,b) were also seen in (c,d). (d) Same larva as (c). Scale bars for (a,c) represent 200 μm and for (b,d) 100 μm.

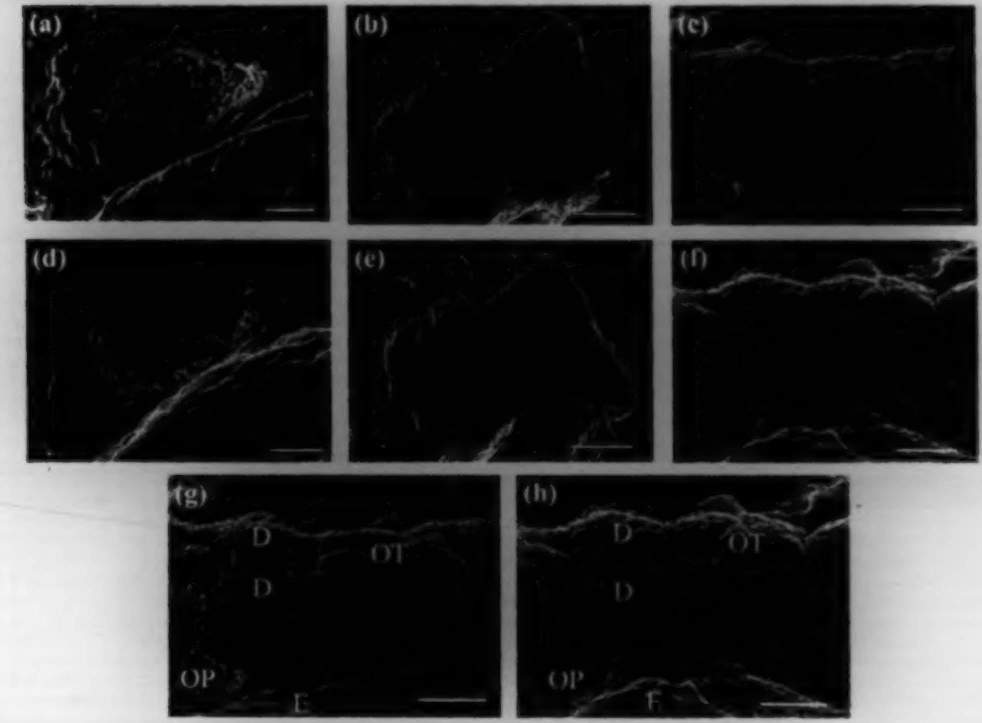

Figure 5.12: Magnified top and lateral views depicting key developmental morphological structures in laser pulse manipulated and control larvae reared to 7 dpf. (a,b,c) Magnified top and lateral views of (a) the olfactory pit, (b) the ear and (c) the neuromeres of the posterior forebrain and dorsal midbrain in laser pulse manipulated larvae. (d,e,f) Magnified top and lateral views of (a) the olfactory pit, (b) the ear and (c) the neuromeres of the posterior forebrain and dorsal midbrain in control larvae. (g,h) Illustrated comparison of dorso-lateral views of the neuromeres in (g) a laser pulse manipulated and (h) control larva at 7 dpf. The dicephalon (D) and optic tectum (OT) shown in (g,h) represent the locations of the posterior part of the anterior forebrain and the dorsal midbrain. Also indicated are the locations of the eye (E) and the olfactory pit (OP). Orientation: anterior (left); posterior (right). Scale bars for (a,d) represent 20 µm and for (b,c,e,f,g) 50 µm.

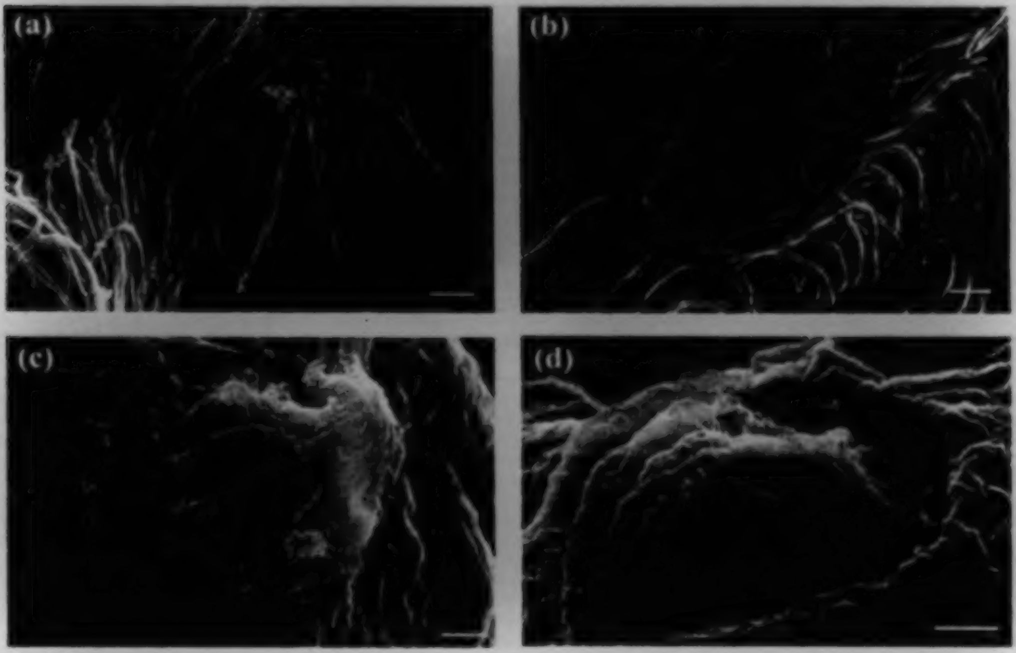

Figure 5.13: High magnification SEM images of the olfactory pit rim and the kinocilia projecting from the crista on the lateral wall of the inner ear in a laser pulse manipulated and control larva reared to 7 dpf. (a) Olfactory pit rim in a laser pulse manipulated and (b) a control larva showing kinocilia covering the inside wall of the olfactory pit. Kinocilia projecting from the lateral crista in (c) a laser pulse manipulated and (d) control larva. Scale bars for (a,b,c,d) represent 1 μm.

Figures 5.12(b) and 5.12(e) both show a mound of cells on the lateral wall of the inner ear with kinocilia projecting into the lumen. The cell mounds in Figure 5.12(b) and 5.12(e) are sensory epithelium (termed crista [141]) that support kinocilia and function to relay information to the zebrafish brain about head movement and angular acceleration [141]. Several kinocilial hair cells projected from the sensory epithelium in the laser pulse manipulated larva (Figure 5.13(c)), which was consistent with observations of the control larva (Figure 5.13(d)). As seen in Figures 5.13(c) and 5.13(d), kinocilia were clumped and bent, unlike in an aqueous environment where kinocilia are polarized. The clumping and bending were believed to be an artifact of the fixing and sputtering required for SEM. Figures 5.12(g) and 5.12(h) show the locations of the posterior forebrain (D; diencephalon) and the dorsal midbrain (OT; optic tectum) [128] of a laser pulse manipulated and control larva.

In addition to the kinocilia associated with the lateral crista, hair cells are also found underlying the calcified otoliths[1] and projecting from the sensory epithelium along the zebrafish lateral line organ [141]. The kinocilia of the otoliths do not project into the lumen like the kinocilia of the crista, rather they are capped by the otoliths and attach to a sensory epithelium termed the macula [140, 141]. Figure 5.14 depicts a 2.5 dpf laser pulse manipulated larva showing these dense otoliths. Similar otoliths were also found in control larvae.

Protrusions (mounds of cells with projecting kinocilia) similar to those seen on the lateral wall of the zebrafish inner ear were also observed patterned along the zebrafish body in control larvae. These protrusions (termed neuromasts [141]) were located anterior to the olfactory pit (Figure 5.12(d)), at the outer rim of the otic capsule

---

[1] The hair cells can only been seen if differentially stained or if the otoliths are de-calcified [140].

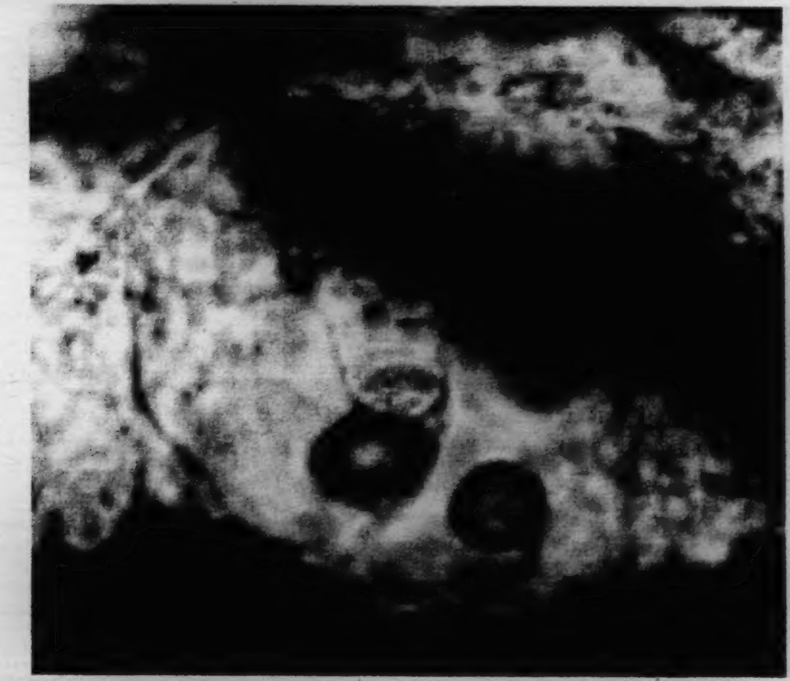

Figure 5.14: LM image of a laser pulse manipulated larva reared to 2.5 dpf showing the dense otoliths of the zebrafish ear defining the location of the macula. The above figure is a cropped image of Figure 4.23 in Chapter 4. Orientation: anterior (left); posterior (right).

(Figure 5.12(e)) and anterior and adjacent to the neuromeres (Figures 5.12(f) and 5.12(h)). Comparing Figures 5.12(d,e,f,h) with Figures 5.12(a,b,c,g), neuromast patterning in laser pulse manipulated larvae was found to be identical to that seen in the controls. Together the striking similarities between the developmental morphological structures of laser pulse manipulated and control larvae observed in Figures 5.10 through 5.13 indicate that the laser did not have any adverse affects on the long-term development of the zebrafish.

A LM dorsal view of a 5 dpf developed laser pulse manipulated larva is presented in Figure 5.15. Developmental morphological structures that have been indicated include the protruding mouth, the eyes and the pectoral fins. This image was extracted from live video, which has been provided in the supplementary CD, Additional File 2 – Chapter 5.

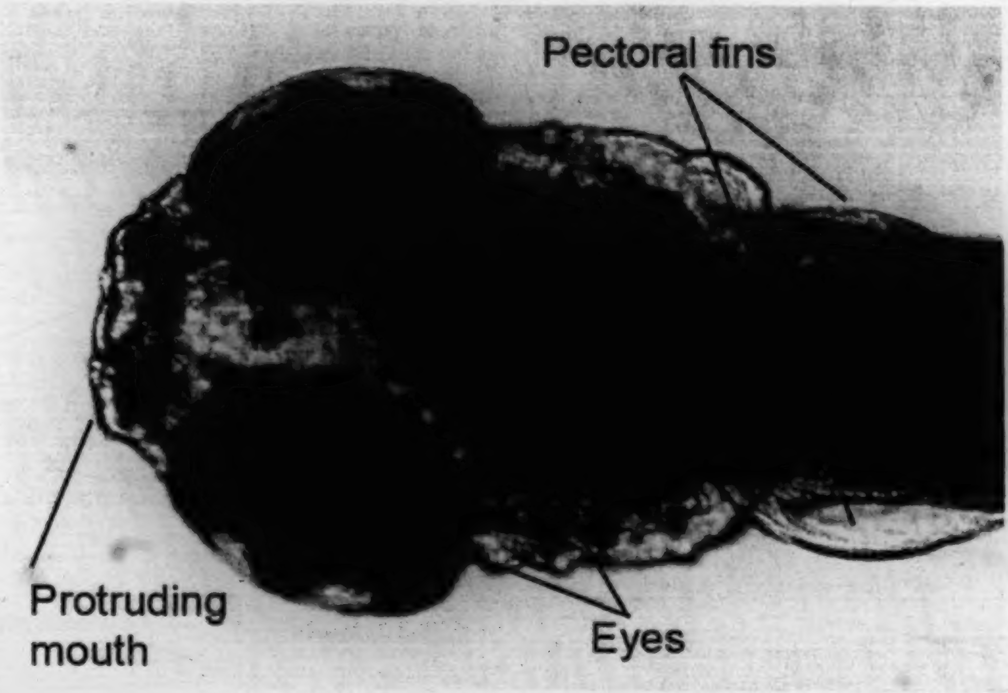

Figure 5.15: Dorsal view of a laser pulse manipulated larva reared to 5 dpf. Developmental morphological structures that have been indicated include the protruding mouth, the eyes and the pectoral fins. The above image was extracted from live video, which has been provided in the supplementary CD, Additional File 2 – Chapter 5.

CHAPTER 6

CONCLUSION AND FUTURE PROSPECTS

6.1 Conclusion and future prospects[1]

Applied femtosecond laser pulses represent a promising tool for manipulating cells and more complicated biological systems such as embryos. By targeting the laser pulses to a region of interest, the selected site can be ablated for removal, dissection or permeabilization, depending on the chosen application. The novelty of this tool is inherent in the ability to focus the femtosecond laser pulse to a desired cellular interface, and it is through the the non-linear multiphoton absorption process discussed in Chapter 1 that the targeted site can be altered without affecting adjacent cellular sites. It is this property that has made the application of femtosecond laser pulses an attractive tool for use in multiple disciplines of research, as evidenced by increasing literature reports [8, 12, 14-17, 19-23, 34, 43, 54, 74, 122, 124, 144-156] demonstrating its use[2]. Despite these studies, however, the full potential of femtosecond laser pulses has yet to be realized. In a similar fashion to the initial development of the laser itself, the femtosecond laser is a tool being developed without having fully elucidated all of its potential uses. The application of femtosecond laser pulses is in some ways developing as a technique "in search of a bioengineering problem". It is through continued research that we will uncover novel applications that will undoubtedly benefit many other biomedical and biological disciplines.

Throughout Chapters 2, 3, 4 and 5, a progressive series of studies demonstrating the multifunctional applications of femtosecond laser pulses was presented. These included the isolation of single cells, cell membrane surgery and the permeabilization of cells and more complicated model systems such as the zebrafish (*Danio rerio*). To confirm the non-invasive application of femtosecond laser pulses, various assays incuding visualizations of cell morphology, SYTO/EB membrane integrity stains, light microscopy and scanning electron microscopy were used to verify the non-destructive use of this cell manipulation tool. Furthermore, each chapter introduced the importance of particular cell or animal model systems, as well as techniques that are currently used to manipulate them. Concluding paragraphs described the objectives of the studies and detailed potential uses for the specific applications described. In the results and discussion, each particular study was discussed in the context of a current or future application for the purpose of providing a motivation for the research. The studies presented in the respective chapters represented a continuation and advancement of studies in previous chapters, with the knowledge gained through observations and experimental findings assisting in the development and execution of the subsequent studies. It is the collection of the embodied work included in this thesis that provides a foundational basis for both the application and study of femtosecond laser pulses to biological material, and a starting point for future work in this exciting field.

---

[1] Portions of this chapter have been published in: Kohli *et al*. Prospects and developments in cell and embryo laser nanosurgery. Interdisciplinary Reviews: Nanomedicine. In press. (**Invited article**).

[2] In the introduction of each chapter a summary of studies using NIR femtosecond laser pulses was provided.

A physiological study

To conclude this thesis it would be instructive to identify a future study that would continue along the path of the published findings contained herein. As briefly mentioned in Chapter 1, the accumulation of heat stresses in organisms exposed to laser pulse induced ablation would be an important property to quantify. Theoretical estimates of the temperature rise in the focal volume, as developed by Vogel *et al*. [5], do provide informative results, but do not necessarily provide a true assessment of the effect of heat and mechanical stress on the biological system studied. Throughout this thesis an estimate of the temperature rise after the application of a single femtosecond laser pulse was provided. Since an 80 MHz femtosecond laser oscillator was used in each of the presented studies, it was expected that both the plasma formed and the temperature within the focal volume would increase due to the interaction of multiple pulses within the 80 MHz repetition train. However, both the plasma and the temperature rise can be controlled through the appropriate choices of laser pulse energy and the number of incident femtosecond laser pulses. In addition to cascade bond-breaking of the biological material in femtosecond laser pulse induced 80 MHz ablation, decomposition of the material may also be influenced by thermal effects. The difficulty, however, is in trying to determine the contribution of each to the ablation process. As mentioned in Chapter 1, cavitation bubbles generated through local heating form on the nanosecond time scale and can continue to expand for microseconds to seconds. Since the incident laser pulse is femtoseconds in duration, the question still remains as to what happens to the biological material before the formation of the cavitation bubble. A more thorough investigation of the contribution of thermal damage would examine the physiological responses of the stressed biological organisms and the various processes occurring to rectify the induced damage. As a proposed physiological study, the induction of heat shock protein 70 (Hsp 70) following femtosecond laser pulse treatment could be assessed. Briefly, HSPs of the 70 kDa family are molecular chaperones that bind to newly forming polypeptides, preventing undesirable interactions with other proteins in the cytoplasm [157-161]. Hsp 70 also assists in the refolding of denatured proteins and the trafficking of other proteins destined for a particular location [159, 162-167]. A variety of stressors can induce heat stress protein production, including chemicals, heat and osmotic stresses. The heat shock response has been studied in the zebrafish exposed to temperatures (i.e. 37 °C) above its ideal thermotolerance (typically 25 to 33 °C [90]) for normal development, as well as in embryos exposed to ethanol, cadmium and copper [157, 160, 163, 165-170]. In a similar experiment, the induction of Hsp 70 in femtosecond laser treated embryos could be analyzed to determine the degree of heat and mechanically induced physiological stresses. By comparing control embryos to laser pulse manipulated embryos, the presence and amount of Hsp 70 could be quantified, thereby providing an understanding of the amount of heat and mechanical stress imparted by femtosecond laser pulses. This physiological study would complement the morphological study presented in Chapter 5.

Preliminary experiments were conducted to determine the amount of Hsp 70 production induced in laser treated chorionated zebrfish embryos (2/4-cell stage) (unpublished[1]). Interestingly, manipulated embryos showed no Hsp 70 induction response (as determined through Western blots[2]). This result was also found for control heat shocked (37 ° C water bath for 1 hr) chorionated embryos[3] (2/4-cell stage). Whether the above results indicate that the induction levels were too low for analysis or that the Hsp70 proteins were turned-over due to long incubation times following the stressor was unknown. Alternatively, the induction response may not be present in early zebrafish development, with Hsp 70 up-regulation occurring only in cell stages after midblastula transition (512-cell stage [90][1]). Further experiments are required to address the above issues.

---

[1] The heat shock study was conducted in collaboration with Dr. Greg Goss and Elizabeth Eorr at the University of Alberta, department of Zoology.

[2] Elizabeth Eorr performed the Western blot studies.

[3] It is important to note that the laser-maniputed and heat shocked embryos continued to develop normally following stress treatment. However, on a few occasions, after 6 to 8 hrs of incubation at 28.5 ± 1 ° C following the stressor, 6 to 7 % of the heat shocked embryos died or were developmentally arrested.

Future prospects

Currently, the major hindrances to the widespread application of femtosecond laser technology to the study of biological materials are the laser's overall size and cost. For instance, high repetition rate laser oscillators can be up to 2 m in length, which makes the transportation of this device difficult. Ideally, if the femtosecond laser is to be used as a clinical tool by biophysicists, biomedical engineers, biologists and chemists in academia, research organizations or governmental labs, then the miniaturization of the technology must be addressed. A commercially available femtosecond laser system that is compact and which can be integrated with optical microscopes would represent a novel tool for studies in human health research. Applications that could directly benefit from a transportable tabletop turn-key femtosecond laser system include research in drug delivery, cancer therapy and transgenics.

A few companies have already realized the importance of developing a compact femtosecond laser system. Currently, femtosecond fiber lasers operating at a pulse duration as short as sub-100 femtoseconds have been designed. Fiber laser systems are reported to be robust and transportable. The typical dimension of the entire fiber based system is as small as 76 (L) x 55 (H) x 22 (W) cm. It is conceivable that currently developed fiber lasers could be integrated into an upright or inverted optical microscope or be used as a standalone optical source to be used in laser-tissue interaction studies.

---

[1] According to Kimmel *et al.* [90], at midblastula (512-cell stage) RNA synthesis increases, which is likely due to the embryo being primed for cell movements.

Forseeable methods for integrating the fiber laser to achieve desired applications are shown in Figures 6.1 and 6.2. In Figure 6.1, a femtosecond fiber laser is coupled to a microfluidic device. Each channel of the microfluidic device could contain various chemical compounds including fluorescent dyes, proteins, DNA or RNA for their introduction into various cell systems. Femtosecond laser pulses produced from the fiber source could be localized to the central region of the microfluidic device (transparent central region of Figure 6.1) for laser pulse irradiation of the chosen biological system.

Analogous to the experimental setups shown in Figures 2.2 through 2.5 in Chapter 2 and Figures 4.7 through 4.10 in Chapter 4, respectively, the entire laser oscillator could be replaced with the femtosecond fiber laser, as depicted in Figure 6.2 of this chapter. In this configuration the laser source could be used to achieve the same applications demonstrated in this thesis, but with a compact, transportable laser system. The pulses from the fiber could be directed onto the membrane of the cell for laser pulse induced poration (bottom illustration of Figure 6.2), or could be localized to the intracellular environment for sub-cellular ablation.

With continued interest in the use of the femtosecond laser for the study of biological material, it can be envisioned that in the near future this tool will be integrated into lifesciences, establishing its status among the prevalent molecular and genetic cell manipulation methods. Through the collaboration of physicists, engineers and cell and developmental biologists, this joint venture will uncover new prospectives and solutions for understanding essential biological systems.

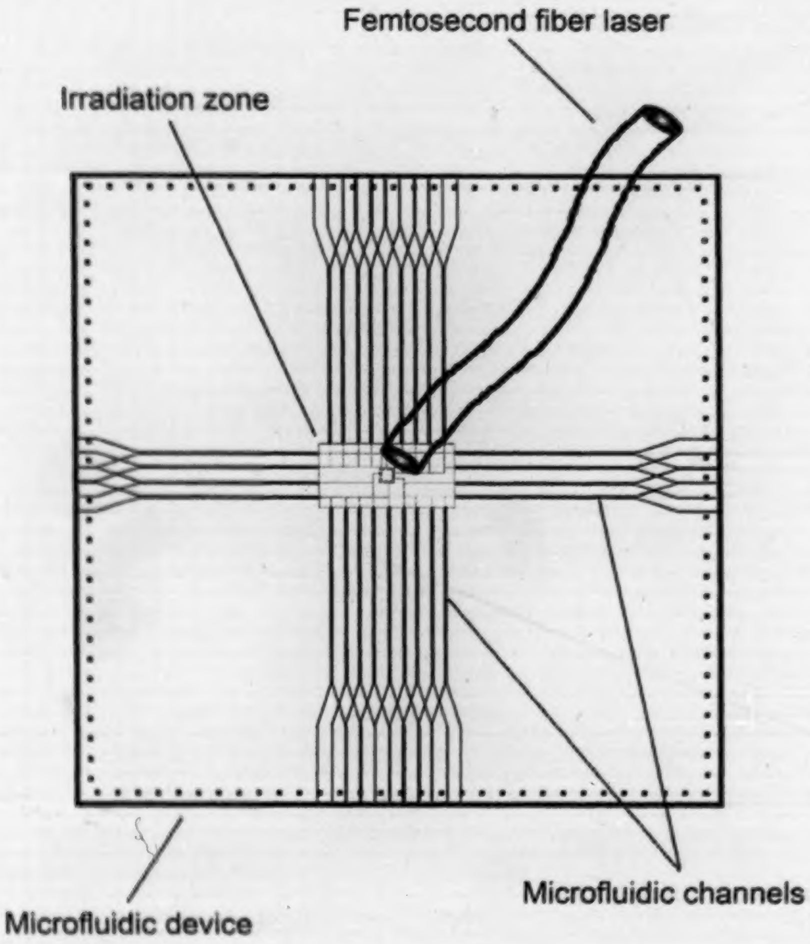
Femtosecond fiber laser
Irradiation zone
Microfluidic device
Microfluidic channels

Figure 6.1: Coupling of a femtosecond fiber laser to a microfluidic channel. Each channel can contain a different chemical compound or cell model system. The application of femtosecond laser pulses is localized to the irradiation zone for the intended application.

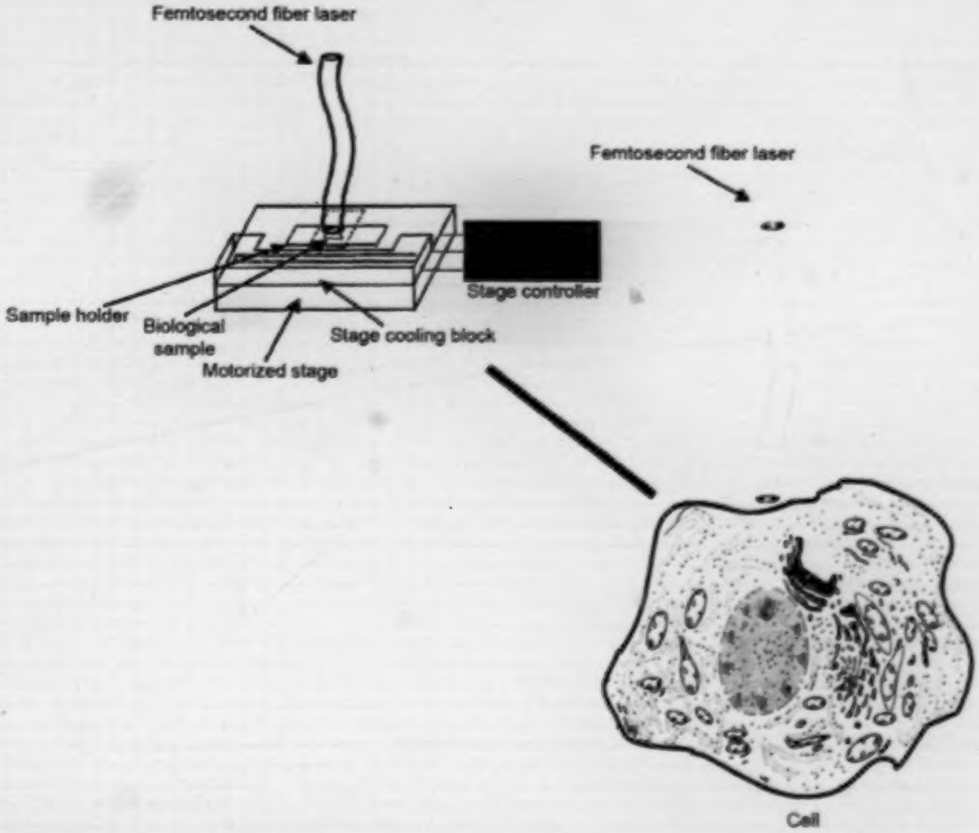
Femtosecond fiber laser
Femtosecond fiber laser
Stage controller
Sample holder
Biological sample
Stage cooling block
Motorized stage
Cell

Figure 6.2: Femtosecond fiber laser in an analogous experimental setup to those shown in Figures 2.2 through 2.5 in Chapter 2 and Figures 4.7 through 4.10 in Chapter 4, respectively. The entire laser oscillator is replaced with the femtosecond fiber laser depicted above. Biological samples placed on the motorized stage are cooled to a set temperature in the manner previously described in section 2.1 in Chapter 2. A stage controller allows for accurate positioning of the biological material under the fiber laser source. The bottom right corner of the image is a magnified view of the interacting region between the fiber and the model system studied (in this case a cell). Laser pulses could be localized onto the biological membrane, or into the intracellular space for sub-cellular ablation studies.

APPENDIX A

A.1 ESTIMATE OF THE PULSE DURATION

The laser oscillator used for the studies in Chapters 2, 3, 4 and 5 can produce laser pulses as short as sub-10 femtoseconds at a center wavelength of ~ 800 nm with a pulse repetition rate of ~ 80 MHz. Assuming a 10 femtosecond laser pulse, the pulse broadening due to optical elements placed in the beam path can be estimated. The source of this pulse broadening is the microscope objective, which consists of several focusing lenses to achieve a diffraction limited irradiance spot size at the focal plane. Two different microscope objectives were used in this thesis, a 0.95 NA 100X air microscope objective and a 1.0 NA 60X water immersion microscope objective. Both of these objectives contained BK7 glass (personal communication with Nikon, Canada), and the total glass thickness in the objective tube ranged from 2 to 2.78 cm for NAs ranging from 0.95 to 1.25 with a typical magnification of 100X (higher NA objectives contain more glass) [171]. Based on the thickness of the glass, an estimate of the broadened pulse duration can be made provided that the group delay dispersion (GDD) of BK7 glass is known.

Xu *et al.* [172] found that when sub-10 femtosecond laser pulses at a center wavelength of 780 nm propagated through 24 mm of BK7 glass, the pulse dispersed. The measured GDD value found by the authors was 465 fs^2/cm [172]. With a known GDD value, the total group velocity dispersion (GVD) induced by the microscope objectives can be estimated based on the total thickness of the glass. Multiplying the GDD value by the glass thickness (2 and 2.78 cm from above) yields the GVD, which ranges from 930 to 1292 fs^2.

Using equation (A.1), the broadened pulse duration can be estimated as [173]

$$\tau_{out} = \tau_{in}\left(1 + 7.68\left[\frac{D}{\tau_{in}^2}\right]^2\right)^{1/2} \tag{A.1}$$

where τ_{out}, τ_{in} and D represent the output pulse duration, the input pulse duration and the GVD coefficient, respectively. With an input pulse duration of 10 femtoseconds and the GVD coefficient ranging from 930 to 1292 fs^2, the pulse duration after the microscope objective is estimated to be between 258 and 358 femtoseconds. The upper limit of the output pulse duration (i.e. 358 femtoseconds) would be the broadened pulse from a 1.25 NA 100X microscope objective [171]. It is therefore expected that the broadened pulse duration for this thesis would be shorter than 358 femtoseconds.

To contrast the GVD values given above to experimental results, Guild *et al.* [174], measured the amount of delay dispersion induced by high NA microscope objectives. The objective tested in Guild *et al.* [174] study that most closely matched the specifications used in this thesis was a 0.9 NA microscope objective at 40X magnification. At a wavelength of 780 nm, the delay dispersion was measured to be 950 ± 100 fs^2 [174]. Taking the upper limit of the dispersion value (i.e. 1050 fs^2) to better represent the microscope objectives used in this thesis, the output broadened pulse duration, as calculated from equation (A.1), was 291 femtoseconds. This value should slightly underestimate the true broadened pulse, as Guild *et al.* [174] measurements were based on a 0.9 NA objective, and not a 0.95 or 1.0 NA microscope objective. However, it is reasonable to assume that the pulse duration at the focus would be close to 291 femtoseconds.

An estimated broadened pulse duration value of 291 femtoseconds was used throughout this thesis to calculate the peak intensity, the ionized electron density and the temperature rise within the focal plane. Since these parameters were calculated based on an estimated value for the broadened pulse duration, it should be noted that they do not represent exact values, but rather are close estimates of what may be expected.

In equation (A.1), the input pulse duration was chosen as 10 femtoseconds, which was considered the bandwidth limited pulse duration. This value can be calculated based on the Titanium:Sapphire laser oscillator output spectrum as measured by the Ocean Optics S2000 spectrometer (Ocean Optics Inc., Dunedin, FL). The emitted wavelength spectrum was found to be between 700 and 900 nm. Therefore, the total wavelength bandwidth, $\Delta\lambda$, was 200 nm. Using equation (A.2) and differentiating to yield equation (A.3), allows an estimate of the frequency bandwidth to be made

$$\nu = \frac{c}{\lambda} \tag{A.2}$$

$$\Delta\nu = \frac{c}{\lambda^2}\Delta\lambda \tag{A.3}$$

where $\nu, c, \lambda, \Delta\lambda$ and $\Delta\nu$ represent the frequency, the speed of light, the center wavelength, the wavelength bandwidth and the frequency bandwidth, respectively. (In equation (A.3) the negative sign is neglected since it is the magnitude of the frequency bandwidth that was considered). With $\Delta\lambda = 200$ nm and $\lambda = 800$ nm, $\Delta\nu = 9.36\text{x}10^{13}$ Hz. Therefore, the bandwidth limited pulse duration, $\tau = \frac{1}{\Delta\nu}$, is 10.6 femtoseconds.

A.2 SAMPLE CALCULATIONS

In Chapters 2, 3, 4 and 5, rough estimates of the peak intensity at the focus, the ionized electron density and the temperature rise after a single femtosecond laser pulse were given. Sample calculations of these values are provided below.

Assuming a pulse energy of 0.56 nJ/pulse (a pulse energy that was used in both Chapters 4 and 5) and a pulse duration of 291 femtoseconds (see section A.1 of Appendix A), the peak power (P_P) at the focus is

$$P_P = \frac{0.56x10^{-9}}{291} = 1.9\ \text{kW/pulse} \tag{A.1}$$

The peak intensity at the focus can be calculated with knowledge of the diffraction limited irradiance spot size given that the radial (d_r) and depth dimension (d_z) of the focused laser spot are of the form [4, 5]

$$d_r = \frac{1.22\lambda}{NA} \quad \text{and} \quad d_z \approx 2\left(\frac{\pi w_0^2}{\lambda}\right) \tag{A.2}$$

where, for example, $NA = 1.0$, $\lambda = 800$ nm and $w_0 = 488$ nm $(d_r/2)$ are the numerical aperture, wavelength of light and the radius of the beam waist, respectively, then $d_r = 976$ nm and $d_z = 1870$ nm. These values represent the irradiance spot size dimension and not the spot size that is reduced through the non-linear multiphoton absorption process (see text in Chapter 1). As viewed in a direction parallel to the ablated surface, the spot size that is observed is d_r. Therefore, since $d_r = 976$ nm (976 nm is the spot size diameter and not the radius as commonly defined in the beam waist), the peak intensity based on the area of d_r is

$$I_p = \frac{P_p}{\text{Area of } d_r} \qquad \text{(A.3)}$$

equal to $2.5\text{x}10^{11}$ W/cm^2.

With the peak intensity defined, the maximum electron density after a single femtosecond laser pulse can be estimated. According to Vogel *et al*. [5], the threshold peak intensity (I_R) required to produce a critical electron density of 10^{21} cm^{-3} (as defined by equation (1.1) in Chapter 1 [7, 13]) at a center wavelength of 800 nm is $I_R = 6.5\text{x}10^{21}$ W/cm^2. In Figure 3(c) of reference [5], the plot of the maximum ionized electron density (ρ_{max}) as a function of I/I_R can provide an estimate of the electron density. With the ratio $I/I_R = 0.04$ (where $I = I_p$, calculated from equation (A.3)), this value corresponds to a maximum electron density of 10^{12} cm^{-3}. This value is based on the graph presented in reference [5]. To relate the electron density to the volumetric energy density, Vogel and colleagues [5] state that the volumetric energy density scales linearly with the maximum ionized electron density. This is an approximation and can be understood by realizing that the energy imparted to the biological material is contained in the ionized electrons. Therefore, energy deposited into the material is distributed among the ionized electrons. For the electrons to be considered quasi ionized, the 10^{12} cm^{-3} electrons (as calculated above) must be located in the conduction band with a minimum kinetic energy equal to the ionization potential of the media (in this case water) [5].

To place the above statements in context, Figure A.1 provides a visual diagram of the ablation events that occur during ionization. In relation to the figure: (A) femtosecond laser pulses are focused onto the cellular material resulting in the excitation of valence

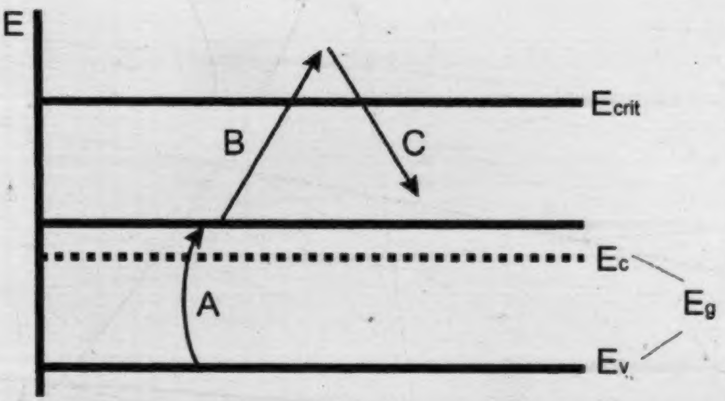

Figure A.1: Diagram depicting the sequence of events involving laser pulse induced ionization. The diagram depicts the case where the Keldysh parameter, γ, is not greater than 1.5. Therefore, the band gap energy of water cannot be used to approximate the effective ionization potential. See text for description. Image adapted from [5, 7].

electrons (E_v; valence energy) to a higher energy state within the conduction band (E_c) [5, 7]. (B) With the electrons in the conduction band, these electrons will absorb laser photons through single photon absorption, achieving a higher energy state within the conduction band [7]. Eventually at an energy above or equal to the critical energy (E_{crit}), impact ionization occurs [5]. (C) Above the critical energy, the electrons impact ionize valence electrons to the conduction band [5]. In the above figure, E_g, is the band gap energy equal to 6.5 eV (assuming water is the ionizing media) as determined by Boyle *et al.* [18]. According to simulations, the ionized electron, (A), is promoted to an energy state slightly higher than the bandgap. The difference in the gained energy (E_v to the energy state above E_c) is referred to as the effective ionization potential [5]. The effective ionization potential depends on the band gap energy and the Keldysh parameter, γ, [5, 7]. The critical energy for impact ionization is defined as 1.5 times the effective ionization potential, and arises from an analysis of the band structure of water. (A full analysis of the band structure is beyond the scope of this thesis. Further information can be found in reference [5, 52]). From Figure A.1, and noting that the ionized electrons must possess a kinetic energy approximately equal to the effective ionization potential, the volumetric energy density as defined by Vogel and colleagues [5] is

$$\varepsilon = \rho_{max}(9/4)\tilde{\Delta} \tag{A.4}$$

where $\tilde{\Delta}$ is the effective ionization potential [5]. Equation (A.4) describes the energy density per unit volume that arises from the ionized electrons with an average kinetic energy of $(9/4)\tilde{\Delta}$. Substituting 10^{12} cm^{-3} for ρ_{max} and assuming $\gamma > 1.5$ (the effective ionization potential is approximated to equal the band gap energy of water) yields a volumetric energy density value of $2.34\text{x}10^{-6}$ J/cm^3. The temperature rise after a single femtosecond pulse is [5]

$$\Delta T = \frac{\varepsilon}{\rho_0 C_p} \tag{A.5}$$

where ρ_0 (1 g/cm^3) and C_p (4.184 J/K $\cdot$ g) are the density of water and the specific heat capacity, respectively. Using the value calculated in equation (A.4), the temperature rise after a single femtosecond laser pulse is $5.6\text{x}10^{-7}$ K.

As previously mentioned in the text of Chapter 1, the value of the ionized electron density represents an overestimate of the true value. This overestimate arises from the fact that Vogel *et al.* [5] used a pulse duration of 100 femtoseconds and not 291 femtoseconds. Regardless, the above values provide informative results regarding the magnitude of the ionized electron density.

APPENDIX B

B.1 CALCULATION OF THE SUCROSE DIAMETER

The diameter of sucrose was estimated by adding all bond lengths along the long axis of the molecule. Figure B.1 depicts the structure of a sucrose molecule [175], as well as the bond length calculation path. Table B.1 presents typical bond lengths [176] measured in angstroms. Adding all of the bonds lengths along the long axis of Figure B.1 yields the long axis diameter of sucrose

$$\begin{aligned} S_{Diameter} &= 2(\text{O-H}) + 2(\text{C-C}) + 8(\text{C-O}) \\ &= 2(0.96\text{ Å}) + 2(1.54\text{ Å}) + 8(1.43\text{ Å}) \\ &= 1.92\text{ Å} + 3.08\text{ Å} + 11.44\text{ Å} \\ &= 1.6\text{ nm} \end{aligned} \qquad \text{(B.1)}$$

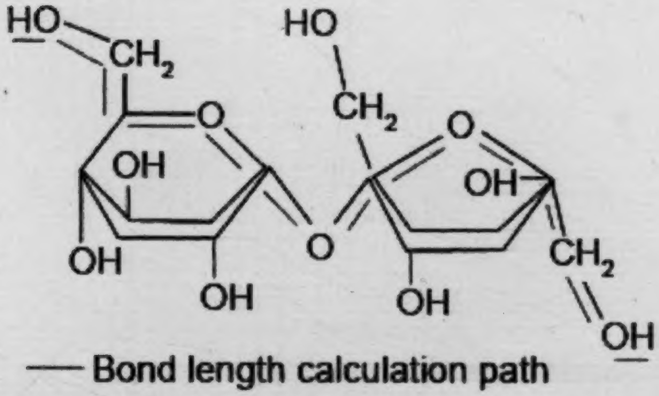

Figure B.1: Structure of a sucrose molecule. Red lines indicate the bond length calculation path used in estimating the sucrose diameter.

BOND LENGTHS (Å)	
Bond	Length
C-C	1.54
O-H	0.96
C-O	1.43

Table B.1: Common bond lengths. Values reproduced from [176].

APPENDIX C

C.1 PORATION INJURY: INDUCED PRESSURE ON THE LASER PULSE INDUCED PORE

According to Finkelstein [64], the equation describing the water flux through a pore is

$$J_w = (1\text{x}10^{-3})\frac{nA}{\delta L}D_w\frac{\Delta C_s}{\Delta x} \quad (\frac{\text{mol}}{\text{cm}^2 \cdot \text{s}}) \qquad \text{(C.1)}$$

where n, A, L, D_w, δ and $\frac{\Delta C_s}{\Delta x}$ represent the number of pores, the area of the pore, the length of the pore, the diffusion coefficient of water, the distance over which the diffusion is calculated and the solute concentration difference as a function of distance, respectively (the pre-factor of $1\text{x}10^{-3}$ arises from the conversion of mol/L to mol/cm^3 with 1 mL = 1 cm^3). The diffusion coefficient of water is the diffusivity value in both sucrose and lipids. Water must passively diffuse through the laser pulse induced pore in the presence of the carbohydrate and the hydrophobic region of the plasma membrane. Using equation (C.1), the velocity of the water molecule, v, passing through the pore is

$$v = \frac{J_w AL}{n_w} \quad (\frac{\text{cm}}{\text{s}}) \qquad \text{(C.2)}$$

with n_w representing the number of moles of water. Assuming that water can be modeled as a sphere of known diameter (as was done for sucrose; Appendix B), the sphere will experience a force [177] (i.e. drag force; the force imparted on the water molecule in the opposite direction to its motion due the presence of lipids and sucrose) according to Stokes relation [177]

$$v = \frac{F}{6R\pi\eta} \quad (\frac{\text{cm}}{\text{s}}) \tag{C.3}$$

where F, R and η are the force, the radius of the water molecule and the viscosity of the solution in which the water is diffusing, repectively. Equating equations (C.2) and (C.3) yields

$$F = \frac{J_w AL6R\pi\eta}{n_w} \quad (\text{N}) \tag{C.4}$$

the imparted force established during diffusion. Dividing equation (C.4) by the area of the pore gives the imparted pressure

$$P_w = \frac{J_w L6R\pi\eta}{n_w} \quad (\frac{\text{N}}{\text{m}^2}) \tag{C.5}$$

with the magnitude of the pressure linearly dependent on the concentration gradient of the solutes

$$P_w = (1\text{x}10^{-3}) \frac{n6\pi AD_w \eta R}{\delta n_w} \frac{\Delta \text{C}_s}{\Delta \text{x}} \quad (\frac{\text{N}}{\text{m}^2}). \tag{C.6}$$

The above equation represents the induced pressure due to diffusing water. This pressure is confined to the area of the pore, as justified in Chapter 3.

APPENDIX D

D.1 SUCROSE AND WATER VOLUME CONTRIBUTION

To calculate the contribution of sucrose and water to the post-permeabilized cell volume, it was assumed that the isotonic volume of the cell was 1715 µm^3 [78]. Suspending a cell in a hyperosmotic sucrose solution (0.2 M) elicited a dehydration response, with the assumption that the cell will dehydrate to 40 % of its isotonic volume [44]. When the cell was permeabilized, the volume of the cell increased due to the passage of both the solute and water into the intracellular environment. From Figure 3.6 in Chapter 3, the kinetics of a cell permeabilized in 0.2 M sucrose resulted in a volume change of ~ 60 %. Therefore,

Isotonic volume = 1715 µm^3
Hypertonic volume = 0.40(1715 µm^3) = 1029 µm^3
New equilibrium volume change = 0.6(1029 µm^3) = 617.4 µm^3
New total equilibrium volume post-laser pulse permeabilization = 1646.4 µm^3

where the new hypertonic volume is smaller than the isotonic volume, as expected. The change in volume of 617.4 µm^3 was necessarily due to the volume of sucrose and water added during permeabilization, 617.4 µm^3 = $V_{sucrose} + V_{water}$. Assuming a spherical geometry for the cells, the diameter of the cell at the new hypertonic volume (1646.5 µm^3) was 14.65 µm. Using Figure 3.10 in Chapter 3, the theoretical sucrose concentration delivered into the cell at 14.65 µm was estimated to be 0.142 M (this value represented the equilibrated concentration). From the concentration, the contribution of sucrose to the total volume of the cell can be calculated

Concentration: 0.142 M = 1.42x10^{-4} mol·cm^{-3}

# of molecules per volume: $(1.42\text{x}10^{-4}\ \text{mol}\cdot\text{cm}^{-3})(6.02\text{x}10^{23}\ \text{molec}\cdot\text{mol}^{-1})$
$= 8.54\text{x}10^{19}\text{molec}\cdot\text{cm}^{-3}$

# of molecules: $(8.54\text{x}10^{19}\text{molec}\cdot\text{cm}^{-3})(1.646\text{x}10^{-9}\text{cm}^{3}) = 1.407\text{x}10^{11}$ molec

# of moles: $(1.407\text{x}10^{11}\ \text{molec})/(6.02\text{x}10^{23}\ \text{molec}\cdot\text{mol}^{-1}) = 2.33\text{x}10^{-13}$ moles

# of grams: $(2.33\text{x}10^{-13}\ \text{moles})(342\ \text{g/mol}) = 7.99\text{x}10^{-11}$ g

$V_{sucrose} = (7.99\text{x}10^{-11}\ \text{g})/(1.587\ \text{g}\cdot\text{cm}^{-3}) = 5.038\text{x}10^{-11}\ \text{cm}^{3}$

Given that the total volume change was 617.4 μm^{-3}, the total volume due to water, V_{water} was

$V_{water} = (6.174\text{x}10^{-10}\ \text{cm}^{3}) - (5.038\text{x}10^{-11}\ \text{cm}^{3}) = 5.67\text{x}10^{-10}\ \text{cm}^{3}$

# of grams: $5.67\text{x}10^{-10}$ g

# of moles: $(5.67\text{x}10^{-10}\ \text{g})/(18\ \text{g}\cdot\text{mol}^{-1}) = 3.15\text{x}10^{-11}$ mol
# of molecules: $(6.02\text{x}10^{23}\ \text{molec}\cdot\text{mol}^{-1})(3.15\text{x}10^{-11}\ \text{mol}) = 1.896\text{x}10^{13}$ molec

and the total percentage of volume change post-laser pulse permeabilization due to water and sucrose was

Volume contribution of water = $[(5.67\text{x}10^{-10}\ \text{cm}^{3})/(6.174\text{x}10^{-10}\ \text{cm}^{3})](100) = 92\ \%$
Volume contribution of sucrose = 8 %.

with the theoretical number of water molecules diffusing into the cell per sucrose molecule equaling 135. Therefore, the relative volumetric contribution of sucrose was negligible in comparison to that of water.

APPENDIX E

E.1 FILTER CUBE

Figure E.1 depicts the general layout of the fluorescence filter cube. The filter consists of exciter and emitter filters, as well as a dichroic mirror. All filters were housed in a cube chamber (termed the filter housing), which fit into the Nikon upright 80i filter wheel. The excitation wavelength was emitted from a mercury gas discharged fluorescence lamp house, with emission intensity peaks ranging from the ultraviolet to the near-infrared (Nikon, Japan). An exciter filter placed at the input of the cube transmited wavelengths within the transmission band of the filter, and the mirror reflected the transmitted light to the sample. Excitation of the sample resulted in fluorescence emission at a given wavelength (depending on the fluorophore), which was transmitted through the mirror towards the emitter. The emitter, which possessed a transmission band, filtered the reflected wavelengths emitted by the sample.

To place the above excitation and emission processes in context, a FITC filter (Chroma Technology Corp., Rockingham, VT; part number 41001) has an exciter wavelength between 457 to 503 nm and an emitter wavelength between 509 to 567 nm. The mirror that reflects and transmits the light for fluorescence capture has a transmission percentage of 0 % within the exciter bandpass, and 90 % within the emitter bandpass (Chroma Technology Corp., Rockhingham, VT). Therefore, in relation to Figure E.1, the exciter allows wavelengths between 457 to 503 nm to be transmitted, while blocking all other wavelengths of light. Since the mirror alows zero transmission for the bandpass wavelengths of the exciter, all of the light is reflected towards the sample. Excitation of the sample results in fluorescence emission, which in this example is assumed to span the green and red wavelength range. Within the transmission bandpass of the mirror, all

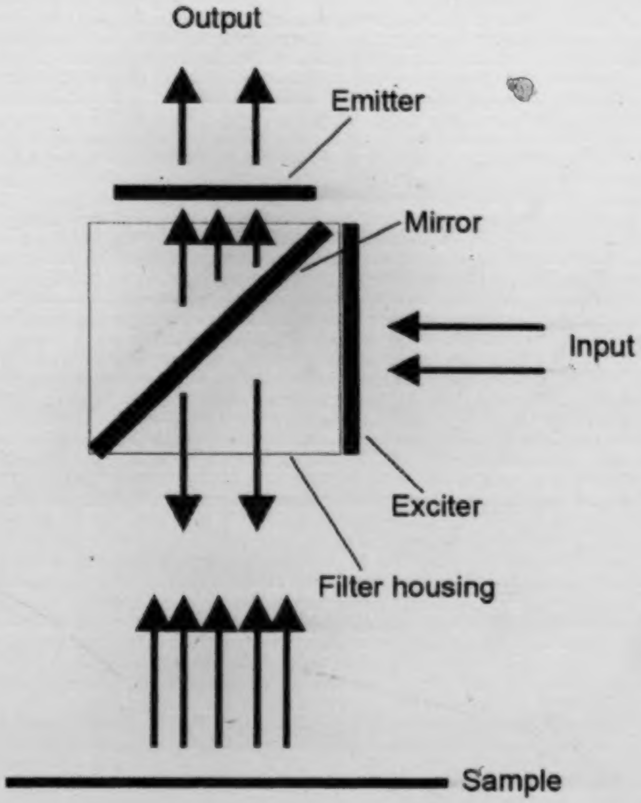
Output
Emitter
Mirror
Input
Exciter
Filter housing
Sample

Figure E.1: Graphic depicting the general layout and mechanism of the fluorescence filter cube.

wavelengths are transmitted and filtered by the emitter bandpass filter, allowing wavelengths between 509 and 567 nm to be detected by the digital camera.

E.2 FLUORESCENCE FILTERS: EXCITATION AND EMISSION WAVELENGTHS

In the studies in chapters 3, 4 and 5, various fluorescence filters were used for epi-fluorescence imaging. All filters were enclosed in a filter housing (previously mentioned in section E.1 of Appendix E) designed for the Nikon upright 80i microscope. Fluorescence filters were purchased from Chroma Technology Corp., Rockingham, VT. The respective exciter and emitter fluorescence wavelengths of each of the filters used are indicated below.

DAPI/TRITC/FITC (part number 6100v2)
Exciter wavelengths: 379 to 401 nm; 474 to 493 nm; 541 to 570 nm
Emitter wavelengths: 452 to 472 nm; 510 to 536 nm; 584 to 627 nm

FITC (part number 41001)
Exciter wavelength: 457 to 503 nm
Emitter wavelength: 509 to 567 nm

Qdot 605 (part number 32108a)
Exciter wavelength: 388 to 454 nm
Emitter wavelength: 574 to 634 nm

GFP (part number 41018; Endow GFP longpass)
Exciter wavelength: 447 to 493 nm
Emitter wavelength: 497 to 1,200 nm

APPENDIX F

CHAPTER 2

MATERIALS AND METHODS

Materials and Methods[1,2]

Preparing the Biosafety Cabinet

To ensure a sterile environment for preparing living cells, the biosafety cabinet was turned on thirty minutes prior to cell culturing. The cabinet chamber was disinfected with a 1:16 ratio of PerCept. PerCept was applied to the cabinet for ten minutes before being removed from the chamber surface using a sterile cloth.

Preparation of culture media

Culture media consisted of Minimal Essential Media (Cat No: 10370-021, Lot No: 1164284, Invitrogen Coporation), Fetal Bovine Serum (Cat No: SV30014.03, Lot No: FMF16368, Hyclone) and L-Glutamine (Lot No: ANA17966, Hyclone). 500 mL of Minimal Essential Media stored at 4 °C and Fetal Bovine Serum and L-Glutamine stored at –21 °C were thawed in a 37 °C water bath. 55 mL of Fetal Bovine Serum was added to the 500 mL Minimal Essential Media. The media was inverted several times to ensure proper solution mixing. 5.5 mL of L-Glutamine was then added to the Minimal Essential Media-Fetal Bovine Serum mixture and inverted numerous times. Remaining Fetal Bovine Serum and L-Glutamine were stored at –21 °C. Culture media was stored at 4 °C.

Culture preparation

The biosafety cabinet was sterilized for ten minutes with a 1:16 ratio of PerCept. Three Falcon culture flasks (Lot No: 353136) with vented caps were sterilized with PerCept and set aside. The culture flasks were labeled as Madin-Darby Canine Kidney

---

[1] Portions of this section have been published in Kohli *et al.* Laser Surg Med. 2005, 37:227-230.

[2] Special thanks to Dr. Akcer and Jayme Tchir for their assistance and training in cell culture preparation.

Cells (MDCK; American Type Culture (ATCC) CCL-34), Chinese hamster fibroblasts (V79-4; American Type Culture Collection (ATCC) CCL-93) and Control. MDCK and V79-4 cells were obtained from a frozen stock preserved in dimethyl sulfoxide at liquid nitrogen temperature. Culture media and frozen cells were warmed to 37 °C using a water bath and transferred to the biosafety cabinet to be sterilized with 1:16 PerCept. 10 mL of the culture media was pipetted into each culture flask using the same pipette. 1 mL of thawed MDCK and V79-4 cells were transferred to their respective labeled culture flask with a resulting cell density of 9×10^4 cells in 11 mL of media (10^6 cells/mL). The control flask was observed under brightfield microscopy to ensure that the media was not contaminated with cells. All three flasks were incubated at 37 °C in a water jacketed incubator in an atmosphere of 95 % air plus 5 % carbon dioxide. Following four to five hours of incubation, the culture flasks were examined under an inverted microscope for the presence of contamination. Media appearing cloudy or containing fungal contaminants (evident as filament structures) were discarded and the culture process was restarted.

Media exchange

Since the cells were obtained from frozen stocks preserved in cryoprotective dimethyl sulfoxide, a media exchange was required to remove this agent in order to avoid toxic effects on cell growth. Culture media was warmed to 37 °C in a water bath. Culture flasks containing cells were removed from the incubator and placed in the sterilized biosafety cabinet. Each flask was properly sterilized using PerCept. Using a 10 mL pipette, the cell culture media was carefully removed from the side opposite the surface containing the adherent cells and discarded. With a new sterilized 10 mL pipette, fresh culture media was carefully added to the flasks on the opposite surface to the adherent cells. Culture flasks were placed back in the incubator to allow for cell growth.

Preparation of a subculture

Culture flasks containing cells were removed from the incubator and placed in the sterilized biosafety cabinet. Flasks were sterilized using PerCept. Trypsin-EDTA (Cat No: 25200-72, Lot No: 1162882, GIBCO) stored at –21 °C and culture media at 4 °C were thawed and warmed in a 37 °C water bath. Using a 10 mL pipette, cell culture media was removed from each flask from the opposite side of the adherent cells and discarded. Cells were gently rinsed with 5 mL of 1X Phosphate Buffer Saline, which was added to the flask surface lacking cells. The culture flask was carefully agitated for 30 seconds to rinse the cells, followed by the removal and discard of Phosphate Buffer Saline. 2 mL of Trypsin-EDTA was then added to each culture flask on the side opposite the adherent cells. Flasks were agitated for 60 seconds and Trypsin-EDTA was removed and discarded. The addition and removal of Trypsin-EDTA was repeated. After the second removal of Trypsin-EDTA, the culture flasks were placed in the incubator for 5 to 10 minutes. During this time, the flasks were periodically examined under inverted brightfield microscopy to ensure that the cells had begun to detach. After observing detachment and rounding of the cells, 5 mL of fresh culture media was added to the flasks. Cells were gently pipetted to remove cell aggregates and the media containing the cells was transferred to a 15 mL falcon tube. A small volume of the cell suspension was injected into the wells of a hemocytometer. Under inverted brightfield microscopy the number of cells within the hemocytometer grid was counted and multiplied by 10,000 to yield the cell density per milliliter. The volume of cells required for the preparation of a new subculture was determined by dividing $4x10^5$ by the cell density per milliliter as determined from the hemocytometer count[1]. The calculated volume of cells was added to a new culture flask containing 10 mL of fresh culture media. All flasks were placed in the incubator until the next subculture process.

Harvesting and plating of cells

Cells in exponential growth phase were harvested by using the previously outlined subculture process. Trypsin-EDTA treated cells were plated onto sterile untreated glass coverslips (12 mm^2 Fisher Brand) and cultured at 37 °C for 12 hrs to allow the cells to attach to the substrate.

Laser pulse surgery of living cells

Membrane surgery and cell isolation of MDCK and V79-4 cells was achieved using a modelocked Titanium:Sapphire laser oscillator. The oscillator produced sub-10 femtosecond laser pulses with a center wavelength at 800 nm and a pulse repetition rate of 80 MHz. Laser pulses with a pulse energy of 5 nJ/pulse[2] were directed and coupled to a modified Zeiss upright microscope (see Figures 2.2 through 2.5), and focused onto the biological specimen using a 0.95 100X high numerical aperture (NA) air microscope objective. From equation (1.2) in Chapter 1, the diffraction limited irradiance spot size (diameter) at the focus of the objective was estimated to be d_r = 1027 nm (λ = 800 nm) with a peak power at the focal plane of 17 kW/pulse (these values were calculated using an estimated broadened pulse duration of 291 femtoseconds; see Appendix A for details). The estimated peak intensity at the focus based on the peak power and the irradiance spot size was 2.1×10^{12} W/cm^2.

---

[1] $4x10^5$ represents the number of cells that must be added to sustain a cell culture for 2 to 3 days before becoming confluent.

[2] This pulse energy represents the value measured entering the microscope objective lens. Fresnel's equations describing the reflection and transmission values through various index media can be used to approximate the amount of average laser power loss. From calculations (not presented in this thesis), the total average laser power loss was a few milliwatts.

For laser pulse surgery, the biological material was cultured on sterile coverslips and placed under the microscope objective and hydrated with a small volume (~ 10-20 μL) of fresh culture media. Cells were placed on an *x-y-z* motorized stage, which was temperature cooled to 4 °C to minimize cell dehydration. White light illuminated the sample in the inverted position, where both the laser light and white light were captured by a charge coupled device (CCD). The CCD was interfaced with a computer, which allowed for the capture of still images, as well as real time video. Images were processed using Photoshop CS2 (Adobe Systems Inc., USA) and CorelDraw (Corel Corp., Canada). A more detailed description of the experimental design can be found in section 2.2 of Chapter 2.

CHAPTER 3

MATERIALS AND METHODS

Materials and Methods[1]

Cell culture preparation

Madin-Darby Canine Kidney cells (MDCK; American Type Culture Collection (ATCC) CCL-34) were prepared using the culture process previously discussed in Chapter 2 Materials and Methods of Appendix F.

Cell micropatterning[2]

A micropatterning method described in [178] was used to prepare a polydimethylsiloxane elastomeric stamp for creating non-adhesive regions of agarose on glass substrates, which allowed for precise control of cell geometry and the analysis of cell viability.

Photolithography[2]

Four-inch silicon wafers were bathed in a piranha solution consisting of sulphuric acid (J.T. Baker, Phillipsburg, NJ) and hydrogen peroxide (J.T. Baker, Phillipsburg, NJ) in a 3-to-1 ratio for 15 min. The wafers were rinsed in deionized water and dried using nitrogen gas. A layer of hexamethyldisilazane (Arch Chemicals, Norwalk, CT) was spin-coated onto the silicon wafers, which were baked at 150 °C for 10 min to improve photoresist adhesion. Following adhesion, a 10 µm layer of Microposit SJR 5740 positive photoresist (Shipley, Marlborough, MA) was spin-coated onto the wafers and the wafers were baked at 115 °C for 6 min. For pattern transfer, the wafers were exposed for 18 sec to UV light at a constant intensity of 18.1 W/cm^2. The pattern was transferred from an acetate mask (produced by high-resolution printing) producing a matrix 30 x 30 μm squares with a well separation of 60 μm.

---

[1] Portions of this section have been published in Kohli *et al.* Biotechnol. Bioeng. 92:7, 889-899.

[2] Special thanks to Dr. Acker for preparing the micropatterns.

Preparation of the polydimethylsiloxane stamps[1]

Polydimethylsiloxane stamps were prepared by mixing a prepolymer and a curing agent in a 10:1 ratio by weight as indicated by the manufacturer (Corning, NY). The polymer was allowed to cure at 70 °C for 1 hr in a vacuum. Following incubation in the vacuum, the polymer was peeled from the wafers and used in the patterning of glass substrates.

Patterning of glass coverslips with agarose[1]

Polydimethylsiloxane stamps were placed pattern side down on glass coverslips. A 6 mg/ml low-melting point agarose (Invitrogen Corporation, Carlsbad, CA) in 40 % ethanol (VWR, Can Lab, Brampton, Ontario, CA) solution was prepared and injected in the channels of the micropatterns. The injected micropatterns were placed in a vacuum chamber for 18 hr to dry. Following drying, the stamps were peeled from the glass leaving behind patterned agarose on the substrate.

Preparation of SYTO 13™ and Ethidium bromide

A 5 mM stock solution of SYTO 13™ (SYTO 13) (Molecular Probes, Eugene, OR) was diluted to a working solution of 25 μM by adding 5 μL of stock SYTO 13 to

---

[1] Special thanks to Jayme Tchir for preparing the polydimethylsiloxane stamps and for patterning the glass coverslips with agarose.

995 µL of fresh culture media (see Chapter 2 Materials and Methods of Appendix F for culture media preparations). For the preparation of Ethidium bromide (EB) (Molecular Probes, Eugene, OR), a stock solution of 25 mM was diluted to a working solution of 0.25 mM by adding 10 µL of stock EB to 990 µL of fresh culture media.

Cell viability assessment

A dual fluorescent stain composed of SYTO 13™ and Ethidium bromide was used to quantify cell viability and integrity of the cell plasma membrane. SYTO 13 is readily permeable to the cell plasma membrane, staining both RNA and DNA fluorescent green [47]. EB, however, is an impermeable dye, which only penetrates cells with damaged membranes to form a red/orange fluorescent complex with DNA [77]. Percent survival was determined using the SYTO 13/EB dual fluorescent membrane integrity assay by calculating the number of SYTO 13 positive cells over the total number of cells.

Cell volume measurements

The kinetic response of permeabilized micropatterned MDCK cells in a hypertonic solution was analyzed using ImageJ analysis software (National Institutes of Health). From captured video of the shrink/swell response of the permeabilized cells, the change in volume of the cell from hypertonic volume to a new hypertonic equilibrium volume was assessed as a function of time. For each analyzed video frame, the diameter of the cell along both the *x*- and *y*-axis were averaged and the total volume of the cell was calculated from the average diameter assuming a spherical geometry.

Preparation of sucrose

0.2, 0.3, 0.4 and 0.5 M solutions of sucrose were prepared in fresh double distilled water (ddH$_2$O). Given that the molecular weight of sucrose is 342.3 g/mol (Sigma-Aldrich, Ont, Canada), each prepared concentration was multiplied by the molecular weight to yield the number of grams of sucrose to be added to 1 L of ddH$_2$O. The final solution volume was adjusted to 100 mL. Each prepared sucrose solution was checked for proper osmolarity using a microosmometer (Precision Systems Inc., Natick, MA; model # 5004) after calibration against a known standard (i.e. 0.29 M).

Estimating the intracellular solute concentration

A modified diffusion equation was used to estimate the theoretical intracellular concentration of a delivered solute through a laser pulse induced transient pore. From Fick's first law, the solute flux is given by [64, 177, 179]

$$J(x,t) = -D_{sw}\frac{\Delta C_s(x,t)}{\Delta x} \qquad \text{(F.1)}$$

where $J(x,t), D_{sw}, C_s, \frac{\Delta C_s(x,t)}{\Delta x}$ represent the diffusion flux, diffusion coefficient of the solute in water (the assumed solvent), the solute concentration and the change in solute concentration as a function of distance. The negative sign in equation (F.1) accounts for the diffusion of the solutes from a region of high concentration to a region of low concentration. Taking the spatial derivative of both sides of equation (F.1) yields Fick's second law of diffusion [64, 179]

$$\frac{\partial C_s(x,t)}{\partial t} = D_{sw} \frac{\partial^2 C_s(x,t)}{\partial x^2} \tag{F.2}$$

where $\frac{\partial C_s(x,t)}{\partial t} = -\frac{\Delta J}{\Delta x}$ [179].

The right hand side of equation (F.2) is the change in the flux diffusion of the solutes in the solvent. Limiting the analysis to an impermeable solute that is placed in the extracellular environment of the cell (only considering a single solute species dissolved in the solvent), it is assumed that irrespective of the permeabilization kinetics, the intracellular delivered solute concentration will never equal the extracellular concentration (i.e. $M_s^i \neq M_s^e$; where $M_s^e \rangle M_s^i$; M_s^i is the molar concentration of the solute in the intracellular environment and M_s^e is the molar concentration of the solute in the extracellular environment; see text for further details). Therefore, M_s^e represents an infinite source and (F.2) is solved [180, 181] for $C_s(x,t)$ with the conditions that $C_s(0,t) = C_0$, $C_s(\infty,t) = 0$ and $C_s(x,0) = 0$ [180, 181]

$$C_s(x,t) = C_0 erfc\left(\frac{x}{2\sqrt{D_{sw}t}}\right) \tag{F.3}$$

where C_0, $erfc$, x and t are the initial solute concentration, complementary error function, spatial distance and time.

According to Finkelstein [64], equation (F.1) can be modified to represent the diffusion through a cylindrical pore

$$J(x,t) = -\frac{nA}{\delta L} D_{sw} \frac{\Delta C_s(x,t)}{\Delta x} \tag{F.4}$$

where n, A, δ and L represent the number of pores, area of the pore, the region over which the diffusion is calculated and the length of the pore (all of which are constants). Therefore, equation (F.3) can be modified to

$$C_s(x,t) = C_0 erfc\left(\frac{x}{2\sqrt{\frac{nAD_{sw}t}{\delta L}}}\right) \qquad \text{(F.5)}$$

with the pore representing the laser pulse induced transient pore created to introduce the impermeant solute into the intracellular environment of the cell[1].

Calculation of the diffusion coefficient

The diffusion coefficient of sucrose in water was estimated using the Einstein-Stokes relation [177, 182], with sucrose modeled as a sphere of known diameter

$$D_{sw} = \frac{K_B T}{6r\pi\eta} \qquad \text{(F.6)}$$

where K_B, T, r and η are the Boltzmann constant, the temperature, the sucrose radius and the viscosity of the solvent (i.e. water). To determine the diameter of the sucrose molecule, bond lengths were added along the long axis of the molecular structure (see Appendix B) yielding a value of 1.6 nm. Since the permeabilized cells were placed on a temperature controlled stage cooled to 4 °C, T in equation (F.6) was set to 277 K, with the viscosity of the solvent at the same temperature equaling 0.001 N·s/m^2 [177].

---

[1] Note that dimensional analysis of (F.5) yields a dimensionless unit for the expression in brackets as expected.

Substitution of the above constants into equation (F.6) results in a diffusion coefficient of 2.536×10^{-6} cm^2/s.

Reversible permabilization of living cells

The reversible permeabilization of micropatterned MDCK cells was achieved using the experimental setup previously described in detail in Chapter 2. Briefly, femtosecond laser pulses were produced from a Titanium:Sapphire laser oscillator that produced sub-10 femtosecond laser pulses at a repetition rate of 80 MHz. The wavelength spectrum of the emitted pulse was 700 to 900 nn, centered at 800 nm. Femtosecond laser pulses were directed towards a beam splitter and reflected into a 0.95 100X high NA air microscope objective (see Figures 2.2, 2.4 and 2.5 of Chapter 2). The input pulse energy coupled into the objective ranged from 2 to 5 nJ/pulse[1] and was focused onto the plasma membrane of living MDCK cells cultured in fresh culture media and plated onto sterile micropatterned slides (micropatterned MDCK cells were placed on a motorized *x-y-z* stage that was temperature controlled to 4 ° C as previously described in Chapter 3).

Focused femtosecond laser pulses were gated with a mechanical shutter, with a shutter duration ~ 10 ms to minimize the delivered laser energy to the biological sample. At the focus of the objective, the diffraction limited irradiance spot size (diameter) could be estimated based on equation (1.2) that was developed in Chapter 1. The estimated spot size was found to be $d_r = 1027$ nm ($\lambda = 800$ nm) with the peak power at the focus ranging from 6.9 kW/pulse (2 nJ/pulse) to 17 kW/pulse (5 nJ/pulse) (these values were calculated using an estimated broadened pulse duration of 291 femtoseconds; see Appendix A for details). The total number of laser pulses irradiating the cell was ~ 800×10^3 with a total delivered laser energy ranging from 1.6 mJ to 4 mJ. From the peak power and irradiance spot size, the peak intensity at the focus was estimated to be between 8.3×10^{11} W/cm^2 and 2.1×10^{12} W/cm^2.

---

[1] These pulse energies represent the values measured entering the microscope objective lens. Fresnel's equations describing the reflection and transmission values through various index media can be used to approximate the amount of average laser power loss. From calculations (not presented in this thesis), the total average laser power loss was a few milliwatts.

To monitor laser pulse induced permeabilization, a monochrome CCD (WAT-902H Watec Monochrome Camera (Aegis Electronics, AZ); horizontal and vertical pixel dimensions of 8.4 μm x 9.8 μm; ½ inch sensor) was mounted at the exit of the imaging port (see Figures 2.2 through 2.5 of Chapter 2). The CCD was interfaced with a computer to allow for capture of still images as well as real time video. The analysis of cell membrane integrity, as determined by the dual fluorescent stain assay (SYTO 13/EB), was performed using a standard upright Zeiss epi-fluorescence microscope[1,2] equipped with the DAPI/TRITC/FITC filter set (Chroma Technologies Corp, Rockingham, VT).

---

[1] Epi-fluorescence imaging of the cells was conducted in Dr. McGann's laboratory in the department of Laboratory Medicine and Pathology at the University of Alberta.

[2] Special thanks to Dr. McGann for allowing access to his fluorescence microscope.

CHAPTER 4

MATERIALS AND METHODS

Materials and Methods[1]

Zebrafish care[2]

Twenty-five adult male and female AB zebrafish were kept in 22 L of UV-treated reverse osmosis water (subsequently referred to as tank water) at a temperature of 28.5 °C. The pH of the tank water was maintained between 6.8 and 7.2 by buffering the solution with sodium bicarbonate. Adult fish were fed three times a day with live Artemia in the morning and trout chow in the afternoon and evening.

Breeding process

Adult female and male AB zebrafish in a ratio of 2:1 were placed in a breeding tank containing 1 L of tank water. The bottom of the breeding tank contained a 2 mm wire mesh that protected fallen eggs from predation by the adult fish. Zebrafish were kept on a regimented light cycle, 10 hr dark/14 hr light, to ensure proper breeding. A divider was placed in the breeding tank, separating the male fish from the females, to prevent the laying and fertilization of eggs during the night. At the onset of the light cycle, the tank water was immediately changed and the dividers were removed. Approximately 20 min after the light cycle, the embryos were harvested.

Embryo dechorionation

Before digesting the proteinaceous chorion, embryos were rinsed with 500 mL of fresh tank water to remove remnants of cellular material and fish excrement. Newly fertilized embryos were dechorionated using the proteolytic enzyme Pronase (Roche Applied Sciences, Indianapolis, IN). A 20 mg/ml stock solution of Pronase was prepared in double distilled water (ddH$_2$O). 50 to 100 µL of Pronase was added to a vial containing 30 to 40 chorionated embryos in 6 mL of fresh tank water. The final concentration of Pronase in solution ranged from 0.16 to 0.33 mg/mL. Embryos in Pronase solution were gently agitated to accelerate the dechorionation process. After observing fragments of the chorion in solution, the embryos were quickly rinsed 4 to 5 times with 30 mL of fresh tank water. Repeated gentle rinses were required to remove remnants of the enzyme, which if present can affect embryo survival. Post-rinsing, dechorionated embryos were transferred to a clean petri dish containing fresh tank water, and were either placed on a slide warmer[1] heated to 27 ± 1 °C or kept at room temperature.

---

[1] Portions of this section have been published in Kohli *et al.* Biotechnol. Bioeng. 98(6), pg. 1230-1241.

[2] Special thanks to Dr. A. Waskiewicz for allowing us to use his zebrafish facility. The handling and care of the zebrafish were performed by Dr. A. Waskiewicz's zebrafish staff.

Preparation of Fluorescein Isothiocyanate (FITC)

A 0.1 mg/ml stock solution of FITC (Sigma-Aldrich, Oakville, ON, Canada) was prepared in tank water. 20 µL of the stock solution was added to embryos (chorionated and dechorionated) suspended in 50 to 70 µL of fresh tank water. The final concentration of FITC in solution ranged from 0.02 to 0.03 mg/mL.

Preparation of Streptavidin-Conjugated quantum dots

20 µL of a 1 µM stock solution of Streptavidin-conjugated quantum dots (Cedarlane Laboratories Ltd., Burlington, ON, Canada) was added to embryos suspended in 49 µL of tank water. The final concentration of the quantum dots in solution was

---

[1] Special thanks to Randy Madryk of the biological microscopy facility for allowing us to borrow his slide warmers.

0.4 μM.

Preparation of Simian-CMV-EGFP[1]

A 2.14 mg/mL stock solution of sCMV-EGFP was prepared using the standard Maxi prep procedure defined in the QIAGEN® plasmid purification handbook. A 600 μg/ml working solution was prepared by diluting the stock solution in fresh tank water. 20 μL of the working solution was added to embryos suspended in 70 μL of tank water. The final concentration of the plasmid in solution was 170 μg/mL.

Fluorescence imaging

Embryo fluorescence was evaluated using a standard FITC filter (Chroma Technology Corp., Rockingham, VT), a qdot 605 filter (Chroma Technology Corp., Rockingham, VT) and a long-pass GFP filter (Chroma Technology Corp., Rockingham, VT). Images were recorded using ACT2U software (Nikon, Japan) and processed using Photoshop CS2 (Adobe Systems Inc., San Jose, CA), CorelDraw8 (Corel Corp., Ottawa, ON, Canada) or GIMP (GIMP Development). Fluorescence and brightfield images were acquired from an upright Nikon 80i microscope (see Figures 4.6 through 4.10 of Chapter 4).

Laser optical setup

The laser pulse manipulation of zebrafish embryos for the delivery of exogenous foreign materials was performed using the experimental setup shown in Figures 4.6

---

[1] Special thanks to Patricia Gongal of Dr. A. Waskiewicz lab for preparing the sCMV-EGFP plasmid construct.

through 4.10 of Chapter 4. Femtosecond laser pulses were generated from a Ti:Sapphire laser oscillator that produced sub-10 femtosecond laser pulses. The emitted pulses had a wavelength spectrum ranging from 700 nm to 900 nm with the center wavelength at 800 nm. Pulses from the oscillator had a repetition rate of 80 MHz with a time delay of 12.5 ns between each pulse. Femtosecond laser pulses were directed into a Nikon upright 80i microscope (Nikon, Japan), as shown in Figures 4.6 through 4.10 of Chapter 4, where the red lines (see Figure 4.6 of Chapter 4) indicate the optical beam path. To direct the laser pulses into the microscope, dichroic mirrors labeled A1 through A3 were used, Figure 4.6. The laser pulses were coupled through the ocular imaging head, B, the imaging block, C and the fluorescence filter chamber, D, into a 1.0 NA water immersion microscope objective, E, Figure 4.6. Zebrafish embryos were placed on the motorized stage, G, and stage movements were controlled by the motor shaft, H, and hand controller J, Figure 4.6.

Laser pulses focused by the microscope objective were targeted onto the embryo either at the blastomere-yolk interface or on the individual blastomere cells. The pulse energy for laser pulse irradiation ranged from 0.5 nJ/pulse to 2.7 nJ/pulse[1], and the laser pulses were gated with a galvo (shutter) at a beam dwell time of < 1 sec to minimize energy deposition (Note: the shutter is not shown in Figures 4.6 through 4.9 of Chapter 4). At the focal plane of the objective, the diffraction limited irradiance spot size (diameter) as calculated by equation (1.2) in Chapter 1 was estimated to be $d_r = 976$ nm

---

[1] These pulse energies represent the values measured entering the microscope objective lens. Fresnel's equations describing the reflection and transmission values through various index media can be used to approximate the amount of average laser power loss. From calculations (not presented in this thesis), the total average laser power loss was a few milliwatts.

(λ = 800 nm). The peak power and peak intensity at the focal spot were calculated to range from 1.7 kW/pulse (0.5 nJ/pulse) to 9.3 kW/pulse (2.7 nJ/pulse) and 2.3×10^{11} W/cm^2 (0.5 nJ/pulse) to 1.2×10^{12} W/cm^2 (2.7 nJ/pulse), respectively (these values were calculated using an estimated broadened pulse duration of 291 femtoseconds; see Appendix A for details).

For the assessment of exogenous delivery, the microscope setup depicted in Figure 4.6 of Chapter 4 was equipped with a fluorescence lamp house located at the rear of the microscope (see Figure 4.8 of Chapter 4). Excitation fluorescence was directed towards the fluorescence filter cubes, which were located in the fluorescence filter chamber, D. To detect fluorescence from FITC, quantum dots or DNA the standard FITC filter (Chroma Technology Corp., Rockingham, VT), qdot 605 filter (Chroma Technology Corp., Rockingham, VT) or long-pass GFP filter (Chroma Technology Corp., Rockingham, VT) was used. Images were captured using the Nikon DS-5M (Nikon, Japan) color CCD, mounted at the imaging port of the microscope (see Figures 4.8 through 4.10 of Chapter 4). Figure 4.10 of Chapter 4 depicts a simplified version of the experimental setup shown in Figures 4.6 through 4.9 of the same chapter. Using this setup, the laser pulse manipulation and permeabilization of developing embryonic cells was demonstrated.

Laser poration, exogenous material delivery and survival analysis

For laser pulse poration, material delivery and survival studies, early cleavage to early blastula stage (2-cell to 128-cell stage) dechorionated (n = 70 to 75) and chorionated (n = 50 to 60) zebrafish embryos were laser pulse porated either near the blastomere-yolk interface or on individual blastomere cells. For material delivery into dechorionated zebrafish embryos, the embryos were bathed in a working solution of FITC, quantum dots or plasmid DNA for ~ 10 to 15 min before laser poration. Chorionated embryos, however, were exposed exclusively to the FITC fluorescent probe for ~ 10 to 15 min before poration. This incubation time was to allow for the probe to diffuse across the chorion into the perivitelline space (the region between the chorion and the embryo). Pervitelline FITC was then introduced into the developing blastomere cells by focusing femtosecond laser pulses beyond the structure of the chorion, as illustrated in Figure 4.16. Both dechorionated and chorionated zebrafish embryos were rinsed several times with fresh tank water before being imaged under epi-fluorescence. Fluorescence imaging was performed 30 to 60 min post-laser manipulation for FITC, ~ 10 min post-laser manipulation for the quantum dots or 24 hrs post-laser manipulation for DNA. Short-term survival assessment of early to mid cleavage stage (2-cell to 8/16-cell stage) laser-porated dechorionated (n = 23) and chorionated (n = 26) embryos in the absence of FITC, quantum dots or plasmid DNA was assessed by rearing laser treated embryos to pec-fin stage. Based on development morphology including symmetric yolk sacs, normal whole body mosaics and the absence of dorsal curvature, survival was determined. All laser treated embryos were compared to control embryos and standard Westerfield [126] images at the same developmental stage.

CHAPTER 5

MATERIALS AND METHODS

Materials and Methods[1]

Zebrafish care[2]

Twenty five to thirty adult male and female AB zebrafish were kept in 22 L of UV treated reverse osmosis water. The temperature of the water was maintained at 28 ± 1 °C with a pH ranging from 6.8 to 7.2. pH adjustments were made by buffering the reverse osmosis water with sodium bicarbonate.

Breeding and harvesting of embryos[2]

Adult male and female AB zebrafish were kept in 1 L of buffered reverse osmosis water. Each of the breeding tanks contained five adult fish consisting of three females and two males. A total of four to five 1 L tanks were set up for simultaneous breeding. A 2 mm wire mesh was placed at the bottom of each breeding tank to protect fallen eggs from predation by the adult fish. The breeding tanks were kept on a 10 hr dark/14 hr light cycle, and embryos were harvested approximately 20 min after the start of the light cycle.

Embryo dechorionation process

Stock Pronase (Roche Applied Sciences, IN, USA) at a concentration of 20 mg/ml was diluted to 10 mg/ml in double distilled water (ddH_2O) to prepare a working solution. 100 µL of 10 mg/ml Pronase was added to a vial containing embryos suspended in 6 mL of buffered reverse osmosis water. The final concentration of Pronase in solution was 0.16 mg/ml. To assist in the dechorionation process, the vial was periodically agitated to assist in the removal of the chorion. After observing fragments of the chorion in solution, the dechorionation process was stopped. Embryos were immediately rinsed 4 to 5 times with 30 mL of freshly buffered reverse osmosis water.

---

[1] Portions of this section have been published in Kohli *et al*. BMC Biotechnol. 8:7, pg. 1-20, 2008.

[2] Special thanks to Dr. A. Waskiewicz for allowing access to his zebrafish facility. The maintenance and care of the fish were handled by Dr. A. Waskiewicz zebrafish staff.

Preparation of Fluorescein Isothiocyanate (FITC)

A 0.1 mg/ml stock solution of FITC (Sigma-Aldrich, ON, Canada) was prepared in ddH_2O. 11 μL of the stock was added to embryos suspended in 50 to 70 μL of buffered reverse osmosis water. The final concentration of FITC in solution was 0.014 to 0.018 mg/ml.

Fluorescence imaging

Fluorescence assessment of exogenously delivered FITC was performed using a standard FITC filter (Chroma Technology Corp., Rockingham, VT). Epi-fluorescence was detected using a Nikon upright 80i microscope. Images were acquired using the Nikon DS-5M color CCD and ACT2U software (Nikon, Japan). Brightfield and fluorescence images were processed using Photoshop CS2 (Adobe Systems Inc., USA). All laser-targeted embryos were exposed to the FITC fluorescent probe for 10 to 15 min. Post-poration, the embryos were rinsed several times with fresh buffered reverse osmosis water. Imaging of the targeted embryos was performed 10 to 15 min post-laser targeting with a constant imaging area and an exposure time of 1.5 sec. Embryos showing autofluorescence (non-laser treated) were exposed, rinsed and imaged using the same procedure described above.

Zebrafish development, survival and morphological integrity

To accurately determine the short- and long-term effects of the applied femtosecond laser pulses, the hatching rates and developmental morphologies of laser-manipulated and control embryos were compared. Throughout embryonic development, from early cleavage (2-cell) to 2 days post-fertilization (dpf), laser-manipulated embryos were visually inspected using LM for differences in hatching rates and for normal morphology, including a straight dorsal axis, well-formed symmetric yolk sac and body plans similar to controls. In addition, all targeted embryos were also compared to standard Westerfield images [126]. Any laser-manipulated hatched embryos not conforming to the above criteria were considered morphologically compromised and non-viable.

A more detailed analysis of short-term survival was performed by comparing key developmental morphological structures in laser-manipulated and control embryos using SEM. The endpoint for determining short-term survival was chosen as 2 dpf. Long-term effects of the applied laser pulses on zebrafish development were assessed by rearing viable hatched laser-manipulated embryos to 7 dpf. SEM mosaics of control and laser-manipulated larvae were examined, with emphasis on developmental morphological structures such as the olfactory pit, otic capsule, otic vesicle, neuromast patterning, kinocilial projections, and brain neuromeres, as well as the whole body plan.

Zebrafish rearing media

The rearing media used in the short- and long-term survival analysis study was different from the aforementioned buffered UV treated reverse osmosis water (Appendix

F of Chapter 4). For the preparation of rearing media, de-ionized water was buffered with 125 mg/L of Instant Ocean (BigAl's aquarium, Edmonton, AB). The pH of de-ionized salt water was maintained between 6.5 and 6.6. The solution was further buffered by adding 4.83 mL of 5 mM sodium bicarbonate per 500 mL of de-ionized salt water (0.05 mM final concentration). The pH of this solution ranged from 7.0 to 7.3[1]. The method by which de-ionized water was buffered by sodium bicarbonate to avoid an acid solution is presented below:

Disassociation of carbonic acid in solution

$$H_2CO_3\,(aq) \Leftrightarrow H^+\,(aq) + HCO_3^-\,(aq) \qquad (1)$$

Disassociation of sodium bicarbonate in solution

$$NaHCO_3\,(aq) \rightarrow Na^+\,(aq) + HCO_3^-\,(aq) \qquad (2)$$

The effects of the rearing media on zebrafish development were tested before use in experimental studies. No short-term (from early cleavage stage (2-cell stage) to 2 dpf) or long-term (2 dpf to 150 dpf) detrimental effects on development were observed.

The fixing and mounting of embryos for SEM[2]

Early to mid cleavage stage embryos (2-cell to 4/8-cell) and 2 and 7 dpf hatched larvae were fixed and mounted for SEM imaging. Embryos and larvae were incubated for 2½ hours in 2 % glutaraldehyde (Sigma-Aldrich, ON, Canada) or 10 % formaldehyde

---

[1] Buffering of de-ionized water was required to avoid an acidic solution. Re-circulated de-ionized water forms carbonic acid resulting from carbon dioxide dissolving in the water.

[2] Special thanks to Randy Mandryk and Rakesh Bhatnagar for their assistance in fixing the zebrafish specimens.

(Fisher Scientific, ON, Canada), both prepared in ddH_2O. Post-incubation, the embryos and larvae were washed 3 to 4 times in ddH_2O with an interval of 15 min between each wash. After complete removal of glutaraldehyde/formaldehyde, graded alcohol steps were performed using 30, 50, 70, 90 and 100 % ethanol (EtOH). The embryos and larvae were bathed for 15 min in 30, 50 and 70 % EtOH, for 5 min in 90 % EtOH and for 10 min in 100 % EtOH. To remove remaining ddH_2O, the samples were washed an additional 3 to 4 times for 10 min in 100 % EtOH. Before mounting the embryos and larvae on SEM stubs, the 100 % EtOH was gradually replaced with hexamethlydisilazane (HMDS) (Fisher Scientific, ON, Canada). Solutions of 75:25, 50:50 and 25:75 % EtOH:HMDS were prepared, and the samples were incubated in each for 10 min. Remaining EtOH was removed by washing the embryos and larvae 3 to 4 times in 100 % HMDS for 10 min. The embryos and larvae were either incubated in 100 % HMDS overnight or immediately mounted on carbon tape SEM stubs. Each stub was allowed to dry for 20 to 30 min before being coated with palladium.

Sputtering[1] and SEM imaging[2]

Embryos and larvae were coated with palladium using the Hummer 6.2 Sputtering System (Anatech Ltd., Hayward, CA). The vacuum of the sputtering chamber was allowed to reach 30 millitorr before being purged with Argon gas. The chamber was purged until the vacuum reached 200 millitorr, after which the vacuum was adjusted to 55 to 65 millitor. The sample stage was rotated and a plasma discharge was maintained for coating the specimens with palladium. Specimens were coated for 90 to 150 sec. All samples were stored in a desiccator before being imaged. SEM imaging was performed using the XL 30 Series Philips ESEM LaB_6 and the Leo 1430 SEM. The accelerating voltage ranged from 10 to 30 kV.

---

[1] Special thanks to Jack Scott for sputtering the zebrafish samples.

[2] Special thanks to Jack Scott and Michael Quong for their assistance and training in SEM imaging.

Optical system, laser poration and delivery

Manipulation of chorionated and dechorionated zebrafish embryos was achieved using the setup shown in Figures 4.6 through 4.10 of Chapter 4. Sub-10 femtosecond laser pulses with a wavelength spectrum from 700 nm to 900 nm, centered at 800 nm, were generated from a Ti:Sapphire laser oscillator. The repetition rate of the oscillator was 80 MHz. The coupling of the laser pulses into the upright Nikon 80i (Nikon, Japan) microscope was identical to the method previously discussed in Appendix F of Chapter 4. Laser pulses were focused with a 1.0 NA 60X water immersion microscope objective to a location near the blastomere-yolk interface or on the blastomere cells in chorionated and dechorionated zebrafish embryos. Embryos were placed on a motorized stage, G, with the stage controlled by adjustments of the motorized shaft, H, and hand controller, J.

The pulse energy for laser-irradiation of the embryos ranged from 0.3 nJ/pulse to 0.63 nJ/pulse[1]. Femtosecond laser pulses were gated with a galvo (shutter) located in front of dichroic mirror A1 (not shown in Figure 4.6 of Chapter 4). At the focus of the objective, F, the estimated diffraction limited irradiance spot size (diameter) was $d_r = 976$ nm ($\lambda = 800$ nm), as calculated from equation (2) in Chapter 1. With the estimation that the pulse had broadend to 291 femtoseconds from sub-10 femtoseconds

---

[1] These pulse energies represent the values measured entering the microscope objective lens. Fresnel's equations describing the reflection and transmission values through various index media can be used to approximate the amount of average laser power loss. From calculations (not presented in this thesis), the total average laser power loss was a few milliwatts.

(see Appendix A), the peak power and peak intensity at the focus were estimated to range from 1 kW/pulse (0.3 nJ/pulse) to 2.2 kW/pulse (0.63 nJ/pulse) and 1.3×10^{11} W/cm^2 (0.3 nJ/pulse) to 2.9×10^{11} W/cm^2 (0.63 nJ/pulse), respectively.

Fluorescence assessment of blastomere-FITC was performed using the same method described in Appendix F of Chapter 4.

Image analysis

ImageJ analysis software (National Institutes of Health) was used to quantify the mean fluorescence intensity per unit area originating from the blastomere cells. The analyzed fluorescence images were captured using the Nikon DS-5M color CCD. This CCD had a sensor size of 8.8 mm (W) x 6.6 mm (H), with a pixel size of 3.4 µm and an effective resolution of 5 million pixels (Nikon, Canada). Images captured with the DS-5M had a 4:3 aspect ratio, with the color pixels arranged in a Bayer grid filter fashion. To accurately determine the mean fluorescence intensity, the image scale in ImageJ was set to 294.12 pixels/mm with an aspect ratio of 4:3 (1.333) in accordance with the CCD specifications. All analyzed images were of the same dimensions. For each image, an area overlying the blastomere cells was defined in the brightfield image and this area was then superimposed onto the fluorescent image of the same embryo. The mean fluorescence intensity was measured in the green channel of the CCD. This mean fluorescence intensity was divided by the blastomere area to give the mean fluorescence intensity per unit area originating from the blastomere cells.

REFERENCES

1. Niemz MH: **Threshold dependence of laser-induced optical breakdown on pulse duration**. *Appl Phys Lett* 1995, **66**(10):1181-1183.

2. Schaffer CB, Nishimura N, Glezer EN, Kim AM-T, Mazur E: **Dynamics of femtosecond laser-induced breakdwon in water from femtoseconds to microseconds**. *Opt Express* 2002, **10**(3):196-203.

3. Vogel A, Busch S, Jungnickel K, Birngruber R: **Mechanisms of Intraocular Photodisruption With Picosecond and Nanosecond Laser Pulses**. *Laser Surg Med* 1994, **15**:32-43.

4. Venugopalan V, III AG, Nahen K, Vogel A: **Role of Laser-Induced Plasma Formation in Pulsed Cellular Microsurgery and Micromanipulation**. *Phys Rev Lett* 2002, **88**(7):078103-078101-078103-078104.

5. Vogel A, Noack J, Huttman G, Paltauf G: **Mechanisms of femtosecond laser nanosurgery of cells and tissues**. *Appl Phys B* 2005, **81**:1015-1047.

6. Noack J, Vogel A: **Laser-Induced Plasma Formation in Water at Nanosecond to Femtosecond Time Scales: Calculation of Thresholds, Absorption Coefficients, and Energy Density**. *IEEE J Quantum Elect* 1999, **33**(8):1156-1167.

7. Schaffer CB, Brodeur A, Mazur E: **Laser-induced breakdown and damage in bulk transparent materials induced by tightly focused femtosecond laser pulses**. *Meas Sci Technol* 2001, **12**:1784-1794.

8. Oraevsky AA, Silva LBD, Rubenchik AM, Feit MD, Glinsky ME, Perry MD, Mammini BM, Small W, Stuart BC: **Plasma Mediated Ablation of Biological**

Tissues with Nanosecond-to-Femtosecond Laser Pulses: Relative Role of Linear and Nonlinear Absorption. *IEEE J Quantum Elect* 1996, **2**(4):801-809.

9. Neev J, Silva LBD, Feit MD, Perry MD, Rubenchik AM, Stuart BC: **Ultrashort Pulse Lasers for Hard Tissue Ablation**. *IEEE Journal of Selected Topics in Quantum Electronics* 1996, **2**(4):790-800.

10. Juhasz T, Hu XH, Turi L, Bor Z: **Dynamics of Shock Waves and Cavitation Bubbles Generated by Picosecond Laser Pulses in Corneal Tissue and Water**. *Laser Surg Med* 1994, **15**:91-98.

11. Kim B-M, Feit MD, Rubenchik AM, Joslin EJ, Celliers PM, Eichler J, Silva LBD: **Influence of pulse duration on ultrashort laser pulse ablation of biological tissues**. *Journal of Biomedical Optics* 2001, **6**(3):332-338.

12. Losel EH, Fischer JP, Gotz MH, Horvath C, Juhasz T, Noack F, Suhm N, Bille JE: **Non-thermal ablation of neural tissue with femtosecond laser pulses**. *Appl Phys B* 1998, **66**:121-128.

13. Niemz M: **Laser-Tissue Interactions: Fundamentals and Applications**, Second edn: Springer-Verlag Berlin Heidelberg New York; 2002.

14. Konig K, Riemann I, Fritzsche W: **Nanodissection of human chromosomes with near-infrared femtosecond laser pulses**. *Opt Lett* 2001, **26**(11):819-821.

15. Kohli V, Acker JP, Elezzabi AY: **Cell nanosurgery using ultrashort (femtosecond) laser pulses: Applications to membrane surgery and cell isolation**. *Laser Surg Med* 2005, **37**:227-230.

16. Kohli V, Elezzabi AY: **Laser surgery of zebrafish (*Danio rerio*) embryos using femtosecond laser pulses: Optimal parameters for exogenous material**

delivery, and the laser's effect on short- and long-term development *BMC Biotechnol* 2008, **8**(7):1-20.

17. Supatto W, Debarre D, Moulia B, Brouzes E, Martin J-L, Farge E, Beaurepaire E: ***In vivo* modulation of morphogenetic movements in *Drosophila* embryos with femtosecond laser pulses.** *PNAS* 2005, **102**(4):1047-1052.

18. Boyle JW, Ghormley JA, Hochanadel CJ, Riley JF: **Production of Hydrated Electrons by Flash Photolysis of Liquid Water.** *J Phys Chem* 1969, **73**(9):2886-2890.

19. Heisterkamp A, Maxwell IZ, Mazur E, Underwood JM, Nickerson JA, Kumar S, Ingber DE: **Pulse energy dependence of subcellular dissection by femtosecond laser pulses.** *Opt Express* 2005, **13**(10):3690-3696.

20. Chung SH, Clark DA, Gabel CV, Mazur E, Samuel AD: **The role of the AFD neuron in C. elegans thermotaxis analyzed using femtosecond laser ablation.** *BMC Neurosci* 2006, **7:30**.

21. Tirlapur UK, Konig K: **Femtosecond near-infrared laser pulses as a versatile non-invasive tool for intra-tissue nanoprocessing in plants without compromising viability.** *Plant J* 2002, **31**(3):365-374.

22. Shen N, Datta D, Schaffer CB, LeDuc P, Ingber DE, Mazur E: **Ablation of cytoskeletal filaments and mitochondria in live cells using femtosecond laser nanoscissor.** *MCB* 2005, **2**(1):17-25.

23. Konig K, Riemann I, Fischer P, Halbhuber K-J: **Intracellular nanosurgery with near infrared femtosecond laser pulses.** *Cell Mol Biol* 1999, **45**(2):195-201.

24. Bauerle D: **Laser Processing and Chemistry**: Springer-Verlag; 2000.

25. Yao YL, Chen H, Zhang W: **Time scale effects in laser material removal: a review**. *Int J Adv Manuf Technol* 2004, **26**(5-6):598-608.

26. Boyd RW: **Nonlinear Optics**, Second edn: Academic Press; 2003.

27. Silfvast WT: **Laser Fundamentals**: Cambridge University Press; 1996.

28. Arnold CL, Heisterkamp A, Ertmer W, Lubatschowski H: **Computational model for nonlinear plasma formation in high NA micromachining of transparent materials and biological cells**. *Opt Lett* 2007, **15**(16):10303-10317.

29. Alberts B, Johnson A, Lewis J, Raff M, Robers K, Walter P: **Molecular biology of the cell**, Fourth Edition edn: Garland Science; 2002.

30. Emmert-Buck MR, Bonner RF, Smith PD, Chuaqui RF, Zhuang Z, Goldstein SR, Weiss RA, Liotta LA: **Laser Capture Microdissection**. *Science* 1996, **274**(5289):998-1001.

31. Espina V, Wulfkuhle Jd, Calvert VS, VanMeter A, Zhou W, Coukos G, Geho DH, III EFP, Liotta LA: **Laser-capture microdissection**. *Nat Protoc* 2006, **1**(2):586-603.

32. Simone NL, Bonner RF, Gillespie JW, Emmert-Buck MR, Liotta LA: **Laser-capture microdissection: opening the microscopic frontier to molecular analysis**. *TIG* 1998, **14**(7):272-276.

33. Bonner RF, Emmert-Buck M, Cole K, Phida T, Chuaqui R, Goldstein S, Liotta LA: **Cell Sampling: Laser Capture Microdissection: Molecular Analysis of Tissue**. *Science* 1997, **278**(5342):1481-1483.

34. Watanabe W, Arakawa N, Matsunaga S, Higashi T, Fukui K, Isobe K, Itoh K: **Femtosecond laser disruption of subcellular organelles in a living cell.** *Opt Express* 2004, **12**:4203-4213.

35. Sacconi L, Tolic-Norrelykke IM, Antolini R, Pavone FS: **Combined intracellular three-dimensional imaging and selective nanosurgery by a nonlinear microscope.** *J Biomed Opt* 2005, **10**(1):014002-014001 - 014002-014005.

36. Maniotis AJ, Chen CS, Ingber DE: **Demonstration of mechanical connections between integrins, cytoskeletal filaments, and nucleoplasm that stabilize nuclear structure.** *Proc Natl Acad Sci* 1997, **94**:849-854.

37. Alenghat FJ, Fabry B, Tsai KY, Goldmann WH, Ingber DE: **Analysis of Cell Mechanics in Single Vinculin-Deficient Cells Using a Magnetic Tweezer.** *Biochem Biophys Res Comm* 2000, **277**:93-99.

38. Fend F, Emmert-Buck MR, Chuaqui R, Cole K, Lee J, Liotta LA, Raffeld M: **Immuno-LCM: Laser Capture Microdissection of Immunostained Frozen Sections for mRNA Analysis.** *Am J Pathol* 1999, **154**(1):61-66.

39. Banks RE, Dunn MJ, Forbes MA, Stanley A, Pappin D, Naven T, Gough M, Harnden P, Selby PJ: **The potential use of laser capture microdissection to selectively obtain distinct populations of cells for proteomic analysis - Preliminary findings.** *Electrophoresis* 1999, **20**:689-700.

40. Roberts SK, Dixon GK, Dunbar SJ, Sanders D: **Laser Ablation of the Cell Wall and Localized Patch Clamping of the Plasma Membrane in Filamentous**

Fungus *Aspergillus*: Characterization of an Anion-Selective Efflux Channel. *New Phytol* 1997, **137**:579-585.

41. Fuhr G, Ronacher B, Krahe R, Fest S, Shirley SG, Rogaschewski S: **UV-laser ablation of sensory cells in living insects.** *Appl Phys A* 1999, **68**:379-385.

42. Soustelle L, Aigouy B, Asensio M-L, Gioangrande A: **UV laser mediated cell selective destruction by confocal microscopy**. *Neurol Development* 2008, **3**(11):1-8.

43. Kohli V, Elezzabi AY: **Prospects and developments in cell and embryo laser nanosurgery**. *Interdisciplinary reviews: Nanomedicine* 2007, **In press. (Invited article).**

44. Elmoazzen HY: **Parameters Affecting Water Permeability Across Biological Cell Membranes.** *Master of Science*. Edmonton: University of Alberta; 2000.

45. Muldrew K, McGann LE: **The Osmotic Rupture Hypothesis of Intracellular Freezing Injury**. *Biophys J* 1994, **66**:532-541.

46. Eroglu A, Russo MJ, Bieganski R, Fowler A, Cheley S, Bayley H, Toner M: **Intracellular trehalose improves the survival of cryopreserved mammalian cells.** *Nat Biotechnol* 2000, **18**:163-167.

47. Yang H, Acker J, Chen A, Mcgann L: **In Situ Assessment Of Cell Viability**. *Cell Transplant* 1998, 7(5):443-451.

48. Chen T, Acker JP, Eroglu A, Cheley S, Bayley H, Fowler A, Toner M: **Beneficial Effect of Intracellular Trehalose on the Membrane Integrity of Dried Mammalian Cells**. *Cryobiology* 2001, **43**:168-181.

49. Russo MJ, Bayley H, Toner M: **Reversible permeabilization of plasma membranes with an engineered switchable pore**. *Nat Biotechnol* 1997, **15**:278-282.

50. Acker JP, Lu X-m, Young V, Cheley S, Bayley H, Fowler A, Toner M: **Measurement of Trehalose Loading of Mammalian Cells Porated With a Metal-Actuated Switchable Pore**. *Biotechnol Bioeng* 2003, **82**(5):525-532.

51. Becker WM, Kleinsmith LJ, Hardin J: **The World of The Cell**, 5 edn: Pearson Education, Inc.; 2003.

52. Kaiser A, Rethfeld B, Vicanek M, Simon G: **Microscopic processes in dielectrics under irradiation by subpicosecond laser pulses**. *Phys Rev B* 2001, **61**(17):11437-11450.

53. Mazur P: **Cryobiology: The Freezing of Biological Systems**. *Science* 1970:939-949.

54. Kohli V, Acker JP, Elezzabi AY: **Reversible permeabilization using high-intensity femtosecond laser pulses: Applications to biopreservation**. *Biotechnol Bioeng* 2005, **92**(7):889-899.

55. Kohli V, Robles V, Cancela ML, Acker JP, Waskiewicz AJ, Elezzabi AY: **An alternative method for delivering exogenous material into developing zebrafish embryos**. *Biotechnol Bioeng* 2007, **98**(6):1230-1241.

56. Culp P, Nusslein-Volhard C, Hopkins N: **High-Frequency Germ-Line Transmission of Plasmid DNA Sequences Injected Into Fertilized Zebrafish Eggs**. *Proc Natl Acad Sci USA* 1991, **88**(18):7953-7957.

57. Robles V, Barbosa V, Herraez MP, Martinez-Paramo S, Cancela ML: **The antifreeze protein type I (AFPI) increases seabream (*Sparus aurata*) embryos tolerance to low temperatures**. *Theriogenology* 2007, **68**(2):284-289.

58. Robles V, Cabrita E, Anel L, Herraez MP: **Microinjection of the antifreeze protein type III (AFPIII) in turbot embryos: toxicity and protein distriubtion.** *Aquaculture* 2006, **261**(4):1299-1306.

59. Acker JP: **Biopreservation of Cells and Tissues**. In: *Tissue Engineering*. Edited by Lee K, and Kaplan, D.: Springer-Verlag; 2005.

60. Diller KR: **Intracellular Freezing: Effect of Extracellular Supercooling.** *Cryobiology* 1975, **12**:480-485.

61. Polge C, Smith AU, Parkes AS: **Revival of Spermatozoa after Vitrification and Dehydration at Low Temperatures**. *Nature* 1949, **164**:666.

62. Lovelock JE: **The Haemolysis Of Human Red Blood Cells By Freezing and Thawing**. *Biochimica et Biophysica Acta International Journal of Biochemistry and Biophysics* 1953, **10**:414-426.

63. Meryman HT: **Osmotic Stress as a Mechanism of Freezing Injury**. *Cryobiology* 1971, **8**:489-500.

64. Finkelstein A: **Water Movement Through Lipid Bilayers, Pores, and Plasma Membranes Theory and Reality**, vol. 4: John Wiley & Sons, Inc.; 1987.

65. Crowe JH, Crowe LM, Carpenter JF, Rudolph AS, Wistrom CA, Spargo BJ, Anchordoguy TJ: **Interactions of sugars with membranes**. *Biochimica et Biophysica Acta* 1988, **947**:367-384.

66. Bayley H: **Building doors into cells**. In: *Sci Am.* vol. 277; 1997: 62-67.

67. Walker B, Kasianowicz J, Krishnasastry M, Bayley H: **A pore-forming protein with a metal-actuated switch**. *Protein Eng* 1994, 7(5):655-662.

68. Tsong TY: **Electroporation of cell membranes**. *Biophys J* 1991, **60**:297-306.

69. Muller F, Lele Z, Váradi L, Menczel L, Orban L: **Efficient transient expression system based on square pulse electroporation and in vivo luciferase assay of fertilized fish eggs**. *FEBS Letters* 1993, **324**(1):27-32.

70. Buono RJ, Linser PJ: **Transient expression of RSVCAT in transgenic zebrafish made by electroporation**. *Mol Mar Biol Biotech* 1992, **1**(4/5):271-275.

71. Golzio M, Teissie J, Rols MP: **Direct visualization at the single-cell level of electrically mediated gene delivery**. *PNAS* 2002, **99**(3):1292-1297.

72. Cerda GA, Thomas JE, Allende ML, Karlstrom RO, Palma V: **Electroporation of DNA, RNA, and morpholinos into zebrafish embryos**: *Methods* 2006, **39**(3):207-211.

73. Mussauer H, Sukhorukov VL, Zimmermann U: **Trehalose Improves Survival of Electrotransfected Mammalian Cells**. *Cytometry* 2001, **45**:161-169.

74. Tirlapur UK, Konig K: **Targeted transfection by femtosecond laser**. *Nature* 2002, **418**:290.

75. Stevenson D, Agate B, Tsampoula X, Fischer P, Brown CTA, Sibbett W, Riches A, Gunn-Moore F, Dholakia K: **Femtosecond optical transfection of cells:viability and efficiency**. *Opt Express* 2006, **14**(16):7125-7133.

76. Baumgart J, Bintig W, Ngezahayo A, Willenbrock S, Escobar HM, Ertmer W, Lubatschowski H, Heisterkamp A: **Quantified femtosecond laser based opto-**

perforation of living GFSHF-17 and MTH53a cells. *Opt Express* 2008, **16**(5):3021-3031.

77. Edidin M: **A Rapid, Quantitative Fluorescence Assay for Cell Damage by Cytotoxic Antibodies**. *J Immunol* 1970, **101**(5):1303-1306.

78. Elmoazzen HY, Chan CCV, Acker JP, Elliott JAW, McGann LE: **The effect of cell size distribution on predicted osmotic responses of cells**. *Cryoletters* 2005, **26**(3):147-158.

79. Crowe JH, Crowe LM, Oliver AE, Tsvetkova N, Wolkers W, Tablin F: **The Trehalose Myth Revisited: Introduction to a Symposium on Stabilization of Cells in the Dry State**. *Cryobiology* 2001, **43**:89-105.

80. Karlsson JOM, Cravalho EG, Toner M: **Intracellular Ice Formation: Causes and Consequences**. *Cryo-Letters* 1993, **14**:323-334.

81. Laale HW: **The biology and use of zebrafish, *Brachydanio rerio* in fisheries research. A literature review**. *J Fish Biol* 1977, **10**:121-173.

82. Weinberg ES: **Analysis of Early Development in the Zebrafish Embryo**. In: *Early Embryonic Development of Animals.* Edited by Hennig W. Berlin Heidelberg: Springer-Verlag; 1992: 91-150.

83. Vogel G: **Zebrafish Earns Its Stripes in Genetic Screens**. *Science* 2000, **288**(5469):1160-1161.

84. Sar AMvd, Appelmelk BJ, Vandenbroucke-Grauls CMJE, Bitter W: **A star with stripes: zebrafish as an infection model**. *Trends Microbiol* 2004, **12**(10):451-457.

85. Hill AJ, Teraoka H, Heideman W, Paterson RE: **REVIEW: Zebrafish as a Model Vetebrate for Investigating Chemical Toxicity**. *Toxicol Sci* 2005, **86**(1):6-19.

86. Dooley K, Zon LI: **Zebrafish: a model system for the study of human disease.** *COGD* 2000, **10**:252-256.

87. Barut BA, Zon LI: **Realizing the potential of zebrafish as a model for human disease**. *Physiol Genomics* 2000, **2**:49-51.

88. Jagadeeswaran P, Sheehan JP: **Analysis of Blood Coagulation in the Zebrafish.** *Blood Cells Mol Dis* 1999, **25**(15):239-249.

89. Warren KS, Wu JC, Pinet F, Fishman MC: **The genetic basis of cardiac function: dissection by zebrafish (*Danio rerio*) screens**. *Phil Trans R Soc Lond B* 2000, **355**:939-944.

90. Kimmel CB, Ballard WW, Kimmel SR, Ulmann B, Schilling TF: **Stages of Embryonic Development of the Zebrafish**. *Developmental Dynamics* 1995, **203**:253-310.

91. Hagedorn M, Kleinhans FW, Artemov D, Pilatus U: **Characterization of a Major Permeability Barrier in the Zebrafish Embryo**. *Biol Reprod* 1998, **59**:1240-1250.

92. Liu X-H, Zhang T, Rawson DM: **Effect of cooling rate and partial removal of yolk on the chiling injury in zebrafish (Danio rerio) embryos**. *Theriogenology* 2001, **55**:1719-1731.

93. Zhang T, Rawson DM: **Feasibility Studies on Vitrification of Intact Zebrafish (Brachydanio rerio) Embryos**. *Cryobiology* 1996, **33**(0001):1-13.

94. Liu X-H, Zhang T, Rawson DM: **The Effect of Partial Removal of Yolk on the Chilling Sensitivity of Zebrafish (*Danio Rerio)* Embryos**. *Cryobiology* 1999, **39**:236-242.

95. Hagedorn M, Kleinhans FW, Wildt DE, Rall WF: **Chill Sensitivity and Cryoprotectant Permeability of Dechorionated Zebrafish Embryos, *Brachydanio rerio***. *Cryobiology* 1997, **34**:251-263.

96. Zhang T, Liu X-H, Rawson DM: **Effects of methanol and developmental arrest on chilling injury in zebrafish (*Danio rerio*) embryos**. *Theriogenology* 2003, **59**:1545-1556.

97. Liu X-H, Zhang T, Rawson DM: **Feasibility of vitrification of zebrafish (*Danio rerio*) embryos using methanol**. *Cryo Letters* 1998, **19**:309-318.

98. Zhang T, Rawson DM, Morris GJ: **Cryopreservation of pre-hatch embryos of zebrafish (*Brachydanio rerio*)**. *Aquat Living Resour* 1993, **6**:145-153.

99. Zhang T, Rawson DM: **Studies on Chilling Sensitivity of Zebrafish (*Brachydanio rerio*) Embryos**. *Cryobiology* 1995, **32**:239-246.

100. Hagedorn M, Perterson A, Mazur P, Kleinhans FW: **High ice nucleation temperature of zebrafish embryos: slow-freezing is not an option.** *Cryobiology* 2004, **49**:181-189.

101. Zhang T, Rawson DM: **Permeability of Dechorionated One-Cell and Six-Somite Zebrafish (*Brachydanio rerio*) Embryos to Water and Methanol.** *Cryobiology* 1998, **37**:13-21.

102. Janik M, Kleinhans FW, Hagedorn M: **Overcoming a Permeability Barrier by Microinjecting Cryoprotectants into Zebrafish Embryos (*Brachydanio rerio*).** *Cryobiology* 2000, **41**:25-34.

103. Hagedorn M, Lance SL, Fonseca DM, Kleinhans FW, Artimov D, Fleischer R, Hoque ATMS, Hamilton MB, Pukazhenthi BS: **Altering Fish Embryos with Aquaporin-3: An Essential Step Toward Successful Cryopreservation.** *Biol Reprod* 2002, **67**:961-966.

104. Kimmel CB, Law RD: **Cell lineage of zebrafish blastomeres, II. Formation of the yolk syncytial layer.** *Dev Biol* 1985, **108**(1):86-93.

105. Kasai M: **Simple and efficient methods for vitrification of mammalian embryos.** *Anim Reprod Sci* 1996, **42**:67-75.

106. Hagedorn M, Kleinhans FW, Freitas R, Liu J, Hsu EW, Wildt DE, Rall WF: **Water Distribution and Permeability of Zebrafish Embryos, *Brachydanio rerio*.** *J Exp Zool* 1997, **278**:356-371.

107. Hagedorn M, Hsu E, Kleinhans FW, Wildt DE: **New Approaches for Studying the Permeability of Fish Embryos: Toward Successful Cryopreservation.** *Cryobiology* 1997, **34**:335-347.

108. Harvey B, Chamberlain JB: **Water Permeability In The Developing Embryo Of the Zebrafish, *Brachydanion Reiro*.** *Can J Zoolog* 1982, **60**:268-270.

109. Robles V, Cabrita E, Kohli V, Herráez MP: **Prospects and Developments in Fish Sperm and Embryo Cryopreservation.** In: *Aquaculture Research Progress.* Edited by Nakamura TK: Nova Science. In press.; 2008.

110. Stuart GW, McMurray JV, Westerfield M: **Replication, integration and stable germ-line transmission of foreign sequences injected into early zebrafish embryos**. *Development* 1988, **103**:403-412.

111. Higashijima S-i, Okamoto H, Ueno N, Hotta Y, Eguchi G: **High-Frequency Generation of Transgenic Zebrafish Which Reliably Express GFP in Whole Muscles or the Whole Body by Using Promoters of Zebrafish Origin**. *Dev Biol* 1997, **192**:289-299.

112. Linney E, Hardison NL, Lonze BE, Lyons S, DiNapoli L: **Transgene Expression in Zebrafish: A Comparison of Retroviral-Vector and DNA-Injection Approaches**. *Dev Biol* 1999, **213**:207-216.

113. Inoue K, Yamashita S, Hata J, Kabeno S, Asada S, Nagahisa E, Fujita T: **Electroporation as a new technique for producing transgenic fish**. *Cell Differ Dev* 1990, **29**:123-128.

114. Powers DA, Hereford L, Cole T, Chen TT, Lin CM, Kight K, Creech K, Dunham R: **Electroporation: a method for transferring genes into the gametes of zebrafish (*Brachydanio rerio*), channel catfish (*Ictalurus punctatus*), and common carp (*Cyprinus carpio*)**. *Mar Mol Biol Biotechnol* 1992, **1**(4/5):301-308.

115. Roeser T, Baier H: **Visumotor Behaviors in Larval Zebrafish after GFP-Guided Laser Ablation of the Optic Tectum**. *J Neurosci* 2003, **23**(9):3726-3734.

116. Yamaguchi M, Yoshimoto E, Kondo S: **Pattern regulation in the stripe of zebrafish suggests an underlying dynamic and autonomous mechanism.** *PNAS* 2007, **104**(12):4790-4793.

117. Yang C-T, Sengelmann RD, Johnson SL: **Larval Melanocyte Regeneration Following Laser Ablation in Zebrafish.** *J Invest Dermatol* 2004, **123**:924-929.

118. Jones JE, Corwin JT: **Regeneration of Sensory Cells after Laser Ablation in the Lateral Line System: Hair Cell Lineage and Macrophage Behavior Revealed by Time-Lapse Video Microscopy.** *J Neurosci* 1996, **16**(2):649-662.

119. Liu KS, Fetcho JR: **Laser Ablations Reveal Functional Relationships of Segmental Hindbrain Neurons in Zebrafish.** *Neuron* 1999, **23**:325-335.

120. Burgess HA, Granato M: **Sensorimotor Gating in Larval Zebrafish.** *The Journal of Neuroscience* 2007, **27**(18):4984-4994.

121. Gahtan E, Tanger p, Baier H: **Visual Prey Capture in Larval Zebrafish Is Controlled by Identified reticulospinal Neurons Downstream of the Tectum.** *The Journal of Neuroscience* 2005, **25**(40):9294-9303.

122. Supatto W, Debarre, D., Farge, E., and Beaurepaire, E.: **Femtosecond pulse-induced microprocessing of live *Drosophila* embryos.** *Med Laser Appl* 2005, **20**:207-216.

123. Yanik MF, Cinar H, Cinar HN, Chisholm AD, Jin Y, Ben-Yakar A: **Functional regeneration after laser axotomy.** *Nature* 2004, **432**:822.

124. Nishimura N, Schaffer CB, Friedman B, Tsai PS, Lyden PD, Kleinfeld D: **Targeted insult to subsurface cortical blood vessel using ultrashort laser pulses: three models of stroke.** *Nat Methods* 2006, **3**(2):99-108.

125. Robles V, Cabrita E, Fletcher GL, Shears MA, King MJ, Herraez MP: **Vitrification assays with embryos from a cold tolerant sub-arctic fish species - The first report of fish embryo survival following vitrification.** *Theriogenology* 2005, **In press**.

126. Westerfield: **Zebrafish Information Network (ZFIN), the Zebrafish International Resource Center**. In. University of Oregon, Eugene, OR 97403-5274; World Wide Web URL: http://zfin.org/.

127. Kimmel CB, Law RD: **Cell lineage of zebrafish blastomeres, I. Cleavage pattern and cytoplasmic bridges between cells**. *Dev Biol* 1985, **108**(1):78-85.

128. Sakaguchi T, Mizuno T, Takeda H: **Pattern formation in zebrafish**. New York: Springer; 2002.

129. Rawson DM, Zhang T, Kalicharan D, Jongebloed WL: **Field emission scanning electron microscopy and transmission electron microscopy studies of the chorion, plasma membrane and syncytial layers of the gastrula-stage embryo of the zebrafish *Brachydanio rerio*: a consideration of the structural and functional relationships with respect to cryoprotectant penetration**. *Aquac Res* 2000, **31**(3):326-336.

130. Rieger S, Kulkarni RP, Darcy D, Fraser SE, Koster RW: **Quantum Dots Are Powerful Multipurpose Vital Labeling Agents in Zebrafish Embryos**. *Dev Dyn* 2005, **234**:670-681.

131. Peters KG, Rao PS, Bell BS, Kindman LA: **Green Fluorescent Fusion Proteins: Powerful Tools for Monitoring Protein Expression in Live Zebrafish Embryos**. *Dev Biol* 1995, **171**:252-257.

132. Cloud JG: **Strategies for introducing foreign DNA into the germ line of fish**. *J Reprod Fert Suppl* 1990, **41**:107-116.

133. Amsterdam A, Lin S, Moss LG, Hopkins N: **Requirements for green fluorescent protein detection in transgenic zebrafish embryos**. *Gene* 1996, **173**:99-103.

134. Amsterdam A, Lin S, Hopkins N: **The *Aequorea victoria* Green Fluorescent Protein Can Be Used as a Reporter in Live Zebrafish Embryos**. *Dev Biol* 1995, **171**:123-129.

135. Maclean N: **Regulation and exploitation of transgenes in fish**. *Mutat Res* 1998, **399**:255-266.

136. Collas P: **Modulation of plasmid DNA methylation and expression in zebrafish embryos**. *Nucleic Acids Res* 1998, **26**(19):4454-4461.

137. Robles DV: **Personal communication**. In. Edmonton, Alberta; 2006.

138. Waskiewicz DA: **Personal Communication**. In. Edmonton; 2006.

139. Lodish H, Berk A, Matsudaira P, Kaiser CA, Krieger M, Scott MP, Zipursky SL, Darnell J: **Molecular Cell Biology**, Fifth edn: W. H. Freeman and Company; 2003.

140. Haddon C, Lewis J: **Early Ear Development in the Embryo of the Zebrafish, *Danio rerio***. *J Comp Neu* 1996, **365**:113-128.

141. Nicolson T: **The Genetics of Hearing and Balance in Zebrafish**. *Annu Rev Genet* 2005, **39**:9-22.

142. Hansen A, Zeiske E: **Development of the olfactory organ in the zebrafish, *Brachydanio rerio***. *J Comp Neu* 2004, **333**(2):289-300.

143. Michel WC, Lubomudrov LM: **Specificity and sensitivity of the olfactory organ of the zebrafish, *Danio rerio***. *J Comp Physiol A* 1995, **177**:191-199.

144. Konig K, Riemann I, Fischer P, Halbhuber K-J: **Intracellular nanosurgery with compact femtosecond laser**. *Part of the 18th Congress of the International Commission for Optics: Otpics for the Next Millennium San Francisco, California, SPIE* 1999, **3749**.

145. Konig K, Krauss O, Riemann I: **Intratissue surgery with 80Mhz nanojoule femtosecond laser pulses in the near infrared**. *Opt Express* 2002, **10**(3):171-176.

146. Konig K, So PTC, Mantulin WW, Gratton E: **Cellular response to near-infrared femtosecond laser pulses in two-photon microscopes**. *Optics Express* 1997, **22**(2):135-136.

147. Kohli V, Acker JP, Elezzabi AY: **Permeabilization and cell surgery using femtosecond laser pulses: an emerging tool for cellular manipulation**. *Optical Interactions with Tissue and Cells XVII Proceedings of the SPIE* 2006, **6084**:268-278.

148. Kohli V, Deli Y, Elezzabi AY: **Femtosecond laser ablation of corneal-like material**. *Submitted* 2007.

149. Kohli V, Deli Y, Elezzabi AY: **Laser-assisted ablation of corneal-like material using focused femtosecond laser pulses.** *LASE Proceedings of SPIE* 2006, **6460**:64600D-64601-64612.

150. Kohli V, Elezzabi AY: **Part I: Embryonic surgery using femtosecond laser pulses for the delivery of exogenous materials and the analysis of gene**

expression. *Proceedings of SPIE, The International Society for Optical Engineering* 2008, **6854**:685413-685411-685419.

151. Tirlapur UK, Konig K, Peuckert C, Krieg R, Halbhuber KJ: **Femtosecond near-infrared laser pulses elicit generation of reactive oxygen species in mammalian cells leading to apoptosis-like death**. *Exp Cell Res* 2001, **263**(1):88-97.

152. Kohli V, Elezzabi AY: **Part II: Morphological analysis of embryonic development following femtosecond laser manipulation**. *Proceedings of SPIE, The International Society for Optical Engineering* 2008, **6854**:685404-685401-685410.

153. Kohli V, Elezzabi AY: **From cells to embryos: The application of femtosecond laser pulses for altering cellular material in complex biological systems** *Proceedings of SPIE, The International Society for Optical Engineering* 2008, **6892**(68920J1-12):2008.

154. Kohli V, Eorr E, Elezzabi AY, Goss G: **Induction of HSP70 following femtosecond laser surgery: A cellular thermometer for detecting heat**. *In preparation* 2008.

155. Zeira E, Manevitch A, Khatchatouriants A, Pappo O, Hyam E, Darash-Yahana M, Tavor E, Honigman A, Lewis A, Galun E: **Femtosecond Infrared Laser - An Efficient and Safe *in Vivo* Gene Delivery System for Prolonged Expression**. *Molecular Therpay* 2003, **8**(2):342-350.

156. Nishimura N, Schaffer, C.B., Li, E.H., and Mazur, E.: **Tissue ablation with 100-fs and 200-ps laser pulses**. *Proceedings of the 20th Annual International*

Conferenece of the IEEE Engineering in Medicine and Biology, Society 1998, **20**(4):1703-1706.

157. Yeh F-L, Hsu T: **Detection of a Spontaneous High Expression of Heat Shock Protein 70 in Developing Zebrafish (*Danio rerio*).** *Biosci Biotechnol Biochem* 2000, **63**(3):592-595.

158. Schlesinger MJ: **Heat Shock Proteins: The Search for Functions.** *Journal of Cell Biology* 1986, **103**:321-325.

159. Ang D, Liberek K, Skowyra D, Zylicz M, Georgopoulos C: **Biological Role and Regulation of the Universally Conserved Heat Shock Proteins**. *Journal of Biological Chemistry* 1991, **266**(36):24233-24236.

160. Basu N, Todgham AE, Ackerman PA, Bibeau MR, Nakano K, Schulte PM, Iwama GK: **Heat shock protein genes and their functional significance in fish**. *Gene* 2002, **295**:173-183.

161. Tavaria M, Gabriele T, Kola I, Anderson RL: **A hitchhiker's guide to the human Hsp70 family**. *Cell Stress & Chaperones* 1996, **1**(1):23-28.

162. Wang G, Huang H, Dai R, Lee K-Y, Lin S, Mivechi NF: **Suppression of Heat Shock Transcription Factor HSF1 in Zebrafish Causes Heat-Induced Apoptosis**. *Genesis* 2001, **30**:195-197.

163. Blechinger SR, Evans TG, Tang PT, Kuwada JY, Jr JTW, Krone PH: **The heat-inducible zebrafish *hsp*70 gene is expressed during normal lens development under non-stress conditions**. *Mechanisms of Development* 2002, **112**:213-215.

164. Craig EA, Gross CA: **Is hsp70 the cellular thermometer?** *TIBS* 1991, **16**:135-140.

165. Krone PH, sass JB, Lele Z: **Heat shock protein gene expression during embryonic development of the zebrafish**. *Cell mol life sci* 1997, **53**:122-129.

166. Lele Z, Engel S, Krone PH: ***hsp47* and *hsp70* Gene Expression Is Differentially Regulated in a Stress- and Tissue-Specific Manner in Zebrafish Embryos**. *Developmental biology* 1997, **21**:123-133.

167. Krone PH, Lele Z, Sass JB: **Heat shock genes and the heat shock response in zebrafish embryos**. *Biochem Cell Biol* 1997, **75**:487-497.

168. Airaksinen S, Jokilehto T, Rabergh CMI, Nikinmaa M: **Heat- and cold-inducible regulation of HSP70 expression in zebrafish ZF4 cells**. *Comparative Biochemistry and Physiology Part B* 2003, **136**:275-282.

169. Airaksinen S, Rabergh CMI, Lahti A, Kaatrasalo A, Sistonen L, Nikinmaa M: **Stressor-dependent regulation of the heat shock response in zebrafish, *Danio rerio***. *Comparative Biochemistry and Physiology Part A* 2003, **134**:839-846.

170. Halloran MC, Sato-Maeda M, Jr JTW, Su F, Lele Z, Krone PH, Kuwada JY, Shoji W: **Laser-induced gene expression in specific cells of transgenic zebrafish**. *Development* 2000, **127**:1953-1960.

171. Tomimatsu K: **Fluid immersion microscope objective lens**. In: *United States Patent and Trademark Office.* vol. 5805346. United States: Nikon Corporation; 1998.

172. Xu L, Nakagawa N, Morita R, Shigekawa H, Yamashita M: **Programmable Chirp Compensation for 6-fs Pulse Generation with a Prism-Pair-Fomred Pulse Shaper**. *IEEE J Quantum Elect* 2000, **36**(8):893-899.

173. Zipfel WR, Williams RM, Webb WW: **Nonlinear magic: multiphoton microscopy in the biosciences.** *Nat Biotech* 2003, **21**(11):1369-1377.

174. Guild JB, Xu C, Webb WW: **Measurement of group delay dispersion of high numerical aperture objectives lenses using two-photon excited fluorescence**. *Appl Opt* 1997, **36**(1):397-401.

175. Purves WK, Orians GH, Heller HC: **Life: The Science of Biology**, Fourth edn: Sinauer Associates, Inc.; 1995.

176. Coleman GJ, Dewar D: **The Addison-Wesley Science Handbook**: Addison-Wesley Ltd.; 1997.

177. Smits AJ: **A physical introduction to fluid mechanics**. New York, NY: John Wiley & Sons, Inc.; 2000.

178. Chen CS, Mrksich M, Huang S, Whitesides GM, Ingber DE: **Micropatterned Surfaces for Control of Cell Shape, Position, and Function**. *Biotechnol Prog* 1998, **14**:356-363.

179. Tien HT, Ottova-Leitmannova A: **MEMBRANE BIOPHYSICS - As viewed from experimental bilayer lipid membranes (Planar Lipid Bilayers and Spherical Lipsomes)**: Elsevier Science B.V.; 2000.

180. Greenberg MD: **Advanced Enginering Mathematics**, Second edn: Prentice-Hall; 1998.

181. Kreyszig E: **Advanced Engineering Mathematics**, Eight edn: Wiley; 1998.

182. Stowe K: **Introduction to statistical mechanics and thermodynamics**: John Wiley & Sons, Inc.; 1984.

VIKRAM KOHLI
Curriculum Vitae

EDUCATION

University of Alberta, Edmonton, Alberta (2003-Present)
Department of Electrical and Computer Engineering
Doctorate of Philosophy, PhD

McMaster University, Hamilton, Ontario (1998-2002)
Department of Engineering Physics
Bachelor of Engineering, B.Eng

INDUSTRIAL CONTRIBUTIONS

Atomic Energy of Canada Ltd. Division of Qinshan Project Plant Control.
Period of employment: 05-2000 – 09-2000
Contributions: Development of analysis software for checking control software residing in DCC memory. Correcting and testing Qinshan's nuclear reactor software.

Atomic Energy of Canada Ltd. Division of Qinshan Project Plant Control
Period of employment: 05-1999 – 09-1999
Contributions: Development of SSCI Varian assembly software for monitoring I/O interrupts in Qinshan's nuclear reactor software. Developed software is running in Qinshan's station in China.

Johnson Controls Int., New Delhi, India. Division of Engineering
Period of employment: 05-1998 – 09-1998
Contributions: Design of the company's network architecture and the development of project control software.

AWARDS AND MEMBERSHIPS

Queen Elizabeth II Doctoral Scholarship. Period held: 05-2006/06-2008.

SPIE Scholarship in Optical Science and Engineering. Period held: 2007.

Presentation award at the 42nd Meeting of the Society of Cryobiology international conference. Minneapolis, Minnesota. July 22-28, 2005.

Member of SPIE – The International Society for Optical Engineering

Member of the University of Alberta SPIE student chapter

TEACHING ASSISTANTSHIPS AND SUPERVISED STUDENTS

Instructor for Photonics (University of Alberta) – EE 471
Period: 09-2007 – 12-2007.

Teaching assistant for Photonics (University of Alberta) - EE 471.
Period: 09-2006 – 12-2006.

Teaching assistant for Electromagnetics (University of Alberta) - EE 315.
Period: 09-2006 – 12-2006, 09-2005 – 12/2005.

Teaching assistant for Physical Electronics (University of Alberta) - EE 452.
Period: 01-2004 – 05-2004.

Teaching assistant for Clocks, Quanta & Chaos (University of Toronto) - Phy 205.
Period: 01-2003 – 05-2003.

Teaching assistant for Experimental Physics (University of Toronto) - Phy 135Y.
Period: 09-2002 – 05-2003.

Student supervised: Muhammad Jabakhanji
Project purpose: Engineering Physics 4th year project – EE 494/495
Project title: Optical imaging using optical coherence tomography (OCT)
Project duration: 01-2005 – 04-2005
Responsibilities include: Assisted the student in the conceptual and experimental design of an OCT system. Also provided training in optics and ultrafast lasers.

Student supervised: Kelvin Chow
Project purpose: Engineering Physics 4th year project – EE 494/495
Project title: Femtosecond laser interaction with biological material
Project duration: 01-2006 – 04-2006
Responsibilities include: Assisted in the development of an optical setup for manipulating live biological material.

Student supervised: June Cheng
Project purpose: Engineering Physics 4th year project – EE 494/495
Project title: Laser-assisted ablation of polymers & glass
Project duration: 01-2006 – 04-2006
Responsibilities include: Training the student on the regenerative amplifier for performing laser ablation experiments. Assisted in the characterization of ablated structures made in polymers and glass.

PUBLISHED JOURNAL ARTICLES

Kohli V., Elezzabi A.Y. Prospects and development in cell and embryo nanosurgery. Wiley Interdisciplinary Reviews: Nanomedicine. 2008. In print. (**invited review article**)

Kohli V., Elezzabi A.Y. Laser surgery of zebrafish (*Danio rerio*) embryos using femtosecond laser pulses: Optimal parameters for exogenous material delivery, and the laser's effect on short- and long-term development. Biomedical Central Biotechnology, 8:7, pgs. 1-20, 2008.

Kohli V. From cells to embryos: The application of femtosecond laser pulses for altering cellular material in complex biological systems. Proceedings of SPIE, The International Society for Optical Engineering, Vol. 6892, pgs. 68920J1-12, 2008 (**invited article**).

Kohli V., Elezzabi A.Y. Part I: Embryonic surgery using femtosecond laser pulses for the delivery of exogenous materials and the analysis of gene expression. Proceedings of SPIE, The International Society for Optical Engineering, Vol. 6854, pgs. 685413-1-9, 2008.

Kohli V., Elezzabi A.Y. Part II: Morphological analysis of embryonic development following femtosecond laser manipulation. Proceedings of SPIE, The International Society for Optical Engineering, Vol. 6854, pgs. 685404-1-10, 2008.

Kohli V., Robles V., Cancela M.L., Acker J.P., Waskiewicz A., Elezzabi A.Y. An alternative method for delivering exogenous material into developing zebrafish embryos. Biotechnology and Bioengineering, 98(6), pgs. 1230-1241, 2007.

Kohli V., Yu. D, Elezzabi, A.Y. Laser-assisted ablation of corneal-like material using focused femtosecond laser pulses. Proceedings of SPIE, The International Society for Optical Engineering, Vol. 6460, pgs. 6460D1-9, 2007.

Kohli V., Acker J.P., Elezzabi A.Y. Permeabilization & Cell Surgery Using Femtosecond Laser Pulses: An emerging tool for cellular manipulation. Proceedings of SPIE, The International Society for Optical Engineering, Vol. 6084, pgs. 608414-11, 2006.

Kohli V., Acker J.P., Elezzabi A.Y. Reversible Permeabilization Using High-Intensity Femtosecond Laser Pulses: Applications to Biopreservation. Biotechnology and Bioengineering. 92(7), pgs. 889-899, 2005.

Kohli V., Elezzabi A.Y., Acker J.P. Cell Nanosurgery Using Ultrashort (Femtosecond) Laser Pulses: Applications to Membrane Surgery and Cell Isolation. Lasers in Surgery and Medicine. 37(3), pgs. 227-230, 2005.

OTHER SCHOLARLY PUBLICATIONS

Kohli V., Elezzabi A.Y. Performing laser surgery and transfection on living embryos. Biomedical Optics and Medical Imaging. SPIE Technical article. DOI: 10.1117/2.1200801.0973. 2008 **(invited article)**

Robles V., Herraez E., Kohli V., Cabrita P. Aquaculture Research Trends: Prospects and Development in sperm and fish embryo cryopreservation. Nova Science Publisher Inc. In press. 2008. **(invited book chapter)**

Kohli V., Robles V., Cancela M.L., Acker J.P., Waskiewicz A., Elezzabi A.Y. **Awarded the journal cover image of Biotechnology and Bioengineering Journal, 98(6)**. 2007.

Kohli V., Elezzabi A.Y., Acker J.P. LASER APPARATUS AND METHOD FOR MANIPULATING CELLS. **United States patent**, PCT/CA2005/001556, International filing date: 11.10.2005.

ORAL CONFERENCE PRESENTATIONS

Kohli V. From cells to embryos: The application of femtosecond laser pulses for altering cellular material in complex biological systems. Photonics West. San Jose, California, USA, January 20-25, 2008 **(invited talk)**.

Kohli V., Elezzabi A.Y. Part I: Embryonic surgery using femtosecond laser pulses for the delivery of exogenous materials and the analysis of gene expression. Photonics West. San Jose, California, USA, January 20-25, 2008.

Kohli V., Elezzabi A.Y. Part II: Morphological analysis of embryonic development following femtosecond laser manipulation. Photonics West. San Jose, California, USA, January 20-25, 2008.

Kohli V., Yu D., Elezzabi A.Y. Laser ablation of corneal-like material using high-intensity femtosecond laser pulses. Photonics West. San Jose, California, USA, January 20-25, 2007.

Kohli V., Acker J.P., Elezzabi A.Y. Femtosecond pulse permeabilization of live mammalian cells. Photonics West. San Jose, California, USA, January 21-26, 2006.

Kohli V., Acker J.P., Elezzabi A.Y. Experimental and Theoretical Analysis of Cell Surgery and Permeabilization. CRYO2005. 42nd Meeting of the Society of Cryobiology, Minneapolis, Minnesota. July 22-28, 2005.

Kohli V., Acker J.P., Elezzabi A.Y. The Applicability of Near-Infrared Femtosecond Laser Pulses for Non-Invasive Studies of Live Mammalian Cells. Extreme Cryo. Calgary, Alberta, Canada. January 29-31, 2005.

Kohli V. Manipulation of Cells Using Ultrashort Laser Pulses. University of Alberta, Department of Laboratory Medicine and Pathology, April 14, 2004 (**invited talk**).